Samarium-Doped Fluorophosphate and Fluoroaluminate Glasses for High-Dose High-Resolution Dosimetry for Microbeam Radiation Therapy

A Thesis Submitted to the

College of Graduate and Postdoctoral Studies

In Partial Fulfilment of the Requirements

for the Degree of

Doctor of Philosophy

in the Division of Biomedical Engineering

University of Saskatchewan

Saskatoon

By

FARLEY CHICILO

Permission to Use

In presenting this thesis in partial fulfillment of the requirements for a Postgraduate degree from the University of Saskatchewan, I agree that the Libraries of this University may make it freely available for inspection. I further agree that permission for copying of this thesis in any manner, in whole or in part, for scholarly purposes may be granted by the professor or professors who supervised my thesis work or, in their absence, by the Chair of the Department or the Head of the College in which my thesis work was done. It is understood that any copying or publication or use of this thesis or parts thereof for financial gain shall not be allowed without my written permission. It is also understood that due recognition shall be given to me and to the University of Saskatchewan in any scholarly use which may be made of any material in my thesis.

Requests for permission to copy or to make other uses of materials in this thesis in whole or part should be addressed to:

Head of the Division of Biomedical Engineering
57 Campus Drive
University of Saskatchewan
Saskatoon, Saskatchewan, Canada
S7N 5A9

OR

College of Graduate and Postdoctoral Studies
University of Saskatchewan
116 Thorvaldson Building, 110 Science Place
Saskatoon, Saskatchewan S7N 5C9 Canada

Abstract

Microbeam Radiation Therapy (MRT) is an important and developing radiotherapy technique that uses spatially fractionated doses, several orders of magnitude larger than that of the doses used in conventional radiation therapy. Healthy tissue displays remarkable resistance to damage caused from microscopically narrow, fractionated, planar beams of x-rays, while showing preferential damage towards cancerous growths, allowing for a high potential towards the treatment of often inoperable tumours. These synchrotron generated, spatially fractionated, planar beams are referred to as microbeams, and have a thickness of 20 – 50 μm and are separated by distances of 100 – 400 μm. The dose delivered at the center of the microbeam can be on the order of thousands of Grays (Gy), whereas the dose between each microbeam should be kept below tens of Gy. An important aspect of MRT is the spatial distribution of the dose delivered to the patient, which must be accurately measured. Ultimately, both high resolution and large dynamic range dosimetric measurements must be done simultaneously.

The objective of this Ph.D. research involves the development and characterization of a dosimetric technique that fulfills the requirements of measuring dose distributions of microbeams. The proposed technique uses the indirect detection of x-rays, where the dose is recorded in a glass plate which can then be readout using a confocal microscopy system. The dose delivered is recorded by using trivalent samarium (Sm^{3+}) doped fluoroaluminate and fluoro-phosphate glasses, where conversion from the trivalent form of samarium to the divalent form (Sm^{2+}) occurs after exposure to x-rays. The extent of this conversion can be readout and digitized with high resolution using a confocal microscopy system that utilizes the easily distinguishable photoluminescent spectra of Sm^{3+} to Sm^{2+}.

The work carried out in this research involves the high resolution recording of microbeam profiles performed at the Canadian synchrotron, using samarium doped glass plates under a variety of irradiation parameters in order to determine their suitability for dosimetric applications. In particular, the dose rate and x-ray energy dependence of these materials is investigated, as well as the determination of the optimum Sm^{3+} dopant concentration. Further, the confocal measurement technique is investigated, as well as the suitability of ion implantation of samarium ions in order to improve the signal readout. Lastly, the change in dose distributions of microbeams is

investigated by performing irradiations over a wide range of monochromatic x-rays, so that the potential effect of the selected energy on MRT treatment planning can be examined.

Acknowledgement

I would like to sincerely express my thanks and gratitude to my supervisor, Dr. Safa Kasap, who has offered me invaluable guidance, support, friendship, and encouragement. His knowledge and passion for the sciences (and cakes) is infectious, and has helped make my studies incredibly worthwhile and memorable. Both Dr. Kasap and my co-supervisor, Dr. Dean Chapman, have been constant sources of inspiration, and have always pushed me further in my understanding of the materials presented, without them I would not have experienced the many rewarding moments as a student that I will carry with me into the future. I would also like to extend my immense gratitude towards Dr. George Belev and Dr. Cyril Koughia, who have aided me throughout my studies, and have always been willing to answer my questions and offer guidance with many experiments. The work performed in this thesis would not have been successful without their tireless assistance, and much of what I have learned, I owe to them.

I am also enormously grateful to Dr. Andy Edgar and Mr. Chris Varoy at the University of Wellington, New Zealand, who synthesized glass materials used in this work, and to Dr. Richard Curry, at the University of Manchester, UK, who performed ion implantation, and allowed me the opportunity to travel and visit his laboratory. Their expertise and input towards this research has been invaluable. I would also like to thank my colleagues for their friendship and support, and I would specifically like to thank Dr. Go Okada, who helped guide me through the beginning of my research.

Not least of all, I would like to sincerely thank my friends and family who have been supportive throughout my studies and my life. Their encouragement, and patience, cannot be understated.

Dedication

I lovingly dedicate this thesis to Carly, who has always believed in me, and who puts up with me and my dog, Quinn, whom I also dedicate this thesis to.

Table of Contents

List of Figures

Figure **Page**

List of Tables

Table **Page**

List of Abbreviations

BMIT	Biomedical Imaging and Therapy (beamline)
BPF	Band-Pass Filter
CB	Conduction Band
CLS	Canadian Light Source
CNS	Central Nervous System
CSDA	Continuous Slowing Down Approximation
CVD	Chemical Vapor Deposition
DM	Dichroic Mirror
DPSS	Diode-Pumped Solid-State
DSC	Differential Scanning Calorimetry
eV	Electron Volt (1 eV = 1.602×10^{-19} J)
FA	Fluoroaluminate
FOV	Field of View
FP	Fluorophosphate
FW@10%	Full Width at 10% of Maximum Value
FWHM	Full Width at Half Maximum
Gy	Gray (Gy = J/kg)
IRF	Instrument Response Function
LED	Light Emitting Diode
LINAC	Linear Accelerator
LPF	Long-Pass Filter
MCNP6	Monte Carlo N-Particles Transport, version 6
MOSFET	Metal-Oxide Semiconductor Field Effect Transistor
MRI	Magnetic Resonance Imaging

MRT	Microbeam Radiation Therapy
MSC	Multi-Slit Collimator
ND Filter	Neutral Density Filter
PL	Photoluminescence
PMT	Photomultiplier Tube
POEC	Phosphorous-Oxygen Electron Centers
POHC	Phosphorous-Oxygen Hole Centers
PVDR	Peak-to-Valley Dose Ratio
QFRS	Quadrature Frequency Resolved Spectroscopy
RAD	Radiation Absorbed Dose
RE	Rare Earth
SRIM	Stopping Range of Ions in Matter
Sm^{2+}	Divalent Samarium
Sm^{3+}	Trivalent Samarium
T_c	Glass Crystallization Temperature
TCSPC	Time Correlated Single Photon Counting System
T_g	Glass Transition Temperature
TLD	Thermoluminecent Dosimeter
UV	Ultraviolet
VB	Valence Band

Chapter 1

Introduction and Organization of the Thesis

The practice of using high energy ionizing radiation for the treatment of cancerous growths in patients has been in use for over a hundred years. Shortly after the discovery of the x-ray by William Roentgen in 1896, high energy photons, called x-rays, were used as a non-invasive, non-surgical, treatment method, which causes lethal damage to tumours within a patient. The disadvantage of standard radiotherapy techniques results from simultaneous damage to healthy tissue during the treatment of tumours, limiting the total dose that can be delivered to a patient (~40 Gy). Microbeam radiation therapy (MRT) uses small, parallel, spatially fractionated x-ray beams which allows for substantially higher doses to be delivered to a patient in a single treatment (500 Gy and higher) while causing minimal damage to healthy tissue in the path of the microbeams. This tissue sparing effect results from the unique irradiation geometry of the microbeams, which are multiple narrow planar beams of x-rays, tens of microns wide and separated by hundreds of microns, shown in Figure 1.1. This technique allows for healthy cells, adjacent to the volume of irradiation, to aid in the repair of damaged tissue, an ability that cancerous growths do not exhibit. The unique qualities of microbeam radiation therapy is therefore well suited for patients with often inoperable tumours, such as spinal, or brain growths, where other available cancer treatment methods may prove to be too great a risk.

The measurement of the unique radiation pattern resulting from MRT provides a dosimetry challenge. That is, the "peak" dose at the center of each microbeam and the "valley" doses between microbeams vary considerably, and both must be simultaneously with high resolution. Current conventional x-ray detection techniques do not exhibit the necessary capabilities required to measure a dynamic range that covers potentially thousands of grays over a distance of several microns. Additionally, a detector should not have a strong dose rate or energy dependence and should be reusable over multiple irradiations. Current dosimetric methods do not satisfy the required measurement of both "peak" and "valley" doses with micron level resolution in two

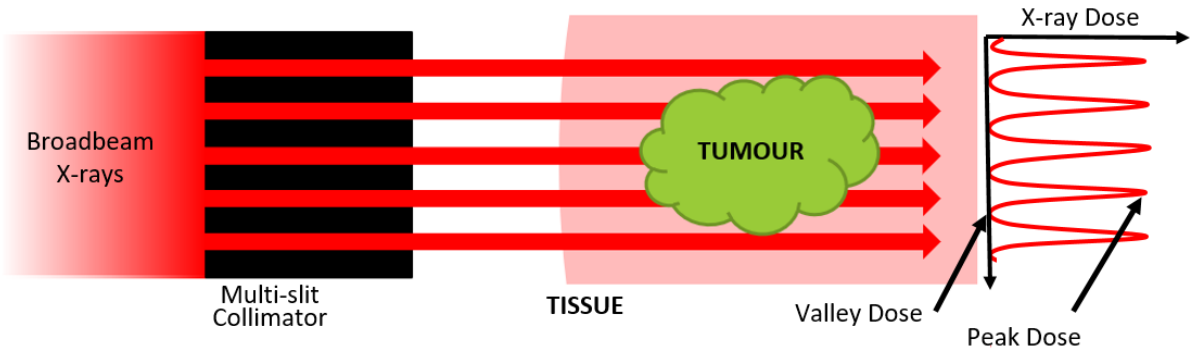

Figure 1.1 Illustration of microbeam radiation therapy. Synchrotron generated collimated x-rays pass through a multislit collimator, which produce a microbeam array of narrow planar beams that penetrate into a patient. Healthy tissue does not show significant damage, whereas tumours shows necrosis after irradiation. The resulting dose profiles has a large value at the center of the microbeam, referred to as a "peak" dose, and an adjacent low dose area, referred to as a "valley" dose.

dimensions. Creating a record of the dose delivered to a patient is crucial, not only for patient care, but also for treatment optimization.

The work of this thesis involves the characterization of a novel, high dose, high-resolution dosimeter, which fulfills the requirements for MRT dosimetry. The dosimetric technique involves measuring valence change of a rare-earth ion after exposure to x-rays. Of the rare earth ions, samarium is of particular interest, since the trivalent and divalent ions have distinct and separable photoluminescent (PL) spectra after excitation, shown in Figure 1.2, and are well suited for detection by photomultiplier tubes (PMTs). When samarium ions are embedded in a suitable host, the conversion of Sm^{3+} to Sm^{2+} can be used as a measurement of the dose delivered. Put differently, the measured number of Sm^{3+}ions converted to Sm^{2+} is a direct measurement of the dose delivered, which can be expressed as

$$\text{Dose} \propto \frac{\text{PL}(Sm^{2+})}{\text{PL}(Sm^{3+})} \tag{1.1}$$

It has been demonstrated that fluoroaluminate (FA) and fluorophosphate (FP) glasses are excellent host materials for Sm^{3+} valence conversion and these materials are reusable, stable, and are capable of measuring doses ranging from less than five Gy, to thousands of Gys. Additionally, since FA and FP glass materials are uniformly doped with samarium ions, the achievable resolution

is largely limited by the readout technique and can reach submicron levels, thus fulfilling the spatial resolution requirements of MRT dosimetry.

The success of MRT relies on highly collimated, high fluence, and high energy x-rays which is produced by a synchrotron source. A large fluence rate allows for the total dose to be delivered to a patient within a very short exposure time. Any movement of the patient will result in the undesirable blurring of the microbeam profile, thus decreasing the effectiveness of the MRT technique. Further, high photon energies (100 keV and up) would be necessary for human patients, since the majority of low energy x-ray photons are absorbed at the surface of the target due to the predominant photoelectric interaction; a high energy is required to deposit adequate dose at the affected area within a material. A successful dosimeter must then be capable of measuring a large

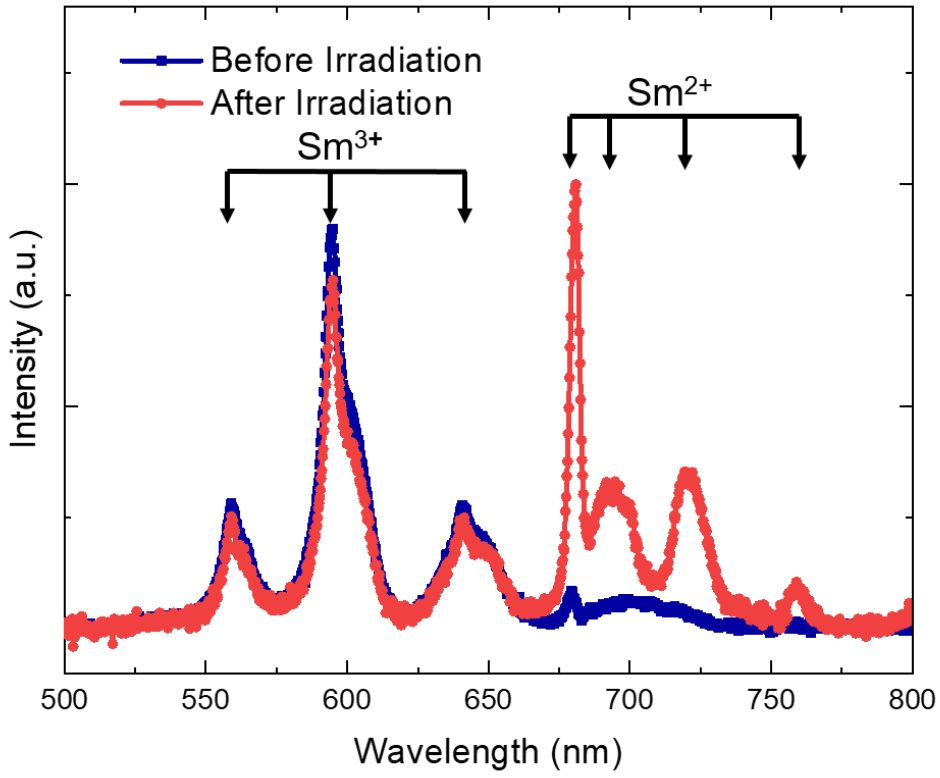

Figure 1.2 Photoluminescent spectra of Sm^{3+} and Sm^{2+} ions before and after irradiation in 1% Sm-doped FA glass. Samples were exposed to an approximate dose of 500 Gy_{air} using a FAXITRON x-ray cabinet. These distinct emission spectra are characteristic of rare earths, owing to the so-called "forbidden" optical transitions present in Sm^{3+} and Sm^{2+} which give sharp emission peaks.

dynamic range with high resolution, be reusable and stable, and the response should be independent of the dose rate, and incident x-ray energy. The findings of this work show that Sm-doped FA and FP glasses synthesized are a powerful tool for the accurate measurement of microbeams at a high resolution and can be used for MRT dosimetry purposes over a wide range of irradiation conditions.

1.1 Objectives of Thesis

The aim of the research in this thesis involves the characterization of Sm-doped FA and FP glasses, which demonstrate the necessary requirements for MRT dosimetry. The properties of Sm-doped FA and FP glasses are investigated along with the measurement techniques, as well as the dose rate and energy dependence of the conversion of these materials. Included in the characterization of the measured response of the Sm-doped materials, is a characterization of the microbeam properties, that is, how modification of the incident x-ray energy can have an overall effect on the spatial dose distributions of the microbeams. Of significant importance to the success of MRT is that adjacent healthy tissue can help in repairing damaged tissue within the path of the microbeam. In order for this to occur, adjacent healthy tissue, which exists in the "valley" of the beam profile, must receive a minimal dose. Therefore, an important consideration in MRT is the so-called peak-to-valley dose ratio (PVDR), which should be maximized for patient treatment. Since Sm-doped FA and FP glasses are capable of measuring doses over a wide dynamic range with micron level resolution, these can then be used to detect subtle changes in the beam profile as the incident energy is changed, as is investigated. The objectives for this research are summarized below,

- Optimization of the total samarium dopant concentration to determine the ideal composition that leads to a high signal to noise ratio, while still maintaining stability of the signal after irradiation.
- Determination of the ideal host material. Both FA and FP glasses have demonstrated successful conversion. However, an investigation into the overall stability and the effect of photodarkening between these host materials is examined.

- Characterization of the measurement technique. Since FA and FP glasses are uniformly doped with Sm-ions, the highest achievable resolution is theoretically limited to the readout instrument, and so the current fluorescent confocal microscopy instrument is characterized.
- Study of the dose rate dependence of FA and FP glasses. The conversion of Sm^{3+} to Sm^{2+} should remain constant, regardless of the fluence of x-rays incident on the sample.
- Study of the energy dependence of FA and FP glasses. Likewise, the conversion of Sm^{3+} to Sm^{2+} should ideally be independent of the incident x-ray energy. If the response of the sample is not independent of energy, then calibration is necessary for the response of the sample at a desired energy.
- Improvement of the readout method. Conversion of Sm^{3+} to Sm^{2+} occurs within the total volume of the bulk Sm-doped glass, which can cause complications in dose calculations. If it is possible to only measure conversion of Sm ions and the resulting PL within a narrow region near the surface of the glass, then readout can be simplified and the dose measured from the sample would then represent a surface dose.
- Optimization of treatment planning. Currently MRT is not at the stage of human trials. Before these trials can be attempted, treatment conditions must be considered under a variety of circumstances, including selecting the optimal incident x-ray energy range to maximize the PVDR. The use of monochromatic x-ray energies can be used to measure how radiation interactions within Sm-doped FA glasses may change over a wide energy range and affect the beam profile. Further, these resulting beam characteristics can then be compared to Monte Carlo simulations that simulate photon and electron transport within a given material thus serving as a verification method to Monte Carlo transport models allowing for accurate predictions of particle transport in a given solid.

1.2 Organization of the Thesis

The organization of this thesis follows a manuscript style format. The published manuscripts are included in chapter 4, 5, and 6 of the thesis. Chapter 2 discusses the relevant theoretical background necessary for understanding the subsequent transcripts. Chapter 3 discusses the experimental methods applied in the research presented in following chapters. Lastly, chapter 7 summarizes the material and suggests ideas for future research.

The basis of chapter 2 involves applicable forms of x-ray production, interactions, and detection methods for MRT. This is followed by a description of rare earth ions, with an emphasis on samarium ions and their properties, and suitable host materials. This chapter also includes a description of the ion implantation process and the application of Sm ion implantation into FA glass materials.

Chapter 3 involves an explanation of the various experimental methods and techniques, which are used to obtain results in the following chapters. These techniques involve sample characterization, irradiation techniques, confocal fluorescent microscopy, data collection, and ion implantation

The manuscript in chapter 4 involves the implantation of Sm-ions in FA glasses, where Sm^{3+} and Sm^{2+} ions reside within a thin plane less than one micron below the surface of the glass. The investigation of the resulting Sm^{3+} to Sm^{2+} conversion after Sm-ion implantation are studied using high energy ion implantation techniques, as well as the resulting photoluminescent signals from the bulk glass samples. Since the measured Sm^{3+} and Sm^{2+} signals are relatively weak when compared to bulk doped samples, there is observable overlapping broad emission signals resulting from "allowed" emission spectra. These "allowed" transitions with fast lifetimes (~1 ns) are attributed to radiation induced defects, and can be separated from the "forbidden" transitions of the Sm^{3+} and Sm^{2+} lifetimes (~1 ms) by measuring PL signals "in phase" and "out of phase". The resulting PL from Sm^{3+} to Sm^{2+} conversion therefore exists at the surface of the material, as opposed within the total volume in bulk doped samples, and the response value measured represents surface dose.

Chapter 5 investigates the response values Sm-dopant concentrations for FA and FP glasses under multiple dose rates and incident x-ray energies. The overall conversion and stability of various Sm mol% dopant concentration is investigated in FA and FP glasses, which considers the response values of these materials under identical irradiation conditions. 1% Sm-doped FA glass is proposed an ideal host material and dopant concentration. These findings lead to the measurement of calibration curves energies ranging from 40 – 120 keV, at doses values ranging from 5 – 2000 Gy. The measured response of 1% Sm doped FA glass at a variety of measured laser focal depths are compared, and the achievable resolution of the current fluorescent confocal microscopy system is investigated.

Chapter 6 investigates how the dose deposited in the valley region and the resulting dose profile may change as a function of the incident x-ray energy. The change in the valley dose can be quantified by measuring the width of the microbeam at 10% of the maximum value (FW@10%) as a function of energy. As the incident x-ray energy is modified, this creates a change in the probability, energy, and direction of scattered and ejected photons and electrons that can cause dose to be deposited outside of the exposed regions that are directly incident to the x-rays within the glass. The measured widths agrees with simulated Monte Carlo values, which model the transportation of electrons and photons within a given material as a function of energy. Using 1% Sm doped FA glasses as a verification method for this model demonstrates the confidence that can be placed in the MCNP6 code. This MCNP6 code can then be used to predict ideal treatment conditions for humans leading to the maximization of the PVDR in tissue. Further, the ideal width of the microbeam is optimized. This determines that there is an ideal slit width range that does not significantly attenuate peak dose, while still maintaining desirable adjacent tissue repairing effect resulting from sufficiently narrow microbeams.

Lastly, Chapter 7 summarizes and concludes the findings of the thesis and suggests possible future works that can be considered in order to improve upon the measurement technique discussed within this work.

Chapter 2

Theoretical Background

The aim of this chapter is to provide the necessary scientific background in order to better understand the content in subsequent chapters of the thesis. The materials covered in this chapter include relevant x-ray production methods, interactions of x-rays with materials, an introduction into microbeam radiation therapy, detection of x-rays and potential dosimeters for microbeam radiation therapy, rare earth ions and their luminescent properties, and ion implantation.

2.1 X-ray Production

X-rays are a form of electromagnetic radiation that have a wavelength several orders of magnitude shorter than that of visible light. These high energy photons were first detected by Wilhelm Röntgen in 1895, referring to the radiation as "X", since the origins were unknown at the time of discovery. Röntgen found that x-rays were able to penetrate through human tissue, yet showed significant contrast in bone, thus realizing the vast potential for medical applications. Since the discovery of the x-ray, there have been a wide range of applications, including industrial, security,

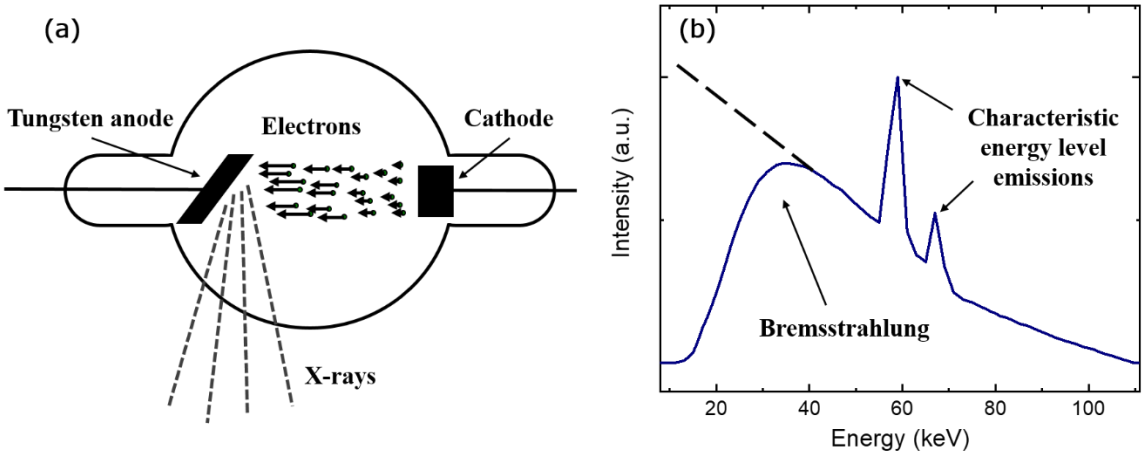

Figure 2.1 (a) Illustration of a standard x-ray tube (b) Typical energy spectrum of an x-ray tube with a tungsten anode operating at a voltage of 110 kVp, calculated using [1]. Dotted line indicates the spectrum before filtration by a thin window with low atomic number.

medicine and many others. The application of x-rays in medicine involves imaging or non-invasive therapeutic applications. X-rays are capable of penetrating and depositing dose within a material, and the predicted range of the x-ray within a material can be tuned by modifying the energy of the incident high energy photon. The tunable nature of x-ray properties can be controlled by the production method and will be discussed in the following section. Since x-rays are not visible to the naked eye, x-ray detection methods are of equal importance to the production, and both must be carefully considered for any application.

X-rays productions considered in this work are performed utilizing two different types of processes. These methods of interest in this work are through the acceleration of charged particles, such as electrons, or via electron decay from a higher energy orbital to a lower orbital within an atom. Bremsstrahlung and synchrotron generated x-rays are examples of x-ray production through accelerating electrons, which are done linearly and centripetally, respectively. The most common method of x-ray production is an x-ray tube, which consists of a cathode electron source and an

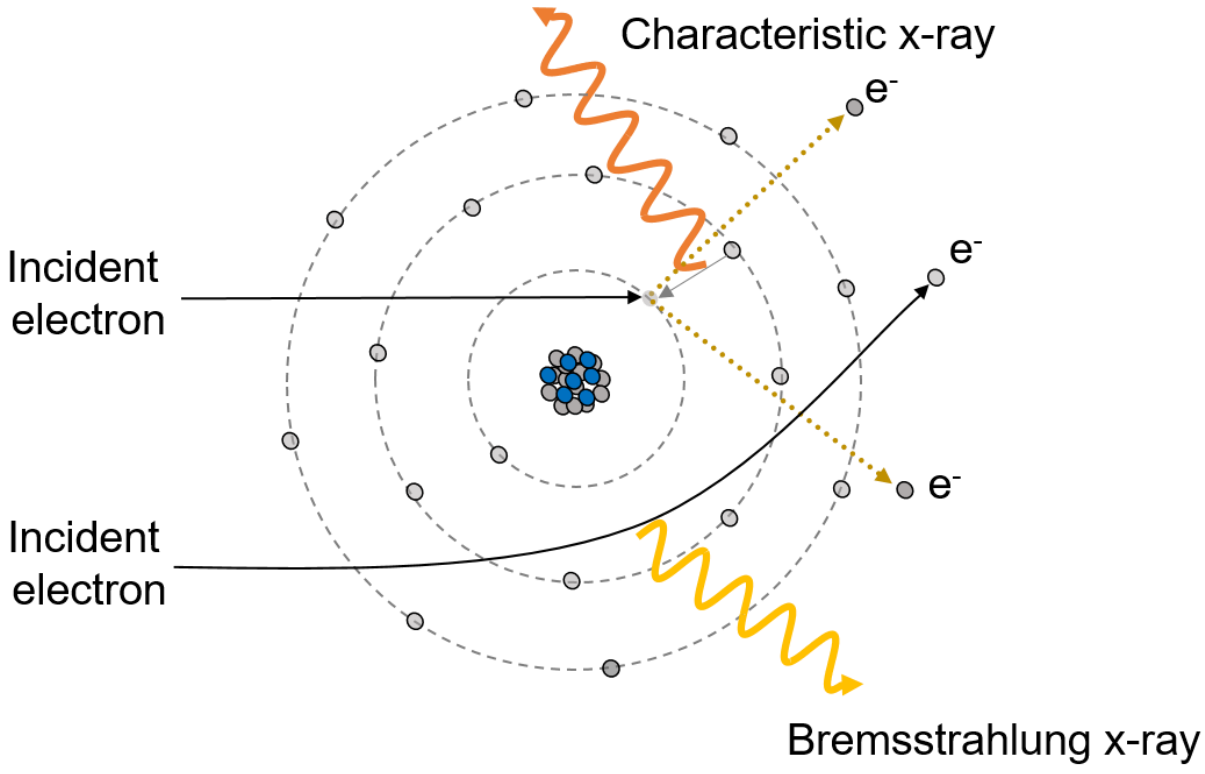

Figure 2.2 Diagram of electron interactions in an atom and the production of x-rays. Top portion demonstrates the method of production for characteristic x-rays, bottom portion demonstrates production of bremsstrahlung x-rays.

anode target within a vacuum tube shown in Figure 2.1 (a). In an x-ray tube, high energy electrons from the cathode bombard the target anode (typically a heavy element such as tungsten, copper, molybdenum, etc.). This bombardment of electrons causes the production of x-rays by bremsstrahlung emission, which results from the deceleration of electrons hitting the target. It also produces characteristic quantified x-ray emissions due to the removal of an inner level electron followed by a relaxation with emission of an x-ray. The resulting x-ray spectrum is a combination of broad emissions (bremsstrahlung) and narrow peak lines specific to the anode material, as shown in Figure 2.1 (b) [1]. This broad shape of the bremsstrahlung emission spectrum is dependent upon the kinetic energy of the electrons and, low energy electrons (shown as the dotted line in Figure 2.1 (b)) are filtered by a window present in x-ray sources, typically made from a material with a low atomic number such as beryllium.

The term "bremsstrahlung" comes from the German word, bremsen, which means, "to brake". Bremsstrahlung radiation, therefore, is used to describe emitted radiation that results from the deceleration, or braking, of electrons which produces a continuous broad spectrum of x-rays. When the voltage across the cathode and anode is increased, electrons have greater kinetic energy and the subsequent deceleration of electrons results from single, or more likely, multiple collisions, which creates a broad emission spectra. These x-rays can be produced by collisions within the atomic nuclei, or from coulomb interactions, which causes the electron path to be bent, producing x-rays in the trajectory of the electron, as shown in the lower half of Figure 2.2. The angular distribution of the x-rays from the anode is large, which creates the fan-like emission depicted in Figure 2.1 (a).

X-rays emitted in the characteristic emission spectra requires an incident electron with sufficient energy to remove an electron from the inner shell, such as a K-shell, of the anode material. The vacancy created in the inner K-shell would then be occupied by an electron from an outer L-shell orbit, which results in the emission of a specific energy x-ray, as shown in the peaks of Figure 2.1 (b). The filling of the unoccupied inner electron state by an outer shell electron emits a quantized photon that is defined by the energy difference between the upper and lower shells, where the separation between energy levels is specific to the material. An illustration of this interaction is shown in the upper portion of Figure 2.2. If accelerated electrons do not strike

electrons in the surrounding orbit, then it likely that electrons will interact with the nuclei via coulomb interactions, causing their path to bend, and produce bremsstrahlung x-rays. The electron interactions shown in Figure 2.2 are the primary processes involved in producing x-rays from a standard cathode source, resulting in the energy spectrum shown in Figure 2.1 (b).

Synchrotron facilities allow for specialized x-ray applications, in that the source is tunable, collimated, and has a high fluence. The unique properties of synchrotron generated x-rays cannot be achieved by an x-ray tube source. Synchrotron generated x-rays are often used for high-resolution imaging, crystallography, spectroscopy, radiation therapy, among other applications. If a magnetic field is applied perpendicular to the motion of electrically charged particle, that charged particle will move in a circular path. When the path of the electron bends, this causes a change in

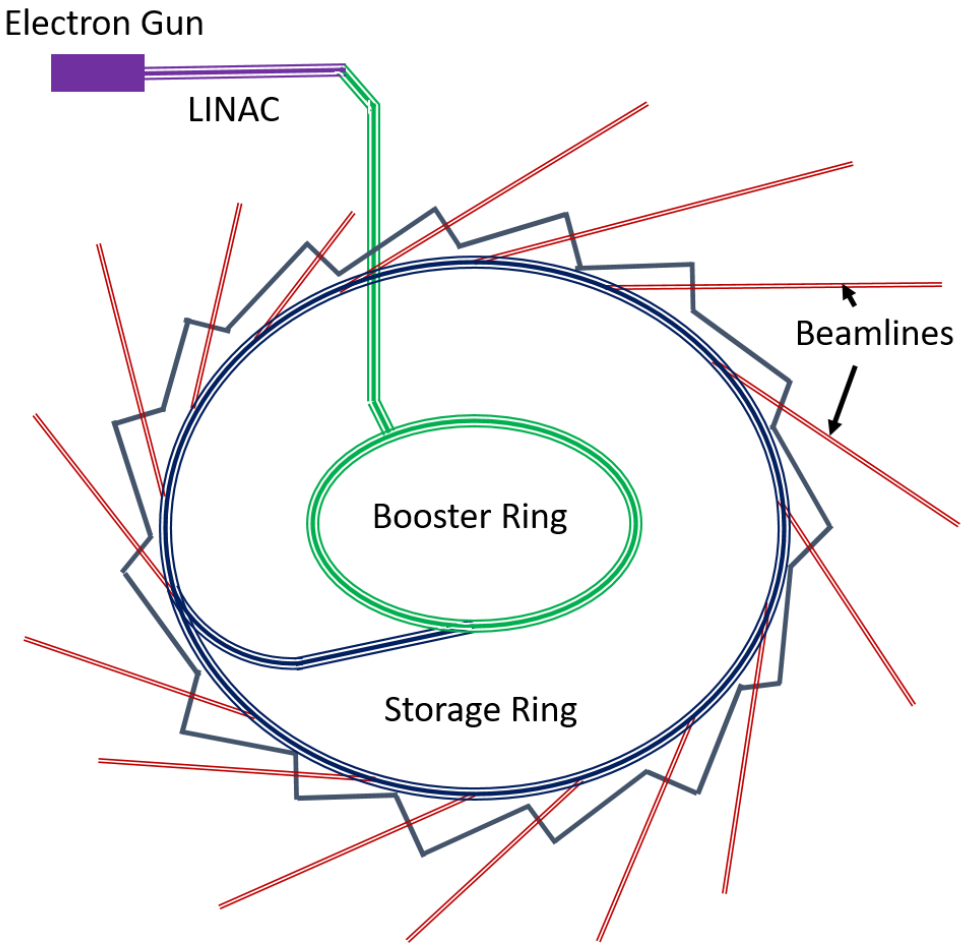

Figure 2.3 Schematic of a synchrotron facility layout.

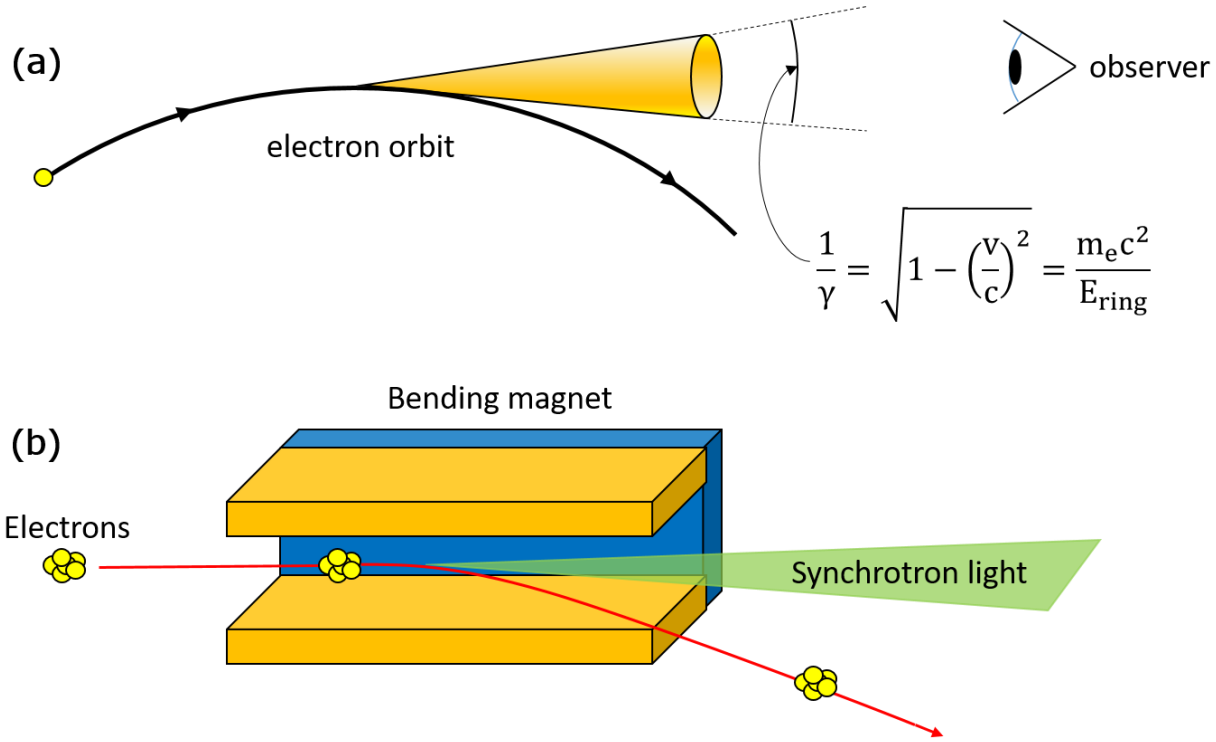

Figure 2.4 (a) X-rays emitted from an electron accelerated centripetally, such as in a synchrotron facility. The radiation is confined to a narrow cone with an opening of 1/γ (b) Dipole bending magnet causes the path of the electrons to be bent, producing synchrotron light.

the velocity vector and causes electromagnetic radiation. When the charged particle (electron) is accelerated centripetally to relativistic speeds, this energy is emitted at high energies in the x-ray region. In order to produce these high energy, intense, and collimated x-rays, an electron gun is used to produce pulses of electrons under vacuum, which are then injected in to a linear accelerator (LINAC) that accelerate electrons to energies in the MeV range. Afterwards, electrons are transferred into the booster ring, where the energy of the electrons are increased further and the electrons reach relativistic speeds. These high energy electrons are then transferred into the storage ring where synchrotron x-rays are emitted towards the surrounding beamlines, as shown in Figure 2.3. The electrons within the storage rings are bent in order to keep them on a centripetal path with the use of bending magnets, shown in Figure 2.4 (b), these bending magnets can be dipole, quadrupole, or sextupole. The x-rays produced from a bend magnet will have a continuous and broad spectrum and the brilliance of the x-rays created by a bend magnet at the center of the beam (assuming a small vertical beam size compared to $\frac{1}{\gamma}$ shown in Figure 2.4 (a) [2]), can be calculated by

$$\left.\frac{d^2\dot{b}}{d\theta d\psi}\right|_{\psi=0} = 1.327 \times 10^{13} E_R^2[\mathrm{GeV}] I[\mathrm{A}] H_2(y); [\mathrm{ph} \cdot \mathrm{s}^{-1} \cdot \mathrm{mr}^{-2} \cdot 0.1\%\mathrm{bw}^{-1}] \qquad (2.1)$$

where E_R is the ring energy in GeV, I is the storage beam current in Amperes, $H_2(y)$ is the taken from the universal flux curve and is a function of energy, $\dot{b}$ is the flux of photons, and θ is the observation angle in the horizontal plane. The radiation angle of the emitted x-rays from a bending magnet is approximately $1/\gamma$ as shown in Figure 2.4 (a), where γ is the relativistic correction factor, and can be calculated by

$$\gamma = \frac{1}{\sqrt{1-(v/c)^2}} = \frac{E_R}{m_e c^2} \qquad (2.2)$$

Once electrons have been injected into the storage ring, emitted x-rays are then directed towards the surrounding beamlines, which are modified to suit the specific technique or application for each beamline. Selection of particular photon energies is performed with the use of a monochromator, which often uses two crystals that allow for the tuning of selected energies with narrow bandwidths. These crystals are typically made from silicon or synthetic diamond, both of which have high crystal order. The first crystal diffracts the polychromatic incident beam as a function of the angle of between the beam and the crystal, the second crystal adjusts the beam height and direction, as shown in Figure 2.5. In order to select a specific wavelength, crystals are

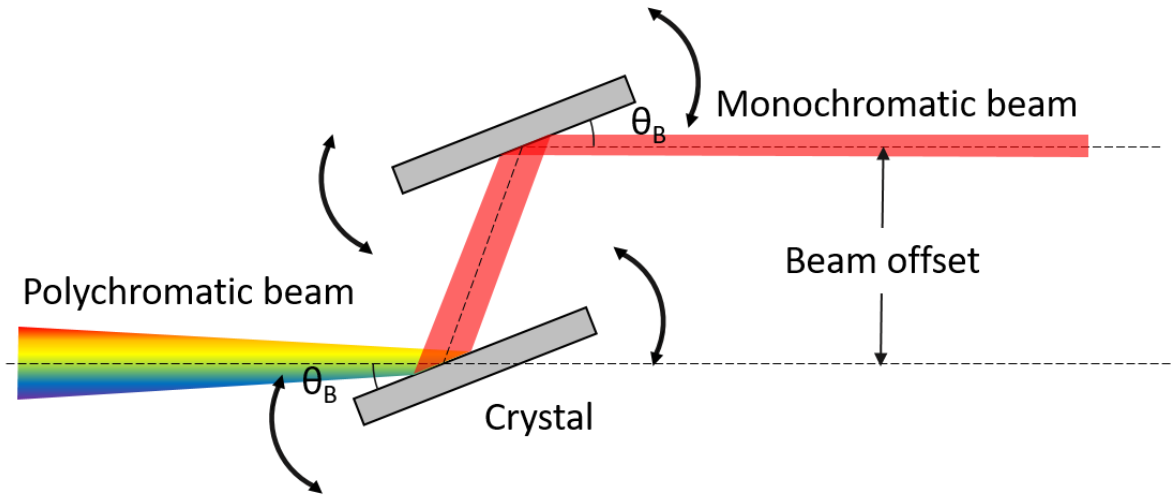

Figure 2.5 Diagram of a double crystal monochromator. Crystals are rotated on an axis to select the desired energy.

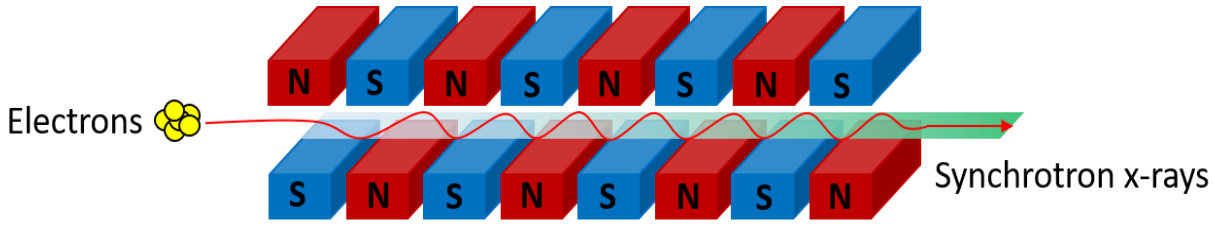

Figure 2.6 Simplified diagram of an insertion device used to produce higher intensity synchrotron light using the periodic arrangement of multipole magnets.

rotated, and in some monochromator geometries, the second crystal can be bent in order to focus the beam. These crystals are often cooled to reduce thermal expansion from the high power of synchrotron x-rays. The desired energy using a double crystal monochromator is selected using Bragg's law, given by,

$$2\, d_{h,k,l}\, \sin\theta_B = n\,\lambda \qquad (2.3)$$

where θ_B is the Bragg angle between the wavevector (incident photon) and the crystal lattice planes, n is an integer that denotes the order of the reflection, λ is the reflected wavelength, and $d_{h,k,l}$ is the interplanar spacing. The interplanar spacing, $d_{h,k,l}$, can be calculated by $d_{h,k,l} = a_0/\sqrt{h^2+k^2+l^2}$ where a_0 is the atomic spacing between atoms and *h*, *k*, and *l* are miller indices that denote the crystal structure of cubic lattices.

The fluence output from the storage ring can be significantly enhanced by the use of multiple magnets with alternating polarity, called insertion devices. Insertion devices are arrays of magnets, shown in Figure 2.6, where the electrons path is bent back and forth as it travels through the device, referred to as wigglers or undulators. The alternating magnetic field causes the path of the electrons to "wiggle" between each set of magnets, and this acceleration causes emission of radiation at each pole. As opposed to bend magnets, insertion devices are typically installed in the linear sections of the storage ring, or at beamlines, in order to optimize beam conditions for experimental applications. Wigglers and undulators have a very similar mechanical construction, however, they can be distinguished by their *K*-factor, a dimensionless constant, which is defined as:

$$K = \frac{eB\lambda_u}{2\pi\beta m_e c} = 93.4\, B[\mathrm{T}]\lambda_u[\mathrm{m}] \qquad (2.4)$$

where e is the charge of an electron, B is the peak magnetic field, λ_u is the period of the insertion device, β is the speed of the electron calculated by $\beta = v/c \approx 1$, m_e is the rest mass of the electron, and c is the speed of light.

When K << 1, the oscillations of the electrons are small, which creates a very narrow "pencil" beam, shown in Figure 2.7. Light emitted at a given pole interferes with that of the following poles, and so the energy spectrum exhibits peaks in the spectrum caused by this interference, as shown in Figure 2.8. The narrow "pencil" beam emitted from an undulator has a radiation angle that is proportional to $1/\sqrt{N}\,\gamma$ where N is the number of poles in the undulator. An undulator uses a low periodic magnetic field which can generate radiation at specific harmonics. Conversely, if K >> 1, coherence effects are no longer significant due to the larger oscillations and

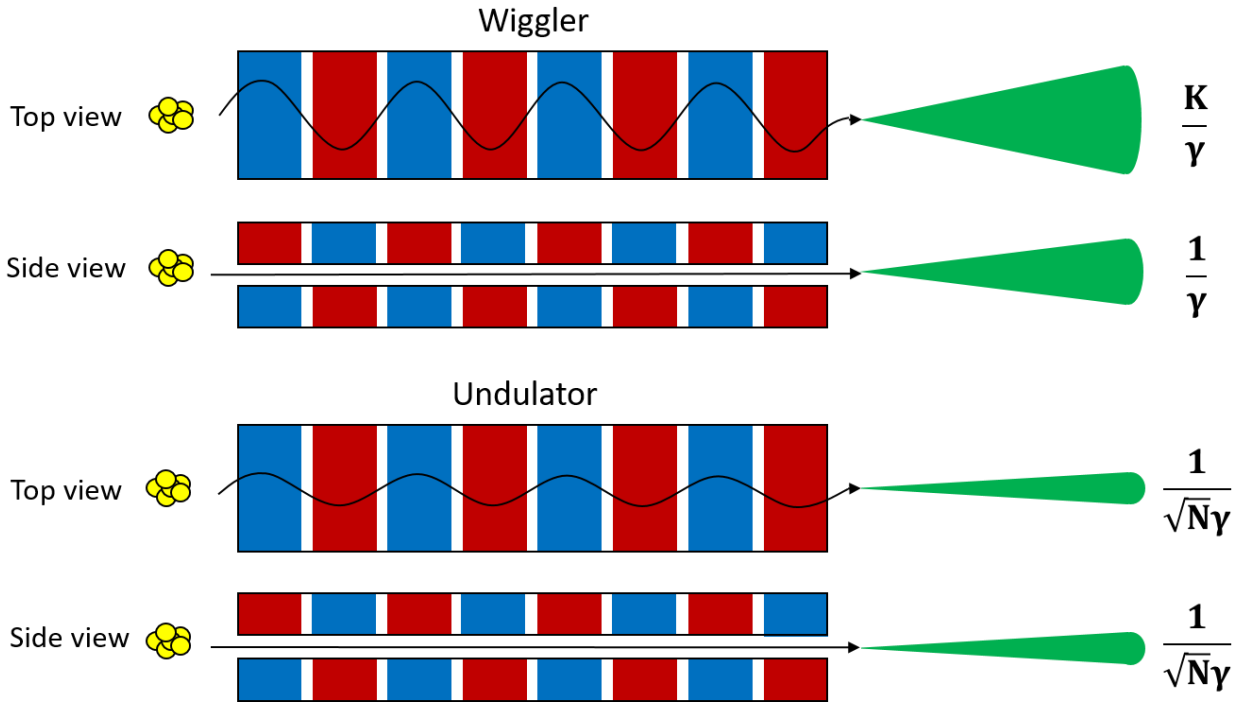

Figure 2.7 Diagrams of insertion devices. A wiggler is shown on the top section which has a wide emission fan. An undulator is shown below which has a pencil like beam resulting from small oscillations of electrons.

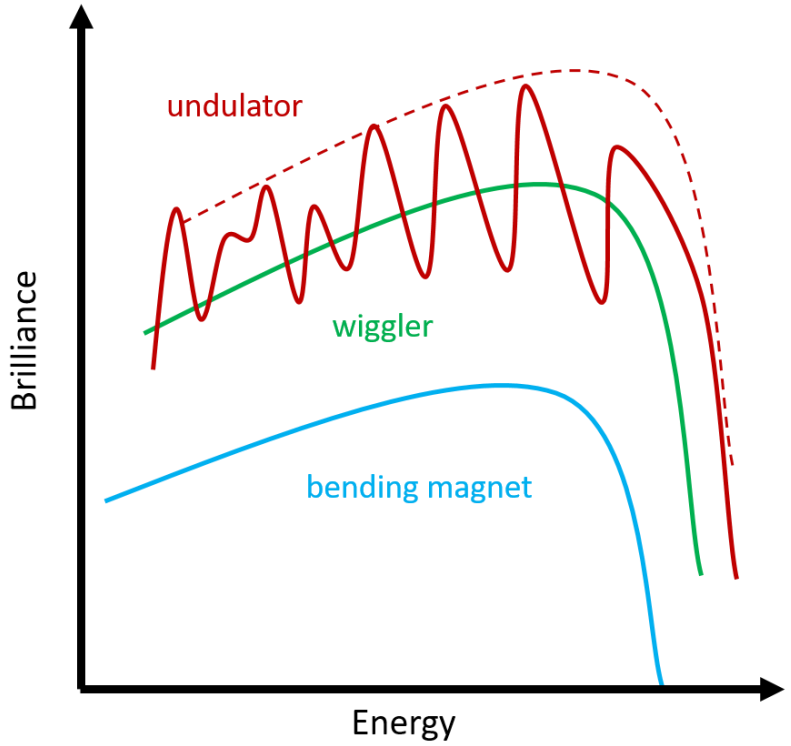

Figure 2.8 Energy vs brilliance for insertion devices used in a synchrotron.

the brilliance increase is broad, as shown in Figure 2.8. This device is categorized as a wiggler, and the emitted radiation beam has more beam divergence than an undulator. The divergence of the beam is proportional to K/γ in the horizontal direction, and $1/\gamma$ in the vertical direction, as shown in Figure 2.7. X-rays generated by a wiggler and an undulator produce a significantly higher brightness and have a shift in energy when compared to those produced by a bending magnet, as shown in Figure 2.8. While the difference in properties between an undulator and a wiggler is typically related to their K-factors, the distinction between the two is not black and white; undulators may exhibit some properties of a wiggler at different energies, particularly when $20 > K > 1$. In this respect, undulators are often defined as $K << 1$ and wigglers as $K >> 1$ [2].

2.2 X-ray Interactions

Since x-rays cannot be observed in the same manner as visible light, the detection of x-rays requires some form of an interaction within a material that is able to produce a measurable change. These interactions are dependent on both the properties of the material and the properties of the

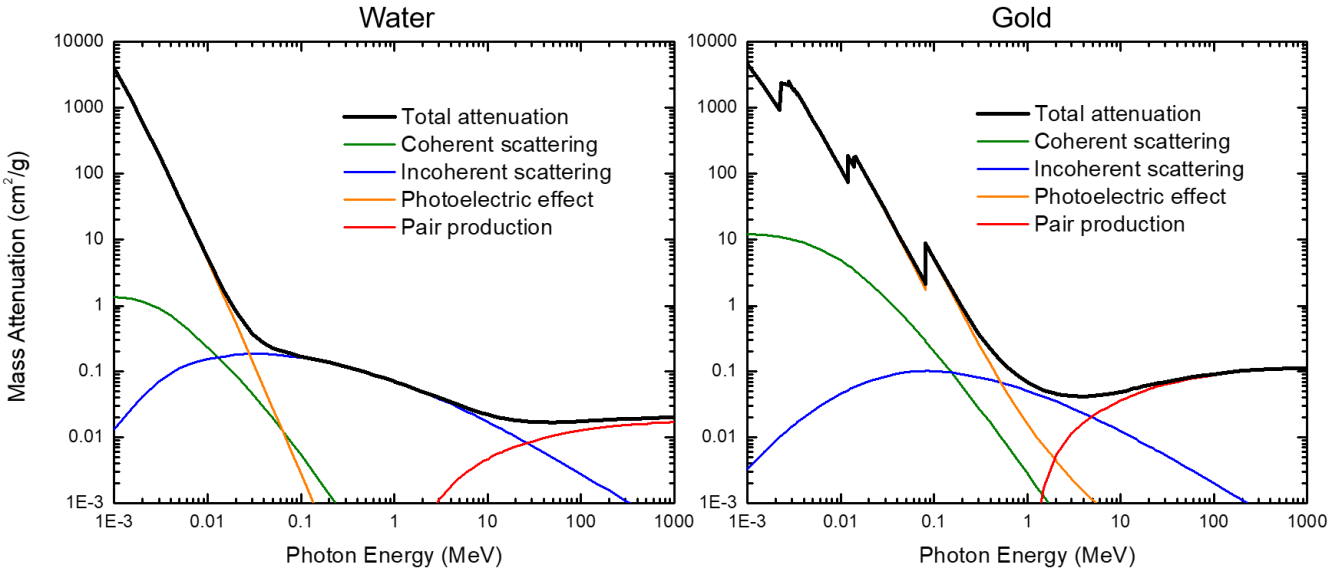

Figure 2.9 Attenuation coefficients and the contributions from various interactions for water (left) and gold (right). Data extracted from [3].

incident x-rays. Materials that contain elements with high atomic numbers are more likely to have a strong interaction with x-rays, thusly, a detector should be able to block x-rays in order to measure the interactions that occur within the material. The way in which x-rays interact with a given material help suit the design of a detector. For high energy x-rays, a detector should have a high atomic number, and should have sufficient thickness so that x-rays do not pass through the material without any interaction. The drop of intensity of x-rays after passing through a given thickness of a material, can be calculated using what is often referred to as the Beer-Lambert law, given by

$$I(\mathrm{t}) = I_0 \mathrm{e}^{-\mu\, t} \tag{2.5}$$

where I_0 is the intensity of the x-rays at the surface of the material, t is the depth travelled from the surface of the material, and μ is the total attenuation coefficient. The total attenuation varies, depending on both the material and the incident energy, and is the sum of multiple radiation interaction cross sections. X-rays can interact within a material by coherent and incoherent scattering, the photoelectric effect, pair production, and photodisintegration. The total attenuation coefficient can then be expressed as the sum of all interactions, where

$$\mu_{\text{total}} = \mu_{\text{coherent}} + \mu_{\text{incoherent}} + \mu_{\text{photoelectric}} + \mu_{\text{pair}} + \mu_{\text{photodisintegration}} \quad (2.6)$$

The probability of interactions differ depending on the incident x-ray energy; at low x-ray energies the photoelectric effect dominates, followed by scattering, pair production, and photo-disintegration. Figure 2.9 shows how the contributions from scattering, photoelectric effect, and pair production, comprise the total attenuation (shown in black) for water and for gold (data extracted from [3]). This illustrates both the material and energy dependence of the attenuation coefficients. Since photodisintegration occurs with high energy gamma rays, it is not shown in Figure 2.9. Further, the x-ray energy region of interest for radiotherapy are hundreds of keV at maximum, and contributions from pair production are negligible. In the case of a material that consists of multiple elements, the attenuation coefficient can be calculated by taking the sum of multiple elements, which is scaled using a weighting factor, which takes the contributions of each element towards the overall mass, given by

$$\mu_{\text{material}} = \sum_i w_i \mu_i \quad (2.7)$$

where w_i is the weighting factor of the element, i, and μ_i is the mass attenuation coefficient for that element.

Illustrations of the x-ray interactions of interest are shown in Figure 2.10, which include the photoelectric effect, Rayleigh scattering (also referred to as elastic or coherent scattering) and Compton scattering (inelastic or incoherent scattering). The photoelectric effect is common at low energies and causes electrons to be ejected from the atomic orbit of their atoms. In the photoelectric effect, the energy of the incident x-ray is absorbed and is transferred to the ejected electron, minus a binding energy. When the empty valency is filled by an outer electron, this causes the emission of a characteristic photon, shown in the top left of Figure 2.10. The attenuation for this interaction has a series of jumps at absorption edges, where the energy of the x-ray corresponds to the energy of an atomic shell, as is visible for gold in Figure 2.9. After a photoelectron is ejected, it can travel in any direction, although there is a higher probability that it will travel in the same direction as the incident x-ray. To a first approximation, assuming that the incident x-ray causes an electron to

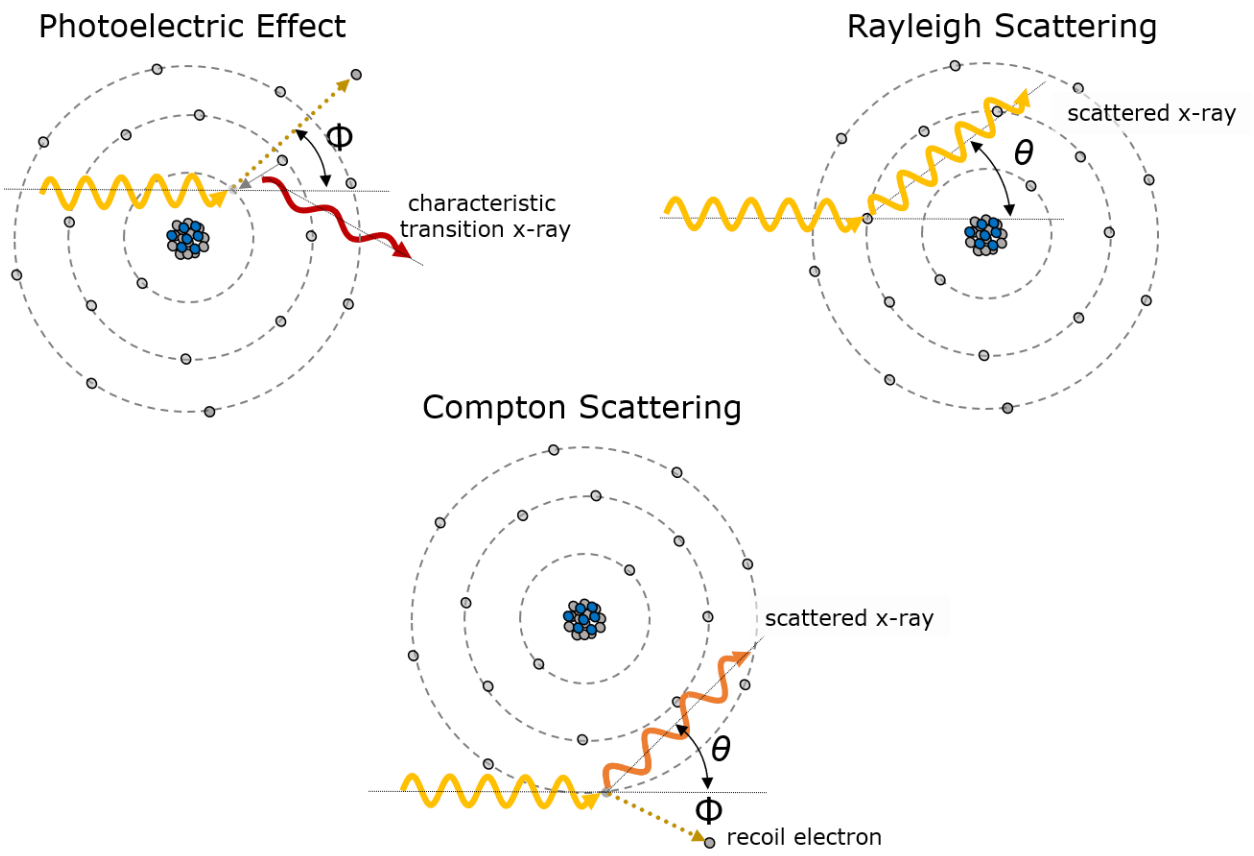

Figure 2.10 Illustrations of x-ray interaction mechanisms commonly encountered in the energy range used in radiotherapy and imaging.

be ejected tangentially to the atomic orbit, the probability per unit solid angle of an electron being emitted with respect to the incident x-ray is proportional to $\cos^2\phi$, where ϕ is the angle of the emitted electron. The distribution of photoelectrons can be predicted using Sauter's equation [4] which is given by

$$\frac{d\sigma}{d\Omega} = \text{const} \times \sin^2\phi \left\{ \frac{(1-\beta^2)^{1/2}}{(1-\beta\cos\phi)^4} - \frac{[1-(1-\beta^2)^{1/2}]}{2(1-\beta^2)^{1/2}(1-\beta\cos\phi)^3} + \frac{2[1-(1-\beta^2)^{1/2}]}{4(1-\beta^2)(1-\beta\cos\phi)^3} \right\} \quad (2.8)$$

where $\beta = \sqrt{1 - (E_{total}/E_{rest})^2}$ and E_{total} is the incident x-ray energy and the rest energy of the electron combined. The result of this equation states that as the incident x-ray energy is increased, the ejection angle of photoelectrons will narrow in the forward direction, shown in Figure 2.11.

Scattering interactions can be categorized as either coherent or incoherent scattering, often referred to as Rayleigh and Compton scattering, respectively. In Rayleigh scattering the incident x-ray scatters off a particle and there is no change in energy, only in the direction, which is shown in the top right of Figure 2.10. In Compton scattering, the incident x-ray causes an electron to be removed, thus ionizing the atom, shown in the bottom of Figure 2.10. The collision causes the photon to be scattered at an angle θ and the electron at an angle of ϕ. The direction in which the photon scatters changes as a function of the incident x-ray and the differential cross section of a scattered photon from an electron can be predicted by the Klein-Nishina formula [5] given by,

$$\frac{d\sigma}{d\Omega} = \frac{1}{2}\alpha^2 r_c^2 \, P(E_\gamma, \theta)^2 [P(E_\gamma, \theta) + P(E_\gamma, \theta)^{-1} - \sin^2\theta] \qquad (2.9)$$

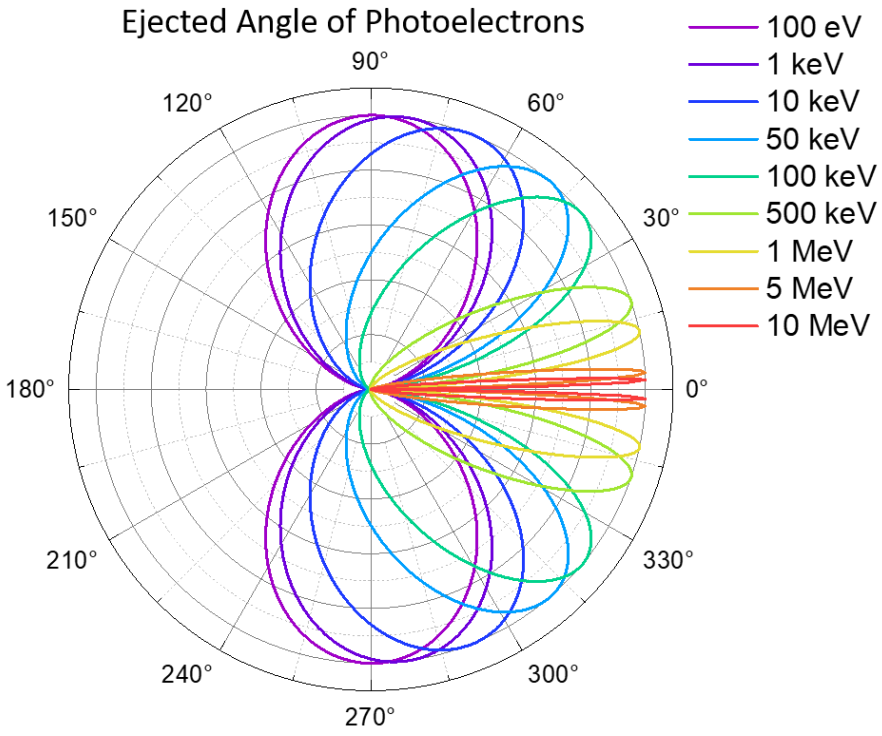

Figure 2.11 Distributions of ejected photoelectrons at various incident photon energies.

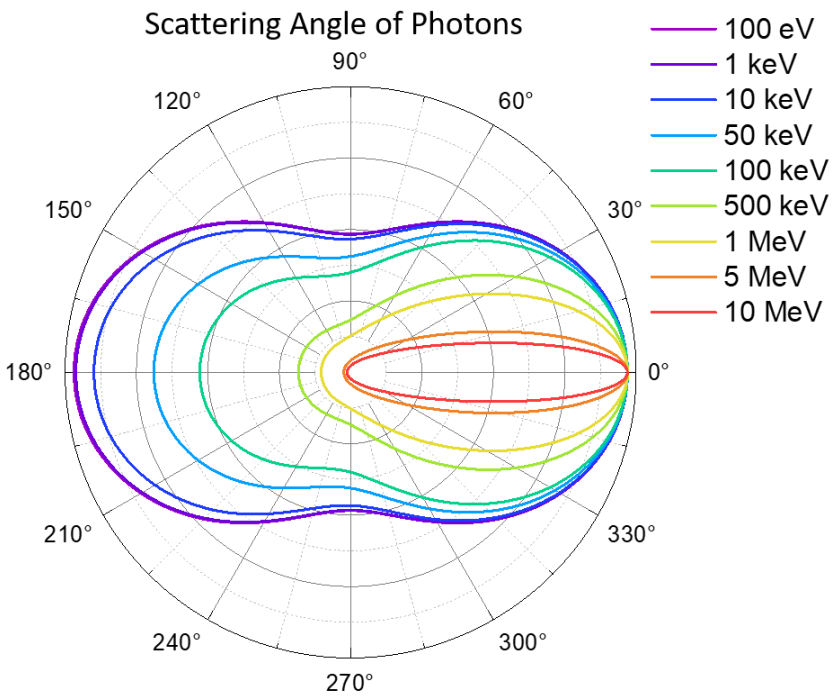

Figure 2.12 Distributions of Compton scattered photons at various incident photon energies.

where α is the fine structure constant, θ is the scattering angle r_c is given by $r_c = \hbar/m_e c$ and m_e is the mass of an electron. $P(E_\gamma,\theta)$ is the ratio of the photon energy before and after the collision, which is given by

$$P(E_\gamma, \theta) = \frac{1}{1 + (E_\gamma/m_e c^2)(1 - cos\theta)} = \frac{\lambda}{\lambda'} \tag{2.10}$$

Figure 2.12 shows the scattering cross section at different photon energies. This indicates that higher energy photons are more likely to be scattered in the forward direction. In Compton scattering, the energy of the photon and the scattered, or recoil electron, can then be calculated by conservation of momentum, where

$$h\nu' = \frac{h\nu}{1 + \frac{h\nu}{m_e c^2}(1 - \cos\theta)} \tag{2.11}$$

$$\cot\phi = \left(1 + \frac{hv}{m_e c^2}\right) \tan\left(\frac{\theta}{2}\right) \qquad (2.12)$$

where hv is the energy of the incident photon, m_e is the mass of an electron, and θ is the angle of the scattered photon. The energy of the ejected electron can then be calculated by $E_{electron}$ = hv - hv'. The energy of the ejected electron is dependent on the ejection angle, where it is maximum in the forward direction (0°) and the photon is backscattered 180°, and minimum when ejected perpendicular to the path of the incident x-ray (90°). Figure 2.13 shows the energy of an ejected electron as a function of the ejection angle for various incident x-ray energies, where the angle of the electron (ϕ) and the photon (θ) is given in equation 2.12. After a photon is scattered, it can then continue and subsequently cause various other radiation interactions before all energy is lost or it exits the material.

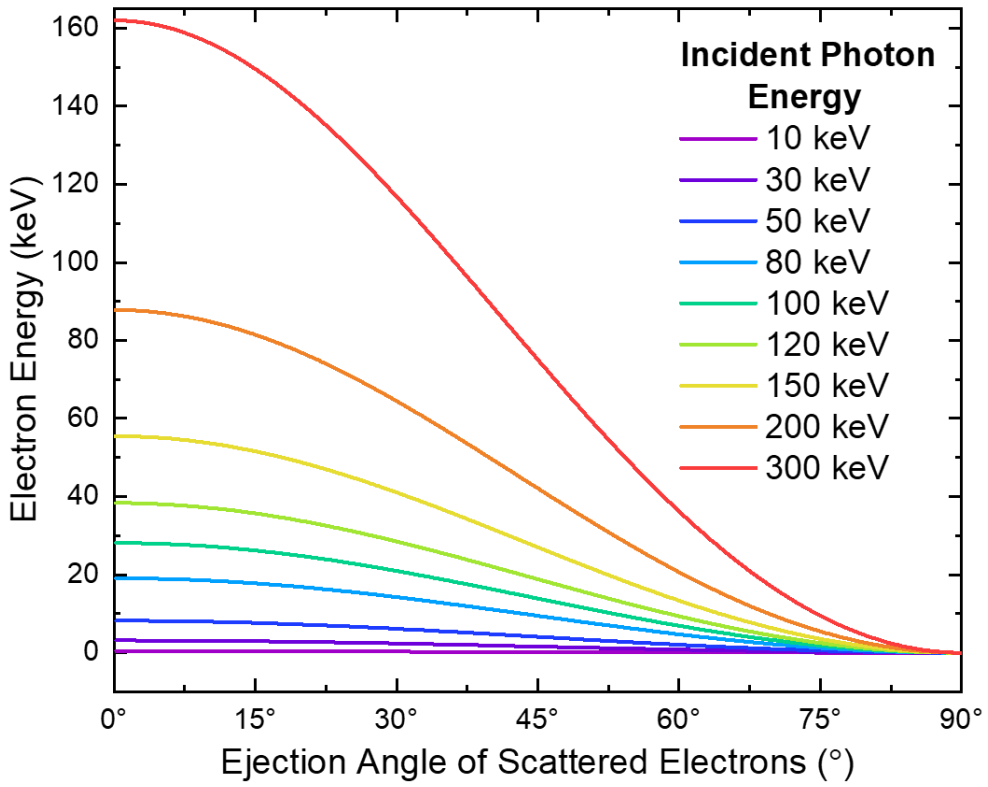

Figure 2.13 Electron energy of scattered electrons as a function of the ejection angle. The energy of a scattered electron is maximum when the incident photon is backscattered. At the energies shown here the energy of a scattered electron will be lower than that of a photoelectron with the same incident x-ray energy.

In radiation interactions, dose represents how much energy is absorbed from ionizing radiation per unit of mass in a material. It is commonly measured in units of Grays (Gy), which translates to 1 Joule per kilogram, or Radiation Absorbed Dose (RAD), where 1 Gy = 100 RAD.. At a single photon energy, the absorbed dose can be calculated by

$$D(E_{\text{ph}}) = \frac{N_{\text{abs}} E_{\text{ph}}}{M} \tag{2.12}$$

where N_{abs} is the number of photons of energy E_{ph} in a material of mass M. The number of photons absorbed that result in energy being deposited is calculated by

$$N_{\text{abs}} = N_0 \frac{\mu_{\text{energy absorbed}}}{\mu_{total}} (1 - e^{-\mu_{\text{total}}\, t}) \tag{2.13}$$

$\mu_{\text{energy absorbed}}$ is the attenuation coefficient for the amount of energy deposited in the material, and is less than μ_{total} since μ_{total} contains contributions from all energy interactions even if they do not deposit energy, such as in the case of Rayleigh scattering. The calculation of total dose deposited in a material using a polychromatic source with a material of a given thickness, L, is a much more complicated calculation and requires integration as a function of energy, and the thickness of the material. For a polychromatic source, the dose delivered to a sample can be calculated by

$$D = \frac{\Delta E_x}{M} = \int_{E_{\text{min}}}^{E_{\text{max}}} \int_0^L \frac{E\, N_0}{\rho A x} \frac{\mu_{EA}(E)}{\mu_T(E)} \left(1 - e^{-\mu_T(E)\, x}\right) dE\, dx \tag{2.14}$$

where ρ is the density of the material, A is the area of irradiation, and x is the depth within the material. Using a polychromatic source over a large depth can make calculating the total dose very complicated. For this reason, surface dose is often given, which is the dose deposited at the surface of the material, and therefore does not require integration of the dose as a function of depth.

In biological tissue, the dose deposited is multiplied by a quality factor (QF), which is dependent on the biological region the radiation is being deposited (lungs, spine, liver, etc.), and the type of radiation. Dose in biological tissue is often given in units of Sievert (Sv) and is referred

to as equivalent or effective dose. Different forms of radiation, such as particle radiation, will cause varying biological effects inside of tissue and so the quality factor incorporates the damaging potential of the radiation within the tissue. For photons, the quality factor is 1, and so we need only consider where the dose is being delivered within the patient. Conversion from units of Gy to Sv is therefore given by,

$$\text{Sievert} = \text{QF} \times \text{Gray} \tag{2.15}$$

2.3 Microbeam Radiation Therapy (MRT)

Radiosurgery is a medical procedure in which radiation is deposited to a specific location within a patient in order to kill cancerous cells or tumours. As opposed to conventional surgery, which requires operating on and removing tissue from a patient, radiosurgery is non-invasive and is often used in areas that are difficult to operate on. Radiation therapy uses ionizing radiation, such as x-rays, γ-rays, protons, or neutrons that are directed towards a targeted area and cause lethal damage

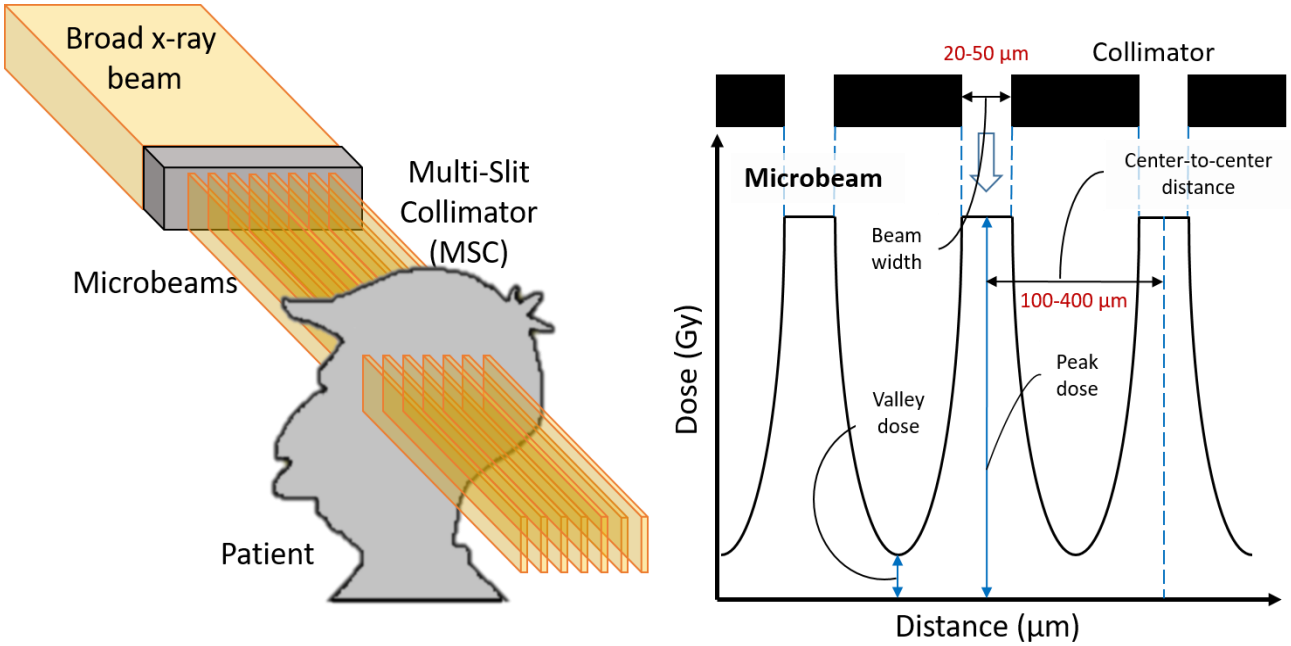

Figure 2.14 Typical dose profile created by collimated x-rays in MRT. Collimated broadbeam x-rays pass through a multislit collimator producing segmented and parallel microbeams of radiation.

to a tumour during irradiation. In the process of damaging tumours through the use of radiosurgery, there is also undesirable damage to healthy tissue that occurs along the path of ionizing radiation. This damage to healthy must be minimized in order to prevent vital organ and structure damage of the patient.

Microbeam Radiation Therapy (MRT) is a novel form of radiation treatment that causes preferential damage to solid tumours while sparing healthy tissue, improving on standard radiotherapy techniques [6]. MRT is a radiotherapy technique that irradiates tumours with microplanar arrays of x-rays generated by a synchrotron source. These microplanar arrays, or microbeams, are parallel planes of x-rays with a separation of 100 – 400 μm and a typical beam width that ranges from 20 – 50 μm. The x-ray beams have the spatial size on the order of human cells, and deposit a maximum lethal dose within the beam path, referred to as the "peak" dose. In order to assure the survival of healthy tissue between beams, the "valley" dose between microbeams must be minimal, kept below a determined threshold value. An example of a microbeam profile is shown in Figure 2.14.

Healthy tissue has shown the ability to recover from lethal doses by utilizing the so called "bystander effect", whereas tumours do not appear to have this ability [7]. While the biological mechanisms of the "bystander effect" are not completely understood, it is thought that blood vessels in tissue adjacent to the beam path helps in the regeneration of cells that have been destroyed by radiation. Another suggestion is that the "bystander effect" relies on neighboring healthy tissue aiding in the repair of damaged tissue by proliferation, migration, and differentiation to produce new, mature, and functional cells [8]. Doses delivered to tissue within the width of the microbeam are on the order of hundreds of Grays, several orders of magnitude higher than the doses used in conventional radiosurgery techniques. The ability to deliver large doses without significant destruction to tissue, while preferentially damaging tumors, allows for MRT to be of substantial use for difficult to treat tumours, such as spinal, or central nervous system (CNS) growths.

The tissue sparing effect associated with narrow beams of radiation has been well known since the late 1950s. Biophysicists Howard J. Curtis, and Charles P. Baker began investigating the biological effects of cosmic radiation on astronauts in preparation for manned space travel [9,10,11,12]. It was found that there was a striking relationship between the size of the beam and the threshold dose delivered for mice. Experiments were performed using 22 MeV deuteron beams and it was found that if large doses were delivered in narrow regions, the overall dose response was low, and tissue showed little destructive biological effects. A histopathology of a mouse brain after irradiation by a deuteron beam is shown in Figure 2.15 (a). Ionization caused by heavy particles are almost entirely linear, and have diameters of ~ 25 μm. Because the "bystander effect" requires radiation to be deposited in a narrow, linear path, therapy using microbeams was not used until 1992 after synchrotrons became more widely used [6]. Successful MRT requires x-rays to pass through narrow slits in a multi-slit collimator (MSC) without significant scattering, and therefore a highly collimated x-ray source such as a synchrotron is required; MRT cannot be performed using common x-ray tube units. In order to successfully perform MRT, x-rays sources must have minimal divergence of x-rays, high fluence, and high incident energies.

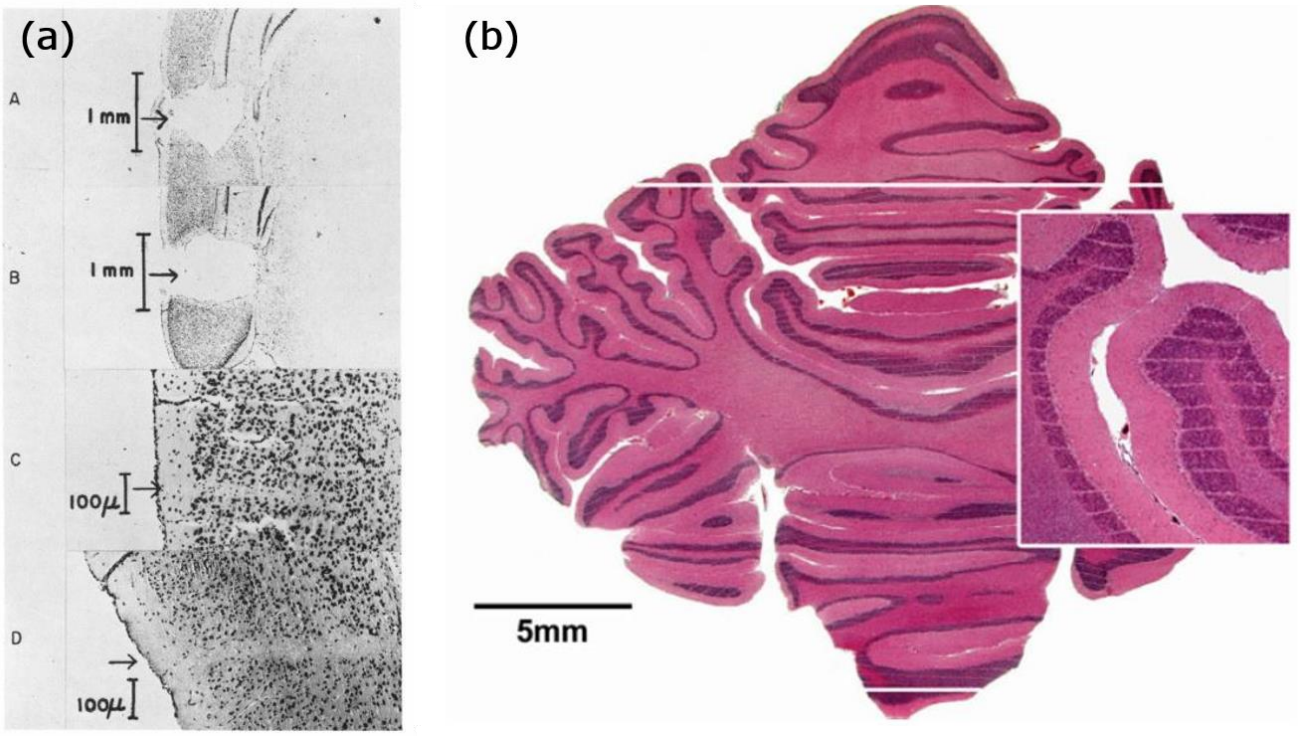

Figure 2.15 (a) Damage caused by a deutron beam within soft tissue [12]. (b) Paths of microbeams can be observed in the histopathology of a piglet brain [13]. Entrance dose of microbeams is 625 Gy

The availability of synchrotrons have allowed for the production of highly collimated x-rays, with divergence on the order of milliradians, and can deliver both high fluence rates and high incident x-ray energies to a patient. Synchrotron generated x-rays produce minimal scattering within a MSC, ensuring sufficient contrast for the production of multiple, parallel, and sharply defined planar beams. These collimators are made of tungsten, or other elements with high atomic numbers in order to block x-rays between microbeams. Bright x-ray sources produce high fluence rates, which allow for therapeutic doses to be delivered in an instant. If there is significant patient movement during irradiation, then the sharply defined beams show signs of "blurring" and the dose is spread over a larger area, thus decreasing the effectiveness of the technique. Low energy x-rays deposit dose very near the surface of an object due to the contributions from the photoelectric effect. However, high energy photons, or hard x-rays, can penetrate deep into tissue and can deposit dose at the region of interest. The incident x-ray energy can be modified to suit the experiment in question, which can range from mice experiments, to larger animals, to eventual human trials. Figure 2.15 (b) shows an example of a piglet brain irradiated with 25 μm wide beams, which shows the narrow tracks of the microbeams penetrating through the brain caused by ionizing damage to the tissue [13]. Overall, the collimation, fluence, and incident x-ray energy must be optimized in order to minimize the valley dose and maximize the peak dose for therapeutic MRT to be effective.

Successful MRT relies heavily on controlling the peak dose and the valley dose; the ratio of the peak-to-valley dose (PVDR) is an important parameter that should be maximized for therapeutic applications. The peak dose is closely related to the total dose delivered from broadbeam irradiation prior to passing through the MSC (as shown in Figure 2.14) and is fairly well understood. The dose deposited in the valleys between microbeams and the PVDR, however, are dependent on a variety of parameters, such as the width of the microbeam, the center-to-center distance between beams, field size, radiation interactions within a patient’s tissue or bone, the distance from the MSC to the patient, etc. In order to optimize treatment effectiveness, the valley dose must be kept as low as possible to maintain the beneficial tissue sparing effect associated with MRT. Overall, the design of synchrotron facilities, selection of energy and dose rate parameters, high resolution dosimetry, and irradiation geometry must be carefully considered before human therapeutic trials are attempted for MRT.

2.4 Detection of X-Rays and Dosimetry in Microbeam Radiation Therapy

X-ray dosimetry requires measuring the produced effects of x-rays as they interact within a medium. Detection of x-rays can be performed by measuring a change in the physical properties of the material, such as, the ionization of a medium, fluorescence, photographic changes, luminescence, to give a few examples. While the detection of x-rays has been well studied in the past, the measurement of the dose profile of a microbeam provides a greater challenge as a result of the unique geometry and dose range of microbeams. Microbeams are a specialized kind of x-ray beam, and a detector must be able to measure a dose range that extends from a few Gy to thousands of Gy, and must be able to do so with high resolution. These planar x-ray microbeams have a separation of a few hundred micrometers, and a typical thickness that ranges from a few tens of micrometers. The dose delivered to the patient at the peak of the microbeam is several hundred gray (Gy) or more, while the low dose region can range from a few Gy to a few dozen Gy. The accurate measurement of the dose distribution is critical for the treatment planning, and a dosimeter for MRT must fulfill the following requirements:

1. Large dynamic range. The range of doses used in MRT can be up to thousands of Gy, far larger than doses delivered in conventional radiotherapy, which is typically less than 40 Gy over multiple treatments.
2. Detection of x-rays on a micrometer level scale. Accurate measurement of the dose profile is essential for optimization of treatment conditions.
3. Capable of detecting x-rays over a wide energy range. Depending on the application, the incident x-ray energy used can vary from 50 – 300 keV, or higher. While it is likely that most dosimeters would require calibration over such a wide range, the ability to measure high and low energy x-rays is important for a detector.

The detection and measurement of conventional x-ray irradiation methods has been well studied [14], however, the unique properties of narrow, high dose microbeams provides a greater challenge for the recording and measurement of dose, and is beyond the capabilities of many common detection methods. Monte Carlo simulations are often used to simulate beam profiles in microbeam radiation therapy, but unless they are verified through experimental tests, the validity of these simulations is not acceptable in a clinical application. Tissue equivalence, cost, dose rate

dependence, energy dependence, and ease of measurement in a dosimeter are also important considerations in the design of a potential dosimeter. Each dosimeter will have distinct advantages and disadvantages. Potential methods for MRT dosimetry of several common experimental and commercial techniques for x-ray measurement [15] are discussed in the following sections.

2.4.1 Ionization Chambers

Ionization chambers are perhaps one of the most commonly available x-ray detection methods in radiation therapy. The measurement of x-rays using ionization chambers is relatively straightforward, and ionization chambers are simple to produce. An ionization chamber is filled with a gas, most commonly air, in which two electrodes are located. A voltage is applied across the two electrodes, creating an electric field. When ionizing radiation, such as an x-ray, is passed between the plates an electron and a positive ion is generated. These particles then move to the plates of opposite polarity due to the electric field. An example of an ionization chamber is shown in Figure 2.16. The detected electric current is then used as a measurement of the total dose

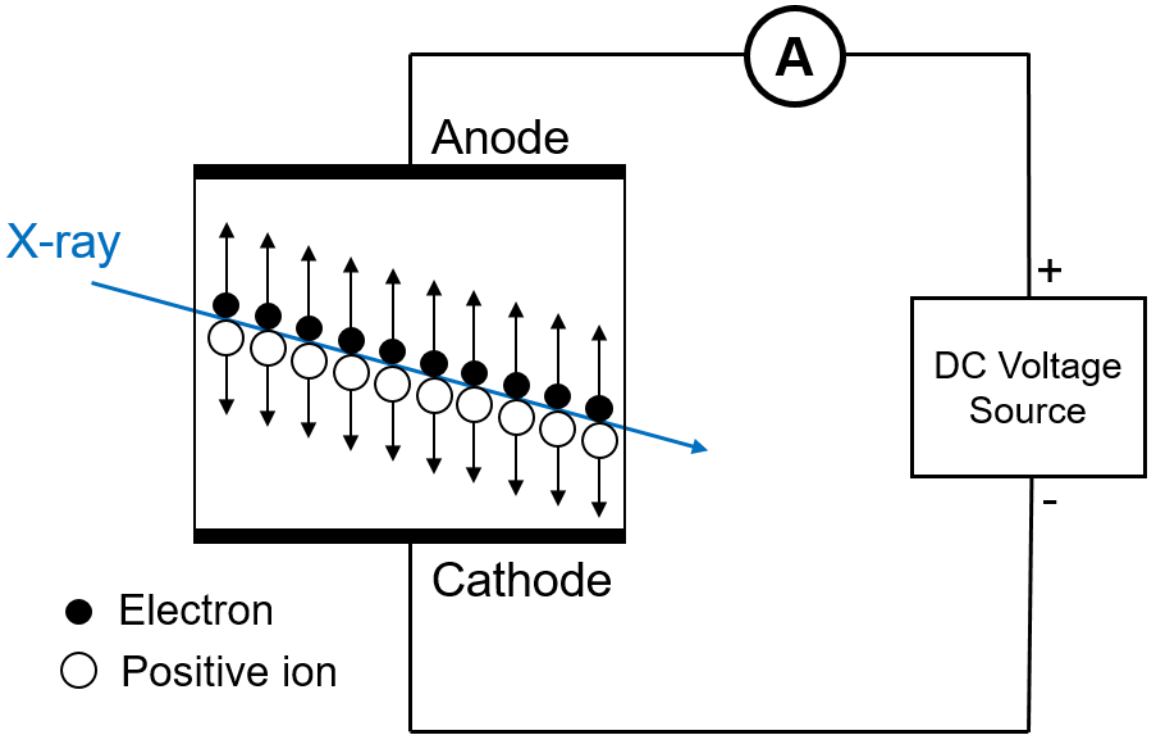

Figure 2.16 Diagram of an ionization chamber. Incident x-rays produce positive and negative charges which are collected and measured by the cathode and anode.

Figure 2.17 Gafchromic film irradiated at the CLS inside a water phantom with a total dose of 200 Gy in air and an incident x-ray energy of 60 keV. Gafchromic film was scanned using a commercially available high resolution scanner (Mustek A3 1200)

delivered. Ionization chambers are popular as a radiation detection method since they are relatively easy to use, do not have a strong energy dependence, and can provide measurements in real time. However, considered as a possible dosimeter for MRT, they lack spatial resolution and do not have the ability to simultaneously distinguish the dose delivered at the peak versus at the valley of a microbeam.

2.4.2 Gafchromic Film

Gafchromic film is a commercially available, self-developing, film that has been created for radiotherapy applications. The principle of the dosimeter is that, as the film is exposed to radiation, the film will then darken and the extent of the darkening can then be readout using an optical scanner or microscopy system, as shown in Figure 2.17. These films typically consist of laminating an active layer that exhibits a colour change between two layers of a material such as polyester [16]. While high scale resolution can be achieved using this technique, the dynamic range does not cover the range required for MRT. For instance, EBT3 Gafchromic films cover a dose range from 0.2 – 10 Gy which is capable of measuring the valley dose region, whereas ultra-high dose dosimetry HD-V2 Gafchromic films includes the dose range of 10 – 1000 Gy, which is important for peak doses. For this reason, it is possible to stack two layers of high and low sensitivity films to cover a larger dynamic range [17]. However, this stacking of films can cause complications in the measurement of surface dose. Further, this technique is an indirect detection method and is sensitive to UV exposure and temperature changes [18].

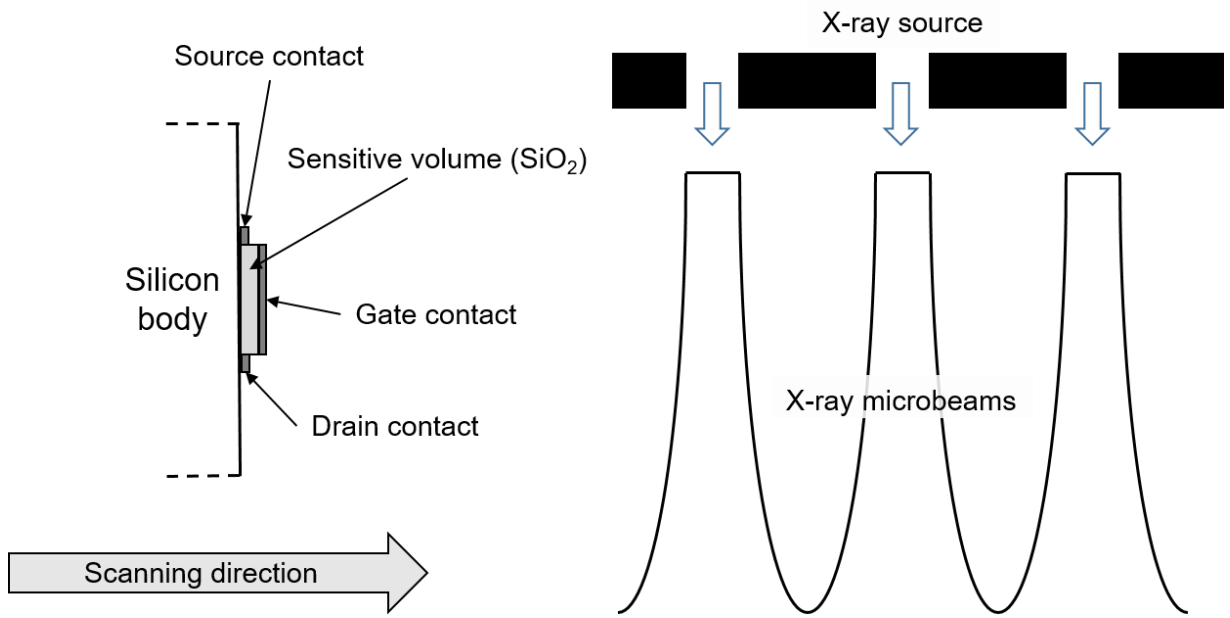

Figure 2.18 Diagram of a MOSFET detector. The sensitive volume is scanned through the path of the microbeams resulting in a one-dimensional measured beamprofile. After [20].

2.4.3 MOSFET Detector

A Metal-Oxide Semiconductor Field Effect Transistor (MOSFET) dosimeter is a sandwich type flash memory semiconductor type device, where an oxide layer (SiO_2) floating gate is located between a substrate and control gate, as shown in Figure 2.18. As ionizing radiation passes through the oxide layer, electrons and holes are created within the layer and the charges are collected through the gate [19]. The radiation induced change in the threshold voltage (V_{TH}) can then be converted into a dose measurement. The detector is oriented perpendicular to the beam direction, and thus the resolution is limited by the width of the oxide layer [20], which can be less than one micron. The limiting factor for this device in MRT dosimetry, is related to the fact that the detected profile is one-dimensional, involves a unique readout method, and would require extensive energy calibration and necessary corrections [15].

2.4.4 MRI Gel Dosimetry

The advantage of gel dosimetry is that the material is close to tissue equivalent and can be characterized in three dimensions. The basis of the technique involves monomers which are

dissolved in a gel matrix and polymerization which occurs after exposure to x-rays. These polymers can then be detected using magnetic resonance imaging (MRI). A primary concern with this technique is that the material has a strong sensitivity to the incident dose rate and the accuracy is poor, less than what can achieved by other dosimetry techniques [15].

2.4.5 Fluorescent Nuclear Track Detector

Fluorescent nuclear track detectors utilize the luminescent properties as a measurement method for radiation dosimetry. Originally designed for applications in neutron and heavy particle dosimetry, aluminum oxide crystals are doped with carbon and magnesium, which create oxygen induced defects within the crystal, and can be produced in a variety of sizes, depending on the application [21]. Upon irradiation, electrons and holes are created, which cause electrons to be trapped by colour centers [22]. These colour centers causes fluorescence around 750 nm, after excitation from a suitable source, and can be readout using a confocal fluorescence microscopy system. Since the material is homogenously doped crystal, the resolution is very high and can reach the submicron level. However, the fluorescence signal saturates after doses of 100 Gy are delivered and therefore does not satisfy the dynamic range requirements needed for MRT dosimetry.

2.4.6 Silicon Strip Detector Dosimetry

A silicon diode dosimeter uses an n-type silicon sandwiched between two p-type silicon strips. If the strip is irradiated, a current from the charged particles is created which can then be measured to determine the dose rate. The measurement of an instantaneous dose rate can then be integrated to measure the total dose delivered, which covers five orders of magnitude, fulfilling the dynamic range requirements for MRT dosimetry. Resolution of this measurement technique, however, is limited to the width of silicon strip, which is between 10 and 50 μm [23], and requires further development before it can be used for MRT dosimetry.

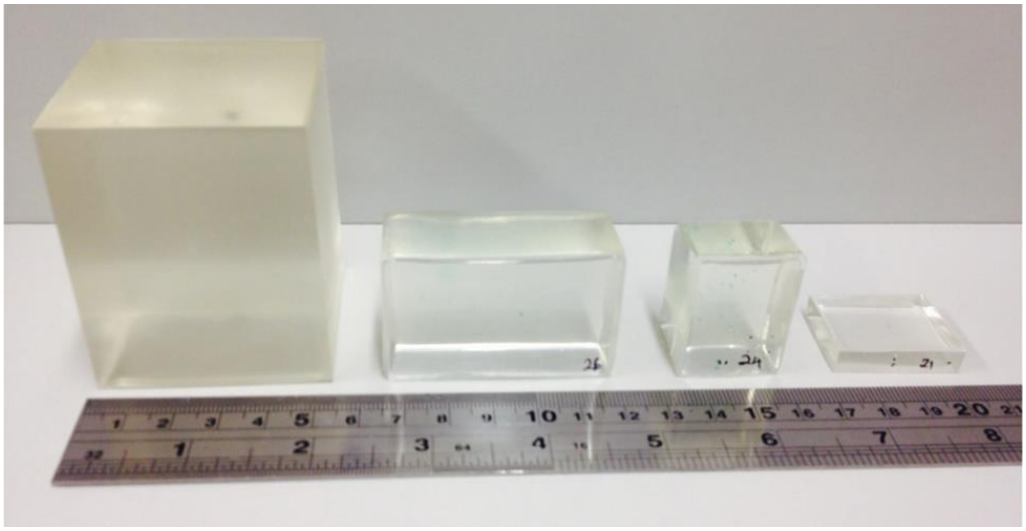

Figure 2.19 Various sizes of PRESAGE 3-D dosimeters prior to irradiation, taken from [24].

2.4.7 PRESAGE 3-D Dosimeter

PRESAGE 3-D dosimetry involves a polymer that undergoes an optical colour change after irradiation. The advantage of the material is that it allows for microbeams to be measured in 3-dimensions and that the material is water equivalent, shown in Figure 2.19. After samples are irradiated they can be readout using a laser confocal fluorescence system. Using a PRESAGE dosimeter, it is possible to visualize microbeam arrays in 3-D using multilayer scanning and computer reconstruction. Additionally, it is possible to measure the beam width and beam characteristics within a macroscopic depth of up to 9 mm [24]. Previous work has shown these materials to measure doses up to 200 Gy, however, the achievable resolution is not sufficient and is larger than 25 μm in most cases.

2.4.8 Thermoluminescence Detectors

A thermoluminescent dosimeter (TLD) involves a crystalline material where, upon exposure to ionizing radiation, holes and electrons are created and trapped within the crystal lattice. Using thermal stimulation, the trapped energy is released in the form of visible light, which can be used as a measurement of the total dose delivered to the dosimeter. A two dimensional TLD system comprising of LiF:Mg,Cu,P (MCP-N) based thermoluminescent foils and a reader equipped with a CCD camera and a large sized heater has been used in the past as an attempt to perform high

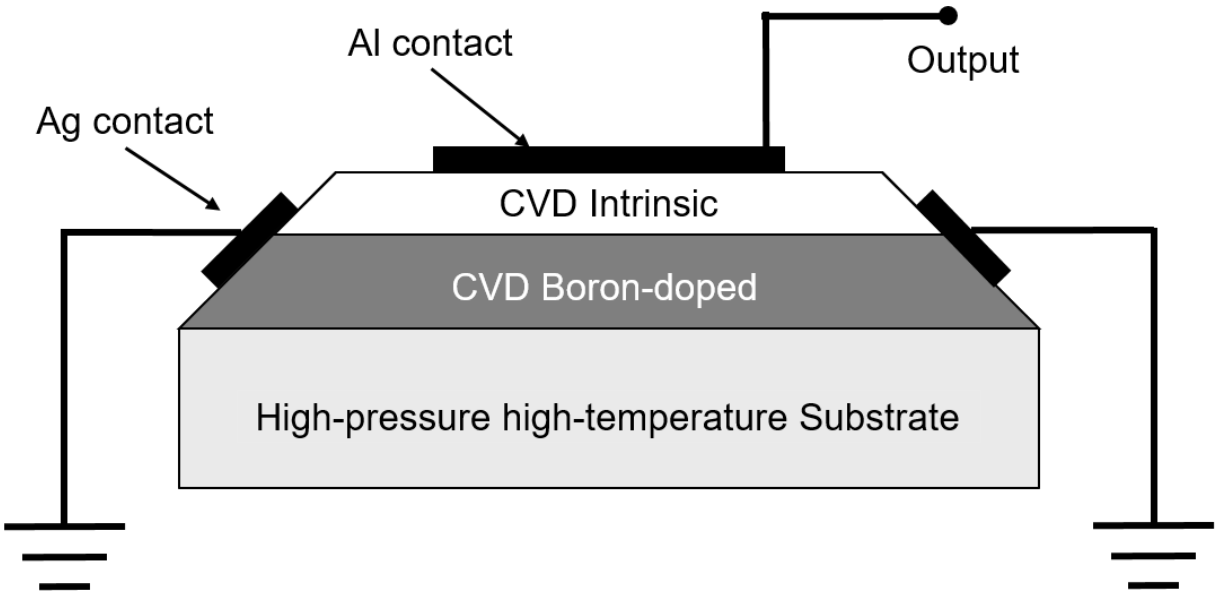

Figure 2.20 Schematic of a CVD single crystal diamond diode. After [26].

resolution dosimetry [25]. This technique is capable of recording peak doses up to 500 Gy with a resolution of around 5 μm [15]. The limiting factor of this technique is the pixel size of the CCD camera, signal fading over time, and light scattering within the detector. While light scattering within the sample can be minimized by making the sample as thin as possible, there has been little research into the improvement of the achievable resolution of the technique over the past ten years.

2.4.9 microDiamond Detector

microDiamond detectors are single crystal diamond detectors designed for high resolution, small field dosimetry. The device is fabricated using a chemical vapor deposition (CVD), which deposits a conductive p-type diamond (doped with boron) on a high temperature, high pressure single crystal substrate [26]. An intrinsic diamond sensing layer is then deposited, which can have thickness as little as 1 μm [27], followed by a deposition of a metal (aluminum) contact. The device operates as a Schottky diode, resulting from the built-in potential at the interface of the metal and intrinsic diamond. A schematic of a single crystal diamond diode is shown in Figure 2.20.

This dosimetry technique has many advantages, in that the material is close to being tissue equivalent, has high sensitivity, and the achievable resolution is controlled by the thickness of the intrinsic single crystal diamond layer. The drawback to microDiamond detectors is that

measurements can only be performed in one dimension, and require some calibration in order to stabilize detector response and dose rate response [28]. Further, these materials can be costly and time consuming to manufacture.

2.5 Rare Earth Ion Doped Glasses

The technique for the measurement of microbeams with high-resolution and large dynamic range proposed in this research, involves detection of the extent of the valence conversion of rare earth ions uniformly doped in a glass material. The photoluminescent spectra of some rare earth (RE) ions have distinguishing characteristics, particularly samarium ions, where the emission spectra of Sm^{3+} and Sm^{2+} do not significantly overlap. Therefore, the measurement of the total dose delivered can be related to the measured intensity of the Sm^{3+} and Sm^{2+} ions. The characteristics of rare earth ions, their luminescent properties, and the host materials are outlined in the following sections.

2.5.1 Rare Earth Ions

Rare earth elements refer to the elements in the periodic table that include scandium, yttrium, and the lanthanides, which range from lanthanum (La, atomic number 57) to lutetium (Lu, atomic number 71. Lanthanides are of particular interest since they can have partially filled 4f orbitals, which make them useful in luminescent applications, lasers, magnets, and a wide variety of other materials. The term "rare earth" is in reference to the relative rarity of these elements found in mining ore deposits; the inclusion of scandium and yttrium to the rare earths category is due to their common discovery with the lanthanides, as well as sharing some similar properties [29]. The unique properties associated with rare elements is due to the electron configurations of the lanthanides. Electrons surrounding an atom will reside within specific orbitals, which are characterized by a principal quantum number, n, and a subshell designation quantum number, $l = n - 1$. These subshells are commonly referred to as s, p, d, f … orbitals, where $l = 0$ for an s orbital, 2 for a p orbital, and so on. Each orbital has their own specific properties, such as the number of electrons required to fill an orbital, radial distance from the nucleus, and the shape of the orbital. According to solutions to the Schrödinger wave equation, the orbital shapes are actually a description of the volume in which an electron is likely to be found surrounding the nucleus,

The specific derivations and solutions to the Schrödinger equation in relation to the orbitals is not discussed here. Of importance however, is the properties of electron orbitals which are characterized by the principle quantum number, n, the orbital quantum number, l, the magnetic quantum number, m_l, which has an integer value ranging from $-l$ to $+l$, and m_s, which describes the electron spin states, and can have values of $m_s = \pm ½$. As these orbitals are filled, electrons must then move to higher and higher principle quantum numbers and subshell designations. The Pauli exclusion principle prevents two electrons from having the same four quantum numbers, and the maximum number of electrons in a subshell is given by $2(2l + 1)$. As an example, a samarium (Sm^0) ion should have the following electron configuration,

Sm: $1s^2\ 2s^2\ 2p^6\ 3s^2\ 3p^6\ 3d^{10}\ 4s^2\ 4p^6\ 4d^{10}\ 5s^2\ 5p^6\ 4f^6\ 6s^2$

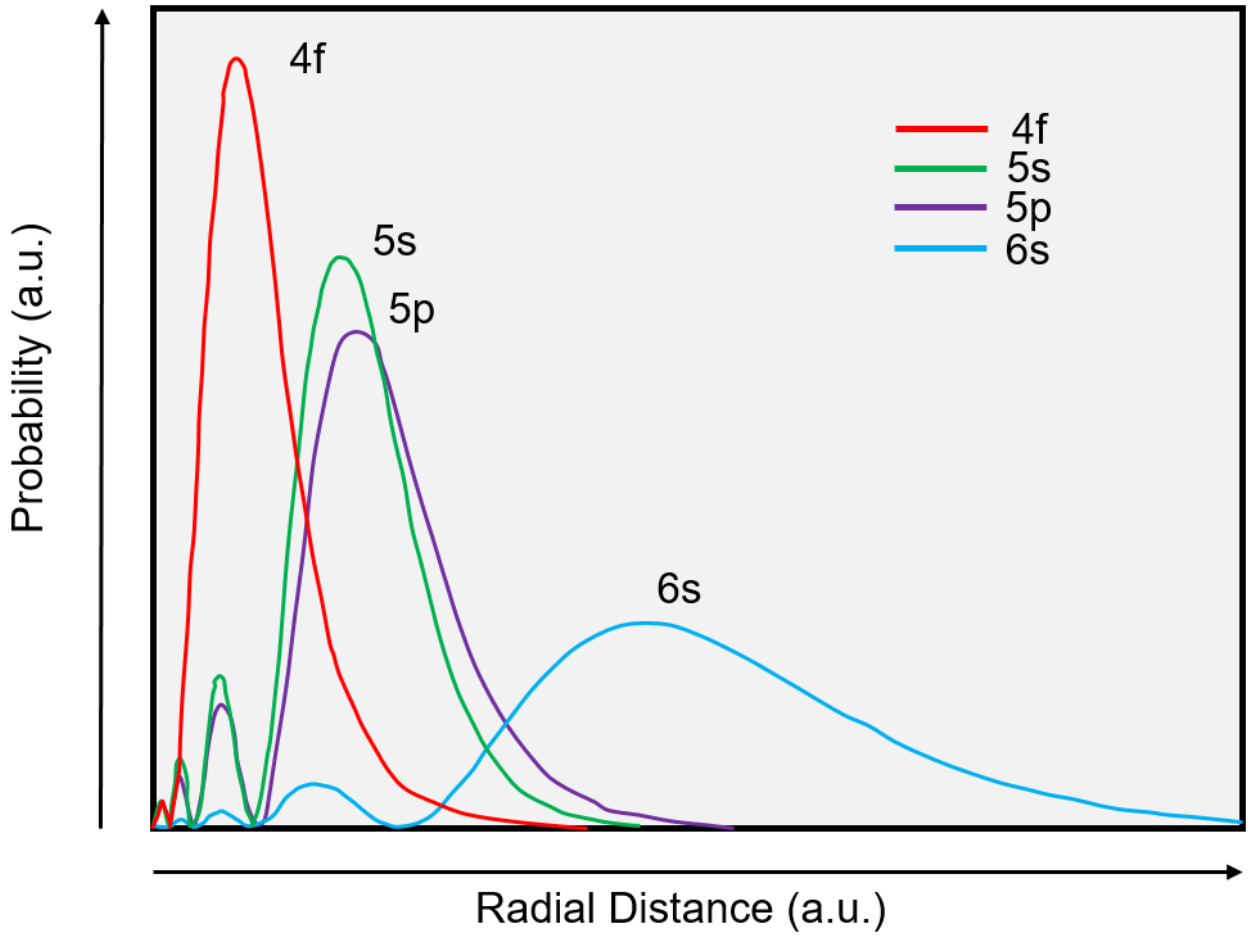

Figure 2.21 Probability versus radial distance from the nuclei for electrons in 4f, 5s, 5p, and 6s orbitals for a Gd^+ ion. After [31].

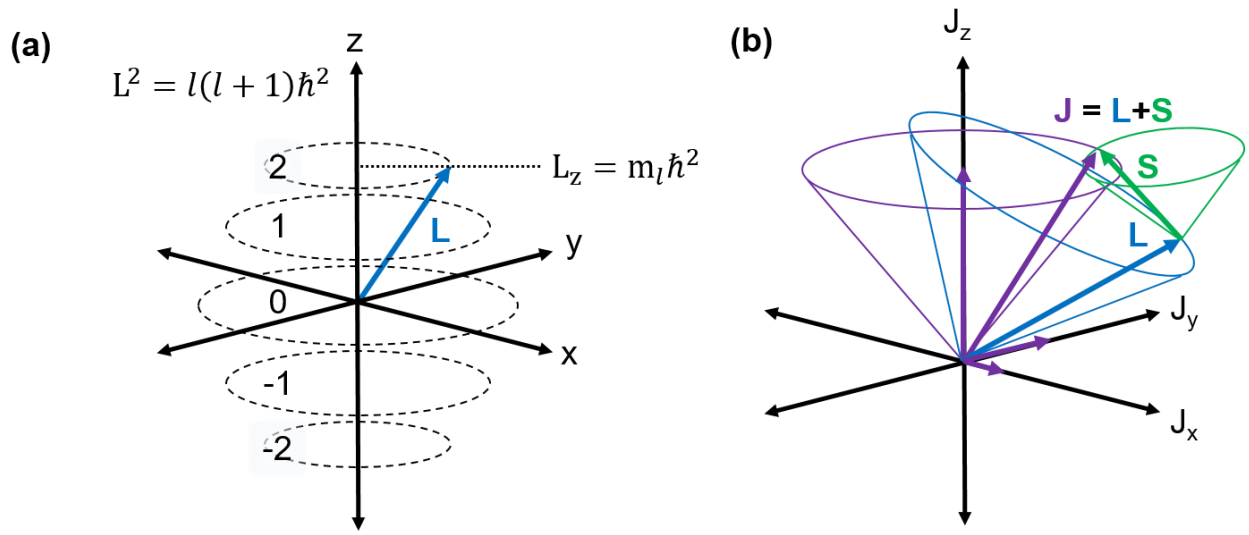

Figure 2.22 (a) Diagram of orbital angular momentum vector, where certain orientation for **L** are dictated by quantum numbers l, and m_l. (b) Diagram of total angular momentum, **J**, which is the combination of orbital angular momentum, **L**, and electron spin, **S**, hence **J** = **L** + **S**. Both the spin vector and orbital momentum vector are pointing upwards in this diagram, but this is not always the case.

Here the superscript above each orbital quantum number denotes the total number of electrons in each orbital. Typically, these configurations are abbreviated by only listing the orbitals after the highest completed noble gas level, since inner shells are shielded and will not lose an electron before the outer electrons are empty. Thus, the electron configuration for a Sm^0 ion can be given as Sm^0: [Xe] $4f^6$ $6s^2$. The unique properties of lathanoids is a result of their incompletely filled 4f orbital shells, which are shielded by the outer $5s^2$ and $5p^6$ shells [30,31]. Figure 2.21 demonstrates that the 5s, 5p, and 6s orbitals have a maximum electron density probability at greater radial distances from the nuclei, thus shielding the inner 4f orbitals from bonding and giving the lanthanoids their characteristic properties.

Orbitals quantum numbers are used to express the properties of the surrounding orbitals. However, the behavior of electrons can be further characterized by their momentum, expressed using quantum numbers of orbital angular momentum, **L**, total electron spin, **S**, and the total angular momentum, **J**. These quantum numbers are commonly expressed in the form $^{(2S+1)}\mathbf{L}_\mathbf{J}$. Orbital angular momentum can be likened to that of classical angular momentum, such as a planet rotating around the sun. In the case of quantum orbital angular momentum, an electron resides within a quantized orbit, as shown in Figure 2.22 (a). Often the orbital angular momentum is given

using letters similar to orbital values, where (S, P, D, F, G, H, …) = (0, 1, 2, 3, 4, 5, …). The vector **S** is used denote the spin of the electron and can be likened to a planet spinning on its axis while orbiting the sun. This is often referred to as the intrinsic momentum, and are said to be up or down, depending on the spin. These values are quantized by spin values of ± ½ , and can point in the same direction as the orbital angular momentum vector, **L**, as is shown in Figure 2.22 (b), or can point in the opposite direction. The total angular momentum vector, **J**, is therefore the sum of the angular momentum and overall spin (**J** = **L** + **S**) and has values of $J = |L - S|, |L - S| + 1, \ldots, L + S$. A diagram of the vectors of **L** and **S** vectors and the resulting **J** vector is shown in Figure 2.22 (b) [32].

Lanthanides are most stable in the 3+ oxidization state, meaning that electrons are more likely to be removed from the $6s^2$ orbital and one from the 4f orbital. The preference for the trivalent state is due, in part, to the 4f orbital electrons having a lower energy which results in outer electrons being removed first, (the exception being La and Ce which have empty or nearly empty 4f orbitals). It is also possible that some lantahnoids can have tetravalent (Ce^{4+}, Pr^{4+}, Nd^{4+}, Tb^{4+}, Dy^{4+}) or divalent states (Nd^{2+}, Sm^{2+}, Eu^{2+}, Dy^{2+}, Tm^{2+}, Yb^{2+}) in solids [30]. Of particular interest

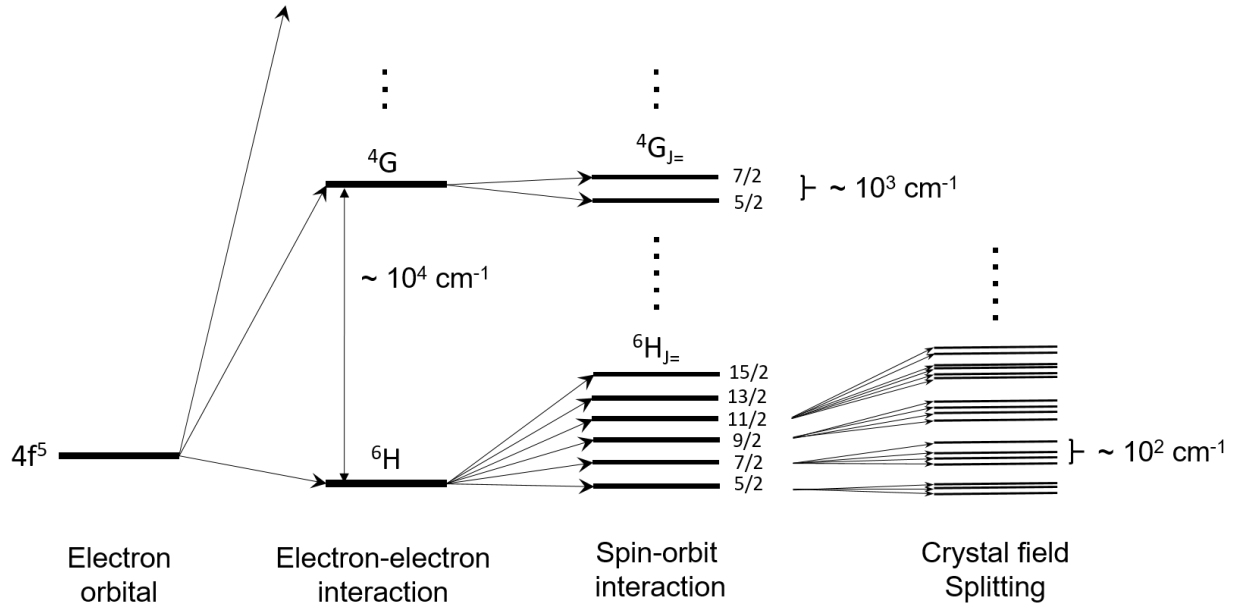

Figure 2.23 Splitting of lower energy levels for Sm^{3+} ion with $4f^5$ electron configuration. Various effects and their strength are given. While the crystal field splitting levels are adapted from [34] the values are largely dependent on the material the ions are present in.

in this work is the Sm^{3+} and Sm^{2+} ions, which have unique and distinct luminescent properties related to their incompletely filled 4f orbitals. These trivalent and divalent ions have electron configurations of [Xe] $4f^5$, and [Xe] $4f^6$, respectively.

Since the 4f electrons of the lanthanoids are shielded by the $5s^2$ and $5p^6$ orbitals, the energy levels of the inner free electrons are only weakly affected by the surrounding environment. This shielding results in transitions that are determined by various electronic interactions within the 4f orbitals. These interactions are arranged in order of strength, from coulomb repulsion to spin orbit coupling and the surrounding crystal field splitting, as shown in Figure 2.23. Electrons in the 4f orbitals interact with each other by coulomb repulsion since electrons have identical charges. This coulomb repulsion results in splitting into different energy levels that belong to the $4f^n$ configuration such as the ^4G, ^6F, ^6H, etc. These terms can then be further split by spin orbit coupling, which results from the electron's magnetic dipole, the orbital momentum, and the field from the nucleus [33]. Taking Sm^{3+} as an example, if we consider the spin multiplicity of the ^6H level, we see that there are 6 possible energy levels from the total angular momentum, **J**, $^6H_{5/2}$, $^6H_{7/2}$, $^6H_{9/2}$, … $^6H_{15/2}$. The spin orbit coupling energy level separations can be relatively large due to the size of the lanthanide nucleus. These fields can be further separated by into what are known as Stark sublevels, which result from the crystal field splitting due to neighbouring ions within the ordered structure. The magnitude of the splitting is largely dependent on the strength of the surrounding crystal field [34]. Overall, the resulting shielded 4f electrons give the result that the transition levels are relatively independent of the host structure and the energy level separation can be given by a Dieke diagram [35-37], which shows energy level separation for lanthanides, as shown in Figure 2.25.

The ground state of an ion can be predicted using Hund's rule, which states that an electron will fill an unoccupied sublevel within the orbital, and that each electron in a singly occupied orbital will have the same spin. Hund's rule is used to calculate the ground levels for Sm^{3+} and Sm^{2+} in Figure 2.24, which uses the following rules [30],

1. The spin multiplicity ($2\mathbf{S} + 1$) is maximum. This occurs when as many electrons are in the spin up state as possible.

2. If there are multiple filled sublevels, the term with the largest **L** value is the ground state
3. For an atom with an outermost subshell that is less than half filled, the lowest total angular momentum, **J**, represents the ground level. If the shell is more than half filled, **J** is maximum for the ground state.

The 4f shell for Sm^{2+} and Sm^{3+} has 5 and 6 electrons, respectively. Using Hund's rule we take the spins to be additive ($\mathbf{S}_{max} = |\sum m_s|$, where all spins are aligned) and **L** to be maximum ($\mathbf{L} = |\sum m_l|$) then we can calculate **J** to be minimum when $|\mathbf{L} - \mathbf{S}|$ for the samarium ions, since the shell is less than half filled.

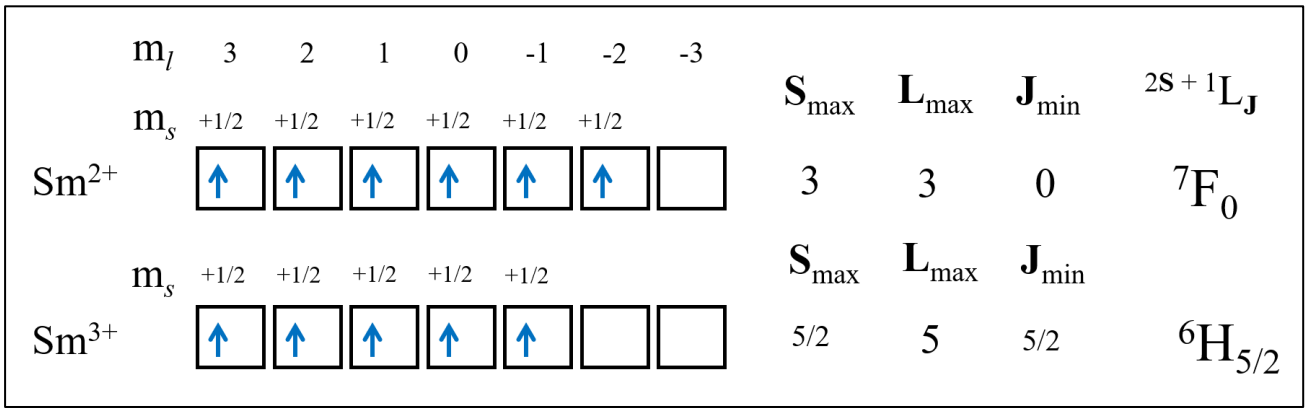

Figure 2.24 Ground states for Sm^{3+} and Sm^{2+} calculated using Hund's rule.

2.5.2 Luminescence of Rare Earth Ions

The term luminescence comes from the Latin word, lumen, meaning light. This term was proposed by Eilhardt Wiedmann, and defined to mean "evolutions of light which do not depend on the temperature of the substance concerned" [38]. Thus, luminescence is distinguished from incandescence, which refers to thermal radiation from a material as it is heated. A luminescent material, also called a phosphor, is a material that converts energy into electromagnetic radiation, often in the visible spectrum, but can also emit in the infrared or ultraviolet region. There are multiple forms of luminescence that converts energy into light, such as cathodoluminescence (from high energy electrons), electroluminescence (using an electric voltage), chemical luminescence (from a chemical reaction), and so on [39]. Of particular interest in this work is photoluminescence, which is the emission of light after photoexcitation.

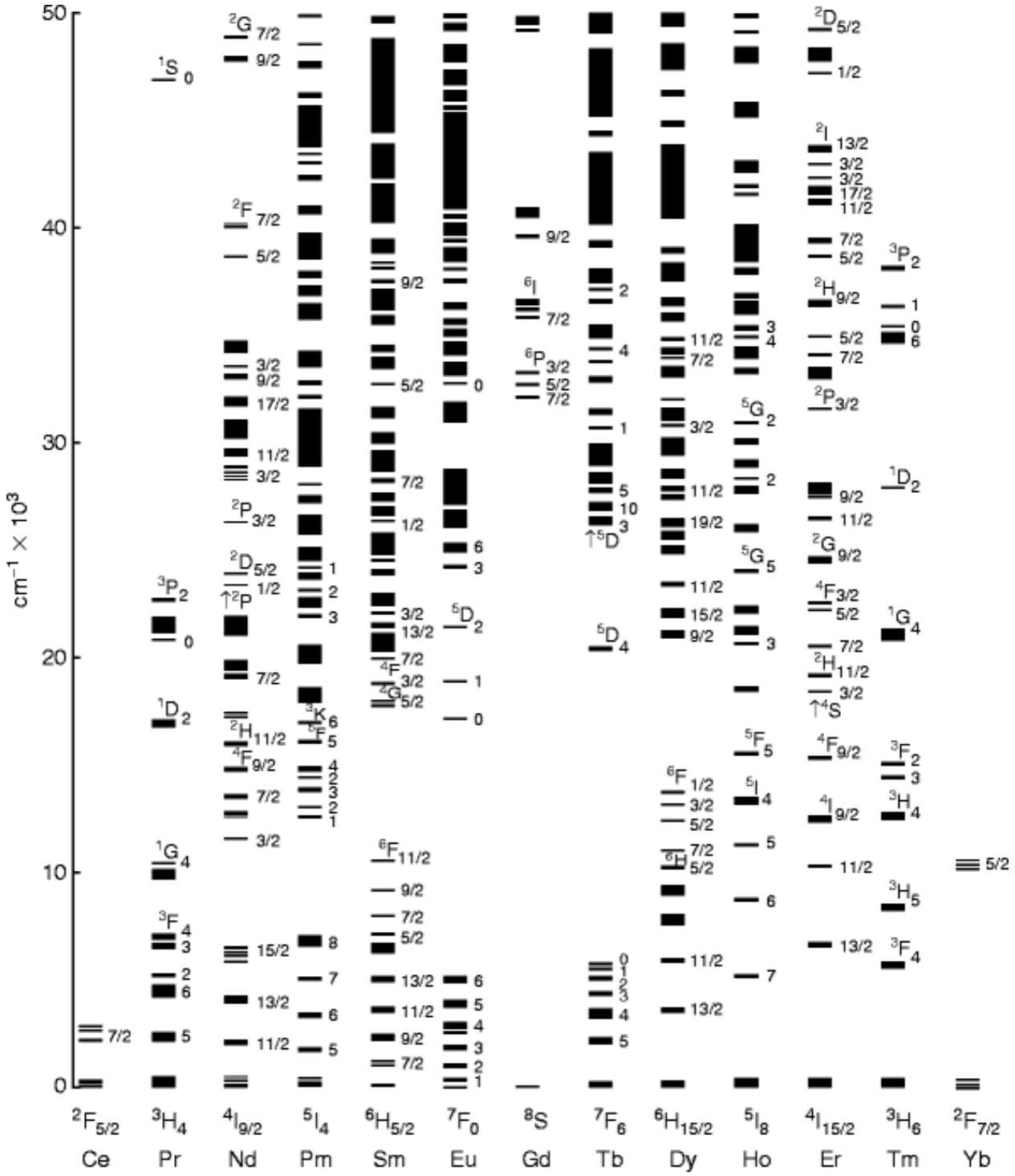

Figure 2.25 Dieke energy level diagram for trivalent rare earths in LaF_3 (From [36]). Lines indicate energy levels of the multiplets and widths of the lines are related to the crystal field splitting strength.

Photoluminescence occurs in a material when an atom interacts with a photon, causing the energy to be absorbed, and, if the photon energy is sufficient, the electron is promoted to a higher energy level. After this electron is excited, the electron will return to the ground state by emitting energy through a photon or phonon in the form of heat. This transition between states is governed by selection rules. These selection rules state whether or not certain transitions are "allowed" or "forbidden". If the electric dipole parity changes from one excited state to another, that is, the orbital quantum number, *l*, changes ($\Delta l = \pm 1$) but the magnetic dipole, or spin, is unaffected, then the transition is allowed and has a high probability of occurring.

An allowed transition occurs when an electron is excited to a higher orbital without changing spin states and then returns to the ground level by emitting a photon. The emission rates of allowed transitions are on the order of nanoseconds, and are often referred to as fluorescence, indicating that the luminescent emission lifetime is very rapid. For ions with electronic configuration of $4f^{n}$, such as samarium, the electric dipole transitions have the same parity, and therefore $4f \rightarrow 4f$ transitions are forbidden. While these transitions are classified as forbidden, they can still occur, albeit at a much slower rate, which produces optical emission at rates that can range from milliseconds to seconds, which is termed phosphorescence. Photoluminescence therefore applies to both fluorescence and phosphorescence emissions, however, they are distinguished by the relative lifetimes and the selection rules that govern these transitions. Optical emission of forbidden $4f \rightarrow 4f$ transitions are possible through magnetic dipole transitions [33,39,40]. These magnetic dipole transitions are governed by selection rules given as

$$\begin{cases} \Delta S = 0 \\ \Delta L = 0, \pm 1 \ (\mathrm{L} = 0 \ \leftrightarrow \mathrm{L} = 0 \text{ is forbidden}) \\ \Delta J = 0, \pm 1 \ (\mathrm{J} = 0 \ \leftrightarrow \mathrm{J} = 0 \text{ is forbidden}) \end{cases} \tag{2.16}$$

Since a photon does not interact with the spin of an electron, the spin quantum numbers do not change. However, a photon does have angular momentum and can change the orbital angular momentum, and by extension the total angular momentum, **J**. Ultimately, the electron states are governed by the Pauli exclusion principle, which states that no two electrons can have the same quantum values in an atom.

For the samarium ions, photoluminescence can be observed if excited by a photon with sufficient energy, which can be predicted by measuring the absorption spectra of a sample. In the case of samarium doped fluoroaluminate (FA) glass, violet or blue wavelengths at either 405 nm or 475 nm can be used to excite Sm^{3+} and Sm^{2+} ions, allowing for measurement of the photoluminescence of the sample, shown in Figure 2.26 [41]. The emission and absorption spectra can be predicted using the Dieke diagram shown in Figure 2.25, which shows the separation of energy levels for trivalent rare earths. The emitted spectra of Sm^{3+} has sharp distinct lines, that are characteristic of the f → f transitions of lanthanide 3+ ions, and these sharp lines can be explained through the use of the Judd-Ofelt theory [42,43]. The Judd-Ofelt theory, in part, states that while electric dipole transitions between 4f → 4f orbitals are "forbidden", magnetic dipole and electric quadrupole transitions are "allowed", although electric quadrupole emissions are very weak. These

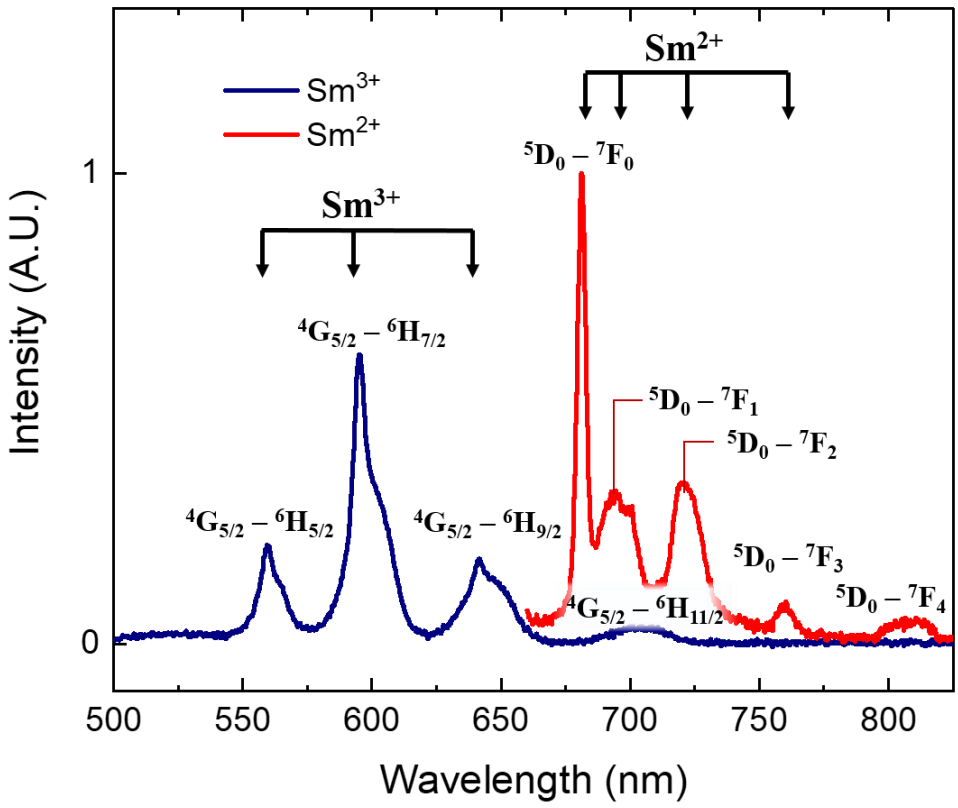

Figure 2.26 Photoluminescent spectra of Sm^{3+} and Sm^{2+} ions in fluoroaluminate glass along with energy level transitions. Data is adapted from [44]. Energy level diagram of Sm^{3+} and Sm^{2+} is shown in Figure 2.27

transitions between energy levels are dictated by the separation between energy levels, and are discrete, resulting in sharp spectral lines

The emission spectra of Sm^{3+} and Sm^{2+} is shown in Figure 2.26 [44], as well as the energy level diagram for Sm^{3+} upon excitation in Figure 2.27. There is clear presence of distinct spectral peaks at approximate emission wavelengths of 559 nm, 595 nm, 641 nm, and 704 nm corresponding to $^4G_{5/2} \rightarrow {}^6H_{5/2}$, $^6H_{7/2}$, $^6H_{9/2}$, and $^6H_{11/2}$ transitions, respectively. In addition, if Sm^{3+} is photoexcited by a source with a wavelength in the blue to ultraviolet region, there is successful emission, regardless of the energy of the incident photon, so long as it is able to excite above the $^4G_{5/2}$ level [40,45,46]. The difference between the absorption energy and the emission energy is called the Stokes shift, where the energy between absorption and emission levels are often emitted in non-radiative forms, such as phonon (thermal) energy. This phonon emission is fast, as opposed to the "forbidden" transitions. The transitions and their probability can be predicted by the Judd-Ofelt theory, which gives the radiative lifetimes of from one excited state to the next dictated by the rates of magnetic dipole, or electric dipole and quadrupole transitions.

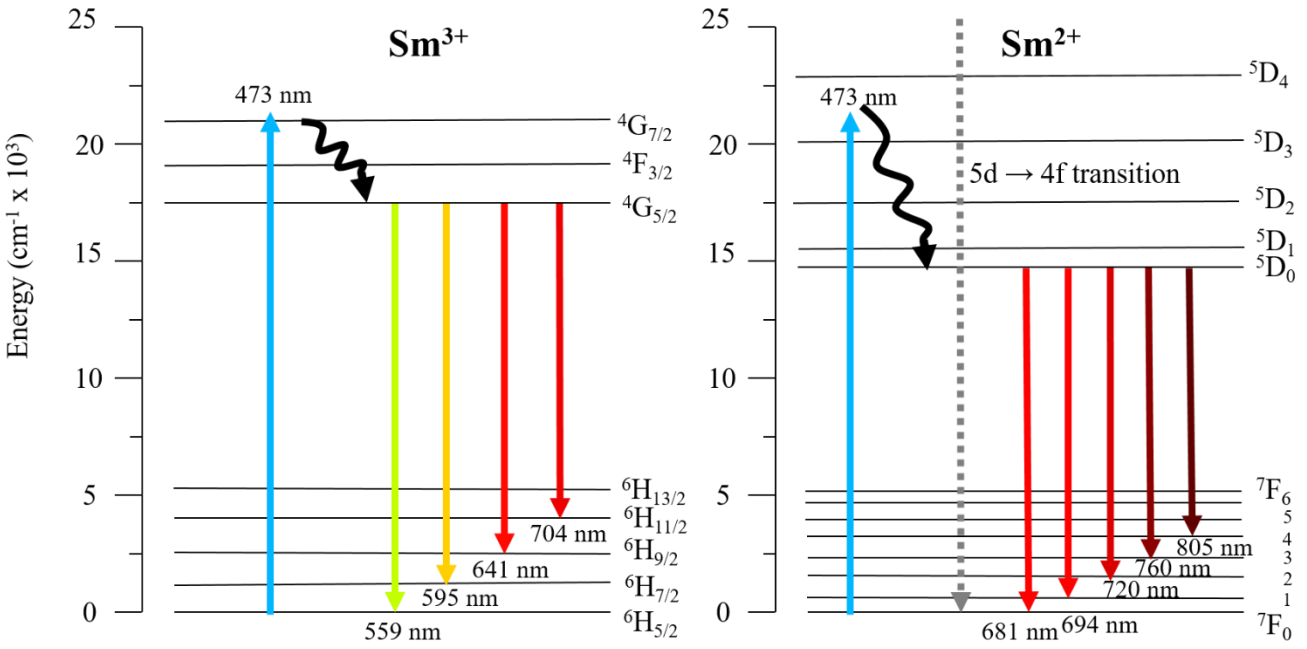

Figure 2.27 Energy level diagram for Sm^{3+} and Sm^{2+} from the photoluminescent spectra shown in Figure 2.26. Using an excitation source of 473 nm, the probable excitation level is shown ,where there is relaxation to the $^4G_{5/2}$ or $^5D_0$ level before photon emission [45].

Trivalent samarium has an odd number of electrons in the 4f shell, which is classified as a Kramer's ion. Kramer's theorem states that if an energy level has a half integer spin, such as the case with a Kramer ion, each energy level is said to be doubly degenerate, meaning that electrons can share an energy level. In the case of Sm^{2+}, there are an even number of electrons in the 4f shell ($4f^6$), which is a non-Kramer's ion and therefore does not have double degeneracy. The ground level for Sm^{2+} is ^7F followed by ^5D, which have seven ($^7F_0$ to $^7F_6$) and five ($^5D_0$ to $^5D_4$) levels, shown in Figure 2.27. Considering the Dieke diagram in Figure 2.25, one would predict that trivalent europium (Eu^{3+}) and Sm^{2+} should behave similarly, since they are both non-Kramer ions with configuration of $4f^6$, that follow the same $^7D \rightarrow {}^5F$ transitions. However, the excited state energy for the $4f^55d^1$ configuration for Sm^{2+} is lower than in the case of Eu^{3+}, which in turn, affects the excitation mechanism compared to that of Eu^{3+} and Sm^{3+}. The photoluminescence of Sm^{2+} involves a $4f^55d^1 \rightarrow 4f^6$ parity allowed transition, and a $4f^6 \rightarrow 4f^6$ forbidden magnetic dipole transition ($^5D_0 \rightarrow {}^7F_{0,\,1,\,2,\,3,\,4}$), resulting in an excitation mechanism that differs from that of other trivalent rare earth ions. The overall result is that Sm^{2+} ions have a higher emission rate than the Kramer ions of Sm^{3+}, as will be discussed in subsequent chapters. This results in Sm^{2+} ions having a larger measured intensity when compared to Sm^{3+} ions, since the radiative lifetime of Sm^{2+} will be faster than that of Sm^{3+} as given by the Judd-Ofelt theory. The position of the $5d^1$ excitation level depends on the crystal field strength, the ligand field, and the temperature and, at room temperature, $4f^6 \rightarrow 4f^6$ transitions can be observed. However, at higher temperatures, it is possible to observe broader, allowed, $4f^55d^1 \rightarrow 4f^6$ transitions resulting from a greater number of electrons occupying a higher orbital level, shown in Figure 2.27 [40].

2.5.3 Rare Earth Host Materials

Rare earth ions can be used as a detection method of high energy radiation by measuring a valence change of RE^{3+} to RE^{2+} which corresponds to the total dose. Since Sm^{3+} and Sm^{2+} have easily distinguishable emission spectra, it is an ideal candidate to use the proportional change in photoluminescence of each ion, which emit in the orange to red region of the visible spectra, to measure the dose delivered. Considering samarium occurs naturally in the trivalent state, the reduction of Sm^{3+} to Sm^{2+} depends on an electron being donated to the 3+ ion after irradiation.

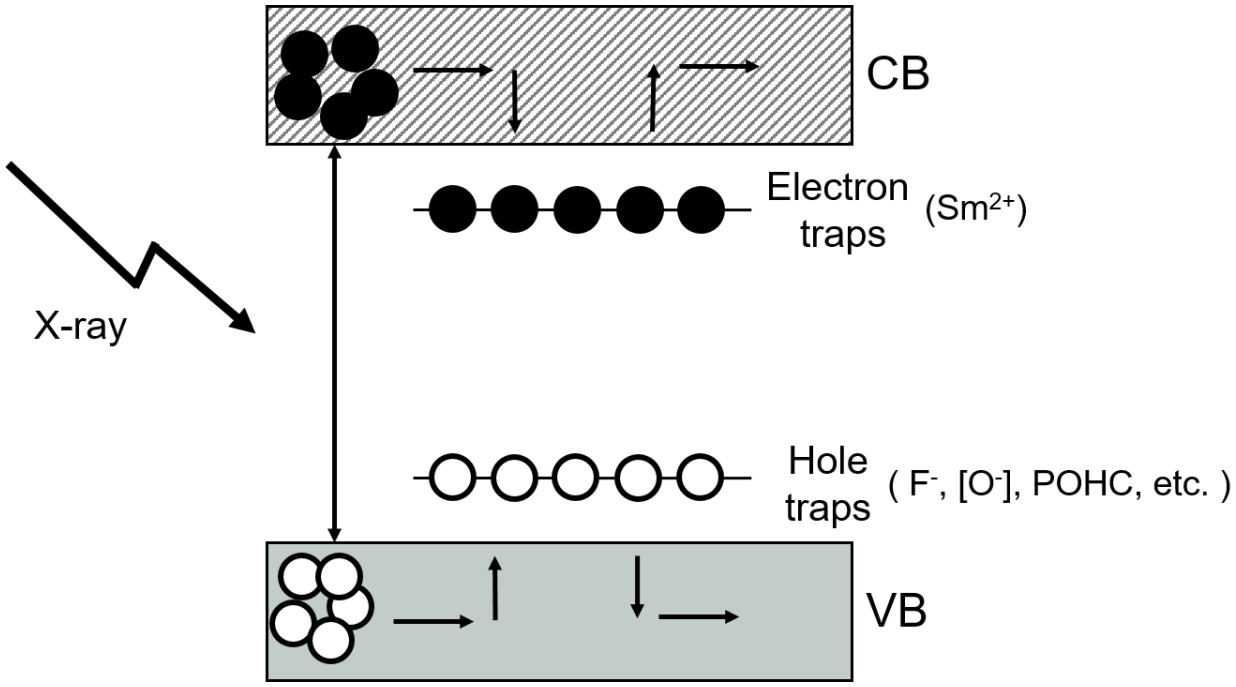

Figure 2.28 Band diagram of a material where electron hole pairs are generated from irradiation of x-rays. These electrons and holes are then in the conduction and are trapped by semi stable electron trapping sites (Sm^{2+}) and hole traps (defects) in the materials. Since these trap sites are relatively shallow, it is possible detrap these charges and return to the original state.

The process of inducing valence conversion of Sm^{3+} in solids is not trivial, but has been demonstrated by various forms of radiation, such as γ-rays, X-rays, β radiation, UV exposure and others [47 - 51]. If we consider an incident x-ray, which generates an electron-hole pair, the electrons are moved into the conduction band (CB) leaving behind a hole in the valence band (VB), as shown in Figure 2.28 [52]. In order to prevent electrons and holes from spontaneous recombination, the holes and electrons must be trapped by sites which are semi stable between the conduction and valence band. Since Sm^{2+} acts as an electron trap, there then must also be impurities or defects within the matrix of the material that act as hole traps. These hole trapping sites vary greatly depending on the host matrix, but they must be present to observe consistent valence conversion. Taking fluoroaluminate (FA) and fluorophosphate (FP) glasses, as an example, where there is evidence of hole traps associated with fluoride and oxygen centers in FA glass [52- 55], and phosphorous-oxide hole centers (POHC) in FP glass [56- 58] which allows for holes to be trapped just outside of the valence band. Valence change in glass ceramics with nanocrystal is also possible [59], however glass materials are preferable for optical applications since they are transparent to light, and can achieve homogenous doping of ions within the solid.

In addition to the presence of hole trapping sites between the valence and conduction band contributing to stable $RE^{3+} \rightarrow RE^{2+}$ conversion, we must also consider the energy level positions of the rare earth valences in relation to the width of the band gap. In order to achieve stable electron trapping and stable hole trapping, the energy levels of the rare earth ions must fall between the valence and conduction band. Figure 2.29 shows the location of various energy levels for trivalent and divalent rare earth atoms within the energy band diagram of a CaF_2 crystal [60]. It is instructive to note that the separation of energy levels between the RE^{3+} and RE^{2+} remains constant, whereas the location of the conduction band and valence band are dependent on the material, and the ions can fall above or below the conduction or valence band. It is therefore straightforward to see, that a material with a large energy bandgap would be more likely for to a valence change of rare earth

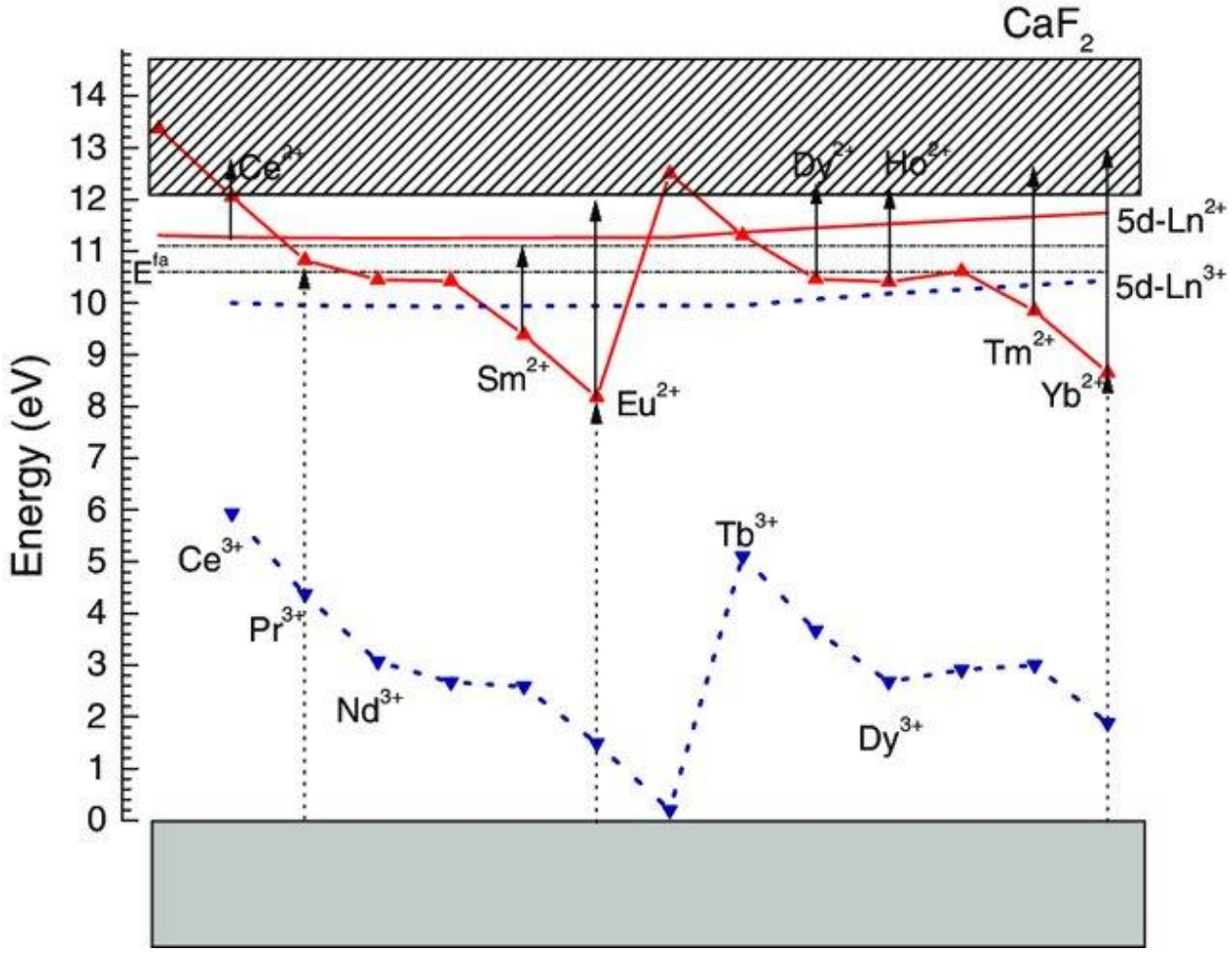

Figure 2.29 Energy levels of rare earth ions in the 3+ and 2+ formation within a CaF_2 crystal. The energy separation between trivalent and diavalent ions remain constant, regardless of the host material. However, the location and separation of the conduction bands and valence bands are material dependent. (From [60]).

ions to be observed after high energy radiation. FA and FP glasses, for example, have comparatively large bandgaps (8.25 eV and 7.8 eV) [61] compared with the majority of glasses (which typically have 2 – 4 eV) and have demonstrated successful conversion of $Sm^{3+} \rightarrow Sm^{2+}$. Additionally, the electron and hole traps between the conduction and valence bands must be sufficiently separated so that the states remain stable. If the energy level of the RE ion is very close to the conduction or valence band, then it is probable that the electrons and holes will be detrap spontaneously and are therefore not stable.

Conversion of Sm^{3+} to Sm^{2+} requires an electron to be accepted by a Sm^{3+} ion. However, if an electron is accepted, a corresponding hole must also be accepted. In examining Figure 2.30, which looks at the concentration of Sm^{3+} dopants compared to the conversion of $Sm^{3+} \rightarrow Sm^{2+}$, we see that, as the total number of electron acceptors is increased, the amount of conversion from trivalent to divalent samarium does not also increase [62]. Put differently, the conversion of Sm^{3+} is governed by a hole trapping process for both FA and FP glasses. This is also evident when we

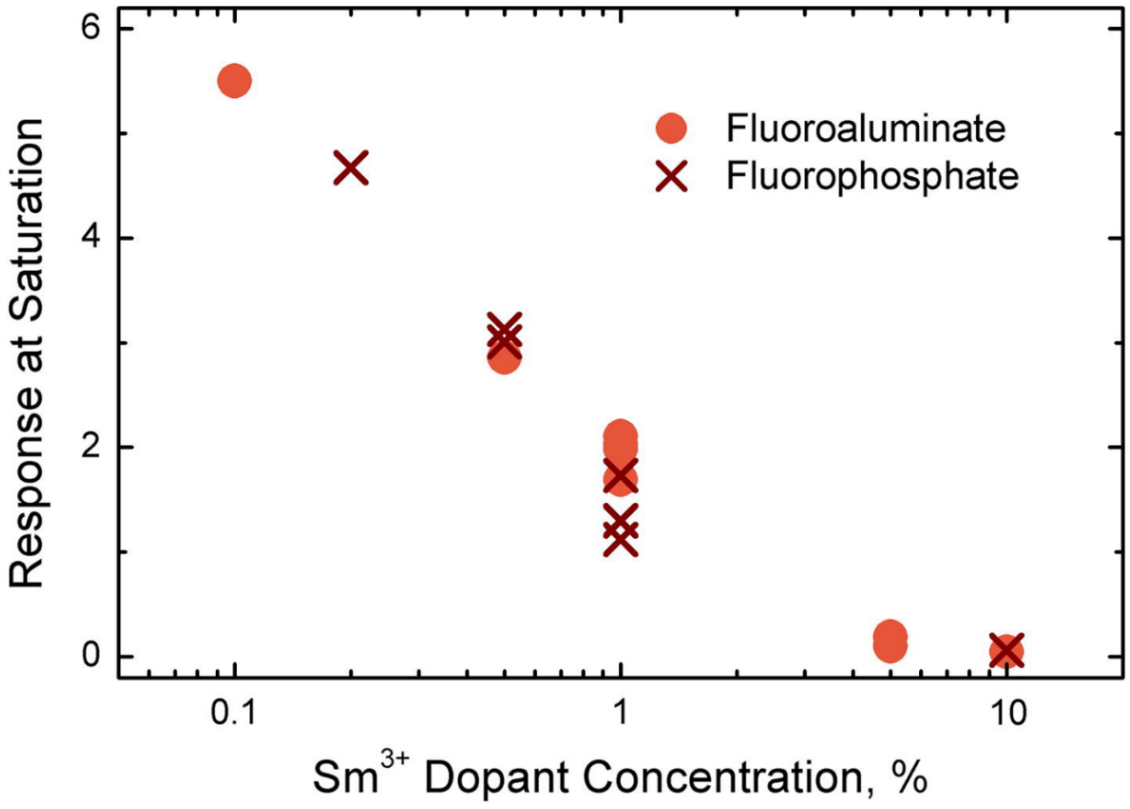

Figure 2.30 Sm^{3+} dopant concentration in mol% compared to conversion (Response) in FA and FP glasses. Response is calculated by taking the ratio of the photoluminescence of Sm^{2+} to that of Sm^{3+}. (From [62]).

consider that when a sample doped with trivalent samarium reaches saturation of the Sm^{2+} signal, there is PL from Sm^{3+} ions, meaning that there are still electron acceptors available.

While conversion of $Sm^{3+} \rightarrow Sm^{2+}$ is essential for dosimetric applications, it is also desirable to achieve reconversion of Sm^{2+} to Sm^{3+} in some instances. If the electron traps and hole

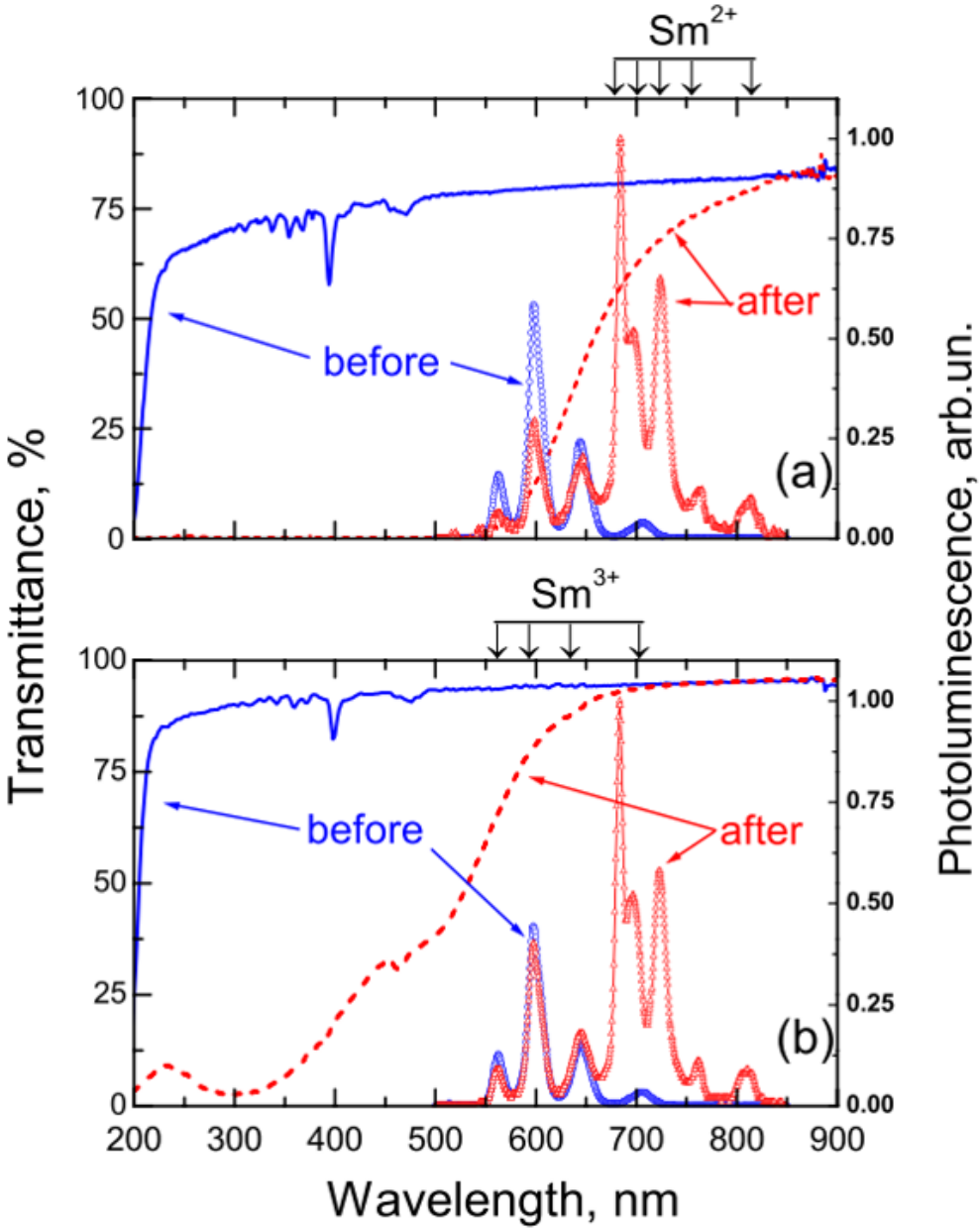

Figure 2.31 Transmission (left axis) and photoluminescence (right axis) of Sm doped FP glass (a) and FA glass (b) before and after irradiation. Although both samples show excellent conversion of $Sm^{3+} \rightarrow Sm^{2+}$, FP glass shows significant darkening and a decrease in transmission in the emission region of Sm^{3+}. (From [63].)

traps can be thermally stimulated or excited through UV exposure, then it possible that the recombination of the ion states can create reusable phosphors. In the case of Sm^{3+} doped FA and FP glasses, if the material is heated above the transition temperature of the glass (440 °C for FA glass, 462 °C for FP [63]), there is a detrapping of holes which causes the divalent state to change back to the trivalent state and almost all ions return to the Sm^{3+} form.

Upon irradiation, the majority of glasses exhibit some form of undesirable photodarkening which causes a change in transmission. The change in absorption spectra for FA and FP glasses as a function of irradiation is shown in Figure 2.31 [63]. This photodarkening is associated with defect centers, sometimes referred to as colour centers, within the material. These defect centers created through exposure to radiation tend to absorb light in the visible spectrum. The extent of photodarkening within a proposed glass host material is an important consideration, since the transmission spectra can change with irradiation, which can consequently affect the intensity of the measured rare earth ion intensity. The decrease in intensity as a function of emission wavelength and x-ray induced photodarkening can be corrected for, but the calculation is not trivial. Therefore, minimal photodarkening is important for a host material for rare earth valence dosimetry.

2.6 Ion Implantation

Ion implantation is a process that uses high energy ions to modify the surface properties of a target material. The changes in the target material properties can be chemical, if the incident ions differ from that of the target material composition, or they can be structural (or both) through damage to the crystal like structure caused by high energy ions. Dopant ions are emitted from a target source and pass through a mass spectrometer, which uses a magnetic field to select atoms with specific mass and charge that are then further accelerated before being implanted in a desired material. The implantation process is performed under vacuum conditions to prevent attenuation of the ions in atmosphere before reaching the target material. A diagram of a typical ion implantation process is shown in Figure 2.32.

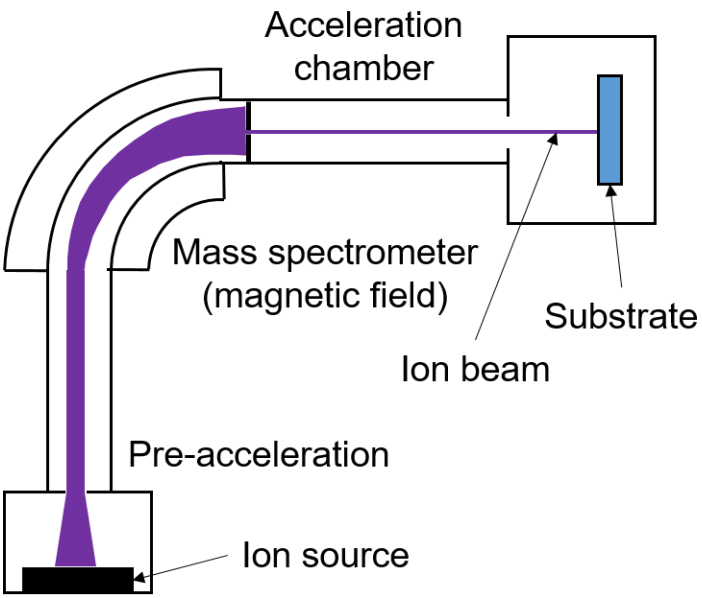

Figure 2.32 Diagram of implantation process.

Implanted ions will cause structural damage to the substrate by displacing ordered atoms within the host matrix structure; the severity of the damage to the ordered matrix depends on the energy and mass of the incident particle, shown in Figure 2.33. The depth at which the dopant ions will be implanted depends on the energy, size, mass, and charge of the ion, and the composition of the target material. Ion implantation sources typically fall into three categories, medium current, which have an energy range of <1 keV to 200 keV, high current, which have energies of 5 keV to 600 keV, and high energy, which can produce ions with energies of up to 6 MeV [64]. As ions penetrate into the solid, they will lose energy and have a broad depth distribution, owing to collisions with target atoms and from drag of overlapping electron orbitals. This energy loss is a gradual process. The stopping power of a particle in a material is described as the loss of energy, E, over a distance length, *x*, and is often written as S(E) where,

$$S(E) = -\frac{dE}{dx} \tag{2.17}$$

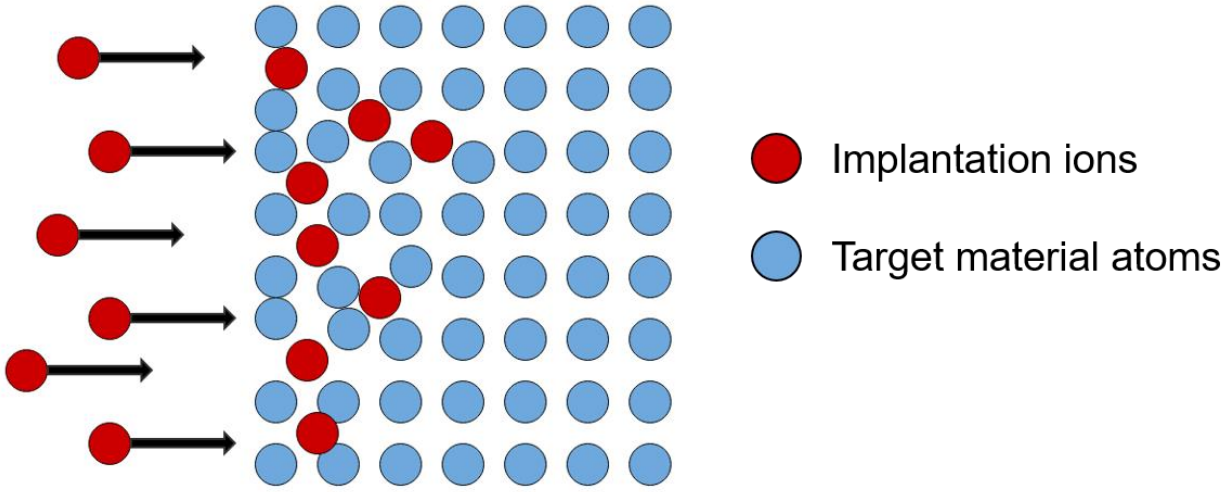

Figure 2.33 Illustration of implantation ions creating damage to the order of the crystal structure of the target material.

The energy loss per distance travelled can be plotted, which shows that the energy loss is relatively constant until a pronounced peak occurs and the particle stops, shown in Figure 2.34 [65]. This peak is called a Bragg peak, and is often used in particle therapy to deposit dose at a specific location, such as a tumour. As the particle is travelling through matter, it ionizes atoms and deposits dose along the path. However, as the particle deposits more and more energy along the path, it also loses velocity, and so the energy deposition results in a large peak very near the particle final position. The mean energy loss per distance travelled for a charged particle with velocity *v*, energy E, and charge z, into a material with a mean excitation potential *I*, can be predicted by the "Bethe-Bloch" equation [66,67] which is given as

$$-\left\langle \frac{\mathrm{dE}}{\mathrm{d}x} \right\rangle = K\, z^2 \frac{Z}{A} \frac{1}{\beta^2} \left[\frac{1}{2} \ln \left(\frac{2 m_e c^2 \beta^2 \gamma^2 T_{\max}}{I^2} \right) - \beta^2 - \frac{\delta(\beta\gamma)}{2} \right] \qquad (2.18)$$

Where $K = 4\pi \mathrm{N_A} r_E^2 m_e c^2$, Z is the atomic number of the absorber, A is the atomic mass of the absorber, $\beta = {}^{v}/_{c}$, $\gamma = 1/\sqrt{1-\beta^2}$, $m_e c^2$ is the electron mass, r_e is the classical electron radius, $\mathrm{N_A}$ is Avogadro's number, $\delta(\beta\gamma)$ is an experimentally determined density effect correction to ionization energy loss, and $T_{\max}$ is the maximum kinetic energy which can be imparted to a free electron in a single collision. For a particle with mass M and momentum $M\beta\gamma c$, $T_{\max}$ is given by,

$$T_{\max} = \frac{2m_e c^2 \beta^2 \gamma^2}{1 + 2\gamma m_e/M + (m_e/M)^2} \tag{2.19}$$

At high (relativistic) energies, the Bethe-Bloch equation agrees well with experimental results [68]. The overall energy loss per distance travelled is used to approximate the path length of an implanted ion, and is often referred to as the continuous slowing down approximation (CSDA) range.

In the case of ion implantation with a heavy ion, such as samarium, the penetration depth into FA glass is very shallow, one micron or less, even at high energies, as will be discussed in a chapter 4. In addition, there is evidence of both Sm^{3+} and Sm^{2+} ions after the implantation process, indicating that electrons are being accepted as a result of high energy implantation. This also means that any photoluminescent spectra resulting from these ions is from Sm ions very near the surface of the glass material, and can be used to measure surface dose, as opposed to the bulk doped sample which has Sm ions present throughout the entire solid.

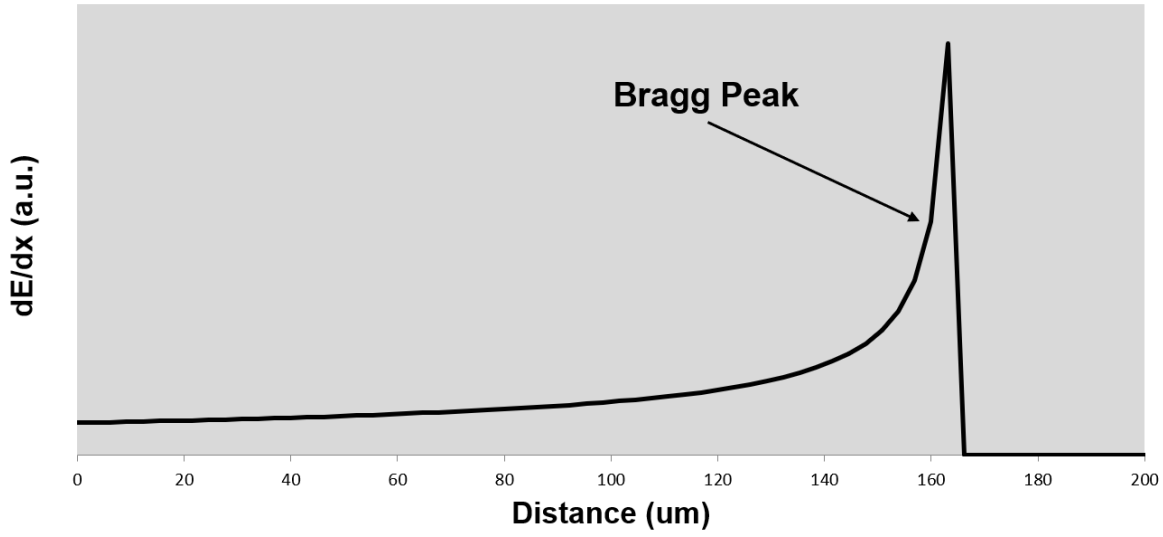

Figure 2.34 Energy loss vs. distance for a 5 MeV alpha particle in SiO_2 calculated using the Bethe-Bloch equation. Note the presence of the Bragg peak, where the majority of the dose is deposited and the particle comes to rest.

2.7 References

[1] Punnoose J, Xu J, Sisniega A, Zbijewski W and Siewerdsen J H, Technical Note: spektr 3.0—A computational tool for x-ray spectrum modeling and analysis Med. Phys. 31 3057–67 (2016)

[2] A. Thompson, I. Lindau, D. Attwood, Y. Liu, E. Gullikson, P. Pianetta, M. Howells, A. Robinson, K. Kim, J. Scofeild, J. Kirz, J. Underwood, J. Korttright, *X-ray data booklet.* Berkeley California, Lawrence Berkley National Laboratory, 2009. Available online: https://xdb.lbl.gov/

[3] M.J. Berger, J.H. Hubbell, S.M. Seltzer, J. Chang, J.S. Coursey, R. Sukumar, D.S. Zucker, K. Olsen, (2010) *XCOM: Photon Cross Sections Database*, NIST Standard Reference Database 8 (XGAM), website: (Accessed Oct 1st, 2019) https://physics.nist.gov/PhysRefData/Xcom/html/xcom1.html

[4] F. Sauter, Über den atomaren Photoeffekt in der K-Schale nach der relativistischen Wellenmechanik Diracs Ann. Physik **403**, 454-88 (1931)

[5] J. A. R. Samson, Angular distributions of photoelectrons and partial photoionization cross-sections, Phil. Trans. Roy. Soc. Lond. A. **268**, 141-6 (1970)

[6] D. N. Slatkin, F. A. Dilmanian, P. Spanne, M. Sandborg, Microbeam radiation therapy. Med. Phys. **19**, 1395-400 (1992)

[7] R. W. Smith, J. Wang, E. Schultke, C. B. Seymour, E. Bräuer-Krisch, J. A. Laissue, H. Blattmann, C. E. Mothersill, "Proteomic changes in the rat brain induced by homogenous irradiation and by the bystander effect resulting from high energy synchrotron X-ray microbeams," Int. J. Rad. Bio. **89:2**, 118-27 (2013)

[8] F. A. Dilmanian, Y. Qu, L. E. Feinendegen, L. A. Pena, T. Bacarian, F. A. Henn, J. Kalef-Ezra, S. Liu, Z. Zhong, and J. W. McDonald, "Tissue-sparing effect of x-ray microplanar beams particularly in the CNS: Is a bystander effect involved?," Exp Hematol **35,** 69-77 (2007).

[9] C. P. Baker, H. J. Curtis, W. Zeman, R. G. Woodley, "The design and calibration of a deuteron microbeam for biological studies," Radiat. Res., **15**, 489-95 (1961)

[10] W. Zeman, H. J. Curtis, C. P. Baker, "Histopathologic effects of high-energy-particle microbeams on the visual cortex of the mouse brain," Radiat. Res., **15**, 496-514 (1961)

[11] W. Zeman, H. J. Curtis, E. L. Gebhard, W. Haymaker, "Tolerance of mouse-brain tissue to high-energy deuterons," Science, **130**, 1760-1 (1959)

[12] H. J. Curtis "Limitations on space flight due to cosmic radiations" Science, **133**, 312-6 (1961) DOI: 10.1126/science.133.3449.312

[13] H. Blattmann, J. Gebbers, E. Bräuer-Krisch, A. Bravin, G. Le Duc, W. Burkard, M. Di Michiel, V. Djonov, D. N. Slatkin, J. Stepanek, J. A. Laissure, "Applications of synchrotron X-

rays to radiotherapy," Nuclear Instruments and Methods in Physics Research Section A: Accelerators, Spectrometers, Detectors and Associated Equipment, **548**, pp. 17-22, (2005)

[14] A. G. Michette and J. C. Buckley, *X-ray Science and Technology*. Bristol ; Philadelphia: Institute of Physics Pub., 1993.

[15] E. Bräuer-Krisch, A. Rosenfeld, M. Lerch, M. Petasecca, M. Akselrod, J. Sykora, J. Bartz, M. Ptaszkiewicz, P. Olko, A. Berg, M. Wieland, S. Doran, T. Brochard, A. Kamlowski, G. Cellere, A. Paccagnella, E. A. Siegbahn, Y. Prezado, I. Martinez-Rovira, A. Bravin, L. Dusseau, P. Berkvens, Potential high resolution dosimeters for MRT. AIP Conf. Proc. **1266**, 89-97 (2010)

[16] V. C Borca, M. Pasquino, G. Russo, P. Grosso, D. Cante, P. Sciacero, G. Girelli, M. R. Porta, S. Tofani, Dosimetric characterization and use of GAFCHROMIC EBT3 film for IMRT dose verification. Journal of Applied Clinical Medical Physics, 14: 158-171. (2013)

[17] J. C. Crosbie, I. Svalbe, S. M. Midgley et al., A method of dosimetry for synchrotron microbeam radiation therapy using radiochromic films of different sensitivity Phys Med Biol 53 (23), 6861 (2008)

[18] B. D. Lynch, J. Kozelka, M. K. Ranade, J. G. Li, W. E. Simon, J. F. Dempsey, Important considerations for radiochromic film dosimetry with flatbed CCD scanners and EBT Gafchromic film, Med. Phys., **33**, 4551-6 (2006)

[19] G. Cellere, A. Paccagnella, IEEE Transaction on Device and Material Reliabilty, **3** (4), 359 (2004)

[20] Siegbahn, E. A., Bräuer-Krisch, E. , Bravin, A. , Nettelbeck, H. , Lerch, M. L. and Rosenfeld, A. B. , MOSFET dosimetry with high spatial resolution in intense synchrotron-generated x-ray microbeams. Med. Phys., **36**: 1128-37 (2009)

[21] J.A. Bartz, G.J. Sykora, E. Bräuer-Krisch, M.S. Akselrod, Imaging and dosimetry of synchrotron microbeam with aluminum oxide fluorescent detectors, Radiation Measurements, **46**, 12, 1936-9 (2011)

[22] G.M. Akselrod, M.S. Akselrod, E.R. Benton, N. Yasuda, A novel Al2O3 fluorescent nuclear track detector for heavy charged particles and neutrons, Nuclear Instruments and Methods in Physics Research Section B: Beam Interactions with Materials and Atoms, **247**, 2, 295-306. (2006)

[23] Povoli, M. et al. Thin Silicon Strip Detectors for Beam Monitoring in Micro-Beam Radiation Therapy. Journal of Instrumentation **10,** P11007 (2015)

[24] Gagliardi, F. M., Cornelius, I. , Blencowe, A. , Franich, R. D. and Geso, M., High resolution 3D imaging of synchrotron generated microbeams. Med. Phys., 42: 6973-6986. (2015)

[25] M. Ptaszkiewicz, E. Braurer-Kirsch, M. Klosowski, L. Czopyk, P. Olko, TLD dosimetry for microbeam radiation therapy at the European Synchrotron Radiation Facility, Radiation Measurements, **43**, 2–6, 990-993, (2008)

[26] S. Almaviva, M. Marinelli, E. Milania, A. Tucciaronea, G. Verona-Rinatia, R. Consorti, A. Petrucci, F. De Notaristefani, I. Ciancaglioni Synthetic single crystal diamond diodes for radiotherapy dosimetry, **594**, 2, 273-7, (2008)

[27] J. Livingstone, A. W. Stevenson, D. J. Butler, D. Häusermann J.F. Adam, Characterization of a synthetic single crystal diamond detector for dosimetry in spatially fractionated synchrotron x-ray fields, Med. Phys., **43**, 4283-4293, (2016)

[28] J. Manuel Lárraga-Gutiérrez et al, Properties of a commercial PTW-60019 synthetic diamond detector for the dosimetry of small radiotherapy beams, Phys. Med. Biol., **60,** 905-24 (2015)

[29] Wells, W. H. and Wells, V. L. The Lanthanides, Rare Earth Elements. In Patty's Toxicology (eds E. Bingham, B. Cohrssen and C. H. Powell). (2012).

[30] S. Cotton, Lanthanide and actinide chemistry, Wiley, Chichester, England ; Hoboken, NJ, (2006)

[31] A.J. Freeman and R.E. Watson. Theoretical Investigation of Some Magnetic and Spectroscopic Properties of Rare-Earth Ions, Phys. Rev.**127**: 2058-2075. (1962)

[32] D. McQuarrie, J. D. Simon, Physical Chemistry: A Molecular Approach. Sausalito, Calif.: U Science, (1997). https://doi.org/10.1021/ed075p545 Accessed online version, Oct 27, 2019.

[33] F. Mark, Quantum optics, an introduction, York: Oxford UP, 2006

[34] Djordević, & Nikolic, Marko & Antić, Željka & Mitrić, M. & Dramicanin, Miroslav. LaYO3: Sm3+ Nanocrystalline Phosphor: Preparation and Emission Properties. Acta Physica Polonica Series a. 120. 303-305. (2011)

[35] Dieke, Gerhard H., and Robert A. Satten. "Spectra and Energy Levels of Rare Earth Ions in Crystals." American Journal of Physics **38**.3, 399-400 (1970)

[36] M. F. Reid, Chapter 284 - Theory of Rare-Earth Electronic Structure and Spectroscopy, Editor(s): Jean-Claude G. Bünzli, Vitalij K. Pecharsky, Handbook on the Physics and Chemistry of Rare Earths, Elsevier, **50**, 47-64 (2016)

[37] Withnall R., Silver J. Physics of Light Emission from Rare-Earth Doped Phosphors. In: Chen J., Cranton W., Fihn M. (eds) Handbook of Visual Display Technology. Springer, Berlin, Heidelberg (2012)

[38] *The Photographic News: A Weekly Record of the Progress of Photography, Volume 22*, "Talk in the studio" Cassell, Petter and Galpin, 1878 (Accessed 0ct 27th 2019) https://books.google.ca/books/about/The_Photographic_News.html?id=0h9wIqHiYSQC&redir_esc=y

[39] G. Blasse, B. C. Grabmaier, Luminescent Materials. Berlin ; New York: Springer-Verlag, 1994. Print.

[40] S. Šakirzanovas (2011) “Novel Sm2+/3+ Phosphors as Luminescence Converter for Near UV Radiation”, (Doctoral dissertation) Retrieved from eLABa – Lithuanian Academic Electronic Library (https://epublications.vu.lt/object/elaba:1998984/)

[41] A. Edgar, C.R. Varoy, C. Koughia, G. Okada, G. Belev, S. Kasap, High-resolution X-ray imaging with samarium-doped fluoroaluminate and fluorophosphate glass, Journal of Non-Crystalline Solids, **377**, 124-8 (2013)

[42] B. R. Judd, Optical Absorption Intensities of Rare-Earth Ions, Phys. Rev., **127**, 3, 750-61 (1962)

[43] G. S. Ofelt, Intensities of Crystal Spectra of Rare-Earth Ions, The Journal of Chemical Physics **37**, 3, 511-520 (1962)

[44] F. Chicilo, G. Okada, G. Belev, D. Chapman, A. Edgar, R. J. Curry, S. Kasap, Instrumentation for high-dose, high-resolution dosimetry for microbeam radiation therapy using samarium-doped fluoroaluminate and fluorophosphate glass plates. Meas. Sci. Technol. **00** (2019)

[45] B.J. Chen, L.F. Shen, E.Y.B. Pun, and H. Lin, "Sm3+-doped germanate glass channel waveguide as light source for minimally invasive photodynamic therapy surgery," Opt. Express 20, 879-889 (2012)

[46] R.S. Fontenot, W.A. Hollerman, K.N. Bhat, et al. Luminescent properties of lanthanide dibenzoylmethide triethylammonium compounds. J. Theor. Appl. Phys. **7**, 30 (2013).

[47] D. L. Griscom, E. J. Friebele, K. J. Long, J. W. Fleming, Fundamental defect centers in glass: Electron spin resonance and optical absorption studies of irradiated phosphorus-doped silica glass and optical fibers. J. Appl. Phys. **54**, 3743-62 (1983)

[48] K. Miura, J. Qiu, S. Fujiwara, S. Sakaguchi, K. Hirao, Three-dimensional optical memory with rewriteable and ultrahigh density using the valence-state change of samarium ions. Appl. Phys.Lett. **80**, 2263-5 (2002)

[49] E. Malchukova, B. Boizot, G. Petite, D. Ghaleb, Optical properties and valence state of Sm ions in aluminoborosilicate glass under β-irradiation. J. Non-Cryst. Solids. **353**, 2397-402 (2007)

[50] A. Nag, T. Kutty, The light induced valence change of europium in Sr_2SiO_4 : Eu involving transient crystal structure. J. Mater. Chem. **14**, 1598-1604 (2004)

[51] H. Luo, A. Bos, P. Dorenbos, Controlled electron-hole trapping and detrapping process in $GdAlO_3$ by valence band engineering. J. Phys. Chem. **120**, 5916-25 (2016)

[52] G. Okada, “Development of a Large-Dose, High-Resolution Dosimetry Technique for Microbeam Radiation Therapy using Samarium-Doped Glasses and Glass-Ceramics” Ph.D dissertation, 2014

[53] T.V. Bocharova, G.O. Karapetyan, A.M. Mironov, N.M. Mishchenkov, N.O. Tagil'steva, Irradiation-induced and postirradiation processes in fluoroaluminate glasses. Inorg Mater. **42**, 671-80 (2006)

[54] D. Griscom, Defect Centers in heavy-metal fluoride glasses: a review. J. Non-Cryst. Solids. **161**, 45-51 (1993)

[55] L. Ruihua, W.Haobing, G. Fuxi, ESR study of temperature dependence of colour centers in γ-ray irradiated fluoride glasses J. Non-Cryst. Solids. **140**, 194-8 (1992)

[56] P. Ebeling, D. Ehrt, and M. Friedrich, "X-ray induced effects in phosphate glasses," Opt Mater. **20**, 101-111 (2002).

[57] S. Vahedi, G. Okada, C. Koughia, R. Sammynaiken, A. Edgar, S. Kasap, ESR study of samarium doped fluorophosphate glasses for high-dose, high-resolution dosimetry. Optical Materials Express. **4**, 1244-56 (2014)

[58] S. Vahedi "Optical and Thermal Properties of Samarium-doped Fluorophosphate and Fluoroaluminate Glasses for High-dosem High-resolution Dosimetry Applications" Ph. D dissertation, 2014

[59] G. Okada, J. Ueda, S. Tanabe, G. Belev, T. Wysokinski, D. Chapman, D. Tonchev, S. Kasap, Samarium-Doped Oxyfluoride Glass-Ceramic as a New Fast Erasable Dosimetric Detector Material for Microbeam Radiation Cancer Therapy Applications at the Canadian Synchrotron. J. Am. Ceram. Soc., **97**, 2147-53. (2014)

[60] Dorenbos, Pieter. Systematic Behaviour in Trivalent Lanthanide Charge Transfer Energies. Journal of Physics: Condensed Matter. **15**. 8417-8434 (2003)

[61] D. Ehrt, T. Kittel, M. Will, S. Nolte, and A. Tünnermann, "Femtosecondlaser-writing in various glasses," Journal of Non-Crystalline Solids, **345-346**, 332-7, (2004)

[62] G. Okada, S. Vahedi, B. Morrell, C. Koughia, G. Belev, T. Wysokinski, D. Chapman, C. Varoy, A. Edgar, S. Kasap, Examination of the dynamic range of Sm-doped glasses for high-dose and high-resolution dosimetric applications in microbeam radiation therapy at the Canadian synchrotron, Optical Materials **35**, 11, 1976-80 (2013)

[63] S. Vahedi, G. Okada, B. Morrell, E. Muzar, C. Koughia, A. Edgar, C. Varoy, G. Belev, T. Wysokinski, D. Chapman, S. Kasap, X-ray Induced Sm3+ to Sm2+ Conversion in Fluorophosphate and Fluoroaluminate Glasses for the Monitoring of High-Doses in Microbeam Radiation Therapy. Journal of Applied Physics, **112** (2012).

[64] L. Rubin, J. Poate, Ion implantation in silicon technology. Industrial Physicist. **9**. 12-15. (2003)

[65] W.H. Bragg, R. Kleeman, On the ionization curves of radium. The London, Edinburgh, and Dublin Philosophical Magazine and Journal of Science, **48**, p 726-38, (1904)

[66] H. Bethe, W. Heitler, P. Dirac Paul, “On the stopping of fast particles and on the creation of positive electrons” Proc. R. Soc. Lond. A, **146** (1934)

[67] K Nakamura, et al (Particle Data Group) “Review of particle physics: Chapt 27 Passage of particles through matter” J. Phys. G: Nucl. Part. Phys. (2010). [Online]

[68] H. Paul, C. Montanari “Electronic Stopping Power of Matter for Ions” International Atomic Energy Agency: Nuclear Data Services, website. (Accessed Nov 1st, 2019) https://www-nds.iaea.org/stopping/

Chapter 3

Methods and Experimental Techniques

This chapter discusses experimental procedures and techniques performed over the course of this research. This content of this chapter will discuss synthesis of detector materials, sample characterization, radiation sources, confocal fluorescence microscopy, and ion implantation.

3.1 Sample Preparation

Synthesis of Sm^{3+} doped fluoride glasses (FA and FP) were performed by our collaborator Dr. Andy Edgar's group at the Victoria University of Wellington. The FA and FP glasses were synthesized using a melt-quenching technique. A melt quenching technique involves the process of mixing chemical compounds which then are loaded into a furnace that is heated to a high temperature, where the mixture fuses. After the compounds have fused, they are removed from the furnace and quenched, where the mixture is placed on a temperature controlled environment. The quenching process is used to minimize internal stresses, such as cracks or other defects, which can affect the optical properties of the material.

In the case of FA and FP glass synthesis, the entire process is performed in a non reactive atmosphere. This is done since FA and FP glasses have a tendency to be hygroscopic [1,2] and so, moisture in the air may affect the desirable defect formations that allow for $Sm^{3+} \rightarrow Sm^{2+}$ conversion. Thus, the starting chemicals are mixed in a dry nitrogen glovebox and loaded into a carbon crucible. The mixture is then melted in a RF furnace at 1000 °C for two hours before it is melt quenched on a temperature controlled titanium plate at 380 °C in an argon atmosphere for eight hours. The compositions for FA and FP glasses in molar percentage is

$$10\%\ MgF_2 \cdot 35\%\ AlF_2 \cdot 20\%\ CaF_2 \cdot 10\%\ SrF_2 \cdot (15 - x)\%\ YF_3 \cdot 10\%\ BaF_2 \cdot x\%\ SmF_3 \text{ [for FA glasses]}$$

$$10\%\ \mathrm{MgF_2}\ \cdot (34.4 - x)\%\ \mathrm{AlF_2}\ \cdot 15.2\%\ \mathrm{SrF_2}\ \cdot 10\%\ \mathrm{Sr(PO_3)_2}$$
$$\cdot\ x\%\ \mathrm{SmF_3}\ [\text{ for FP glasses}]$$

here x is the doping concentration of SmF_3 which can vary from 0.1 to 10%. In the case of fluoroaluminate glass samples synthesized for Sm-ion implantation (discussed in chapter 4). The samples were synthesized using the same chemical composition shown above, but without any samarium present in the material, and x = 0%.

Once samples have been synthesized and sent to the University of Saskatchewan, they are often cut and polished to suit the design of a specific experiment. Samples used for MRT irradiations performed at the Canadian light source (CLS) are often cut to dimensions that allow for multiple microbeams to irradiate the samples. These samples have approximate dimensions of 2 × 3 mm and are cut using a rotating blade precision cutter (ImpTech Europe). These samples are polished to a near optical quality finish using grinder/polisher equipment (Minimet 1000). The polishing of the samples surfaces are done in stages, where the sample is first ground using 600 grit silicon carbide grain and ethylene glycol for lubrication, to ensure that the surfaces of the glass are parallel. Afterwards, the grain size is reduced to 0.05 µm alumina powder and the surface of the glass sample is polished until the glass has an optical quality with almost no scratches or surface defects, allowing the resulting PL to be easily readout.

3.2 Sample Characterization

After Samples are synthesized, the characteristics of the glasses are measured, including the photoluminescence spectra, characteristic lifetimes of the emission wavelengths, valence conversion tests, and thermal properties. The following section outlines some of the techniques used for measuring the properties of the materials, as well as the x-ray sources that are used to test for successful conversion of $Sm^{3+} \rightarrow Sm^{2+}$.

3.2.1 Photoluminescent Spectra

The characterization of the photoluminescent (PL) spectra is an important aspect in samarium valence dosimetry. As the sample is exposed to x-rays, there is consistent conversion from Sm^{3+}

to Sm^{2+}, and this valence change can be quantified through a variety of measurement techniques used to collect and digitize photoluminescence from a sample. The photoluminescence of Sm-doped glass plates, after appropriate excitation, produce sharp spectral lines that are characteristic of Sm^{3+} and Sm^{2+} ions. These signals can be easily separated, and the ratio of the PL of these two ions can then be used as a measurement of the dose delivered. The details of Sm ion PL properties and valence conversion have been discussed in section 2.5.

The PL of glass plates containing Sm^{3+} and Sm^{2+} ions in this work have been measured by using three experimental set ups in the lab. Each measurement technique has advantages specific to the application, but the overall principle for collecting PL spectra remains consistent for all instruments. First, the sample is exposed to an appropriate excitation source, afterwards the resulting emission spectra of interest is selected and directed towards a detection device that digitizes the signal. PL measurements used in this research are performed using a spectrometer, monochromator setup, or confocal fluorescence microscopy system.

Measurement of the photon intensity versus wavelength for a given sample is done using a portable spectrometer (StellarNet EPP2000CXR-SR-200) which collects light through a fiber

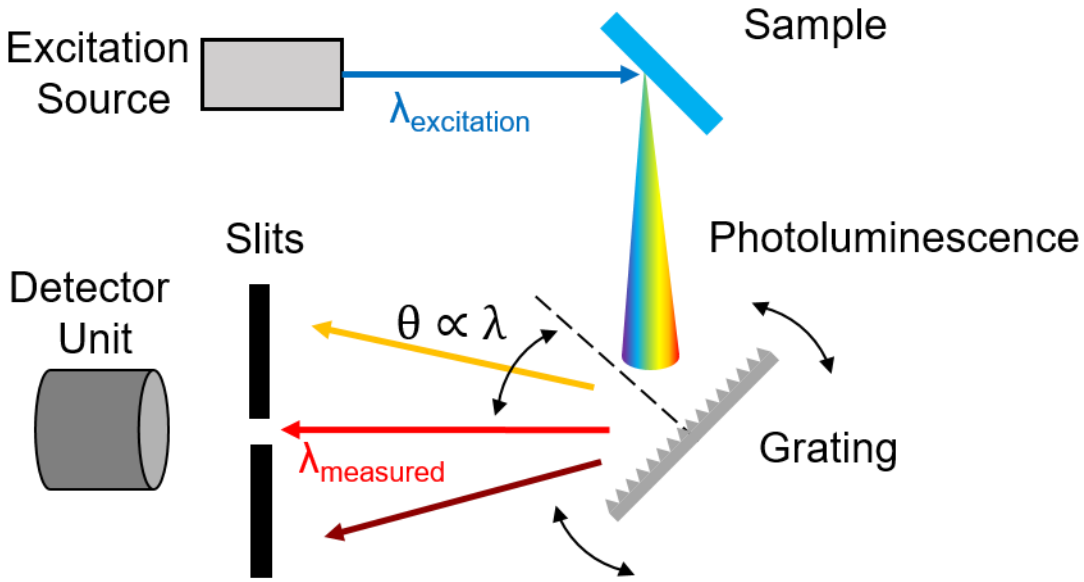

Figure 3.1 Diagram of a photoluminescent experimental set-up using a monochromator. The collection technique applies to both spectrometer and monochromator setups. This diagram illustrates selecting and measuring a narrow wavelength range, as is the case of a monochromator. For spectrometers, the entire spectra is measured simultaneously using a linear image sensor.

optic cable and is directed towards a holographic grating that disperses light. The angle at which each wavelength of light is dispersed is given by $sin(\theta) = \frac{n\lambda}{d}$ where n is an integer value of the order of refraction, d is the spatial period of the grating, and λ is the wavelength of light. This dispersed light is then directed towards a linear image sensor, which measures each wavelength within the detection range (280 -900 nm) and digitizes the results to be readout by a computer. Samples are excited using a suitable LED or laser source incident on the glass, and the resulting PL is collected through a fiber optic cable attached to an integrating sphere or lens.

Another technique for measuring the PL is a monochromator (Oriel Cornerstone 1/8m), which uses the same dispersion principle as a spectrometer. In the case of a monochromator, however, each wavelength of interest is scanned and measured using a photodetector, as shown in Figure 3.1. Use of a monochromator allows for a wider detection range, since the attached photo detection unit can by tuned for the region of interest, from the UV to the IR regions, with high resolution. This technique can also be coupled with a lock in amplifier and a waveform generator, which allows for measurement of characteristic decay times for a given wavelength, which will be discussed in the following section. The final measurement technique, confocal microscopy, allows for a two dimensional readout, and will be discussed in section 3.2.3.

3.2.2 Lifetime and Phase Measurements

The measurement of photoluminescent decay times is an important property of a given material, particularly in the application of photoluminescence of rare earth doped materials, the physics of which have been discussed in section 2.5. The characteristic decay time of photoluminescent signals in this work is measured using a monochromator and photodetector unit, a pulsed modulated laser source, and a lock in amplifier. As the intensity of the excitation source is modulated at a specified frequency, the PL intensity at a given wavelength can be measured as a function of time. This technique allows a PL center to emit upon excitation, followed by a decay of the PL signal, during which there is no excitation. If the characteristic decay time is slow compared to the pulsed frequency of the excitation source, the resulting PL can be detected in regions where there is no incident excitation, as shown in Figure 3.2. This decay time can then be fitted by an exponential function to determine the PL lifetime at the measured wavelength.

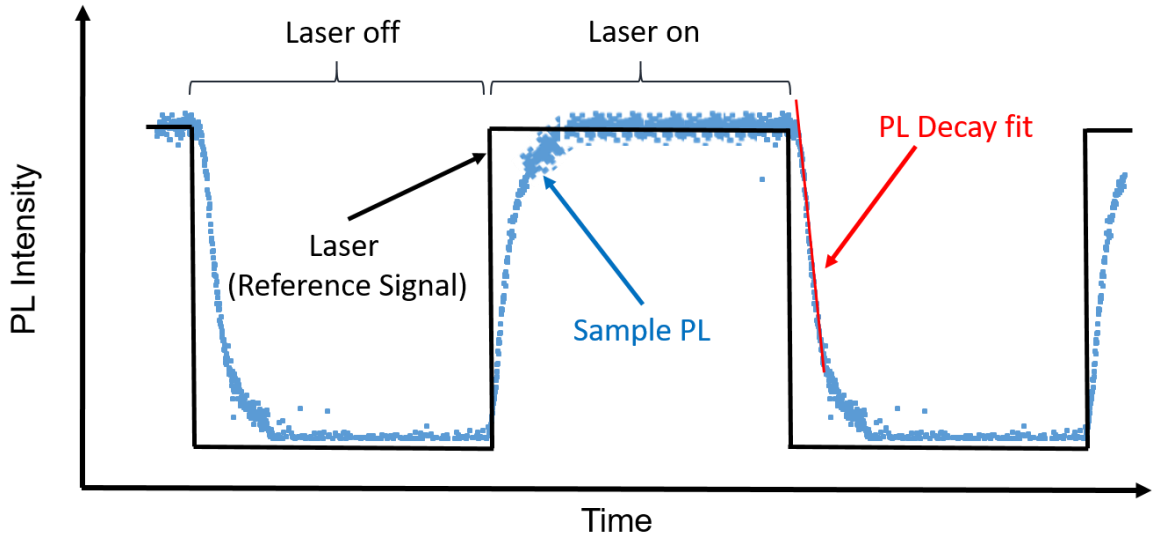

Figure 3.2 Measurement of the characteristic PL decay of a sample where the decay time can be measured after the sample has been excited and there is persistent PL intensity. This decay curve can be fitted using an exponential to measure the characteristic decay

The lifetime properties of a PL signal at a specific wavelength can also be measured by a quadrature frequency resolved technique which involves modifying the frequency of the incident pulsed laser source and measuring the change in signal response through the use of a lock in amplifier. This change is measured by the taking the modulation of the incident excitation source (laser) as a reference signal, and measuring a PL signal from the desired wavelength "out of phase" from this reference signal. In reality, the pulsed laser intensity shape more closely resembles a sin wave that that of the step function shown in Figure 3.2, so by considering a 90 degree phase change for a sin wave, the signal is changed from a peak to a trough. Thus, when discussing collecting a signal that is "out of phase" by 90°, the signal is measured at a trough region, where an "in phase" signal is at the peak region. For this reason the technique of measuring signals out of phase is called quadrature frequency resolved spectroscopy (QFRS) [3,4]. At lower frequencies, the sample is excited by the pulsed source, and between pulses, the PL of the signal completely decays, shown in the top section of Figure 3.3 (a). Conversely, if the pulsed laser frequency is high, the short pulse does not allow for the sample to adequately absorb energy, and the resulting out of phase measurement is weak, shown in the bottom section of Figure 3.3 (a). Therefore, if the frequency is scanned from low to high, it is possible to find a value that will correspond to a maximum out of phase PL signal, and this is directly related to the intensity of PL decay times between pulses.

An example of lifetime measurements using this technique for Sm^{3+} and Sm^{2+} is shown in Figure 3.3 (b), which shows that the ions reach a maximum signal between 20 – 100 Hz, corresponding to decay lifetimes in the millisecond range.

The technique of measuring PL out of phase from the reference signal can also be used to separate overlapping signals from multiple emission processes, provided the lifetimes of these processes are sufficiently different. Using a pulsed laser, a sample is excited and the resulting PL is collected using a monochromator and detection device. This signal, as well as the reference signal from the pulsed laser is sent to a lock in amplifier which can then output a spectra that is "in phase" or "out of phase" in regards to the reference excitation source. If the signal is "in phase", the spectra will show all signals present while the laser source is exciting the sample, if the measured signal is "out of phase", then the resulting spectra will preferentially show a signal that is greater at the selected frequency. A diagram of the set up is shown in Figure 3.4.

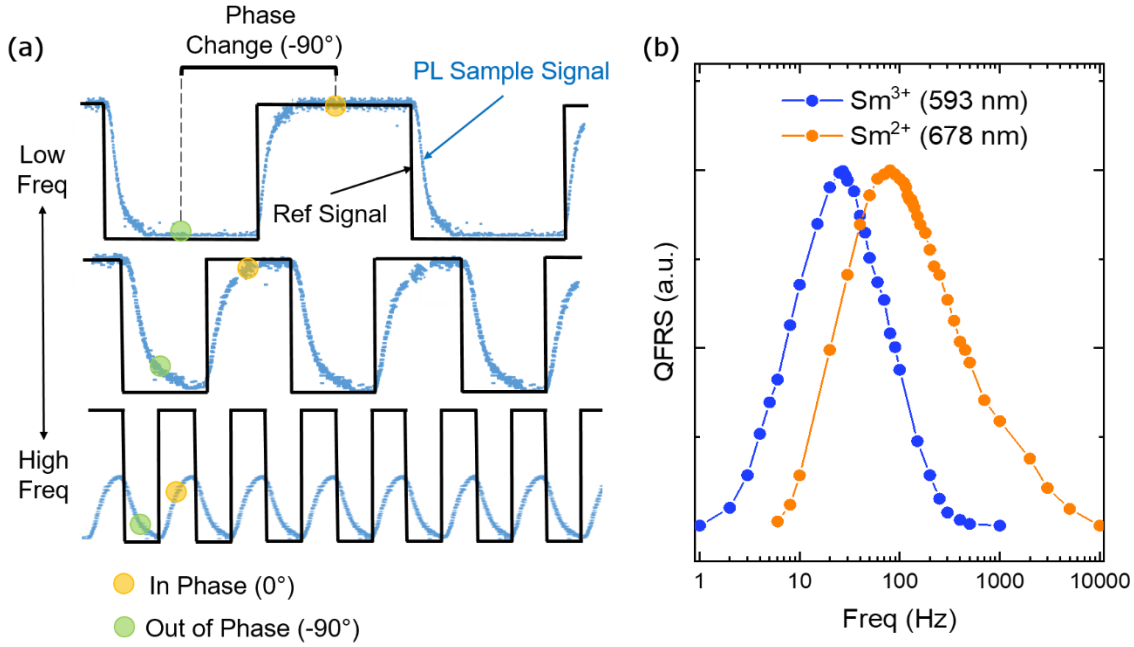

Figure 3.3 (a) Effect of excitation source's pulse frequency on out of phase measurements. If the pulse frequency is too low, the signal decays between pulses and results in a low signal. If the pulse frequency is too high, the ion is not sufficiently excited which also results in a low signal. (b) Example of Sm^{3+} and Sm^{2+} ion lifetime measurements by using quadrature frequency resolved measurements.

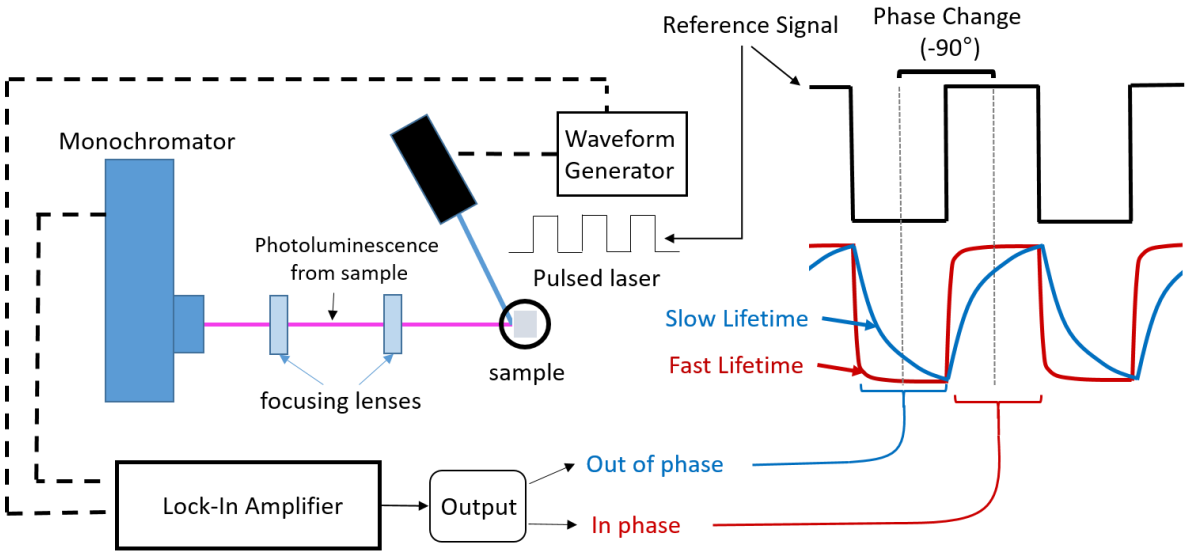

Figure 3.4 Diagram of experimental set up for measuring PL signals in and out of phase from the reference signal.

3.2.3 Thermal Analysis

Analysis of the thermal properties of glass samples was performed using a differential scanning calorimetry (DSC) instrument, which measures physical changes in the sample as a function of temperature, such as the glass transition (T_g) and crystallization (T_c) temperatures. Glass samples are, ground, weighed, and sealed in hermetic aluminum pans before being scanned over a temperature range of 20 °C to 590 °C at a heating rate of 5 °C/min. These measurements are performed using a TA Instruments Q100 DSC, which detects the heat flow in the hermetic pan and compares these values to an empty reference pan. As the sample undergoes a physical process such as crystallization, there is a change in the heat flow between samples and this change is measured as a function of temperature. Figure 3.5 shows the DSC Q100 instrument, as well as a thermal curve produced using the instrument.

3.2.4 Annealing and UV exposure

Once samples have been exposed to x-rays and conversion from Sm^{3+} to Sm^{2+} is achieved, the conversion can be reversed through either exposure from a ultraviolet (UV) source, or through thermal annealing. Thermal annealing is accomplished by heating the sample above the measured

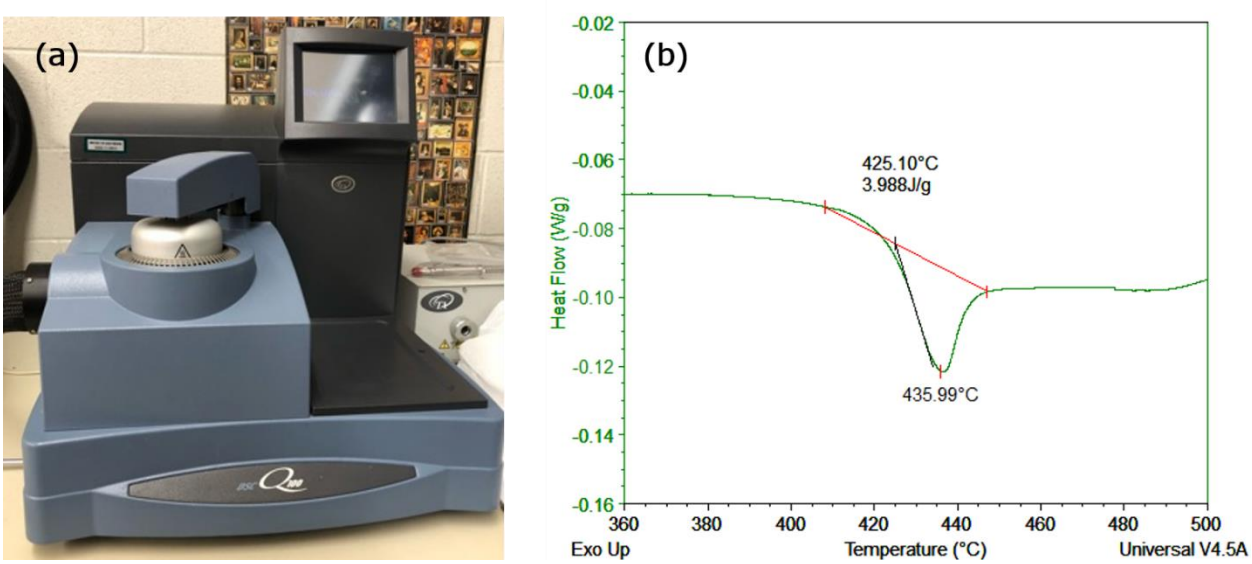

Figure 3.5 (a) TA Instruments Q100 differential scanning calorimeter (DSC). (b) Thermal curve of FA glass prepared without any Sm, which shows the transition temperature (T_g) for the glass.

transition temperature, which is performed using a CMF1100 furnace at 475 °C for 30 minutes, in the case of FA and FP glasses.

In this work, UV exposure was performed using an UV LED with a wavelength of 365 nm and an output power of 1.6 W. The sample was placed in close proximity to the LED and was exposed for 90 minutes, shown in Figure 3.6 (b). Both UV exposure and annealing were able to convert Sm^{2+} ions back to the original Sm^{3+} state. Figure 3.6 (a) shows the CMF1100 annealing furnace, and the UV exposure setup used in this research. After samples have been annealed or exposed to UV light, the spectra of the samples are once again measured to ensure that reconversion from Sm^{2+} to Sm^{3+} is successful. Although Sm-doped FA and FP glass samples have been shown to be erasable, after multiple of x-ray exposures and erasure, there is evidence of persistent Sm^{2+} signals, even after prolonged UV exposure and thermal annealing. Overall, each sample can be reused approximately 10 times without significant change to the measure response value of the sample. All results obtained from bulk Sm-doped samples reported in this work were exposed to x-rays as prepared, meaning that no annealing or UV exposure was performed prior to irradiation.

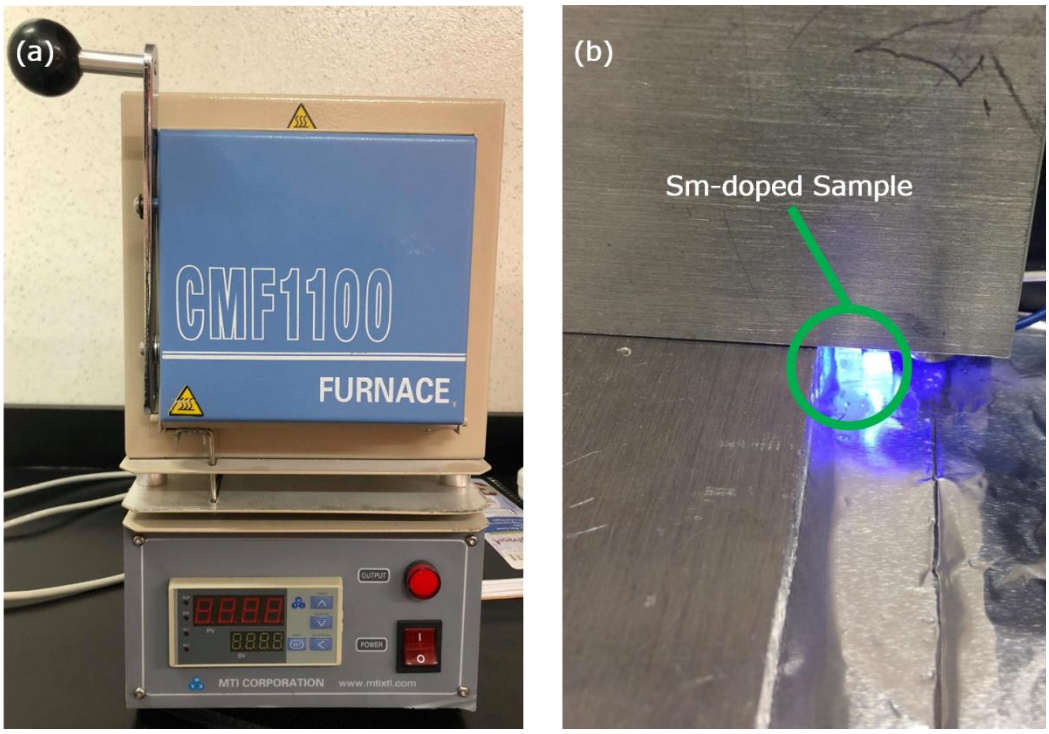

Figure 3.6 (a) Annealing CMF1100 furnace. (b) UV exposure of sample using 365 nm LED.

3.3 X-ray Irradiation

Materials used in this research were exposed to x-rays using either a commercially available x-ray cabinet tube source, or at the Canadian synchrotron facility (CLS). For preliminary and investigative results, sample were irradiated using the x-ray cabinet source due to availability. Once the appropriate samples have been selected, they were brought the CLS for further experiments. The x-ray production methods of these sources have been discussed in section 2.1.

3.3.1 X-ray Tube Source

Sm-bulk doped and ion implanted samples were tested in order to determine if the valence Sm^{3+} to Sm^{2+} could be achieved before further experiments were performed, since experimental time at the CLS is limited and the x-ray cabinet (43855D, Faxitron X-Ray, LLC) is readily available. The Faxitron system, shown in Figure 3.7 (a), uses a conventional x-ray tube, the physics of which has

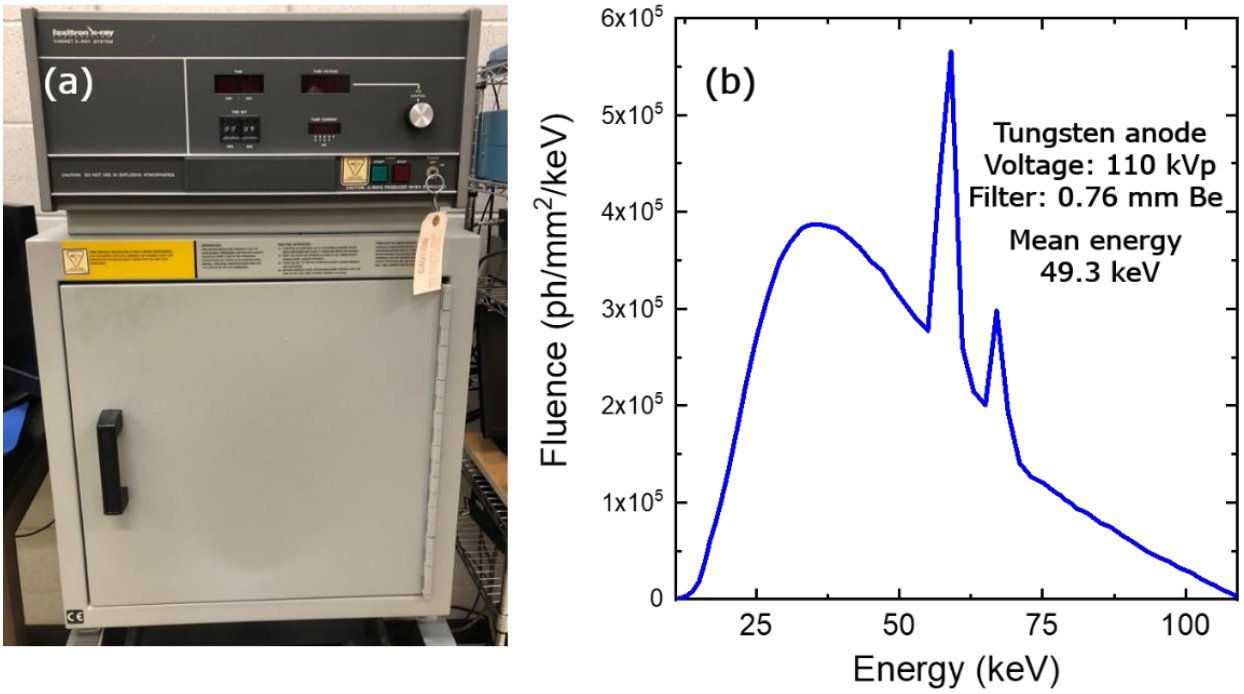

Figure 3.7 (a) Faxitron x-ray cabinet. (b) Simulated x-ray spectra for Faxitron cabinet with a voltage of 100 kVp.

been discussed in section 2.1. This tube source produces polychromatic x-rays emitted in a fan like pattern with an energy spectrum shown in Figure 3.7 (b). The energy spectrum is simulated using an online tool with a voltage of 110 kVp, which gives a mean energy of 49.3 keV [5]. This simulation technique is similar to methods that have been described in detail elsewhere [6-8]. The power supply of the Faxitron has a maximum voltage of 110 kVp, with a fixed current of approximately 3mA. X-rays produced in the cabinet pass through a 0.76 mm thick beryllium window. The position of the sample, relative to the x-ray source, can be adjusted; for maximum exposure, the sample is moved to as close to as is possible in order to deliver large doses in sufficient time. Using an ionization chamber (Keithley 35050), the dose rate at a distance of 6 cm from the source was estimated to be ~ 40 Gy/min in air operating at a voltage of 110 kVp.

3.3.2 Synchrotron X-ray Source

Samples which have shown successful Sm^{3+} to Sm^{2+} conversion are taken to the Canadian light source for use in microbeam dosimetry experiments. An important application of the Biomedical

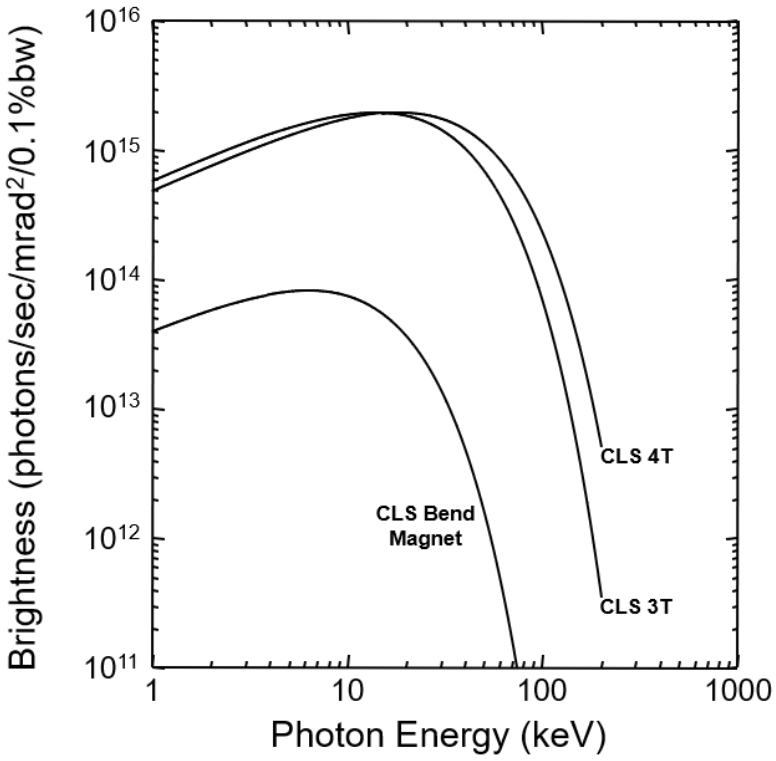

Figure 3.8 Spectral brightness of the synchrotron comparing the bend magnet and the BMIT wiggler at fields of 3T and 4T. After [9].

Imaging and Therapy (BMIT) facility at the 05ID beamline at the CLS is MRT research, which allows access to high energy, high fluence x-rays as well as a custom built multi-slit collimator designed for MRT experiments.

The BMIT 05ID beamline has access to a wiggler, which can increase the fluence of x-rays delivered to the sample, and a monochromator, which allows for the selection of single energy x-rays with a resolution of $\Delta E/E \times 10^{-3}$. The CLS has a storage ring energy of 2.9 GeV and a maximum storage ring current of 250 mA (at the time experiments were performed) which produces x-rays with a critical energy of 7.5 keV. This critical energy can be increased by use of the 05ID beamline wiggler, which has a maximum magnetic field of 4.3 T. Additionally, the fluence of x-rays can be modified by adjusting the wiggler field, as shown in Figure 3.8 [9]. The selection of monochromatic x-ray energies is performed through the use of a bent Laue monochromator with a range of 25-150 keV. For the experiments performed the maximum dose rate of was measured to be approximately 5 Gy/s, with an incident energy of 50 keV and a wiggler field of 4 T.

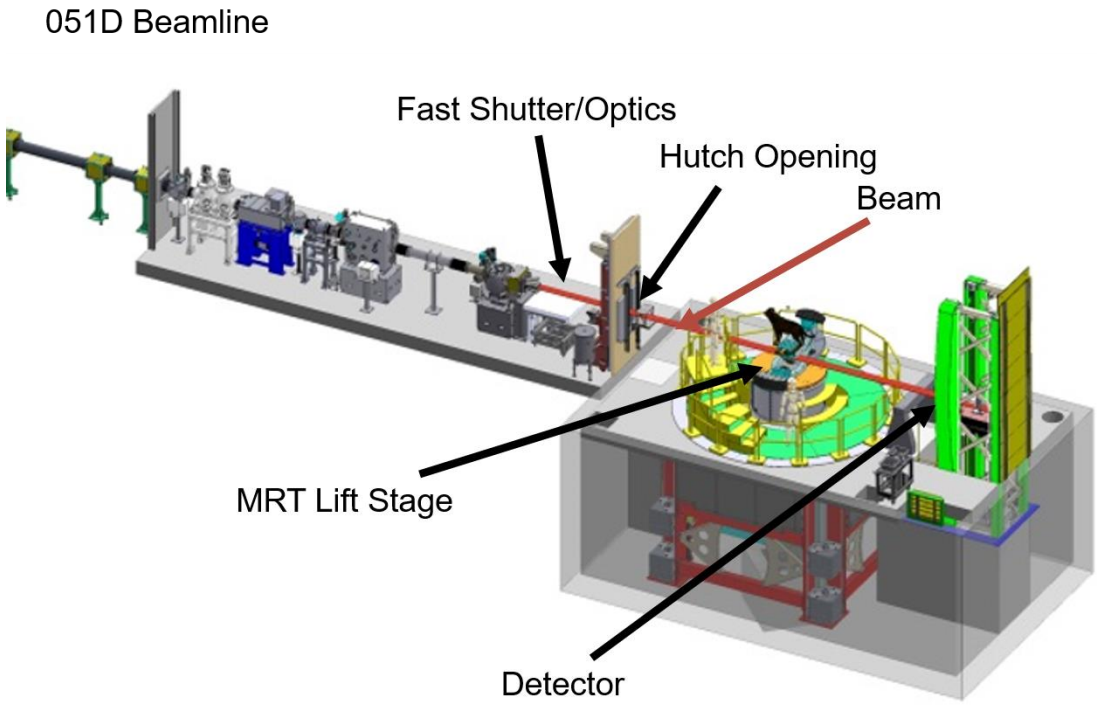

Figure 3.9 Schematic of the 05ID beamline at the CLS. After [10].

Irradiation experiments performed at the 05ID beamline were performed using a shutter to control the dose delivered to the sample. Figure 3.9 illustrates the schematic of the beamline [10], which shows the location of a fast shutter which controls the dose delivered to the sample which is determined by a high dose ionization chamber (31022, PTW-Freiburg). The ionization chamber is placed in the beam path at the hutch opening, which monitors the dose rate used to calculate the dose delivered to the surface of the sample. The samples to be irradiated are located at the center of the MRT lift stage. Once the shutter has been opened, the monochromatic (spatially) broadbeam is incident on the multi-slit collimator which has a slit width of 50 μm, and a center to center distance of 400 μm with 75 total slits (manufactured by Usinage et Nouvelles Technologies). Samples are placed a distance of 25 cm behind the collimator, as shown in Figure 3.10. The alignment of the MSC can be adjusted using rotational and translational stages which control the rotation, pitch, and yaw of the MSC. These motorized stages are adjusted from in the control room and the MSC is rotated until a maximum fluence of x-rays is measured using the available x-ray detection system.

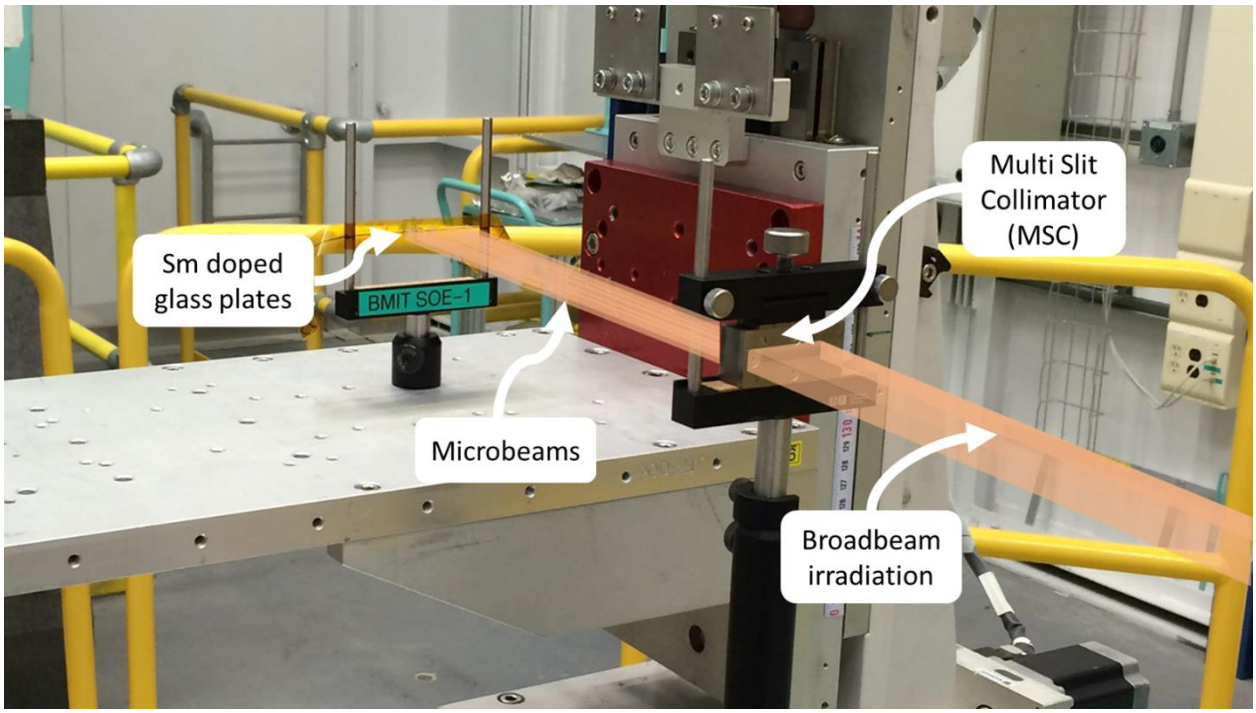

Figure 3.10 Experimental set up of multi slit collimator and Sm-doped glass samples.

After alignment of the MSC, Sm-doped glass samples are held in place using Kapton tape and irradiated, where the total dose delivered to the samples is controlled using the fast shutter and ionization chamber. Irradiations performed within the hutch are carried out in the dark, and are immediately wrapped in tinfoil after irradiation to prevent exposure to light until the samples are read out. Gafchromic film was also irradiated using the same experimental set up to verify alignment and for possible comparison purposes.

3.4 Confocal Fluorescent Microscopy

Confocal microscopy is a key aspect of the experiments performed in this research. Sm-doped glass samples are indirect dosimeters, meaning the dose information is stored in the materials and must be recorded and digitized by measuring the conversion of Sm^{3+} to Sm^{2+} ions. Sm-doped glass plates are read out using a confocal fluorescent microscopy system, many of the details of this system are discussed in Chapter 5. This section will cover some of the specific details of the confocal microscopy system and discuss the design, data acquisition, and signal processing used for the work presented in this thesis.

3.4.1 Optical Set Up

The confocal microscopy set up is a purpose-built instrument designed for the detection of PL signals resulting from Sm^{3+} and Sm^{2+} ions. The system is a refurbished from a prior system (Multiprobe 2001 CLSM, Molecular Dynamics) and the optics design remain largely unchanged. An illustration of the optical layout of the confocal microscope is shown in Figure 3.11.

The confocal microscope uses a 473 nm laser (DHOM-L-473-50, Ultralasers Inc.) which is selected as a suitable excitation source for exciting both Sm^{3+} and Sm^{2+} ions. The laser passes through a filter wheel, which has a blue filter (BPF470) and an orange filter (BPF590) which is used to either suppress or allow the near infrared emission from the pump source used to increase the output energy of the laser. This pump emission is also used for surface detection of the glass, which allows for the confocal system to measure the reflection of the 808 nm source without exposing the sample to the blue wavelength, which may cause optical bleaching of the samples. The spectra of the laser emission and the pump laser are shown in Figure 3.12. The mechanical shutter allows for the beam to either be blocked or pass through, and the intensity of the laser incident on the sample can be controlled through the use of neutral density filters (ND). A dichroic mirror reflects light shorter than 570 nm (DM570), and any longer wavelengths will pass through. Note that at near infrared wavelengths, there is a slight increase in reflectance, allowing for the pump laser to be reflected and directed towards the surface of the sample for detection [11]. The scanning unit utilizes a pair of mirrors that are controlled with a stepper motor (y-direction), and a galvanometer (x-direction), which allows for a two dimensional scan of the sample. The beam is focused using an objective lens to excite a small field of view. The two available objective lenses are 20× (PlanApo 20×/0.75 NA, Nikon) and a 10× (10×/0.3NA, Meopta), which have fields of view (FOV) of approximately 1 mm and 2 mm in diameter, respectively. The sample is then raster scanned at a selected focal depth over the FOV of the objective lens. The intensity of the excitation source delivered is adjusted through the voltage and use of neutral density filters and is measured to be 0.5 μW at the sample location using a powermeter (PM100D, Thorlabs, Inc.).

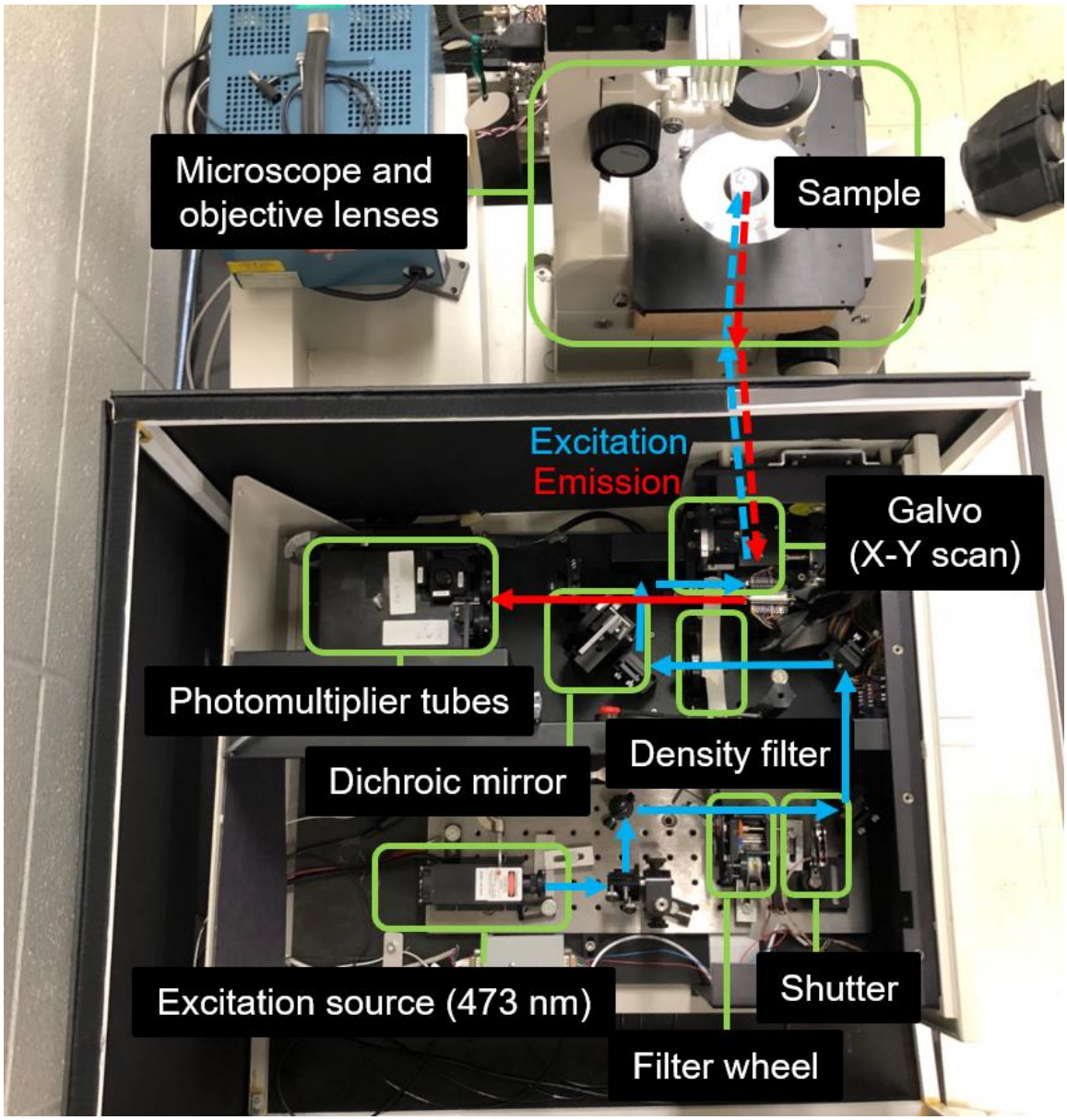

Figure 3.11 Confocal microscope and optics used in the research for collection of Sm^{3+} and Sm^{2+} PL signals.

Once the Sm^{3+} and Sm^{2+} ions have been excited, they emit separable PL signals which are detected by the confocal microscopy system through the use of photomultiplier tubes (PMTs). Once the sample has been excited, the signal is guided towards the photomultiplier tubes, and focused using an achromatic lens and pinhole. Each photomultiplier tube is tuned to collect the emission spectra of either Sm^{3+} or Sm^{2+} through the use of a dichroic mirror (DM650) which separates the two signals. These signals are then directed towards the PMTs which are shielded by

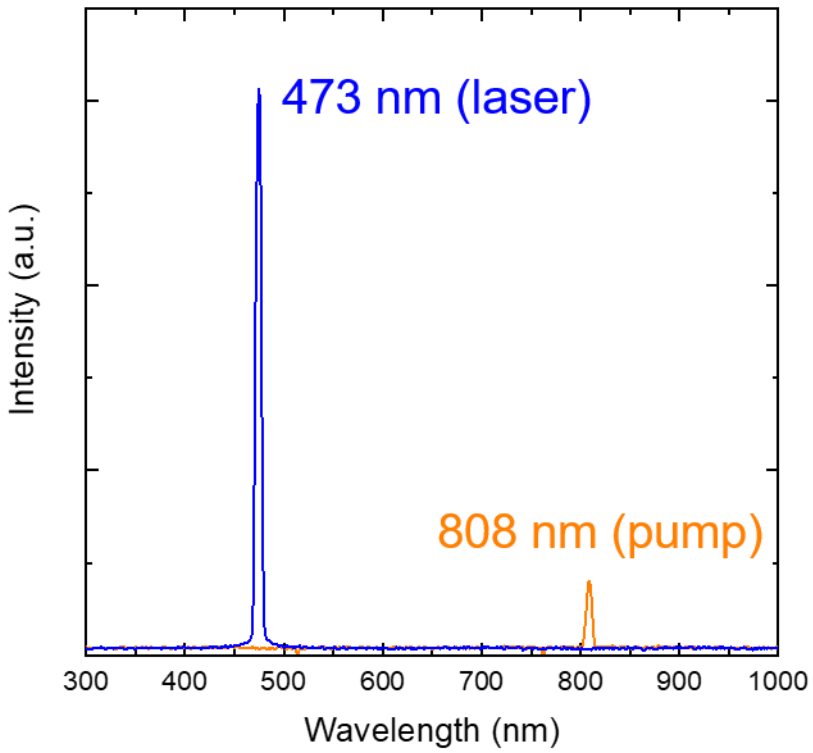

Figure 3.12 Emission spectra of the excitation source, showing the lasing and pump wavelengths. Intensities are not to scale, but are intended to show that the pump laser is significantly weaker than the emission wavelength.

bandpass (BPF600) and longpass (LPF660) collecting the Sm^{3+} and Sm^{2+} PL signals, respectively. The optimization of the collection of the PL signals of these ions is covered in greater detail in chapter 5.

3.4.2 Data Collection

After photoluminescent signals have been detected by the PMTs, they are digitized and recorded onto a computer using a custom LabVIEW program. The computer is equipped with a data acquisition board (DAC, USB-6009, National Instruments) which communicates through a USB cable. The user interface, shown in Figure 3.13, has several functions, which includes:

- Selection of filters for excitation source
- Surface detection of glass sample
- Scanning of samples in X, Y, or Z direction

- Dark noise background subtraction
- Selection of image resolution
- Measurement of target area
- Laser voltage
- Dwell time between each pixel
- PMT signal sampling rate
- Averaging values for noise reduction
- Email notification
- Automatic laser shut off after measurement

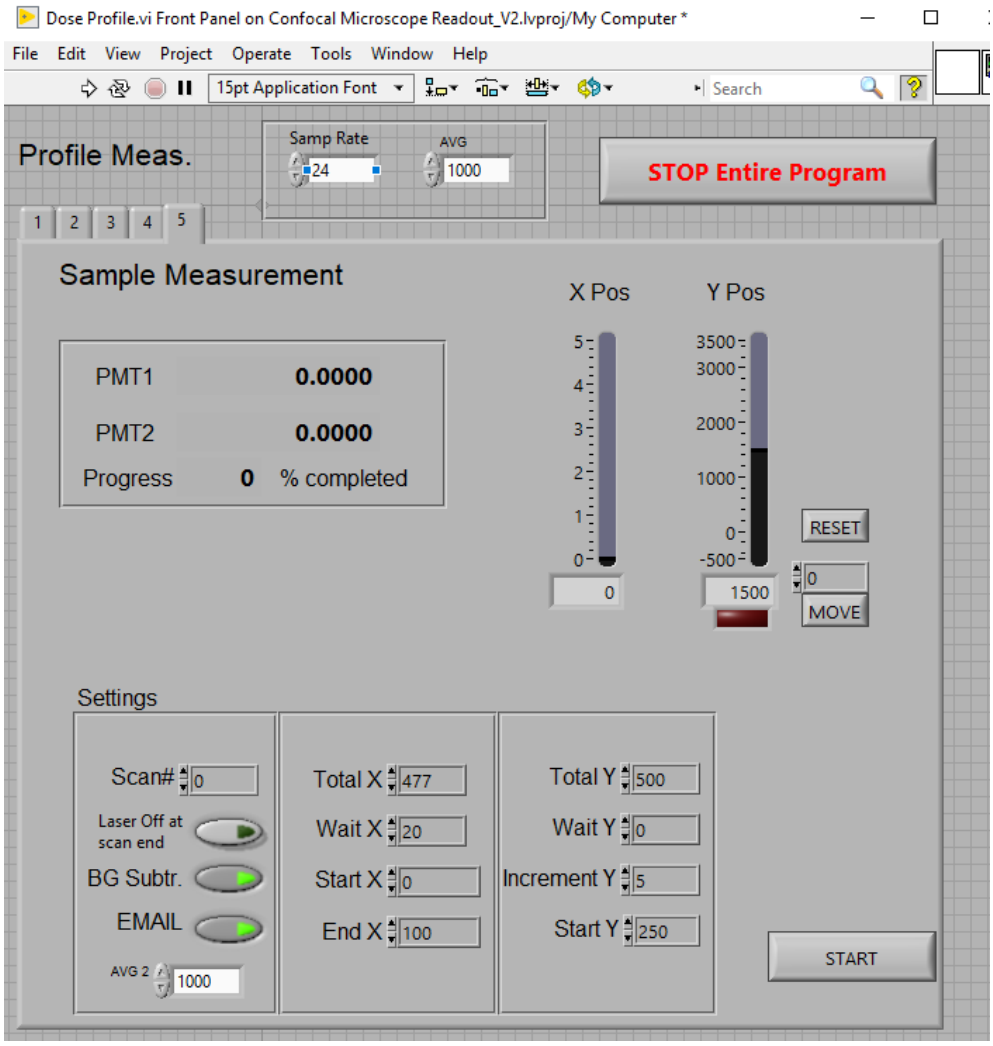

Figure 3.13 User interface for LabVIEW program used to control the confocal microscopy instrument set up.

The galvanometer (galvo) controls the angle of an x-scanning mirror which changes the scanning position of the laser in the horizontal direction. The smallest step size in the horizontal direction is 0.50 µm and 0.25 µm for the 10× and 20× objective lenses, respectively. Movement in the y-direction and z-direction are controlled by micro-stepper motors with a minimum travel distance of 0.70 µm and 0.35 µm for the 10× and 20× objective lenses for y-travel, and 0.1 µm the z-direction.

3.4.3 Image Processing

A critical consideration for the accurate measurement of microbeams is the averaging of the two dimensional image into a one dimension beam profile. Since changes to the beam characteristics occur on the order of micrometers, any small misalignment has the potential to cause an error in the results. In order to ensure that the microbeams are perpendicular to the x-axis, a MATLAB code was written to processes the irradiated microbeam images collected from the confocal microscope. First, the ratio of the values from the PMT tuned to Sm^{2+} is divided by the PMT tuned to Sm^{3+} for both the irradiated sample and a background non-irradiated sample. Next, the background is subtracted from the sample with the irradiated microbeam. Lastly, a normalization matrix is applied to remove any non-uniformities due to optical distortion across the FOV. The

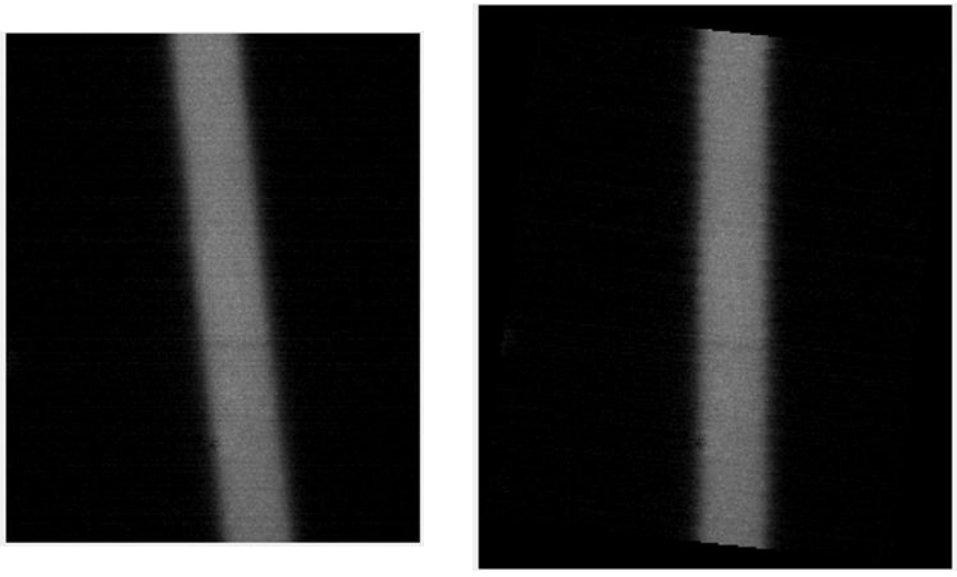

Figure 3.14 (Left) Microbeam after background subtraction, normalization and cropping (Right) Same microbeam section after a Gaussian fit is applied and the minimum FWHM as a function of rotation is found.

normalization matrix is experimentally determined from uniformly irradiated samples. These uniformly irradiated samples are 1% Sm-doped FA glasses which are scanned through a broadbeam monochromatic 50 keV, 500 Gy exposure multiple times ensuring a constant dose is delivered. Since the dose delivered to the sample is constant, the response value at each point across the FOV should be constant, and is used to remove any non uniformities resulting from the measurement process.

Once single microbeam samples have been measured and the background is subtracted, the region of interest is selected on the processed image and a curve fitting tool present in MATLAB fits a first order Gaussian to each line of data along the y-axis. The image is then rotated in 0.001° steps until a minimum FWHM is found as a function of rotational angle. Once the image is correctly oriented, the microbeam is averaged from a 2 dimensional image into a 1 dimensional profile. An example of a rotated microbeam is shown in Figure 3.14.

3.5 Ion Implantation

Ion implanted samples were used in this research to investigate the possibility of achieving Sm^{3+} to Sm^{2+} conversion of implantation ions very near the surface of FA glass samples. FA glass plate samples with no Sm present were synthesized at the University of Wellington, and were then polished to optical quality on both surfaces of the sample. The ion implantation was then performed by collaborators, Richard Curry and Russel Gwilliam at the University of Surrey at the Ion Beam Center (IBC). $^{152}Sm^{+}$ ions were implanted into FA glass samples at an energy of 2 MeV inside a vacuum chamber. Multiple fluences were achieved in order to determine the optimum concentration for implantation processes. The results of this work is discussed in greater detail in the following chapter.

3.6 References

[1] J. Lucas, Fluoride glasses, J. Mater. Sci. **24**, 1–13 (1989)

[2] M. Poulain, A. Soufiane, Y. Messaddeq, M. Aegerter, "Fluoride glasses: Synthesis and properties", Braz. J. Phys.. **22**, 205-17, (1992)

[3] T. Aoki, S. Komedoori, S. Kobayashi, C. Fujihashi, A. Ganjoo, K. Shimakawa, "Photoluminescence lifetime distribution of a-Si:H and a-Ge:H expanded to nanosecond region using wide-band frequency-resolved spectroscopy", Journal of Non-Crystalline Solids, **299–302**, Part 1, 642-7, (2002)

[4] K. Koughia, D. Saitou, T. Aoki, M. Munzar, S.O. Kasap, "Photoluminescence lifetime spectrum in erbium doped Ge–Ga–S glasses", Journal of Non-Crystalline Solids, **352**, Issues 23–25, page 2420-4 (2006)

[5] "Simulation of X-ray Spectra" [Online] https://www.oem-xray-components.siemens.com/x-ray-spectra-simulation (accessed Nov. 24, 2016)

[6] J. M. Boone and J. A. Seibert, An accurate method for computer-generating tungsten anode x-ray spectra from 30 to 140 kV, Med. Phys., **24**, 1661-70, (1997)

[7] J. M. Boone, Spectral modeling and compilation of quantum fluence in radiography and mammography, in Proceedings of the SPIE, J. T. Dobbins III and J. M. Boone, Eds., vol. 3336, 592-601.(1998) [Online] http://proceedings.spiedigitallibrary.org/proceeding.aspx?articleid=942360

[8] Punnoose J, Xu J, Sisniega A, Zbijewski W and Siewerdsen J H Technical Note: spektr 3.0—A computational tool for x-ray spectrum modeling and analysis Med. Phys. **31** 3057–67 (2016)

[9] D. Chapman, *BIOE850: Unit 1-X-ray Production* [Course presentation]

[10] "Biomedial Imging and Therapy Facility" [Online] https://bmit.lightsource.ca/ (accessed Nov 29, 2019)

[11] "Longpass Dichroic Mirrors/Beamsplitters" *Thorlabs, Inc.* Thorlabs, 2019. [Online] https://www.thorlabs.com/newgrouppage9.cfm?objectgroup_id=3313 (Accessed Nov. 30, 2019)

Chapter 4

X-ray Induced Sm-ion Valence Conversion in Sm-ion Implanted Fluoroaluminate Glasses Towards High-dose Radiation Measurement

Published as:

Farley Chicilo, Cyril Koughia, Richard Curry, Russel Gwilliam, Ruben Ahumada-Lazo, Andy Edgar, David J. Binks, Dean Chapman, and Safa Kasap. "X-ray induced Sm-ion valence conversion in Sm-ion implanted fluoroaluminate glasses towards high-dose radiation measurement", *J Mater Sci: Mater. Electron.* **30**, 16740–16746 (Accepted March 23rd, 2019) doi:10.1007/s10854-019-01212-4

Author contributions:

The main experimental work, data analysis, and manuscript preparation in this work was performed by Farley Chicilo. Richard Curry, Cyril Koughia, and Ruben Ahumada-Lazo contributed to this work in experiments represented in Figure 4.1, 4.5, and 4.7, respectively. Fluoroaluminate glasses were synthesized by Andy Edgar at the University of Wellington in New Zealand, and Sm-ion implantation was performed by Richard Curry and Russel Gwilliam at the Ion Beam Centre at the University of Surrey. Andy Edgar, Cyril Koughia, and Safa Kasap contributed to the preparation of the manuscript, including providing comments and suggestions for the manuscript.

4.1 Abstract

Ion implantation of Sm-ions^{+} has been tested in fabricating 2D detectors for microbeam radiation therapy (MRT). Sm-ions have been successfully implanted into fluoroaluminate (FA) glasses. The implantation concentration was chosen to be 5×10^{15} ions/cm^2 and the ions were implanted at an energy of 2 MeV. After implantation, samarium ions resided within a thin plane very near the surface in the glass, which is expected to be beneficial for 2D imaging. Following implantation, photoluminescence (PL) spectra indicate that the embedded Sm-ions are in the form of Sm^{2+} and

Sm^{3+}. Subsequent annealing around the glass transition temperature (475 °C) converts all Sm^{2+} ions into Sm^{3+}. Under X-ray irradiation, a partial conversion of Sm^{3+} into Sm^{2+} has been observed which may be used as measure of the X-ray dose delivered into the sample. QFRS (quadrature-frequency-resolved-spectroscopy) measurements on PL prominent emissions from Sm^{3+} and Sm^{2+} ions show that the PL decays associated with various transitions are in the 0.1 to 100 ms range (slow transitions). X-ray irradiation has led also to the appearance of broad and intense photoluminescence bands associated with X-ray induced structural defects in the host glass as confirmed in the unimplanted FA glasses. The generation of hole trapping centers in the host glass leads to the capture of photogenerated holes and thus allows the electrons to convert Sm^{3+} to Sm^{2+}. Defect related PL decays signals were measured to be in the nanosecond region. These unwanted defect related fast decaying signals have been separated from slow Sm^{2+} and Sm^{3+} photoluminescence signals by using an "out-of-phase" PL measurements through a phase-sensitive photodetection technique with a modulated excitation laser diode and a lock-in amplifier. Overall, the Sm-ion implanted fluoroaluminate glass shows the successful conversion from the trivalent form of samarium (Sm^{3+}) to the divalent form (Sm^{3+}) under X-ray irradiation over a large dynamic range of X-ray intensities (800 Gy in air).

4.2. Introduction

Microbeam radiation therapy (MRT) is a new and promising form of cancer radiation treatment which has the potential to greatly improve existing radiation therapy techniques. MRT relies on the differing responses of healthy tissues and tumour cells to narrow microbeams of X-ray radiation. These microbeams have a typical width of 20-50 μm and are separated by hundreds of microns [1,2]. Previous studies have shown that targeting the central nervous system of vertebrates shows a remarkable resistance to multiple parallel narrow microbeams with minimal damage to mature healthy tissue, while preferentially damaging harmful tumours [3-5]. This technique allows for the delivery of substantial doses to the patient by using collimated synchrotron radiation passed through a multi-slit collimator creating narrow, parallel, and uniformly separated microbeams. The characteristics of microbeams need to be accurately measured for patient safety and must be done so with high spatial resolution as well as simultaneously measuring both peak and valley doses,

which can differ by hundreds of Grays. In other words, a two-dimensional (2D) cross-sectional image of the energy distribution in microbeams is required.

Many possible technical solutions to the problem of microbeam dosimetry have been previously discussed, including Si strip detectors, Gafchromic films, and MOSFET detectors, among others [6]. One of the promising ways is to use the valence conversion of rare earth ions which is known to occur under a variety of excitations, from X-rays to beta radiation [7-9]. Among other rare earths, samarium ions are of particular interest, since the photoluminescence (PL) spectra of divalent and trivalent ions are distinguishably different and they are located in the orange-red part of spectrum where they can be easily detected by common photomultiplier tubes (PMT). Previously, we have shown that fluoroaluminate (FA) and fluorophosphate (FP) glasses are excellent hosts allowing effective Sm valence conversion which is erasable/reversible under UV illumination and/or thermal treatment [10 - 17]. High spatial resolution measurements on micrometer scale are based on a confocal microscopy system tuned to the emission wavelengths of Sm^{3+} and Sm^{2+}. The drawback of the approach is that the Sm valence conversion occurs throughout the glass volume and to obtain a two-dimensional cross-sectional picture of microbeams within this volume requires a sophisticated confocal microscopy system. To overcome this drawback we opted to investigate the possibility of implanting samarium ions into FA glasses which would create a quasi 2D distribution of Sm ions and, in the case of successful Sm^{3+} to Sm^{2+} conversion, would substantially simplify the readout system.

In the present paper, we discuss the details of Sm-ion implantation into FA glass. Conversion of Sm^{3+} to Sm^{2+} depends strongly on the host material, and FA glass was selected as it has previously shown excellent conversion and does not exhibit significant photodarkening in the same emission region as samarium ions. We show that after implantation most ions reside in Sm^{2+} form. Further annealing successfully converts Sm^{2+} to Sm^{3+}, which may be desirably re-converted back to Sm^{2+} by X-ray irradiation. We show also that X-ray irradiation leads to formation of optically active structural defects generating broad and intense PL bands obscuring Sm-ion emission. We investigate the temporal characteristics of these defect PL bands and develop a method of separating slow and weak Sm emission from fast and intense defect emission. Overall, we conclude that Sm ion implantation has certain potential in application as MRT detector.

4.3 Experimental Procedure

Fluoroaluminate glasses were synthesized using a conventional melt-quenching technique following the procedure described in detail earlier [10 - 17]. In short, the starting materials were mixed in a glove box in a dry nitrogen atmosphere and loaded in a carbon crucible. The mixture was then melted in an RF furnace at 1000 °C for 120 min and was quenched on a temperature controlled plate at 380 °C for 8 hours in an argon atmosphere. The composition in molar percentage is $10.0MgF_2 – 35.0AlF_2 – 20.0CaF_2 – 10.0SrF_2 – 15.0YF_3 – 10.0\ BaF_2$. Once the samples were synthesized they were sent to the Ion Beam Centre at the University of Surrey where Sm^+-ions were implanted into the FA glasses at an energy of 2 MeV and the selected ion implanted fluence was 5×10^{15} ions/cm^2.

Following ion-implantation, the samples were annealed and X-ray irradiated. The annealing was done using a compact furnace for 30 minutes at a temperature of 475 °C in air, which is above the glass transition temperature T_g of the particular glass. The T_g was measured to be approximately 440 °C using a DSC Q100 thermal analysis system (TA Instruments) where the sample was heated at a rate of 5 °C/min. The X-ray irradiation was performed using a FAXITRON X-ray cabinet with a tungsten anode operating at 110 kVp at an approximate dose of 40 Gy/min in air. This quoted dose value represents the dose in air at the sample entrance and not the dose deposited in the sample. The mean energy for the polychromatic X-ray source was 49.3 keV from the fluence simulations given at the Seimens website [18]. The exposure rate was determined by an ionization chamber (Keithley 35050). The glasses were cut and polished flat for X-ray exposure and optical measurements.

PL spectra were excited by a 450 nm laser diode driven by a waveform generator. The spectra were dispersed by a Cornerstone 1/8 m monochromator with a holographic grating of 1200 lines/mm and a blaze wavelength of 750 nm. The signal was detected using a photomultiplier tube with an approximate spectral sensitivity range from 300 – 800 nm connected to a SR830 DSP lock in amplifier to enable phase-sensitive PL measurements to be carried out. QFRS (quadrature-frequency-resolved-spectroscopy) spectra of Sm^{3+} and Sm^{2+} were captured as a function of modulation frequency. The QFRS method is explained in detail elsewhere [19 - 24].

Measurements of the fast and broad PL decays were recorded using a time correlated single photon counting (TCSPC) system. This employs a mode-locked Ti:sapphire laser (Mai-Tai HP, spectra physics) to produce 100 fs pulses at a repetition rate of 80 MHz at 900 nm wavelength. The repetition rate was reduced to 1 MHz by an acousto-optic pulse picker (APE select) and the initial wavelength halved (to 450 nm) via second harmonic generation (APE harmonic generator). These pulses were used to excite the sample with an average power of 0.6 mW. The PL emission of the samples was collected and focused into a monochromator (Spex 1870c) and detected both of the PL peaks observed in the spectrum by a multi-channel plate (Hamamatsu R3809U-50). A 455 nm long pass filter was placed in front of the detector to reduce the amount of light scattered from the excitation laser. The time correlation of the detected photons was performed with the use of a PC electronic card from Edinburgh Instruments. The measured instrument response function (IRF) for this system is about 0.1 ns. All the measurements were performed at room temperature.

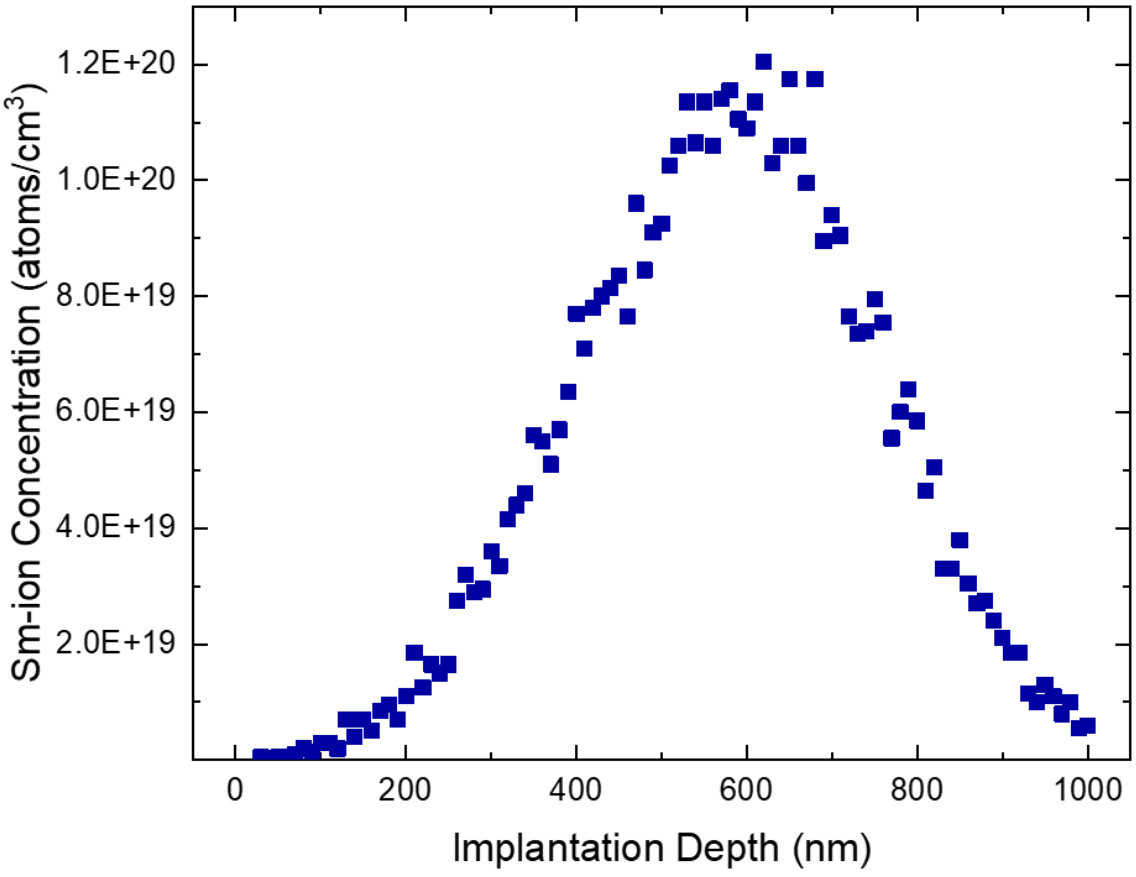

Figure 4.1 Simulated implantation depth and ion concentration of 2 MeV Sm+ ions in FA glass with a fluence of 5×10^{15} ions/cm2 using Monte Carlo simulations by the SRIM program [25].

4.4 Results

Figure 4.1 shows the calculated distribution of Sm species (ions and atoms) versus implantation depth in FA glass immediately after ion implantation using the simulations of stopping range of ions in matter (SRIM) software [25]. The maximum available energy of 2 MeV was selected in order for the relatively heavy Sm ions to reach a sufficient implantation depth of approximately 600 nm in the FA glass material, as shown in Figure 4.1. The implanted dose of 5×10^{15} ions/cm^2 yields a peak Sm concentration of 1.2×10^{20} atoms/cm^3 corresponding to a peak concentration of ~0.2 at%. The actual Sm distribution will vary from the SRIM calculation due to the sputter rate

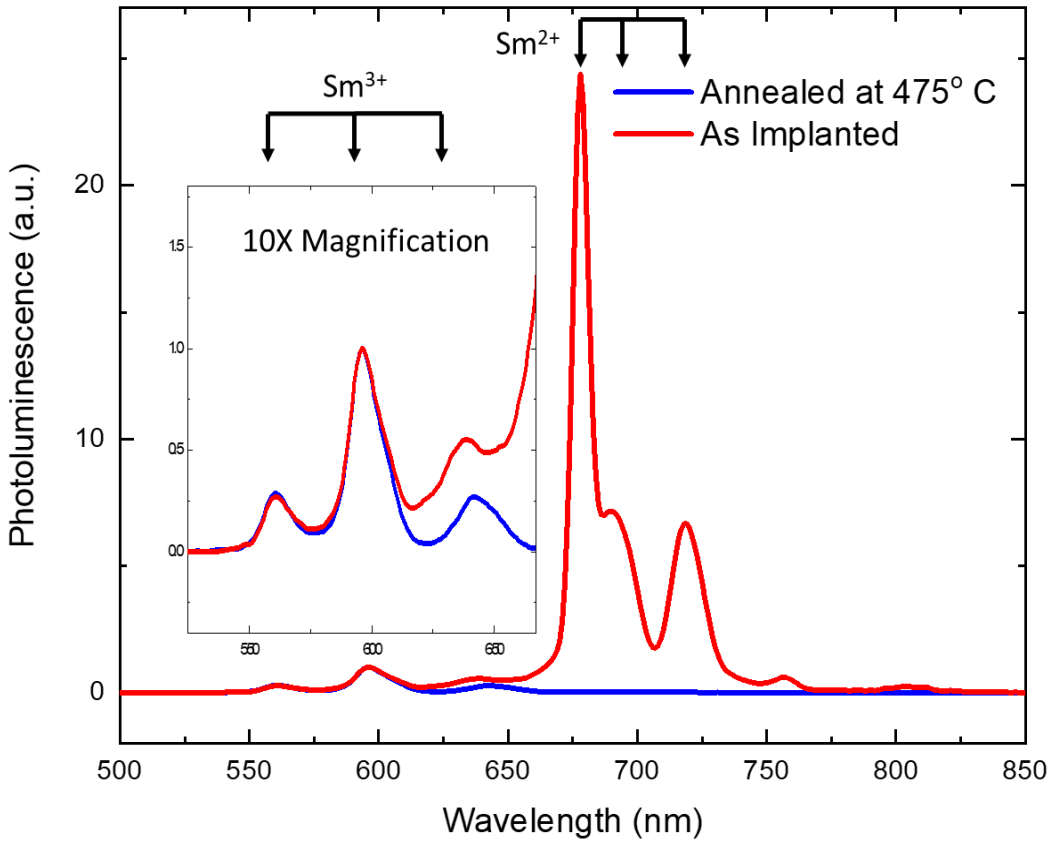

Figure 4.2 PL spectra of Sm-ion implanted FA glass as implanted (red) and after annealing at 475° C (blue). Only the main emission bands important for ions/spectra identification are marked by arrows. PL spectra were taken with "out of phase (–90°)" synchronization with modulated laser excitation at a frequency of 27 Hz. Excitation wavelength is 450 nm. Spectra are not corrected for PMT spectral sensitivity. The insert shows the magnified part of the Sm^{3+} spectrum.

(~7 atoms/ion) resulting in a loss of ~100 nm from the glass surface and a spreading of the final Sm profile. Further modification will occur during the post implantation annealing.

The photoluminescence (PL) spectra observed after the Sm-implantation are shown in Figure 4.2, which demonstrates that the implanted Sm-ions are Sm^{2+} and Sm^{3+} ions. The measured PL spectra exhibit a combination of Sm^{2+} and Sm^{3+} PL bands. After annealing the Sm-ion implanted sample at a temperature of 475° C for 30 min, the presence of PL emission from Sm^{2+} was completely eliminated from the sample, shown as the blue line in Figure 4.2. It is worthwhile to note that the integrated intensity of the PL signals from the Sm-ion implanted samples is several orders of magnitude less than those of the bulk doped samples, most likely because of the smaller content of Sm ions. However, we are able to reliably detect Sm related PL in ion-implanted samples which makes them interesting for further investigation for MRT dosimetry.

The PL spectra observed after the X-ray irradiation of the Sm ion-implanted samples is shown in Figure 4.3 in which phase-sensitive PL detection was used. Figure 4.3 (a) illustrates the necessity and efficiency of "out-of-phase" measurements in the detection of Sm-ion related emissions. The PL excitation modulation frequency was set to 27 Hz for reasons explained below. Figure 4.3 (a) demonstrates the appearance of broad emission bands (tentatively related to X-ray induced structural defects which may be related to induced color centers reported earlier [12 - 17]) which may be effectively suppressed by using "out-of-phase" measurements due to the large difference in characteristic decay times of the PL of Sm-ions and defects. Upon irradiation, it is possible to get the desirable conversion of Sm-doped FA glass from Sm^{3+} to Sm^{2+}, which serves as a measurement of the X-ray dose delivered to the sample. In Figure 4.3 (b) we see a consistent increase of Sm^{2+} contribution as the total dose (in air) is increased in steps of 200 Gy_{air} up to 800 Gy_{air}. Figure 4.4 shows the dependence of the Response of the Sm-implanted glass to the incident dose in which Response is defined as

$$\text{Response} = \frac{\text{Integration of PL}(Sm^{2+})\text{spectrum over the } Sm^{2+} \text{ band}}{\text{Integration of PL}(Sm^{3+})\text{spectrum over the } Sm^{3+} \text{ band}} \qquad (4.1)$$

It can be seen that over the ranges of doses used, the Response is approximately linear within experimental errors, in agreement with earlier reports of Sm-ion conversion in X-ray

irradiated Sm-doped bulk FA glasses [12 - 17]. The choice of a modulation frequency of 27 Hz is justified by Figure 4.5 which shows that 27 Hz lies midway between peaks of QFRS spectra of Sm^{3+} and Sm^{2+} and well below all possible peaks related to defect PL. It is worth noting here that the appearance of defect related PL bands in the FA glass was not reported in earlier research [14 - 17]. This may be connected to the less intense PL Sm-ion signals from surface-doped FA glass compared to volume-doped FA glass.

Figure 4.6 (a) show the PL spectra from undoped FA glass before and after X-ray irradiation. Figure 4.7 shows the PL intensity vs time results from pulse excitation. These shed more light on the properties of these defect related emission bands and are the result of experiments which have been performed on Sm-free glass. As part of the investigation into these materials, we irradiated FA glass without the presence of Sm and found the broad defect spectra were present and increased after irradiation as shown in Figure 4.6 (a). It is important to note that the detection

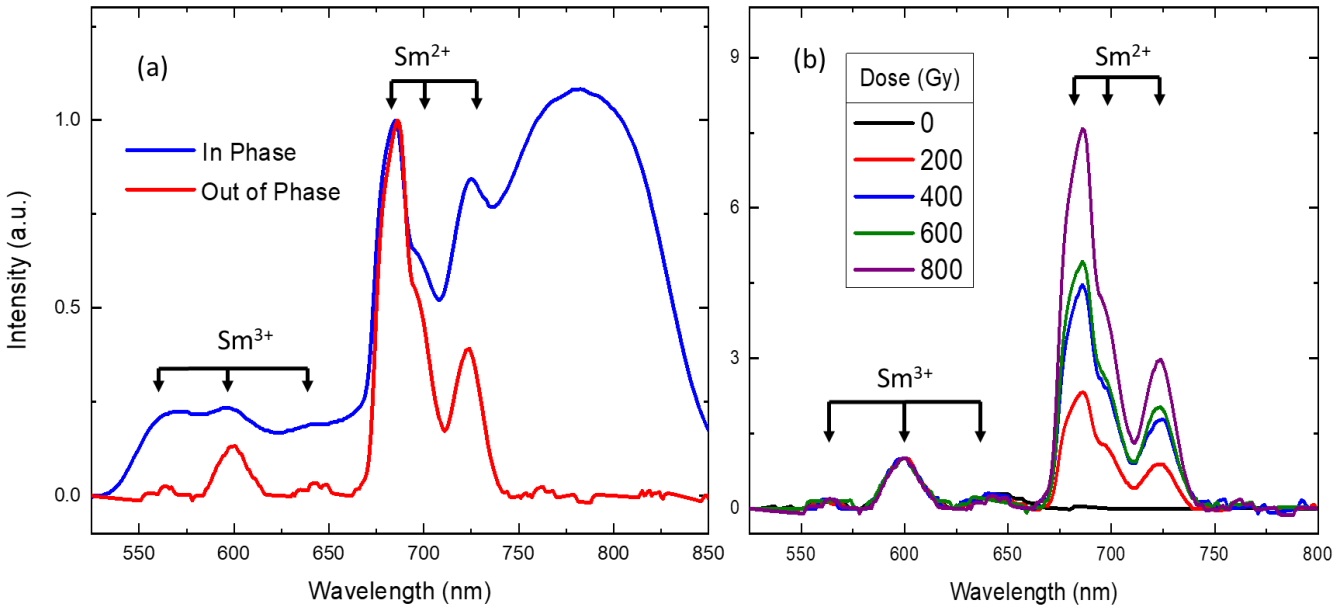

Figure 4.3 (a) Comparison of PL signals of Sm-ion implanted FA glass measured for "in-phase" (blue) and "out-of-phase (–90 °)" (red) synchronizations with modulated laser diode excitation. Red curve presents only "slow" PL bands associated with Sm ions, while "blue" curve presents contributions from all PL centers including defect centers associated with the damage created by ion implantation and X-ray irradiation. The sample was irradiated with an approximate dose of 800 Gy_{air} following annealing at a temperature of 475 °C. Excitation wavelength is 450 nm. Excitation modulation is 27 Hz. (b) Influence of X-ray dose on PL spectra of Sm-ion implanted FA glass. Spectra are normalized to the 593 nm peak associated with Sm^{3+} ions. All measurements are done in "out-of-phase (-90°)" mode. Spectra are not corrected for PMT spectral sensitivity.

range of the PMT is up to 850 nm, while the actual PL signature from this signal extends beyond this range. Figure 4.6 (b) shows spectra of the broad emission defects of a Sm-ion sample after irradiation as collected by an InGaAs detector where we see that the peak of the broad emission spectra is approximately 925 nm. Figure 4.6 (a) clearly shows that similar spectra in the implanted samples (Figure 4.3(a)) originate from defect formation related to the glass matrix itself and not related to the any Sm-ions

Subsequent experiments using a TCSPC system for measurement of the PL decays of these broad emission defects were found to be on the order of nanoseconds. The PL decays recorded using the single photon counting at the center of the emission peaks at 570 nm and 780 nm are shown in Figure 4.7.

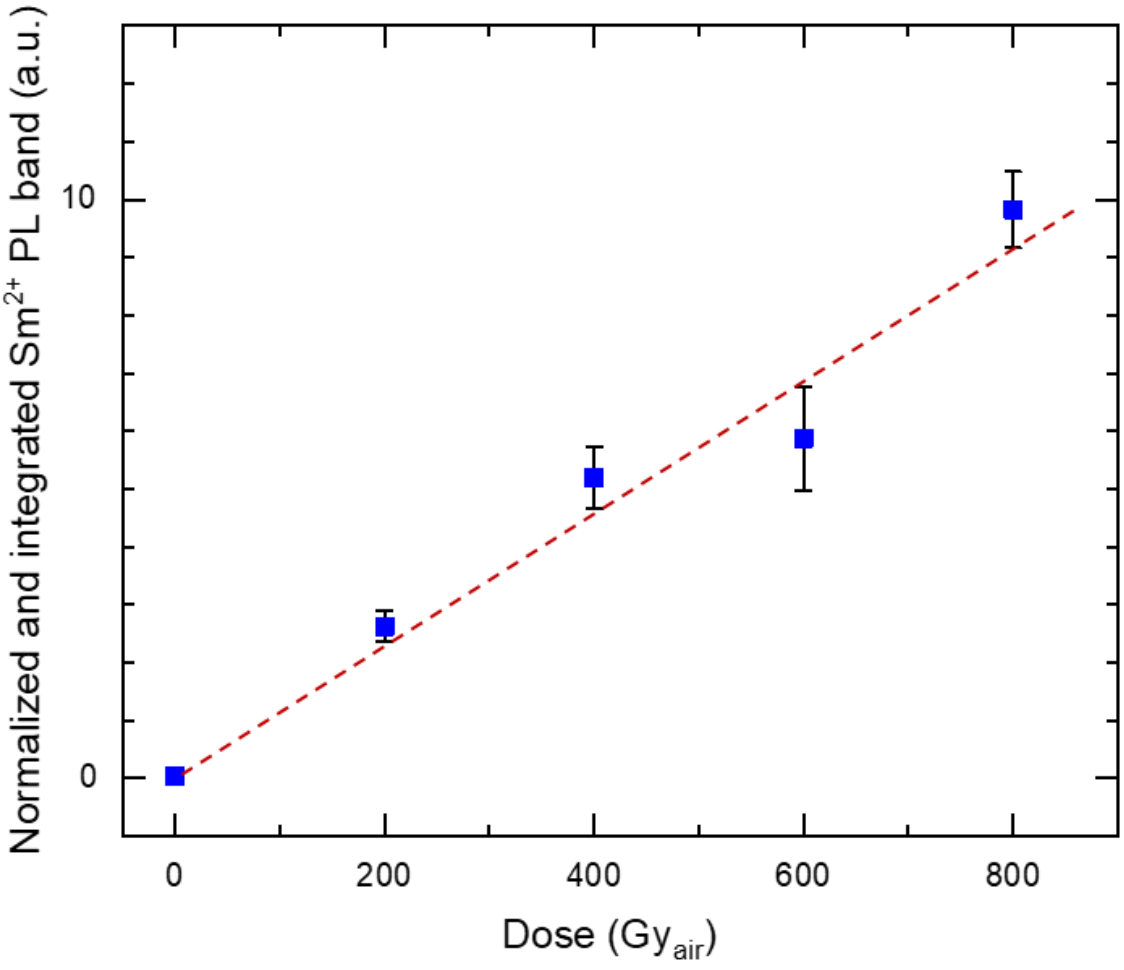

Figure 4.4 Response vs. incident dose in air. Response is the integration of normalized Sm^{2+} PL intensity from 660-800 nm.

4.5 Discussion

Previous work with Sm-doped FA glass samples for large dose measurements examined the conversion from Sm^{3+} to Sm^{2+} in homogeneously doped bulk samples [11 - 17]. In these papers, it was shown that it was possible to erase the Sm^{2+} after irradiation by annealing the sample above the glass transition temperature. In the case of 1% Sm doped FA glass, the glass transition temperature was measured to be 440° C. X-rays induce defects in the host glass material, these defects then capture the holes and allow for electrons to cause conversion from Sm^{3+} to Sm^{2+}. Sm-ions present in the FA glass allows for conversion from the trivalent to divalent form by the presence of hole centers which are commonly associated with fluorine complexes and oxygen contamination [26,27]. The conversion process of Sm^{3+} to Sm^{2+} is controlled by a hole trapping

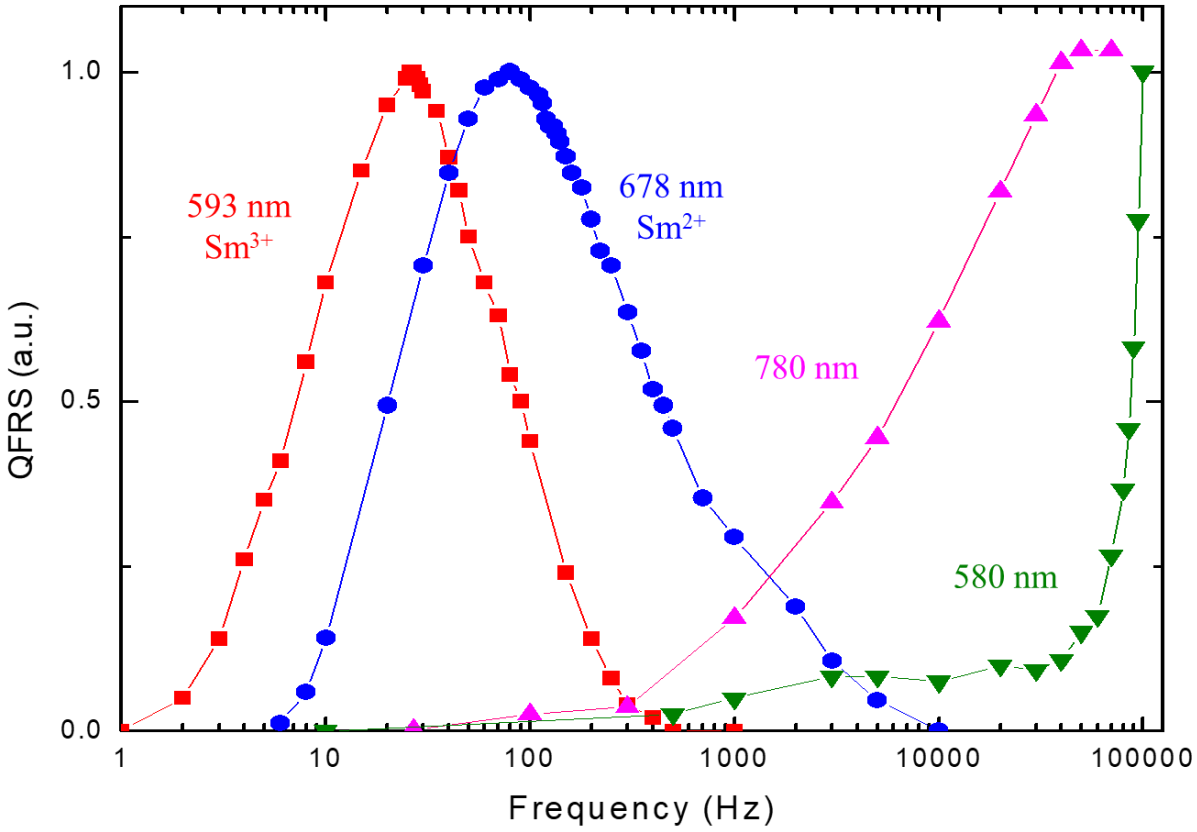

Figure 4.5 QFRS spectra of the various PL bands present in the Sm-ion implanted glass. The peak frequencies correspond approximately to the inverse lifetimes of corresponding radiative transitions. The PL bands centered at around 593 and 678 nm may be attributed to Sm^{3+} and Sm^{2+} with radiate lifetimes around 4 ms and 10 ms, respectively. Broad PL bands with peaks around 780 nm and 580 nm exhibit radiative lifetimes too short to be measured by the present experimental setup and their PL decay times are presented in Figure 4.7.

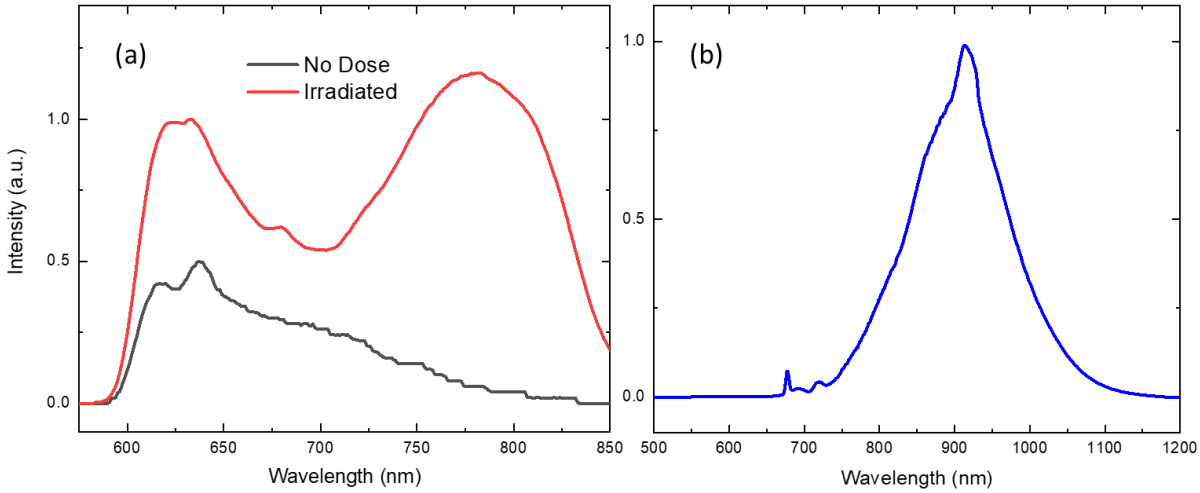

Figure 4.6 a) Comparison of PL spectra of irradiated and non-irradiated undoped (Sm free) FA glass. The PL is collected "in phase" using a PMT which has a detection range ending around 850 nm. b) PL spectra of Sm-ion implanted X-ray irradiated FA glass. The spectrum is collected using no modulation and an InGaAs detector (with detection range up to 1750 nm) showing the real maximum of defect related emission at around 915 nm. Sm^{2+} emission is just a small blip around 700 nm. In all experiments the approximate air dose is 2400 Gy. Spectra are not corrected for PMT nor InGaAs detector spectral sensitivities.

process, and not by electron trapping. This is apparent due to the fact that Sm^{3+} signals remain after saturation of the bulk Sm-doped FA glass sample, indicating that Sm^{3+} is still available to capture electrons, while hole traps are fully occupied.

Ion implantation is a well-established method which is widely used for the modification of the structural properties of a medium for a variety of electronic and optoelectronic applications [28 -31]. In the case of our Sm-ion doped FA glass, the primary goal was to implant Sm ions and prepare a doped sample with a specific valence state and to achieve the desirable effect of reduction of Sm^{3+} to Sm^{2+} through X-ray irradiation, similarly to previous works that had been done involving bulk (volume) doped FA glasses [11 - 17]. Figure 4.2 and Figure 4.3 clearly illustrate that it is indeed possible to implant the FA glass with Sm-ions which are incorporated as Sm^{2+} and Sm^{3+} ions in the as implanted sample. The presence of both are apparent from the PL spectra, which clearly exhibit the $^4G_{5/2} \rightarrow {}^6H_{7/2}$ and $^5D_0 \rightarrow {}^7F_0$ transitions, corresponding to the most intense PL peaks at 593 nm for Sm^{3+} and 678 nm for Sm^{2+}, respectively. Annealing the implanted samples around T_g, converts all Sm^{2+} ions to Sm^{3+}. X-ray exposure then leads to the deposition of radiation

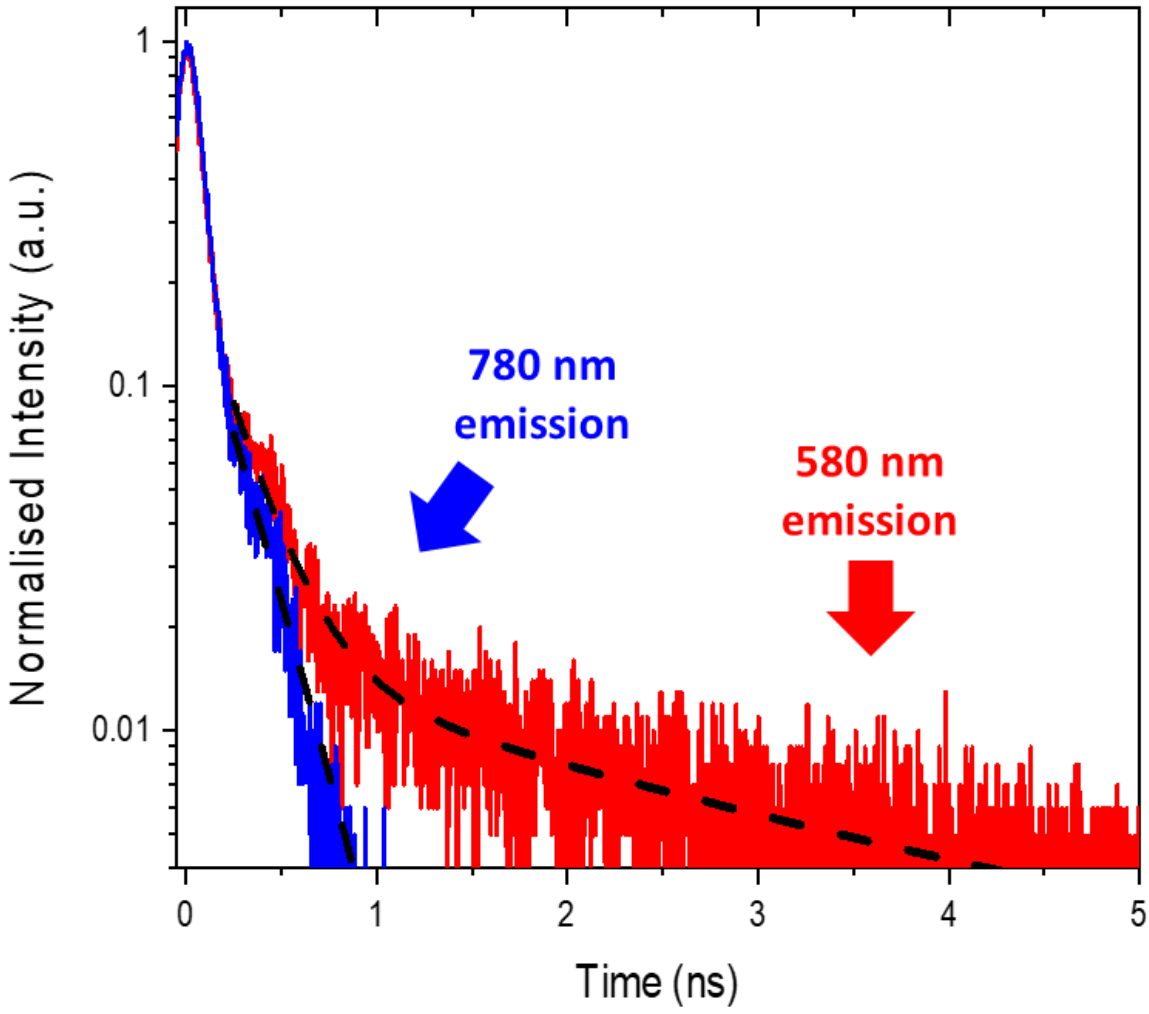

Figure 4.7 Lifetime measurements of broad PL bands with peaks around 780 nm and 580 nm. Measurements were taken of undoped (i.e. Sm free) FA glass. The sample was irradiated with an approximate dose of 2400 Gy in air. These transients were fitted by a bi-exponential decay function of the form $\tau_{PL} = y_0 + A_1 e^{-x/\tau_1} + A_2 e^{-x/\tau_2}$, where y_0 is an offset, τ_i $(i = 1,2)$ are the time constants and A_i are their corresponding amplitudes. A good fit was obtained with time constant values of $\tau_1 = 0.22 \pm 0.01$ ns and $\tau_2 = 2.5 \pm 0.1$ ns for 580 nm emission. For the 780 nm emission only the faster ($\tau_1 = 0.22 \pm 0.01$ ns) seems to be present.

energy into the sample, which creates defects, most significantly hole traps, in the host. The absorption of an X-ray knocks out a primary electron from an inner shell of an atom which then ionizes the medium to generate many electrons and holes. Holes are captured by the X-ray generated hole traps and the electrons convert the Sm^{3+} to Sm^{2+}. The peak intensity of the Sm^{2+} PL emission is proportional to the total number of converted Sm^{2+} ions and hence can be used to measure the delivered dose as discussed previously [10 - 17].

Additionally, the presence of PL signals from Sm^{2+} and Sm^{3+} were found to be partially overlapped by broad emission spectra, as shown in Figure 4.3 (a) and Figure 4.6 (a). The appearance of broad overlapping emission spectra appears to correspond with X-ray induced defects, primarily in the red to infrared region extending from 700−1100 nm. These emission bands have very fast PL decay times and can be easily separated from the slower emissions of Sm^{3+} and Sm^{2+} by using "out-of-phase" phase sensitive PL measuring technique as shown in Figure 4.3 (b).

It is quite possible that the broad emission spectra, detected in the present paper, correlate with X-ray induced photodarkening in FA and FP (fluorophosphates) glass samples reported earlier in bulk doped glasses [12 - 17]. Commonly, this darkening is associated with the appearance of hole trap centers which are tentatively identified as fluorine and oxygen centers [26,27]. Thermal treatment can cause the Sm-ions to be converted from Sm^{2+} back to Sm^{3+} and can repair implantation damage through annealing which allows for samples to be re-used multiple times.

4.6 Conclusions

Sm-ions have been successfully implanted into fluoroaluminate glasses. Following implantation, Sm-ions in the glass host were found to be in Sm^{2+} and Sm^{3+} valences. Annealing the samples at the glass transition temperature converts all Sm^{2+}-ions into Sm^{3+}. Under X-ray irradiation, we have observed partial conversion of Sm^{3+} into Sm^{2+} along the lines of what we have reported previously on bulk Sm-doped samples. The X-ray irradiation has also led to the appearance of broad and intense photoluminescence bands, associated with X-ray induced structural defects. PL emission decay times for these bands were measured to be in the nanosecond range, therefore useful Sm^{2+} and Sm^{3+} photoluminescence signals could be easily separated from the defect-related PL by using an "out-of-phase" photoluminescence signal in a phase-sensitive PL photodetection technique that uses a modulated excitation laser source. After implantation, the Sm-ions reside within a thin plane very near the surface in the glass, resulting in both the measurement of an effective surface dose as well as assuring that any photoluminescence from Sm-ions are not significantly attenuated before collection. Overall, Sm-ion implanted FA glass has shown successful conversion from the trivalent form (Sm^{3+}) to the divalent (Sm^{2+}) form of Sm, which have different PL signatures and hence these signatures can be used to measure the incident dose. The valence conversion was

achieved up to the highest dose accessed in this work, 800 Gy_{air} and the converted fraction of Sm^{3+} to Sm^{2+} (as indicated by the integrated Sm^{2+} PL band) is nearly linear with incident dose.

4.7 Acknowledgements:

We thank Natural Sciences and Engineering Research Council of Canada (NSERC) for financial support and the New Zealand Ministry of Business, Innovation, and Employment. Ruben Ahumada-Lazo thanks CONACYT for provision of the scholarships 284566/399936. This work was supported by The Royal Society (London) through an International Exchange Award (IE160035) and by the UK Engineering and Physical Sciences Research Council (EPSRC) grant EP/N020057/2. We would also like to thank Chris Varoy for his previous work on FA and FP glass samples that lead to the refinement of the glass making process.

4.7 References

[1]D. N. Slatkin, F. A. Dilmanian, P. Spanne, M. Sandborg, Microbeam radiation therapy. Med. Phys. **19**, 1395-400 (1992)

[2] H. Blattmann, J. Gebbers, E. Br€auer-Krisch, A. Bravin, G. Le Duc, W. Burkard, M. Di Michiel, V. Djonov, D. N. Slatkin, J. Stepanek, J. A. Laissure, Applications of synchrotron x-rays to radiotherapy. Nucl. Instrum. Methods Phys. Res., Sect. A. **548**, 17–22 (2005)

[3] A. Dilmanian, Z. Zhong, T. Bacarian, H. Benveniste, P. Romanelli, R. Wang, J. Welwart, T. Yuasa, E. M. Rosen, D. J. Anschel, Interlaced xray microplanar beams: A radiosurgery approach with clinical potential. Proc. Natl. Acad. Sci. U.S.A. **103** 9709–14 (2006)

[4] C. Crosbie, R. L. Anderson, K. Rothkamm, C. M. Restall, L. Cann, S. Ruwanpura, S. Meachem, N. Yagi, I. Svalbe, R. A. Lewis, B. R. G. Williams, P. A. W. Rogers, Tumor cell response to synchrotron microbeam radiation therapy differs markedly from cells in normal tissues. Int. J. Radiat. Oncol. Biol. Phys. **77**, 886–94 (2010)

[5] E. Brauer-Krisch, R. Serduc, E. A. Siegbahn, G. Le Duc, Y. Prezado, A. Bravin, H. Blattmann, J. A. Laissue, Effects of pulsed, spatially fractionated, microscopic synchrotron x-ray beams on normal and tumoral brain tissue. Mutat. Res. Mutat. Res. **704**, 160–6 (2010)

[6] E. Bräuer-Krisch, A. Rosenfeld, M. Lerch, M. Petasecca, M. Akselrod, J. Sykora, J. Bartz, M. Ptaszkiewicz, P. Olko, A. Berg, M. Wieland, S. Doran, T. Brochard, A. Kamlowski, G. Cellere, A. Paccagnella, E. A. Siegbahn, Y. Prezado, I. Martinez-Rovira, A. Bravin, L. Dusseau, P. Berkvens, Potential high resolution dosimeters for MRT. AIP Conf. Proc. **1266**, 89-97 (2010)

[7] D. L. Griscom, E. J. Friebele, K. J. Long, J. W. Fleming, Fundamental defect centers in glass: Electron spin resonance and optical absorption studies of irradiated phosphorus-doped silica glass and optical fibers. J. Appl. Phys. **54**, 3743-62 (1983)

[8] K. Miura, J. Qiu, S. Fujiwara, S. Sakaguchi, K. Hirao, Three-dimensional optical memory with rewriteable and ultrahigh density using the valence-state change of samarium ions. Appl. Phys.Lett. **80**, 2263-5 (2002)

[9] E. Malchukova, B. Boizot, G. Petite, D. Ghaleb, Optical properties and valence state of Sm ions in aluminoborosilicate glass under β-irradiation. J. Non-Cryst. Solids. **353**, 2397-402 (2007).

[10] S. Vahedi, G. Okada, C. Koughia, R. Sammynaiken, A. Edgar, S. Kasap, ESR study of samarium doped fluorophosphate glasses for high-dose, high-resolution dosimetry. Optical Materials Express. **4**, 1244-56 (2014)

[11] G. Okada, J. Ueda, S. Tanabe, G. Belev, T. Wysokinski, D. Chapman, D. Tonchev, S. Kasap, Samarium-doped oxyfluoride glass-ceramic as a new fast erasable dosimetric detector material for microbeam radiation cancer therapy applications at the Canadian synchrotron. J. American Ceramic Society. **97**, 1976-80 (2014)

[12] B. Morrell, G. Okada, S. Vahedi, C. Koughia, A. Edgar, C. Varoy, G. Belev, T. Wysokinski, D. Chapman, R. Sammynaiken, S. Kasap, Optically erasable samarium-doped fluorophosphate glasses for high-dose measurement in microbeam radiation therapy. J. Appl. Phys. **115**, 063107 (2014)

[13] G. Belev, G. Okada, D. Tonchev, C. Koughia, C. Varoy, A. Egar, T. Wysokinski, D. Chapman, S. Kasap, Valency conversion of samarium ions under high dose synchrotron generated x-ray radiation. Phys. Status Solidi C. **8**, 2822-25 (2011)

[14] A. Edgar, C. Varoy, C. Koughia, G. Okada, G. Belev, S. Kasap, High-resolution x-ray imaging with samarium-doped fluoroaluminate and fluorophosphate glass. Journal of Non-Crystalline Solids. **377**, 124-128 (2013)

[15] S. Vahedi, G. Okada, B. Morrell, E. Muzar, C. Koughia, A. Edgar, C. Varoy, G. Belev, T. Wysokinski, D. Chapman, S. Kasap, X-ray induced Sm3+ to Sm2+ conversion in fluorophosphate and fluoroaluminate glasses for the monitoring of high-doses in microbeam radiation therapy. Journal of Applied Physics. **112**, 073108 (2012)

[16] G. Okada, B. Morrell, C. Koughia, A. Edgar, C. Varoy, G. Belev, T. Wysokinski, D. Chapman, S. Kasap, Spatially resolved measurement of high doses in microbeam radiation therapy using samarium doped fluorophosphate glasses. Applied Physics Letters. **99**, 121105 (2011)

[17] G. Okada, S. Vahedi, B. Morrell, C. Koughia, G. Belev, T. Wysokinski, D. Chapman, C. Varoy, A. Edgar, S. Kasap, Examination of the dynamic range of Sm-doped glasses for high-dose and high-resolution dosimetric applications in microbeam radiation therapy at the Canadian synchrotron. Optical Materials. **35**, 1976-80 (2013)

[18] https://www.oem-xray-components.siemens.com/x-ray-spectra-simulation (accessed on 27 February 2019)

[19] K. Koughia, D. Saitou, T. Aoki, M. Munzar, S.O. Kasap, Photoluminescence lifetime spectrum in erbium doped Ge-Ga-S glasses. J. Non. Cryst. Solids. **352,** 2420–4 (2006)

[20] S.O. Kasap, K. Koughia, M. Munzar, D. Tonchev, D. Saitou, T. Aoki, Recent photoluminescence research on chalcogenide glasses for photonics applications. J. Non. Cryst. Solids. **353**, 1364-71 (2007)

[21] K. Koughia, M. Munzar, T. Aoki, S. Kasap, Photoluminescence spectra and lifetimes of $^4I_{13/2}$ - $^4I_{15/2}$ and $^4I_{11/2}$ -$^4I_{15/2}$transitions in erbium doped GeGaSe and GeGaS glasses. J. Mater. Sci. Mater. Electron. **18**, 153-7 (2007)

[22] T. Aoki, D. Saitou, K. Fujimoto, C. Fujihashi, K. Shimakawa, K. Koughia, S.O. Kasap, Quadrature frequency resolved spectroscopy (QFRS) of radiative transitions of Er^{3+} and Nd^{3+} ions in chalcogenide glasses (ChGs). J. Phys. Conf. Ser. **253,** (2010)

[23] L. Strizik, V. Prokop, J. Hrabovsky, T. Wagner, T. Aoki, Quadrature frequency resolved spectroscopy of upconversion photoluminescence in GeGaS:Er^{3+}: I. Determination of energy transfer upconversion parameter. J. Mater. Sci. Mater. Electron. **28**, 7053-63 (2017)

[24] T. Aoki, L. Strizik, J. Hrabovsky, T. Wagner, Quadrature frequency resolved spectroscopy of upconversion photoluminescence in GeGaS:Er^{3+}; II. Elucidating excitation mechanisms of red emission besides green emission. J. Mater. Sci. Mater. Electron. **28**, 7077-82 (2017)

[25] J. Zeigler, The stopping range of ions with matter, www.srim.org (accessed on 17 February 2019)

[26] P. Ebeling, D. Ehrt, M. Friedrich, X-ray induced effects in phosphate glasses. Optical Materials. **20**, 101-11 (2002)

[27] D. Griscom, Defect centers in heavy-metal fluoride glasses: a review. Journal of Non-crystalline Solids. **161**, 45-51 (1993)

[28] F. Chen, X. Wang, K. Wang, Development of ion-implanted optical waveguides in optical materials: A review. Optical Materials. **29**. 1523-42 (2007)

[29] P. Townsend, P. Chandler, L. Zhang, Optical effects of ion implantation. Cambridge University Press, Cambridge (1994).

[30] C. Buchal, Ion implantation for optical applications. Nuclear Instruments and Methods in Physics Research Section B: Beam Interactions with Materials and Atoms. **96**, 370-3 (1995)

[31] J. Leonard, D. Cohen, B. Yonkee, R. Farrell, T. Margalith, S. Lee, S. DenBaars, J. Speck, S. Nakamura, Nonpolar III-nitride vertical-cavity surface-emitting lasers incorporating an ion implanted aperture. Appl. Phys. Lett. **107**, 011102 (2015)

Chapter 5

Instrumentation for High-Dose, High-Resolution Dosimetry for Microbeam Radiation Therapy using Samarium-Doped Fluoroaluminate and Fluorophosphate Glass Plates

Published as:

Farley Chicilo, Go Okada, George Belev, Dean Chapman, Andy Edgar, Richard Curry, and Safa Kasap "Instrumentation for High-Dose, High-Resolution Dosimetry for Microbeam Radiation Therapy using Samarium-Doped Fluoroaluminate and Fluorophosphate Glass Plates", *Meas. Sci. Technol.*, **31**, 015201 (Accepted September 2nd 2019) https://doi.org/10.1088/1361-6501/ab404e

Author contributions:

The main experimental work, data analysis, and manuscript preparation in this work was performed by Farley Chicilo. Go Okada provided the spectra measurements of the confocal fluorescence excitation, emission, and spectral response values shown in Figure 5.2. The fluorescent microspheres shown in Figure 5.6 were measured by Go Okada and George Belev. George Belev also assisted with monochromatic irradiations performed at the CLS. Samples were synthesized by Andy Edgar at the University of Wellington for this work, who also offered comments and suggestions for improving the manuscript. Sm-ion implantation of the FA glass samples were performed by Richard Curry at the Ion Beam Centre at the University of Surrey. Safa Kasap and Dean Chapman assisted with the preparation of the manuscript and offered comments and suggestions.

5.1 Abstract

We show that 1% Sm-doped fluoroaluminate (FA) glass plate and a suitably modified fluorescence confocal microscope provide an excellent radiation detection platform for high-dose measurements at high resolution down to the micron scale. We have used a custom-modified

fluoroscopic confocal microscope apparatus to scan, separate, detect, and digitize the photoluminescence signals from Sm^{3+} and Sm^{2+} ions in both FA and fluorophosphates (FP) glasses within a selected focal depth of the microscope below the sample surface. The response (*R*) of Sm-doped FA and FP glass plates to incident x-ray radiation was studied in detail in which *R* was defined as the difference in the ratio of photoluminescence (PL) signals from Sm^{2+} and Sm^{3+} before and after irradiation. We report on a number of important issues related to the use of these Sm-doped FA and FP glass plates in microbeam radiation therapy (MRT) dosimetry: The dependence of the Sm^{3+} to Sm^{2+} conversion, and hence *R* on the dose rate over some four orders of magnitude; the energy dependence of *R* at a given dose rate for both FA and FP samples with various concentrations of Sm^{3+} doping; *R* vs dose behavior at different energies up to 2000 Gy_{air} and the derivation of the detector calibration curves; the stability of the Sm-doped plates after they have been exposed; the instrumental limits of the present measurement technique.

5.2 Introduction

There are currently a number of techniques for the measurement of radiation dose along with a variety of potential materials for use in dosimetry as reviewed, for example, in [1 - 7]. Of particular interest is the dosimetery that would be required in the implementation of Microbeam Radiation Therapy (MRT), which is a promising synchrotron-based cancer treatment technique. MRT has been shown to have the potential to improve upon spatially broadbeam radiotherapy methods. The MRT technique is based on the noticeably different responses of tumors and healthy tissue after irradiation by multiple narrow and parallel planar beams of irradiation. In MRT, highly collimated x-rays pass through a multi-slit collimator (MSC), segmenting the incident x-ray radiation before it is delivered to a patient. It has been shown that healthy tissue adjacent to the narrow sections of irradiation helps with the repair of damaged tissues, whereas tumors do not show this ability, allowing for substantial doses to be delivered to a patient with minimal damage to healthy tissue. There have been many papers in the last ten to fifteen years that address various issues related to the use of MRT and its benefits in cancer treatment [8 - 14]. The technique requires a high incident x-ray energy and must be able to deliver large doses to a patient in a very short timescale in order to maintain the desirable tissue sparing effect associated with the technique.

The accurate measurement of these microbeams is essential for patient care and for treatment planning. The "peak" dose at the center of the microbeam and the "valley" dose between the adjacent microbeams can differ by hundreds of grays over a distance of several microns and incident x-ray energies of interest can vary from 50 – 250 keV. In order to satisfy the dosimetry requirements of MRT, a detector must be able to simultaneously measure both a peak and valley dose with a spatial resolution on the scale of microns, and must be able to do so over a large energy range and at high dose rates. Ultimately, a two-dimensional (2D) cross-sectional image of the dose distribution is required.

Multiple techniques for the measurement of these microbeams have been previously discussed, including Gafchromic films, MOSFET detectors, Si strip detectors, single crystal diamond detectors, polymer gels, fluorescent nuclear track detectors, etc.; see examples in [15 - 20]. The technique must be able to measure doses from a few Grays to thousands of Grays and over various energy ranges. A major problem with many dosimetric materials is the saturation of the sensitivity at high dose or a limited dynamic range that is unable to simultaneously measure both the range from the valley dose (a few Grays) to the peak dose (thousands of grays); a known-problem that has been already discussed in the literature (e.g. [21]). A promising measurement method involves using the valence conversion of rare earth ions which, when embedded in a suitable material, can serve as a measurement of the delivered dose. Upon irradiation with various forms of excitation, such as x-rays, β and γ-irradiation, and photoexcitation, rare earths have shown the ability to change their valence state in various media [22 - 26]. Of particular interest among the rare earths is samarium, since the emission spectra of Sm^{3+} and Sm^{2+} ions are easily distinguishable and emit in the orange and red regions of the spectrum respectively, which are well suited for detection by photomultiplier tubes (PMTs).

The conversion process for Sm^{3+} to Sm^{2+} is strongly dependent on the host material. Previous work has shown that Sm-doped FP and FA glasses can be used as dosimetric detectors, which have the capability of measuring both large doses and the peak-to-valley dose ratio (PVDR) at high resolution, both are important considerations in the future success of MRT. These Sm-doped glass plate dosimeters utilize the distinguishable photoluminescence (PL) signals from the conversion of Sm^{3+} to Sm^{2+} as a function of the dose delivered. These PL signals are then measured using a modified fluorescence confocal microscopy detection system that is tuned to the emission

wavelengths of these ions. Using this method it has been shown that resolution on the order of microns can be achieved [27 - 35].This works investigates one of the most important issues in the calibration of any detector for accurate dose measurement: the dependence of the response of the detector to the incident x-ray energy and the incident dose rate. We have examined the conversion of Sm^{3+} to Sm^{2+} of Sm-doped FA and FP glasses over a wide range of dose rates (four orders of magnitude) and energy values (35 to 130 keV) and how these Sm-doped plates can be calibrated so that they measure the correct incident dose.

In the present paper, we discuss the conversion of Sm^{3+} to Sm^{2+} in these materials and how the conversion process is affected by the dose rate and incident x-ray energy. An important factor in the success of MRT is the high incident dose rate which helps minimize any "smearing" of the microbeams that may occur from the patient's movement, or from micron level shifts resulting from vascular flow within the irradiated tissue. An additional important consideration is that of the incident x-ray energy; the energy must be high enough to penetrate deeply into patient tissue and ensure that sufficient dose is delivered to the desired region. Ideally, the response of a dosimeter should be independent of the incident x-ray energy as well as the incident dose rate. In practice, however, a dosimeter response needs to be calibrated when the energy range of the incident x-rays is large [36].

The measurement of the PL from Sm^{3+} and Sm^{2+} ions was implemented by using a fluorescence confocal microscope as mentioned above. We have also examined the dependence of the response (Sm^{3+} to Sm^{2+} conversion) of the Sm-doped glasses on the focal depth below the sample surface in the confocal microscope measurements as a function of x-ray energy. If the response of the dosimetric plate depends on the focal depth into the sample, this dependence needs to be included in the calibration characteristics.

The dependence of the Sm^{3+} to Sm^{2+} conversion on the amount of Sm doping in FA and FP glasses has been examined previously [28,33]. In this work we extend the previous study by examining the stability of the Sm-doped glasses shortly after they have been irradiated up to a period of 15 days. Most importantly, we examine the energy dependence of the Sm^{3+} to Sm^{2+} conversion for different amounts of Sm-doping at a given dose. The Sm-doped FA glass plates in

this work are able to measure doses up to 2×10^3 Gy in air and the measurement is independent of the dose rate; an important factor in the use of this technique in MRT.

5.3 Sm^{3+}-Doped Fluoroaluminate and Fluorophosphate Glass Plates

Sm doped glasses were synthesized using a melt quenching technique previously described in detail elsewhere [27 - 35]. Starting materials were mixed in a glove box in a dry nitrogen atmosphere and loaded in a carbon crucible where the mixture was then melted in an RF furnace at 1000 °C for 120 minutes. The glass was then quenched on a temperature controlled plate at 380 °C for 8 hours in an argon atmosphere in order to relieve internal stress and prevent cracking. The composition for FA glass in molar percentage is $10.0MgF_2 – 35.0AlF_3 – 20.0CaF_2 – 10.0SrF_2 – (15 – x)YF_3 – 10.0BaF_2 – xSmF_3$ and for FP glass is $10.0MgF_2 – (34.4 – x)AlF_3 – 30.4CaF_2 – 15.2SrF_2 – 10.0Sr(PO_3)_2 – xSmF_3$ where x is the concentration of SmF_3, which can be varied from 0.1% to 10%. Following synthesis, the glass materials were polished and cut into approximately 2 mm by 3 mm rectangular pieces for subsequent experiments. A typical glass plate thickness was ~1.5 mm. All percentages quoted hereafter are in mol.%. Some 120 samples were prepared for all the measurements. The density of the samples were measured by using the Archimedes principle of change in the measured weight of the sample in a liquid of known density. The sample density was 3.74 g cm^{-3}. The refractive index of the samples was approximately 1.5 over the PL wavelengths used in this work [37,38].

One of the FA glass samples (where $x = 0$ in the composition formula) was ion-implanted near the surface of the sample as described previously [35]. The ion-implantation generated a distribution of Sm^{2+} ions within a depth 1 μm and a peak concentration located at a 0.60 μm depth from the surface. The luminescence properties of these glasses have been already described [35]. The purpose of this Sm^{2+} ion-implanted sample is to provide a verification for the axial luminescence collection range in the confocal photoluminescence confocal microscope.

5.4 Single Energy and Polychromatic X-Ray Irradiation, Dose and Dose Rate Delivery

Polished and cut samples were taken to the Biomedical Imaging and Therapy (BMIT) 05ID-2 beamline at the Canadian Light Source (CLS, the Canadian synchrotron), for x-ray irradiations. Using the facilities at the BMIT beamline the incident x-ray energy is tuned using a bent Laue

double-crystal monochromator, which allows for monochromatic incident high energy x-rays to be selected with a resolution ($\Delta E/E$) of 10^{-3}. When performing the irradiations for dose rate and energy dependence experiments, the total dose delivered to each sample was kept constant at 200 Gy_{air} (Gy in air) as measured by an ionization chamber (model 31022, PTW-Freiburg). For dose rate measurements, the incident x-ray energy was kept constant at 50 keV, which is closest to the peak photon flux rate for the BMIT beamline and allows the maximum dose rate range to be delivered to a sample. It is important to emphasize that all dose rate measurements were done at one given energy and the total dose was kept constant. Likewise, for the samples irradiated while investigating the energy dependence experiments, the incident dose rate was kept constant at 175 mGy/s, which is the quoted dose value in air at the surface of the sample i.e. entrance dose in air. The incident x-ray energy was selected using a monochromator where the x-ray energy range was between 35 keV and 130 keV. The energy range is similar to that recently used in an MRT optimization study [39]. In order to modify the delivered dose rate to each sample, the wiggler magnetic field was modified between 2 and 3.9 T and additional aluminum filters were placed in the beam path to reduce the dose rate without modifying the x-ray energy. In the case of all samples, a 1 mm aluminum filter was present in the beam. Irradiation of collimated microbeams on Sm-doped glass plates were performed using a tungsten multislit collimator (MSC) with a slit width of 50 μm where the slits are separated by 400 μm (center-to-center distance). The collimator was manufactured by Usinage et Nouvelles Technologies, Morbier, France. Samples were irradiated in the dark and wrapped in aluminum foil until readout experiments were performed using a modified fluorescence confocal microscope described below.

X-ray irradiation experiments involving PL spectra and signal stability were completed using a FAXITRON x-ray cabinet with a tungsten anode operating at 110 kVp at an approximate dose rate of 40 Gy/min in air. This dose value represents the dose delivered in air at the surface of the sample, and not within the sample itself. The FAXITRON x-ray source is polychromatic with a mean energy of 49.3 keV taken from fluence by [40]. The exposure rate was measured by an ionization chamber (Keithley 35050). PL spectra of irradiated samples were measured using an ASEQ fiber input mini-spectrometer with spectral resolution better than 1 nm. The excitation source used was a 405 nm laser diode.

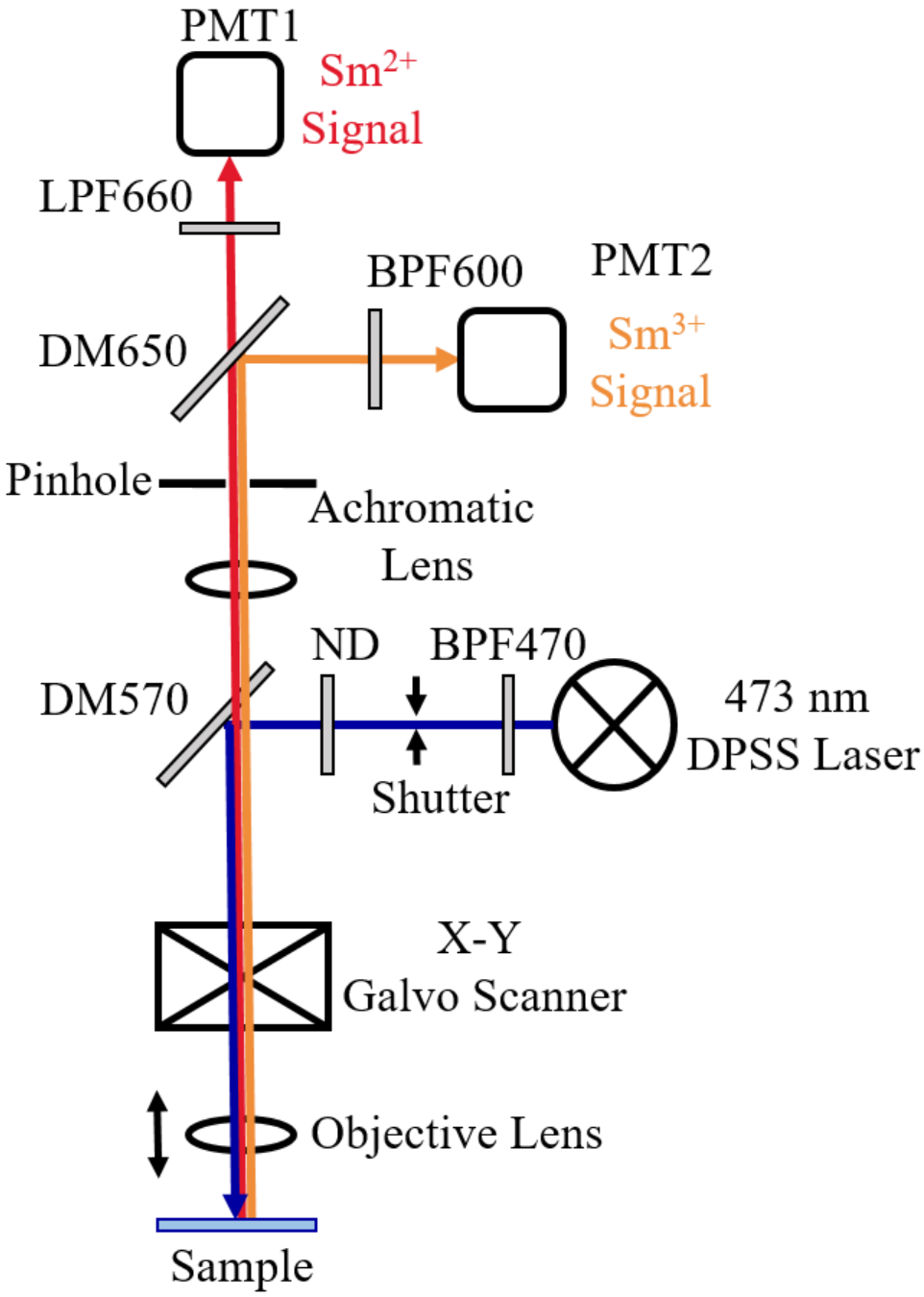

Figure 5.1 An illustration of the confocal microscopy set up used in measuring Sm-doped glass plates. The excitation source is a 473 nm diode-pumped solid-state (DPSS) laser, which has an adjustable focal depth within the glass samples and an intensity that can be modified through the use of neutral density filters (ND). Emission from Sm^{3+} and Sm^{2+} ions are filtered through dichroic mirrors (DM), and then collected simultaneously by two separate photomultiplier tubes tuned to the Sm^{3+} and Sm^{2+} wavelengths through the use of band-pass (BPF) and long-pass filters (LPF). The detection ranges of these PMTs are given in Figure 5.2. The available objective are 10×/0.3NA (Meopta) and 20×/0.75NA (Nikon) and the available pinhole sizes are 200, 100, and 50 µm.

5.5 Optical Measurement Technique: Modified Fluorescence Confocal Microscope

Response values for samples irradiated were measured using a custom confocal fluorescence microscopy readout system, which has been described in some detail previously [27 - 33]. Figure 5.1 shows a schematic of the confocal microscopy apparatus. The apparatus was a modified commercial confocal microscope (MultiProbe 2001 TM CLSM, Molecular Dynamics). The excitation beam at 473 nm (blue) was generated by a diode-pumped solid-state (DPSS) laser, whose beam is reflected by a 570 nm dichroic mirror (DM) towards an objective lens that focuses the laser at a selected focal depth within the sample. The intensity of the blue excitation laser beam in readout during confocal scanning was 0.5 μW. Upon excitation, Sm^{3+} and Sm^{2+} ions emit distinct and separable PL signals which are collected from the objective lens and guided towards a set of photomultiplier tubes (PMT). These signals are focused using an achromatic lens onto a pinhole and the resulting beam is then directed towards a 650 nm dichroic mirror which separates the Sm^{3+} and Sm^{2+} signals towards two separate PMTs fronted with a 600 nm band-pass filter (BPF) and a 660 nm long-pass filter (LPF), respectively. Figure 5.2 shows the spectral characteristics of the excitation and the two photomultiplier tubes with filters. The Sm^{3+} and Sm^{2+} signals are measured simultaneously and PL signals are digitized for calculation of the response of the Sm-doped glass plate.

The use of the confocal readout system requires the objective lens to be suitably placed below the sample so that the focal point in the sample that determines the volume of collection is well defined. This process is achieved by using a filter to block the 473 nm emission from the DPSS laser and allow the pump laser diode emission (λ = 808 nm) from the blue laser to pass through a filter. The reflection of this 808 nm beam from the sample surface is then recorded by changing the objective lens height from the sample surface, until a maximum reflection from the surface is registered. Once the location of the sample surface is known, the actual depth of the focal point inside the sample from the surface can be easily determined through straightforward optics. A movement of the objective by a distance *D* corresponds to the movement of the focal point in the sample by *d* where $d = D/n$, where *n* is the refractive index of the sample, as shown in Figure 5.3 (a). The motion *D* is measured and converted to *d* in plots where the PL measurements were recorded as a function of distance from the sample.

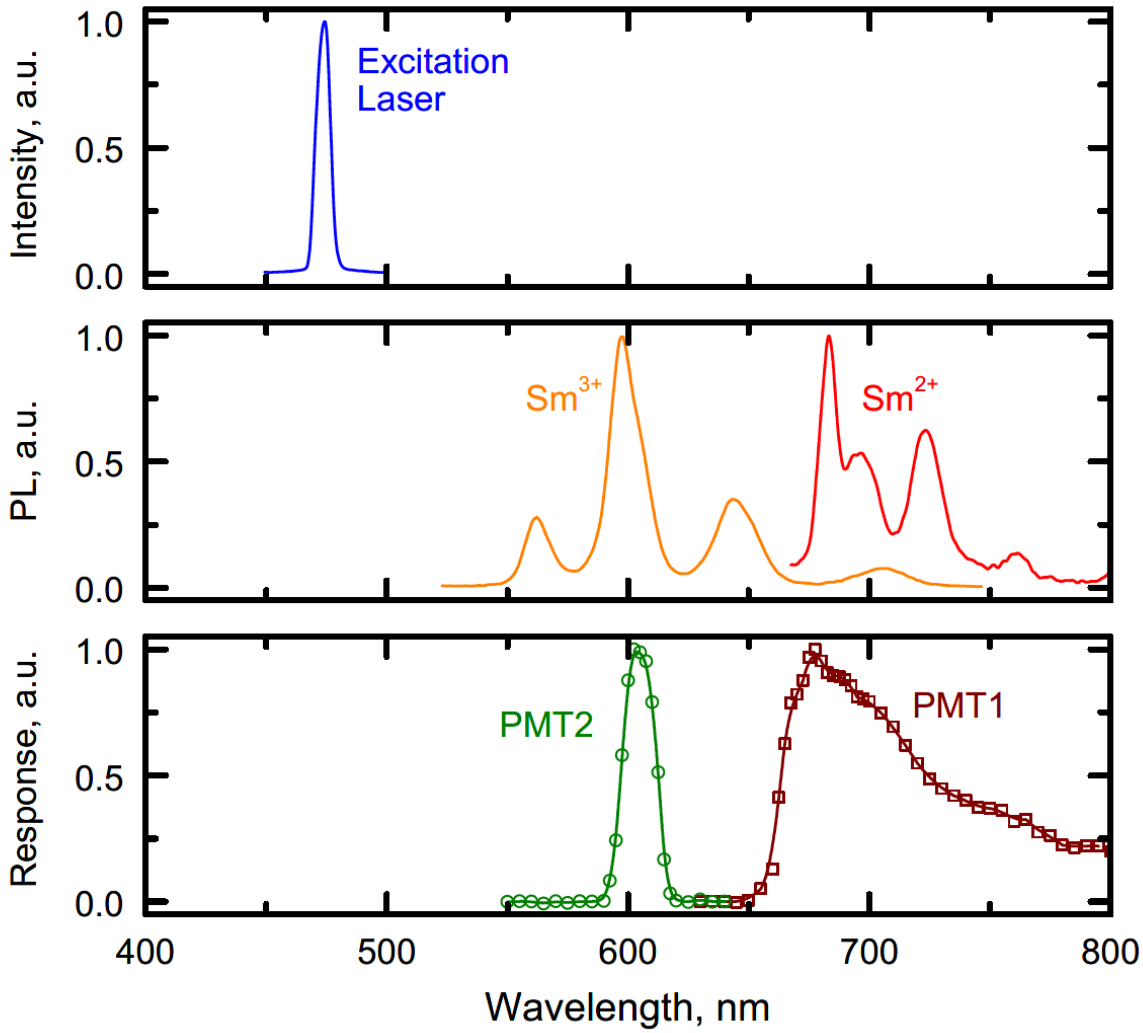

Figure 5.2 Upper figure shows the excitation spectrum centered at 473 nm. The middle figures show the PL spectra from Sm^{3+} and Sm^{2+} ions. The lower figure shows the spectral response of the two photomultiplier tubes with their respective filters; long-pass for PMT1 and band-pass for PMT2. The detection ranges are 595 – 615 nm (FWHM) for PMT2 (Sm^{3+}) and 660 – 720 nm (FWHM) for PMT1 (Sm^{2+}).

It is important to identify the laser excitation volume and the volume from which the PL signals are collected in the confocal microscope set-up in Figure 5.1. As shown in Figure 5.3 (b), the 470 nm excitation volume includes the cone-volume above the focal point up to the sample surface and the cone-volume below the focal point. The volume responsible for the PL signals however is different in the vertical (z) and lateral (x, y) directions. The vertical range Δz of signal collection, the *vertical resolution*, for an infinitely small pinhole would also be diffraction limited. In the present case, to obtain the best signal-to-noise ratio over a very large dynamic range (from

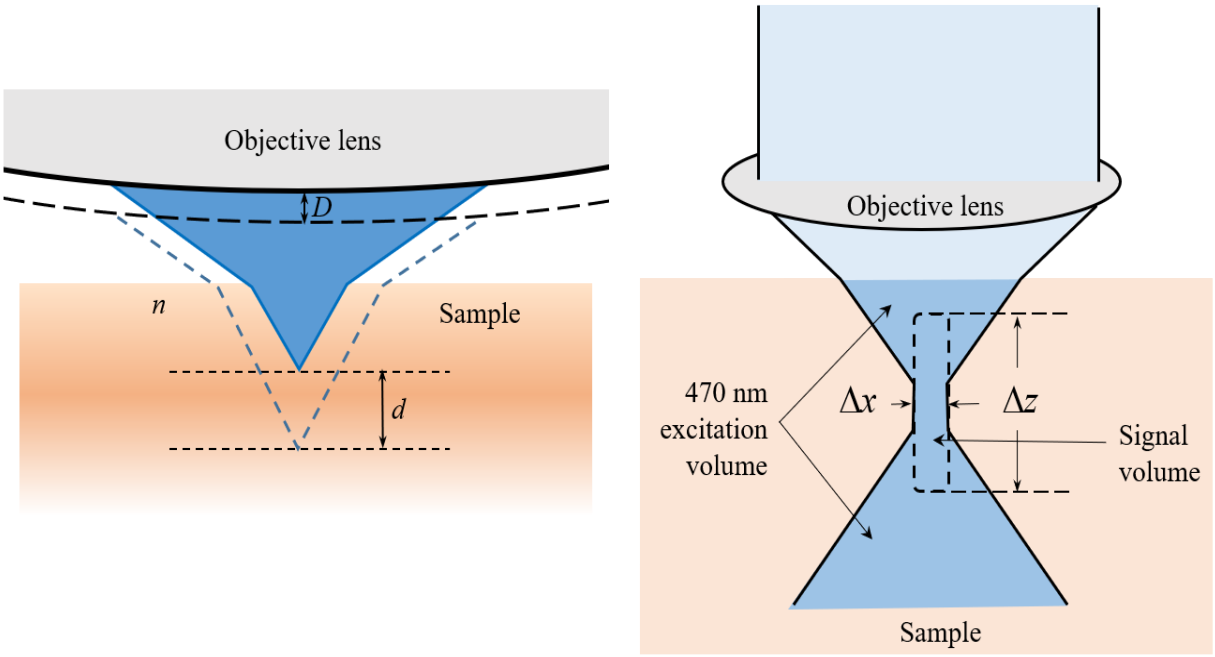

Figure 5.3 (a) Schematic illustration of the motion of the objective lens and the movement of the focal point inside the sample. The objective lens moves by D and the focal point by d and the two are related through the refractive index. (b) The 470 nm excitation volume inside the sample defined by the objective lens is shown as shaded in darker blue. The luminescence signals within the width of the focal point and the vertical range Δz are measured.

5 – 2000 Gy), the highest pinhole size was selected (200 μm) so the vertical range Δ*z* was much larger than the diffraction limited value and is determined experimentally as described below.

Figure 5.4 shows the PMT1 signal obtained from the Sm^{2+}-ion implanted FA glass as a function of distance *d* below the surface. The signal peak is roughly at 1 μm and the PMT1 signal decays and is half at about $d \approx 21$ μm. The full width at half maximum (FWHM) vertical range Δ*z* for PL signal collection is therefore about 42 μm. This vertical range Δ*z* represents approximately the vertical resolution of the confocal microscope used and, in the current application, it is significantly larger than typical confocal applications where Δ*z* would be a few microns; the present measurement uses a large pinhole to capture PL signals with acceptable S/N ratio at the low dose range. The significance of the results in Figure 5.4, is that if we place the focal point at $d = 20$ μm, then the vertical region from the surface to a depth of about 40 μm will primarily contribute to the PL signal, that is, we can exclude the spurious PL signals from the regions below

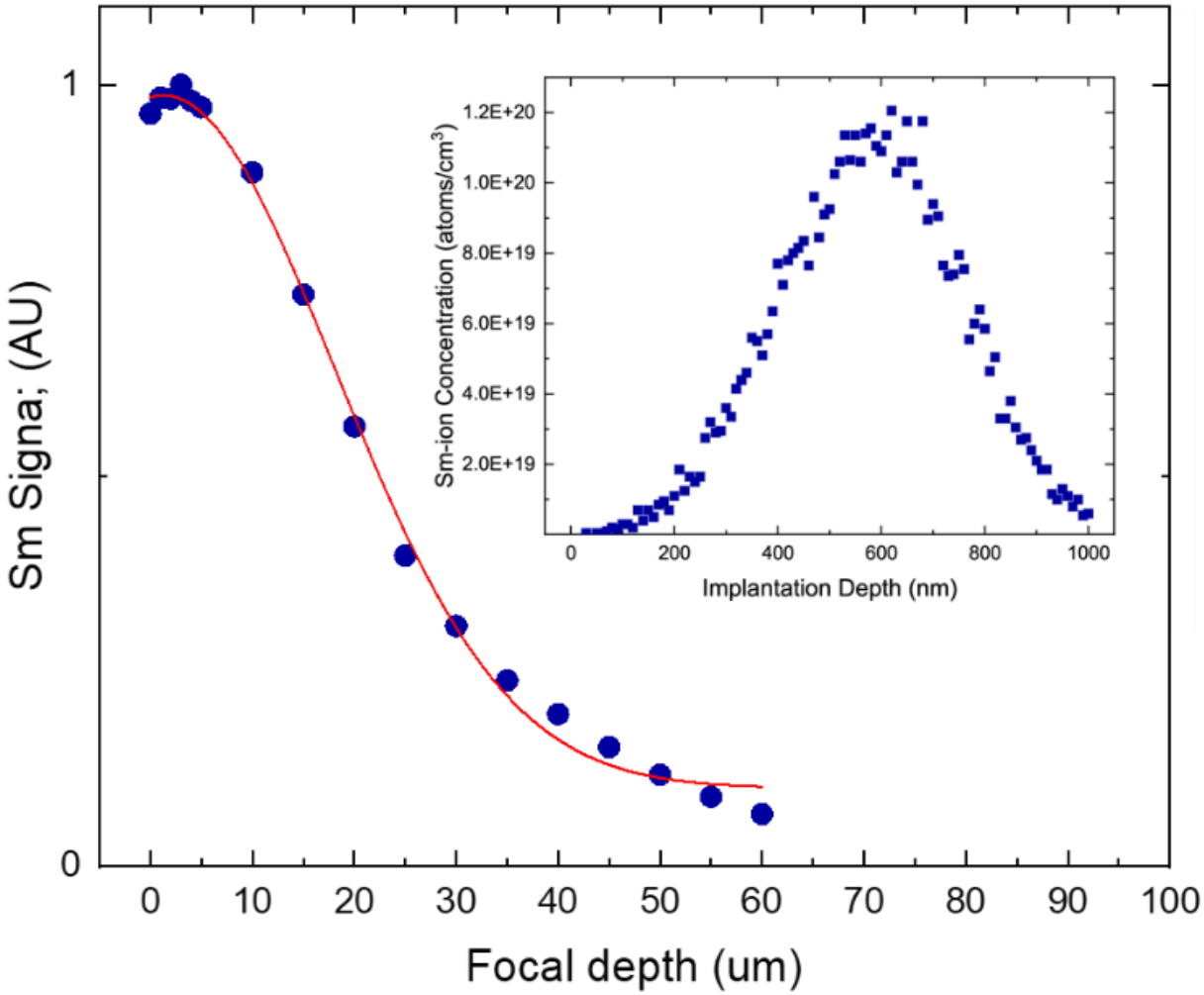

Figure 5.4 The PL(Sm^{2+}) signal from ion-implanted Sm^{2+} ions within 1 μm from the surface of a FA glass plate. Ion implantation peak is at 0.60 μm as shown in the insert [35]. The solid line is the best Gaussian curve fit with a half width at half maximum that is 21 μm.

and laterally further than Δx (the width of the focal point). Figure 5.4 shows the Sm^{3+} signal from PMT2 as a function of d. As expected this signal increases with d as the PL capture range is moved more into the sample. As will be shown below in the results section, the response of the Sm-doped plate to x-ray exposure remains constant up to about $d \approx 20$ μm, which is the d chosen in this work. There is one more distinct advantage to using a confocal microscope to probe only the depth Δz from the surface, which is roughly 40 μm. Over this distance, the radiation induced photodarkening is negligible, where this had to be considered in examining the PL from the whole sample with a thickness of a few millimeters as shown in reference [32], and included in the dosimetric response.

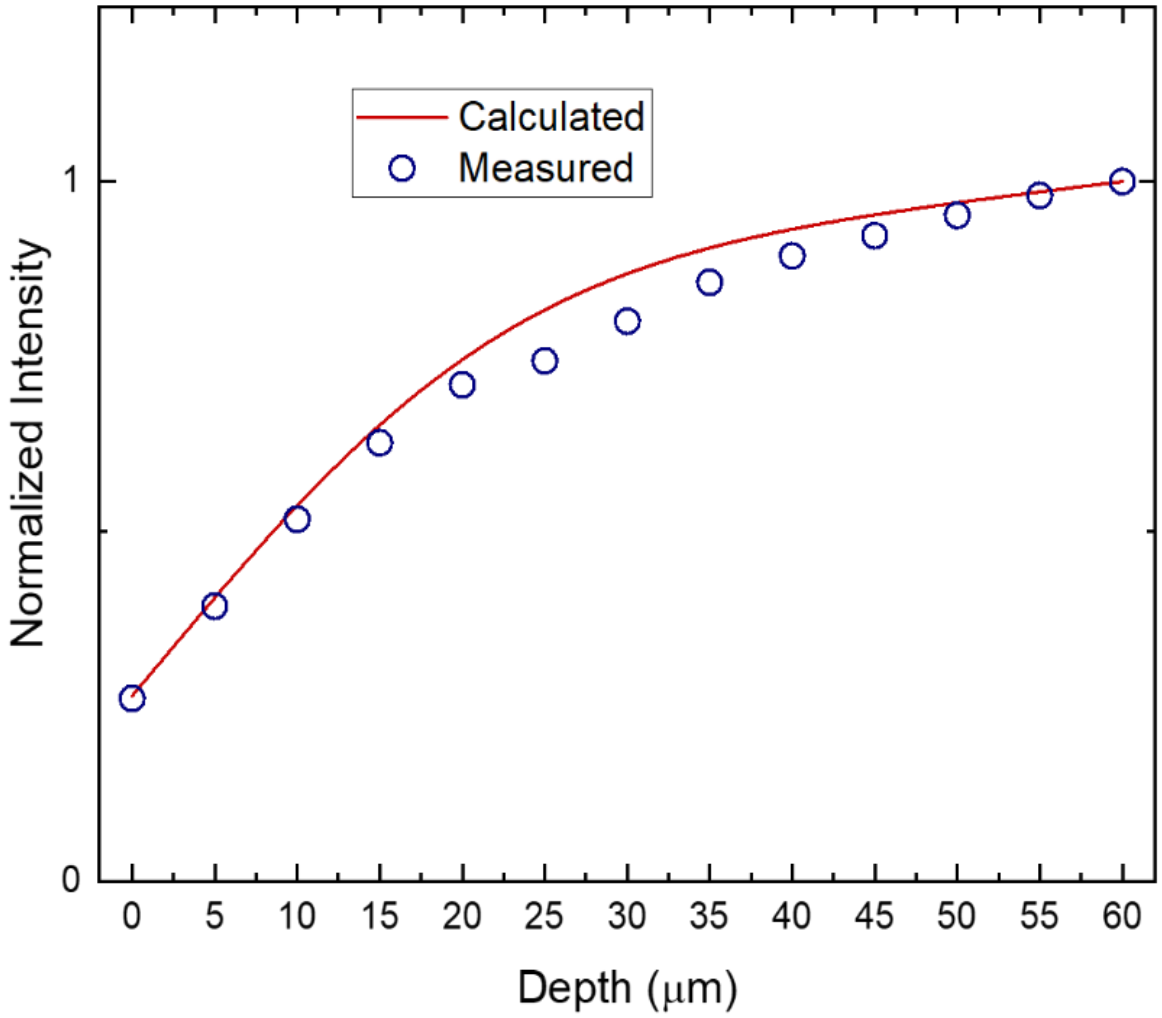

Figure 5.5 The PL signal vs distance from the sample surface. The blue dots represent Sm^{3+} values measured in 1% bulk Sm-doped FA glass and the red line is calculated from the fitted Gaussian signal from an ion implanted sample where Sm^{2+} ions reside within a depth of 600 nm, as shown in Figure 5.4, integrated from 10 μm outside the glass surface to 60 μm within the sample.

5.6 Lateral Resolution in Optical Measurements and the Spatial Microbeam Profile

In the lateral direction, the resolution defined as Δx in Figure 5.3 (b), is determined by diffraction effects and depends on the lens objective characteristics (numerical aperture, NA) and the wavelength of interest, λ, through the relationship $\Delta x \approx 0.61\lambda/NA$ [41]. For $\lambda \approx 700$ nm and NA = 0.75 for the objective lens used, $\Delta x \approx 0.5$ μm. Figure 5.6 demonstrates the high image resolving

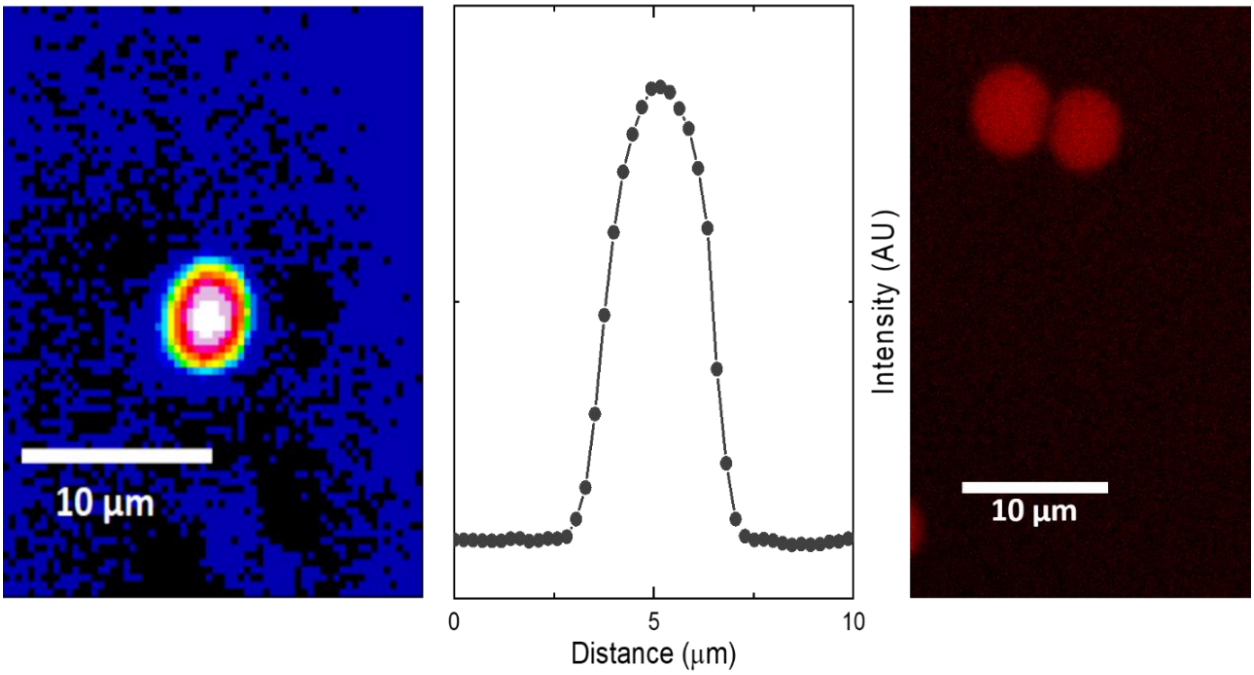

Figure 5.6 (left) An image of 4 µm fluorescent microsphere which was acquired using the confocal fluorescence microscopy readout system used in this work with the 20× objective. (center) the measured 1D profile of the 2D imaged microsphere from confocal fluorescence microscopy. (right) 4 µm fluorescent microspheres as measured by a 2-photon confocal microscope.

power of the current system by displaying the XY scanned PL from a 4 µm fluorescent microsphere, obtained from MultiSpeck™ Multispectral Fluorescence Microscopy Standard, Molecular Probes.

The measurements in Figure 5.6 were independently verified by imaging the same slide on a commercial two-photon microscope (Prairie Technology Ultima IV). The lateral resolution of the microscope was calibrated with a stage micrometer 2mm/0.01mm with overall accuracy 0.0015mm (S20, Pyser Optics).

The resolution capability of the microscope was also examined by scanning a 1951 USAF resolution plate collected through the reflection of the incident laser on the target of the surface through the 20× objective lens. The image from the latter scan is shown in Figure 5.7, and shows group 6 and 7 of the resolution plate, where the smallest line widths are 4.38 µm and 2.19 µm, respectively. They can be easily resolved.

The scanning speed of the confocal microscope system is largely dependent on the desired resolution and field of view. The system uses a galvo mirror to achieve a rectangular raster scanning method, where the image is scanned left to right in the *x*-direction and then is moved down to the next line in the *y*-direction where the process is repeated. Using the 20× objective lens gives an approximate field of view (FOV) of 0.75 × 0.75 mm. A typical scan setting using the 20× objective lens collects an image with approximately 500 × 500 pixels, although higher resolutions can be achieved (2500 × 2500 pixels). The reason for selecting a lower resolution is due to the relatively long PL decay lifetimes of the Sm^{3+} and Sm^{2+} ions, due to so called "forbidden" 4f → 4f transitions that are characteristic of samarium ions, which are between 4 and 10 ms [35]. Signal

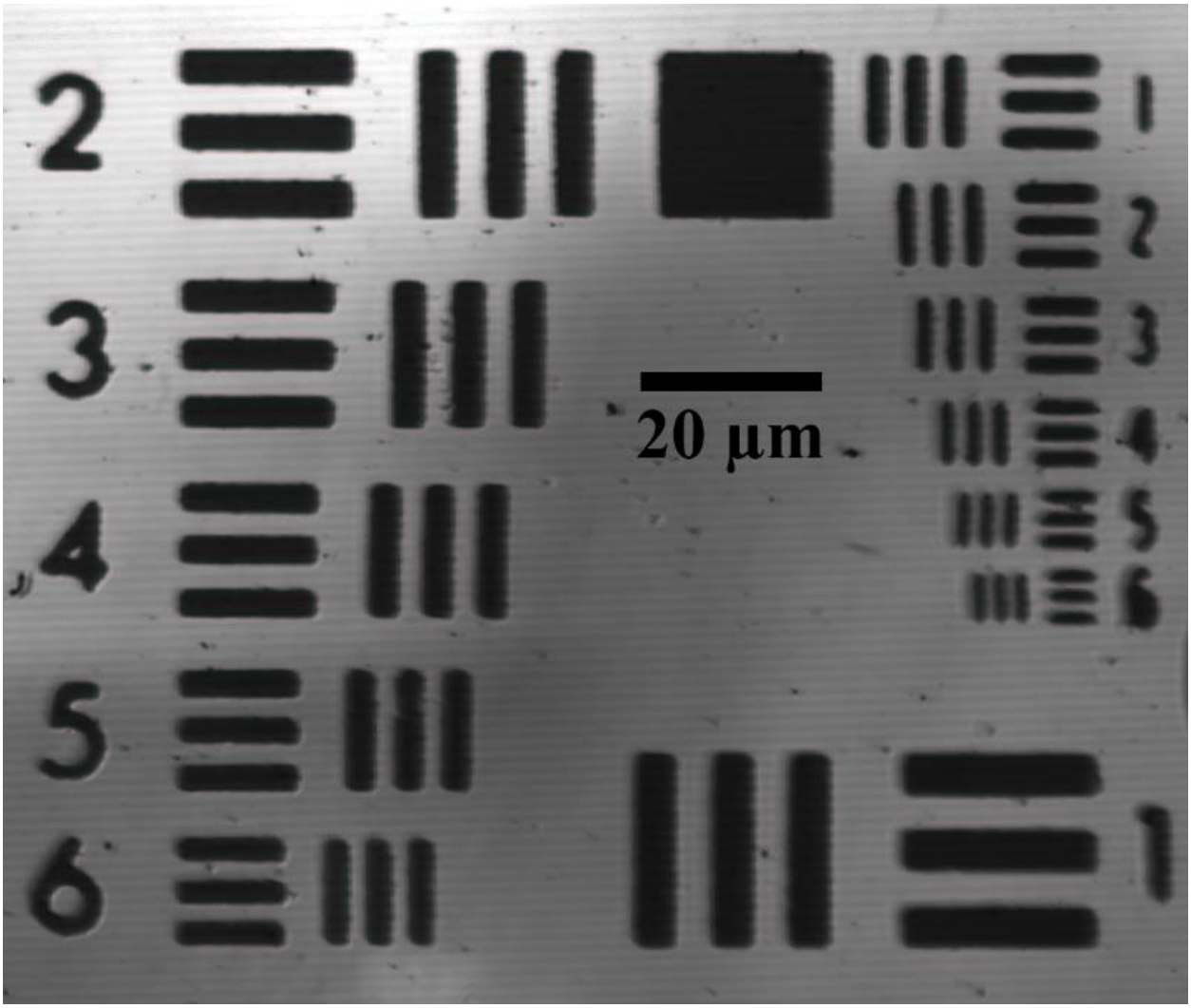

Figure 5.7 Image of a 1951 USAF resolution plate collected through the reflection of the incident laser on the target surface through a 20× objective lens. This image shows group 6 and 7 of the resolution plate where the smallest line widths are 4.38 µm and 2.19 µm, respectively.

collection requires a dwell time at each pixel that is larger than the PL lifetime decays of the Sm ions, and so each pixel is excited for 20 ms before moving to the adjacent pixel. The Time it takes to scan a field of view along *x* is 500 pixels × 0.02 s or 5.3 s. The scan of the whole field of view (500 × 500 pixels) is then 5000 s or about 1.4 h. At the highest achievable resolution (2500 × 2500 pixels) this time approximately is 34.7 h. This measurement time could be reduced significantly by scanning only the region of interest within the FOV or creating a more efficient scanning method. Further, samarium doped oxyfluoride glass ceramics have been shown to be capable of high resolution microbeam dosimetry, and exhibit parity-allowed 5d → 4f transitions which have PL decay lifetimes on the order of nanoseconds [28], cutting the read-out time from hours to minutes.

A spatial profile of a microbeam as recorded on a Sm^{3+}-doped FA glass plate under x-ray irradiation at the Canadian Light Source is shown in Figure 5.8. The image on the left is a 2D image of a single irradiated microbeam on a 1% Sm-doped FA glass slide where the incident beam

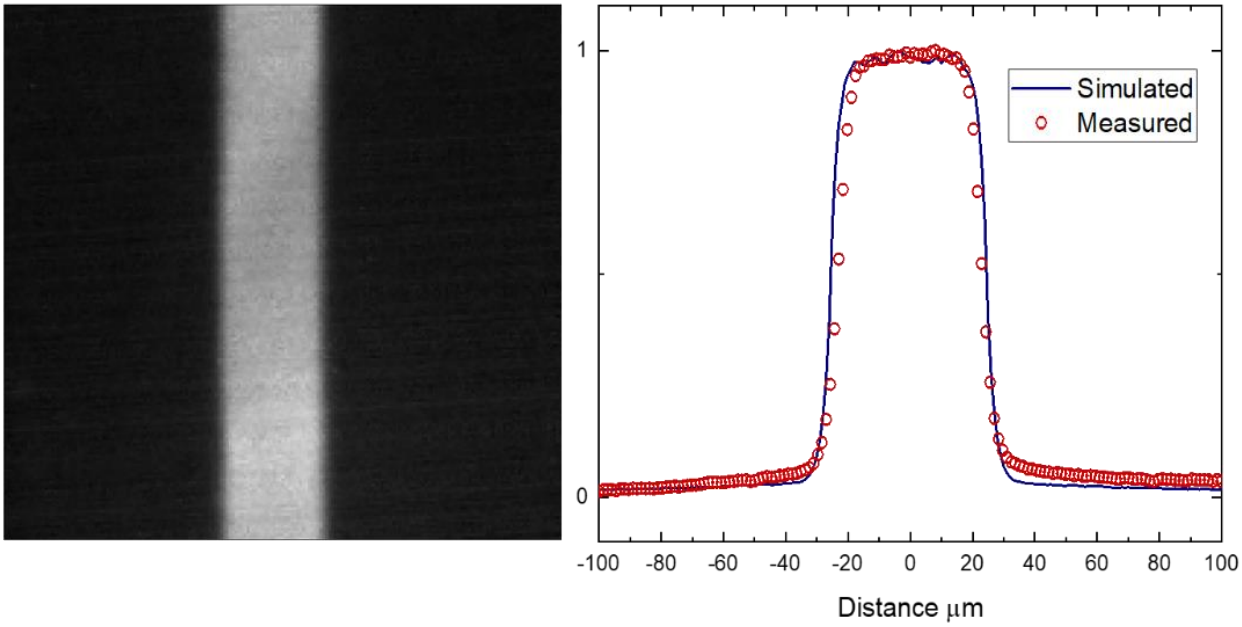

Figure 5.8 (left) 2D image of a single irradiated microbeam on a 1% Sm-doped FA glass slide performed at the CLS. The incident x-ray energy was selected to be 50 keV and the total dose delivered was 200 Gy_{air} prior to passing through the collimator. The collimator has a slit width of 50 μm and the peaks are separated by a distance of 400 μm, center to center. (right) Plotted 1D profile of shown 2D image. The red circles indicate measured values of the microbeam profile and the blue lines indicate the modeled beamshape through Monte Carlo simulations [43] with the MCNP [42] radiation transport computer code of monochromatic 50 keV x-rays incident on 1% Sm-doped FA glass. These measured profiles agree well with simulations and the energy dependence on the microbeam shape will be discussed in greater detail in an upcoming paper.

was put through a MSC. The incident x-ray energy was selected to be 50 keV and the total dose delivered was measured as 200 Gy_{air} before passing through the collimator. The collimator has a series of 50 µm slits which are separated by a distance of 400 µm, center to center. The circles in the plot on the right of Figure 5.8 are the experimental points from the confocal lateral scan whereas the solid curve is a Monte Carlo simulation of the beam through the collimator [42 - 44]. The measured profile agrees very well with simulations and highlights the high resolution that can be obtained with these Sm-doped glasses in a fluorescence confocal microscope readout. This work only considered the systematic calibration of the system for dose measurement and does not report XY scans of PL images for studying the beam shape at different energies; this will be reported in the future.

5.7 X-Ray Response Calibration Curves and Equations

The change of valence from Sm^{3+} to Sm^{2+} upon x-ray irradiation can be used as measure of the x-ray dose delivered. Previous work with Sm-doped FA and FP glasses examined the conversion of Sm^{3+} to Sm^{2+} over a wide range of doses and demonstrated the reusability of bulk doped samples by reversing the valence change from Sm^{2+} to Sm^{3+} after extended UV exposure or annealing above the glass transition temperature [27 - 35]. The glass transition temperatures for FA and FP glasses were measured to be 440 °C and 462 °C, respectively. The Sm^{3+} ions act as electron trapping centers in order to become Sm^{2+}. It appears as though the conversion process is controlled by hole trapping, since, once the glass samples have reached saturation (no further conversion to Sm^{2+}), the presence of Sm^{3+} ions can still be observed. Additionally, increasing the overall doping concentration of Sm^{3+} ions does not lead to a greater number of valence conversions to Sm^{2+}. Figure 5.9 shows the distinct and separable PL spectra and primary atomic excitation levels of Sm^{3+} and Sm^{2+} in 1% Sm doped FA glass before and after irradiation. The response *R*, as opposed to responsivity (which is response per unit input into the sensor) of a Sm-doped glass plate detector is defined as,

$$\text{Response} \equiv \frac{I_{PMT(2+)}}{I_{PMT(3+)}}_{\text{Irradiated}} - \frac{I_{PMT(2+)}}{I_{PMT(3+)}}_{\text{Non-irradiated}} \tag{5.1}$$

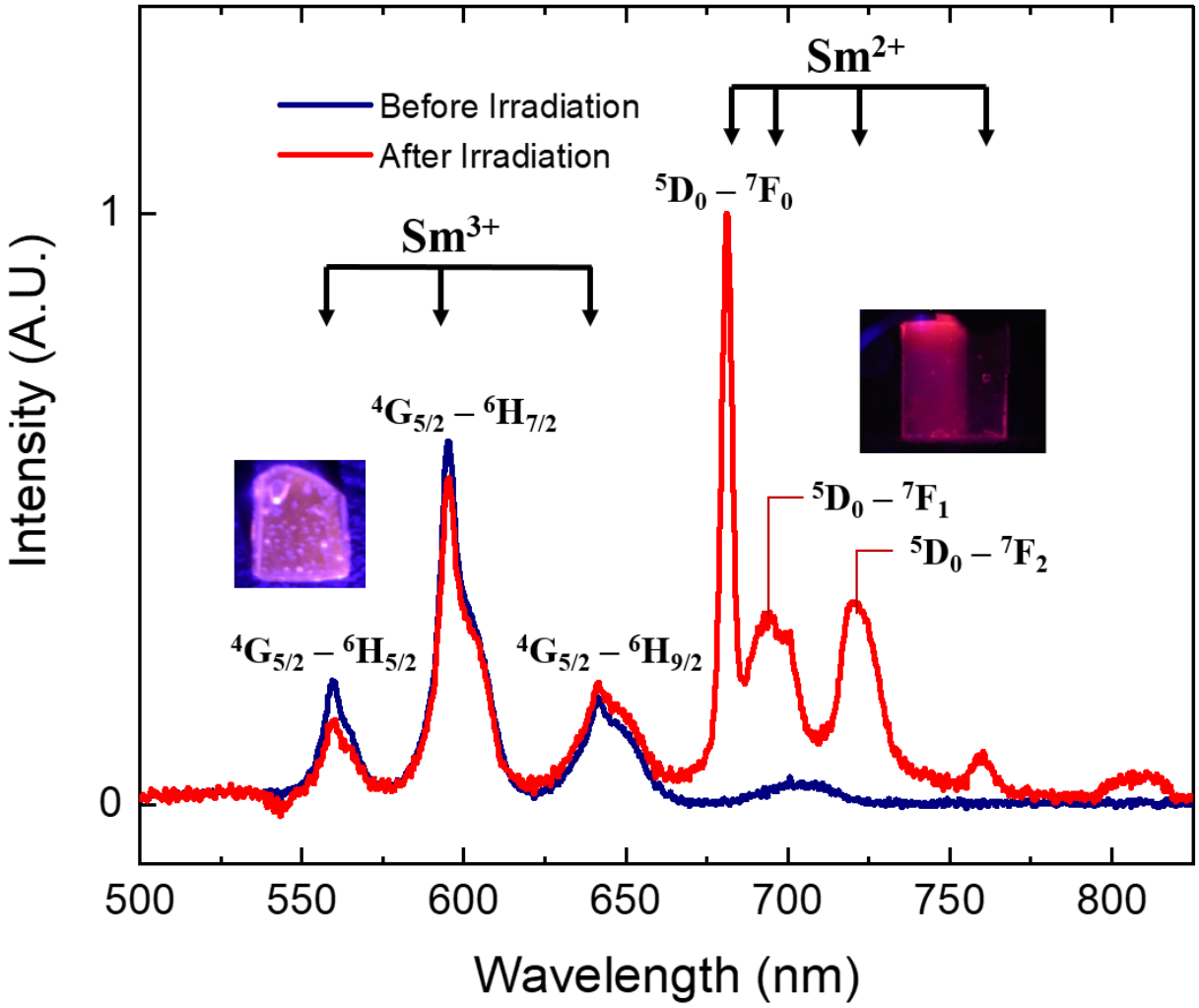

Figure 5.9 PL spectra of 1% Sm doped FA glass before and after irradiation using a FAXITRON x-ray cabinet. The emission spectra of Sm^{3+} and Sm^{2+} are shown. The sample has been irradiated with an approximate dose of 1500 Gy_{air}. The left photo is the unexposed sample under UV excitation. The right photo is a sample that has been exposed a large dose. The image of red luminescence from the exposed glass was taken using a filter that suppressed wavelengths below 660 nm.

where $I_{PMT(2+)}$ and $I_{PMT(3+)}$ are the measured signal intensities from the two photomultiplier tubes which measure the emissions from Sm^{2+} and Sm^{3+} through a 660 nm long-pass filter ($I_{PMT(2+)}$)and a 660 nm band-pass filter ($I_{PMT(3+)}$), respectively as shown in Figure 5.2. It is possible to formulate a more rigorous definition for the conversion and hence the response by examining the whole PL spectra before and after irradiation and deriving the weighting coefficients needed to combine the individual PL(Sm^{3+}) and PL(Sm^{2+}) to generate the overall spectrum from the irradiated sample as

demonstrated in [32]. This approach was not used here due to the computational times involved in finding the weighting factors as well as the distinct advantage of implementing the definition above in the hardware i.e. by using two separate PMTs with filters to capture the Sm^{3+} and Sm^{2+} emission bands. During readout there is some unavoidable bleaching of the Sm^{2+} as the result of the excitation source, thus the calculated response of the sample is taken as the average response within the 0.5 second period following the opening of the shutter.

Previous works have shown that varying the concentration of Sm dopants within the bulk sample leads to differing conversion rates of the Sm ions, most notably, the lower the concentration, the larger the number of ions converted from Sm^{3+} to Sm^{2+} and thus greater the response of the material [28,34]. It has also been shown that the host glass material plays a role in the dynamic range of the dosimeter; prior work has shown that both FA and FP glasses have

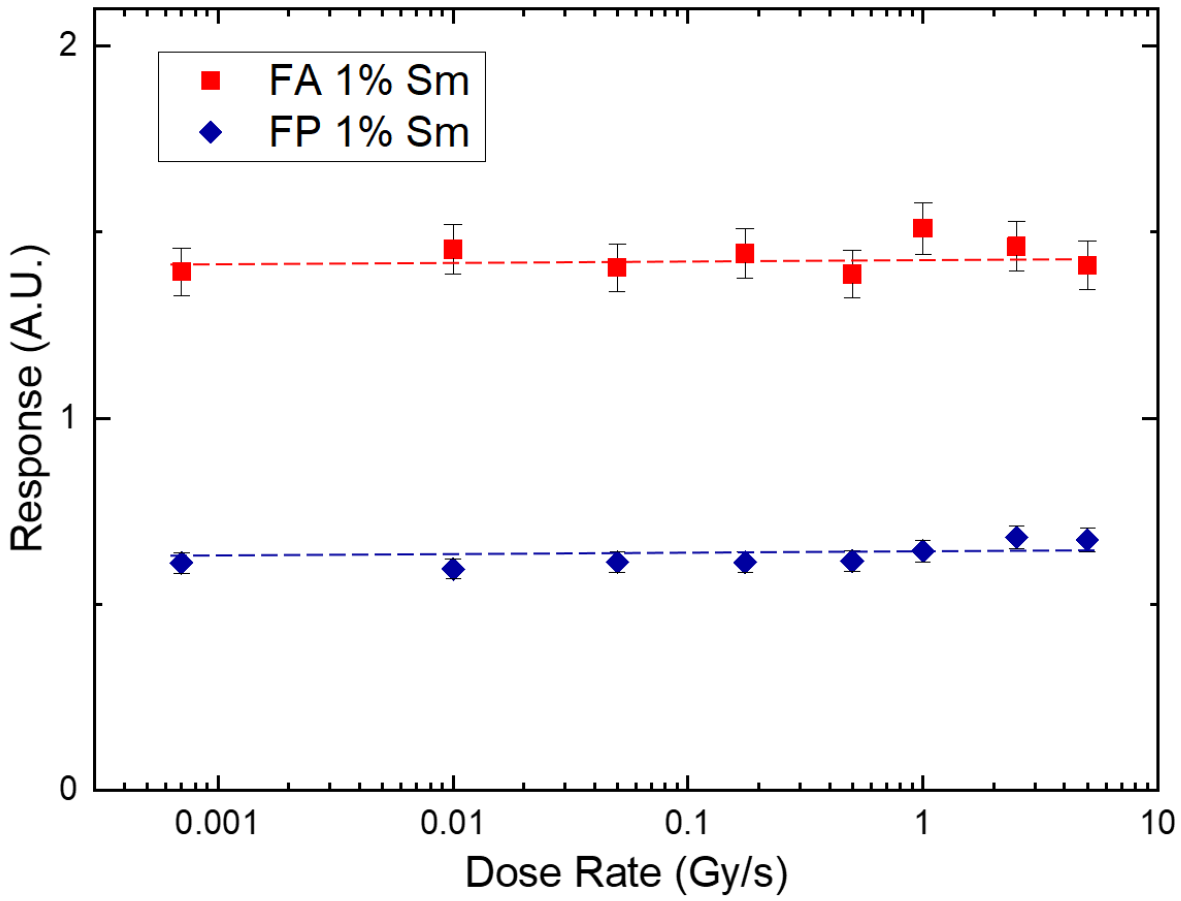

Figure 5.10 Response values (Ratio of PL(Sm^{2+})/PL(Sm^{3+})) of 1% Sm doped FA and FP glasses as a function of delivered dose rate to the sample. All samples were irradiated with a total dose of 200 Gy in air as measured by an ionization chamber with incident x-ray energy of 50 keV.

exhibited a dynamic range of 1 Gy_{air} to 10 kGy_{air} [34]. For the purposes of this research, we have investigated multiple Sm dopant concentrations embedded in two hosts, FA and FP, to study the effect of the dose rate and energy of x-rays on the conversion from Sm^{3+} to Sm^{2+}. It is also instructive to note that while FA and FP glass materials have been shown to be excellent host materials for the valance conversion of Sm-ions, photodarkening is present within the glasses after large doses have been deposited. This is particularly strong in FP glasses, which causes the transmittance to drop in the same region of wavelengths as the emission of Sm^{3+} [32]. There is a very small change in the transmission at 600 nm with x-ray irradiation in FA glasses, so the photodarkening of FA glasses was ignored. Error bars are determined by measuring the standard deviation of the response across a two dimensional uniformly irradiated glass plate. A total of 120,531 data points (response values) were measured and the standard deviation was found to be 4.57%. The latter represent the error in the response value.

The response values after irradiating 1% Sm doped FA and FP glasses over a dose rate range that covers roughly four orders of magnitude were measured. Figure 5.10 shows that there is no evidence of a dose rate dependence from the lowest (0.7 mGy_{air}/s) to the highest (5 Gy_{air}/s) dose rates available at the BMIT beamline at the CLS using monochromatic energy x-rays. It is possible to achieve higher dose rates by using a polychromatic beam, but the goal of this experiment was to show whether there is any dependence at all on the dose rate at a given energy. In all samples, the incident x-ray energy was selected to be 50 keV and the overall dose delivered was chosen as 200 Gy_{air} as measured by a high dose ionization chamber. The choice of 50 keV x-ray energy was based on peak photon flux rates at the CLS and, of course, the need to relate the present work to previous experiments at the CLS where 50 keV was used. The results from Figure 5.10 clearly show that the response R is independent of the dose rate in both of the host glass materials. This is a distinct advantage since the dose calibration curve for relating the response to the actual dose does not need to be modified for different dose rates, i.e. the calibration curve can be used under all dose rates.

The x-ray energy dependence of the response was measured for both Sm-doped glasses, FA and FP, as shown in Figure 5.11 from 35 to 130 keV. For all irradiated glasses in Figure 5.11 the dose rate was kept constant at 0.175 Gy_{air}/s and the total dose delivered was maintained at 200 Gy_{air}. Notice that there is a strong dependence on the x-ray energy as the Sm-dopant concentration

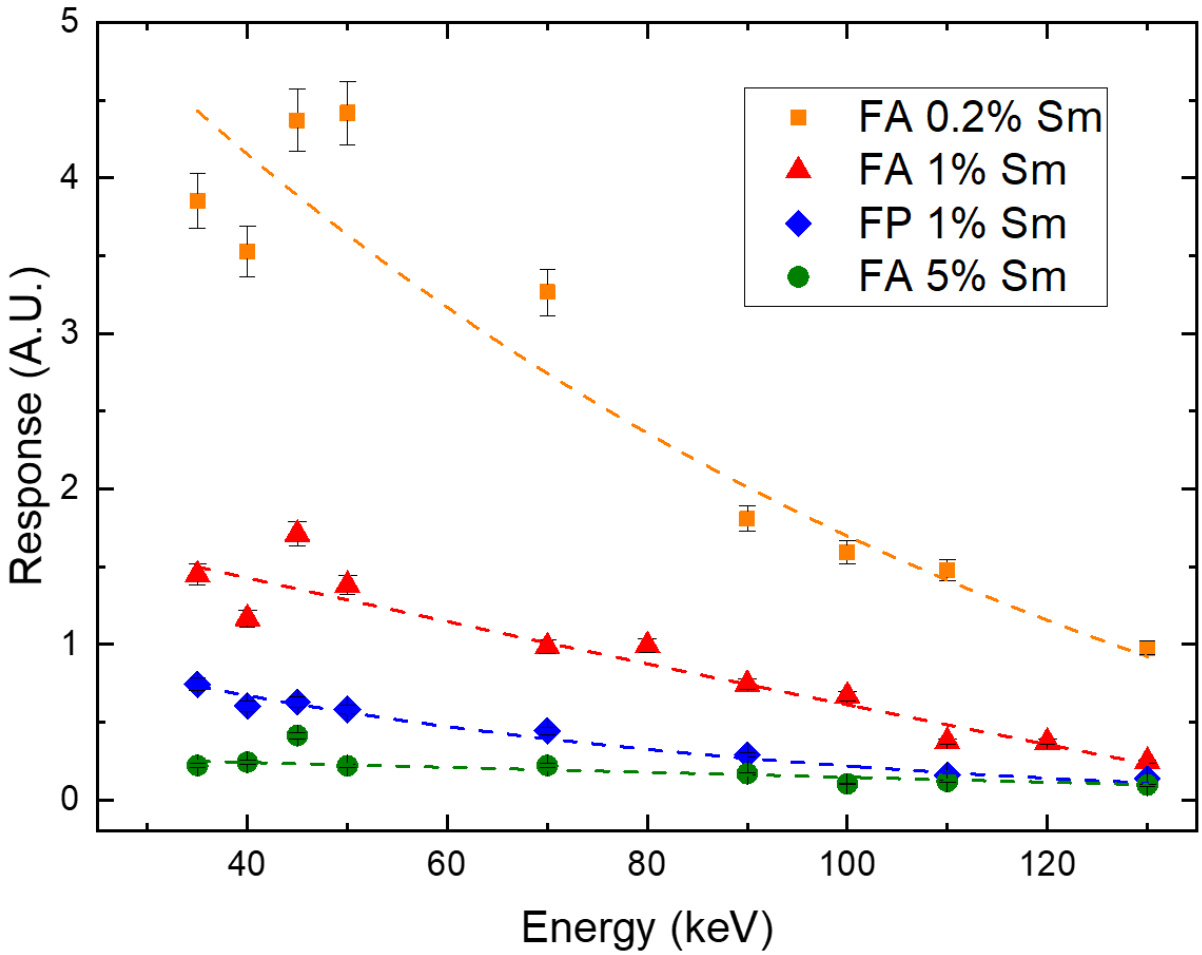

Figure 5.11 Response values (Ratio of PL(Sm^{2+})/PL(Sm^{3+})) of Sm doped FA and FP glasses. All samples were irradiated with a dose of 200 Gy in air as measured by an ionization chamber and the dose rate was set to be 175mGy/s. For all dopant concentrations and host glass materials, the response values decrease as a function of energy with the range of 35 to 130 keV. As the dopant concentration is increased the overall conversion of Sm^{3+} to Sm^{2+} decreases.

is decreased from 5% to 0.2% in FA glass. 5% Sm doped FA glass shows not only a much smaller response but also a much weaker energy dependence, while the 1% Sm doped FA glass exhibits a large response and a stronger x-ray energy dependence than that for 5% Sm. 1% Sm doped FP glass has a smaller response and a weak energy dependence.

Figure 5.12 compares the dose response curve for 1% Sm-doped FA glass with energies ranging from 40 – 120 keV. Each point on the graph corresponds to an individual piece of sample, meaning that the total dose is not an accumulative dose. Put differently, using a new sample for each dose (exposure) avoids using a single sample in multiple irradiations. These results indicate

that, for a wide range of energies, the dose delivered can be measured from a range of 5 Gy to 2000 Gy, which covers the dose range for most MRT applications. The response (*R*) vs Dose *(D)* measurements have been plotted on a log-log scale in Figure 5.12. Although the initial rise is linear, as the dose becomes larger, the linearity is lost. The simplest assumption would be a first order kinetic equation for the rate of conversion under a limited supply, which implies an exponential rise towards saturation i.e.

$$R = R_o[1-\exp(-D/D_o)] \tag{5.2}$$

where R_o and D_o are the constants. The best fit parameters of Equation 5.2 to the data in Figure 5.12 are shown in Table 5.1. It can be seen that Equation (5.2) provides a good fit to the data over

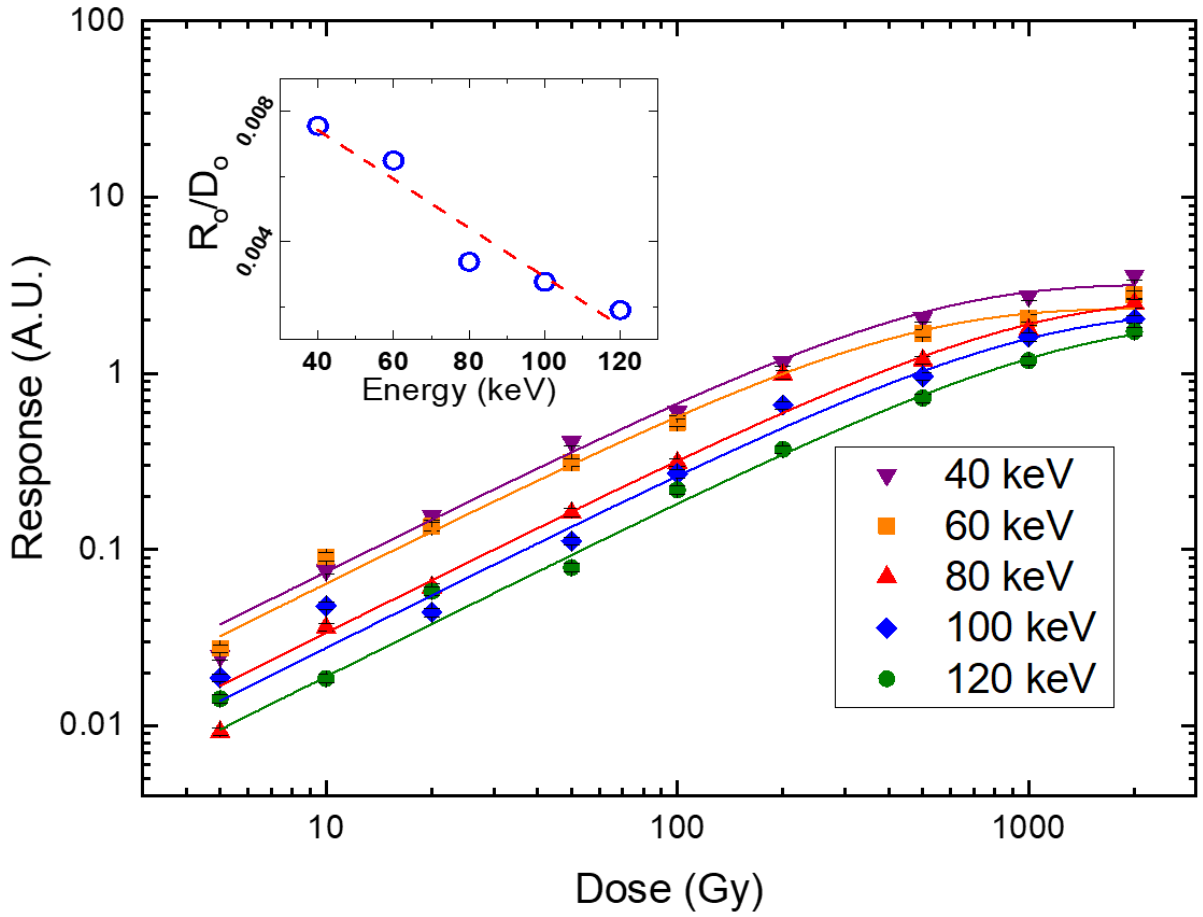

Figure 5.12 Response values (Ratio of PL(Sm^{2+})/PL(Sm^{3+})) of 1% Sm doped FA glass at multiple energies from 5 – 2000 Gy. Exponential fits are shown in Table 5.1. Each dot represents an individual piece of glass sample, that is, the dose shown is not cumulative. Equation for fitted line in the insert where R_o/D_o vs. E is plotted is $(R_o/D_o) = (0.01043 \pm 0.001) - (7.5\times10^{-5} \pm 1.18\times10^{-5})E$.

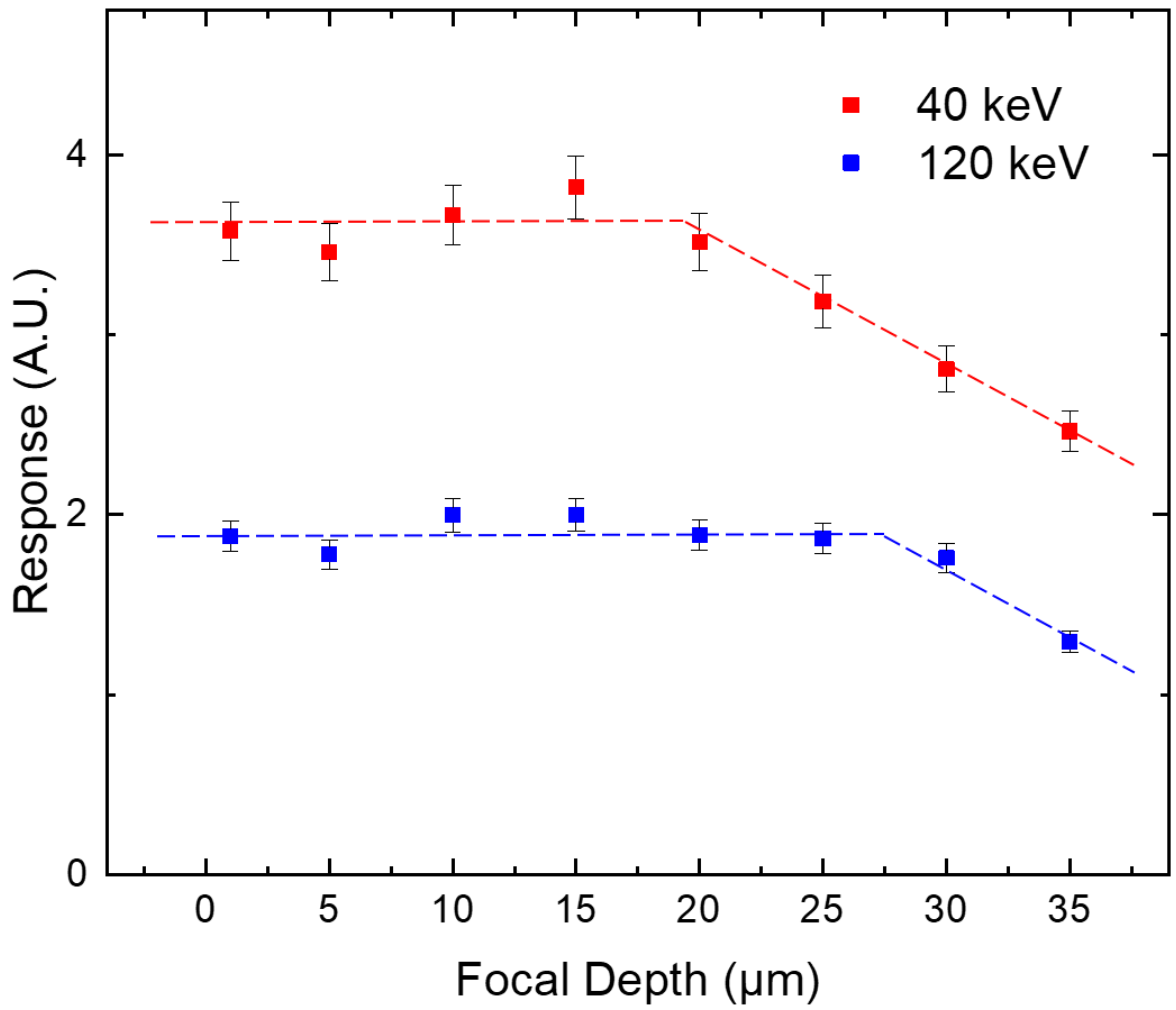

Figure 5.13 Response of irradiated 1% Sm FA glasses as the focal depth of the incident laser in the fluorescent confocal microscopy (shown in Figure 5.1) is modified at two different energies, 40 keV and 120 keV. The total dose delivered to each sample is 1 kGy using a monochromatic x-ray energy synchrotron source. As the incident x-ray energy is increased the conversion of Sm^{3+} ions to $Sm^{2+}$is constant within a larger volume in the glass material. The vertical axis is the same for both.

the whole dose range and energy range. Under low doses, $R = (R_o/D_o)D$ i.e. R is linearly proportional to the incident dose. The ratio R_o/D_o represent the slope of the initial linear rise in R vs D and hence the initial sensitivity of the detector glass. The inset in Figure 5.12 shows R_o/D_o vs. x-ray energy E and it can be seen that R_o/D_o decreases with the photon energy, which accounts for the lower dose-sensitivity at higher energies. As a point of interest, a parabolic fit was also tried in which $R = aD - bD^2$, where the second term causes the fall of R below the linear behavior as D increases. While the parabolic equation also has two constants as Equation (5.2), the fit to the parabolic equation was found to be worse. A power law fit of the form $R = AD^m$ (where A and m

are constant) yields R^2 coefficients that are worse than both the exponential and the parabolic forms. The curves in Figure 5.12 serve as the calibration curves for the 1% Sm^{3+}-doped FA glasses at different x-ray energies. We can also speculate on the saturation behavior by noting that the dose needed to reach 90% saturation $D_{90} = 2.3D_o$ which, from Table 5.1, is 2,335 Gy at 120 keV.

For all the previous figures in this work, the total focal depth from the sample surface (d) has been set to 20 μm as discussed in Section 2. However, by changing the incident energy, this can also play an important factor in the response of the Sm-doped glass material as a function of both the incident x-ray energy and the selected confocal depth. Prior published work involving Sm-doped FA glasses irradiated at the CLS had used an energy of 50 keV and a focal depth of 20 μm to measure the response values [28,34]. Figure 5.13 compares the focal depth against the response values for two x-ray energies, 40 keV and 120 keV, and shows that response can be shown to be constant as the focal depth increases up to a certain depth, depending on the incident x-ray energy, then the response decreases. Increasing the focal depth beyond 40 μm and attenuation of the emitted light within the host glass begins to affect the collection of light as well as the decrease in the Sm^{2+} concentration. These results indicate that over such a large energy range as is investigated in this paper, the energy dependence can influence the response values and requires careful attention during calibration.

As part of the work in this paper, multiple concentrations of Sm-dopants have been investigated towards characterizing the energy and dose rate dependence of FA and FP glass samples. Figure 5.10 and Figure 5.11 show that the host glass material (FA vs FP) and smaller concentrations of Sm-dopants in the host glass (0.2 to 5 % Sm) give rise to a larger conversion of Sm^{3+} to Sm^{2+} under the same irradiation conditions. An important consideration in these materials is the overall stability of the sample, that is, the response of the sample should not change between the time of irradiation and readout. Figure 5.14 shows the change in the response R of various Sm-doped glass plates as a function of time right after irradiation up to 15 days. As can be seen from Figure 5.14, the Sm-dopant concentration plays an important role in the stability of the samples. The spontaneous reconversion from Sm^{2+} to Sm^{3+} appears to be related to the availability of hole traps, since 1% Sm-doped FA glass appears to be very stable after irradiation, whereas the response of 0.2% Sm-doped FA glass appears to decrease noticeably immediately after irradiation. Regardless of concentration, it appears that the response values of all samples appear to be stable

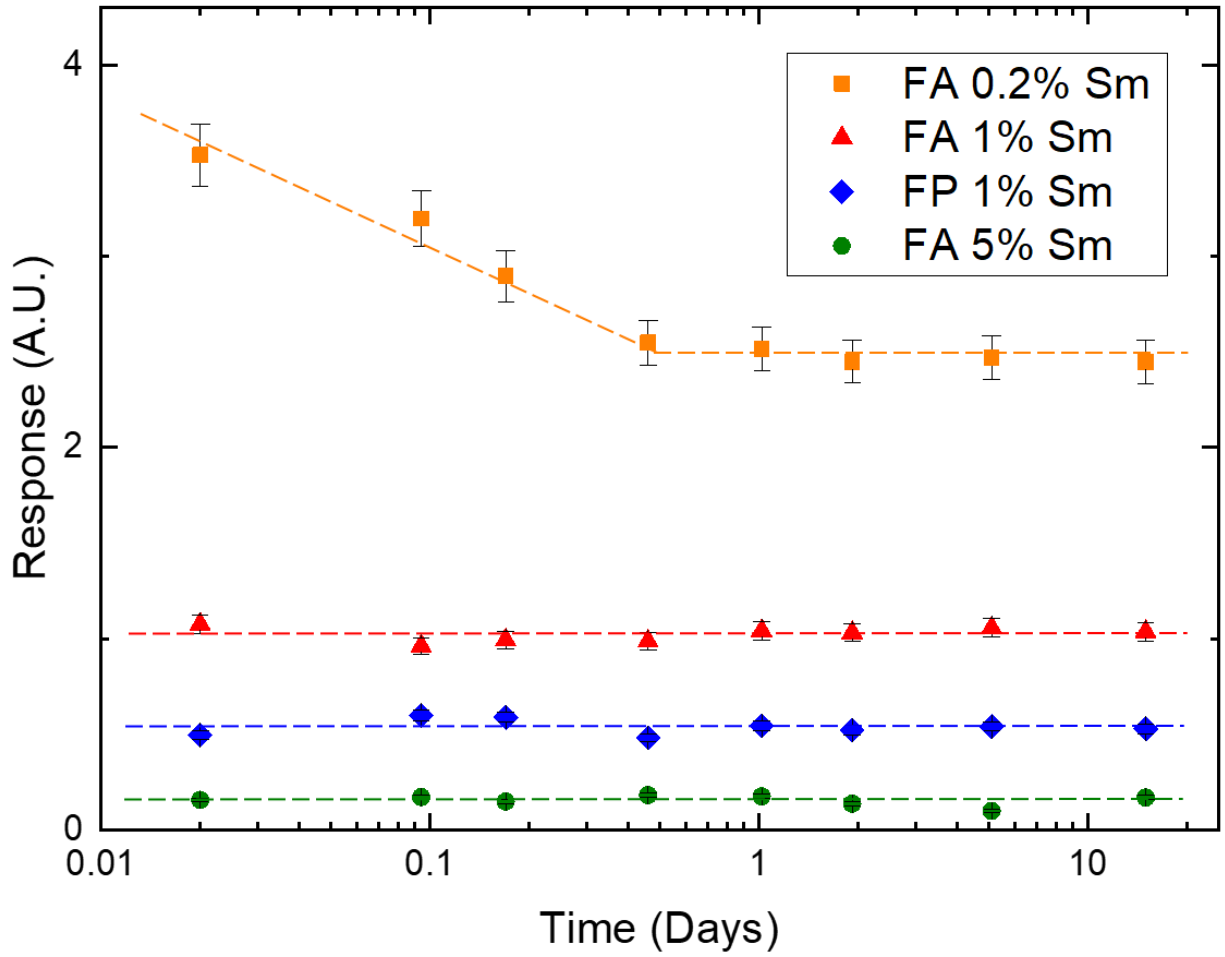

Figure 5.14 Stability of varying Sm-dopant concentrations and host glass materials over time. All samples have been irradiated with an approximate dose of 500 Gy using a FAXITRON x-ray cabinet. Each data point represents an individual sample. It appears as though lower Sm-dopant concentrations are less stable after irradiation, although all samples appear to be stable after approximately 1 day.

after 24 hours following the cessation of irradiation. The above result indicate that 1% Sm-doping is the most suitable concentration for dosimetric purposes due to the stability of the irradiated signal and the capability of detecting response values over a wide range of incident x-ray energies. While 0.2% Sm is more sensitive (Figure 5.11), its stability is worse than 1% Sm (Figure 5.14).

5.8 Discussion and Critique

Previous work with Sm-doped FA and FP glasses examined the conversion of Sm^{3+} to Sm^{2+} over large dose ranges and how these samples could be shown to be reusable through the process of UV

exposure or thermal annealing around the glass transition temperature by reconverting the Sm^{2+} ions back to their original Sm^{3+} state, demonstrating their usefulness as a dosimetric detector for MRT. Overall it has been shown that after long periods of irradiation, photodarkening is present in both FA and FP glass samples, although the changes in absorbance for FA glasses are primarily in the UV region, whereas FP glasses can become so dark that they may become of little use for high-dose dosimetry. These results confirm the findings of this research, which show that when 1% Sm-dopant FA and FP samples are exposed to identical irradiation conditions, the response values are higher for FA glasses than FP as shown in Figure 5.10, Figure 5.11, and Figure 5.14. Overall, the properties of FP glasses are better understood than those of FA glasses, which makes them useful for research purposes. FP glasses have evidence of phosphorous-oxygen hole and electron centers (POHC and POEC) which have been well studied [27], while the hole traps within FA glasses are tentatively associated with fluorine complexes and oxygen contamination [45 - 48]. The conversion of Sm^{3+} to Sm^{2+} is controlled by a hole trapping process, which is clearly evident when we compare the overall response values of FA glass samples in which the Sm-dopant concentration has been varied, as in Figure 5.10 and Figure 5.14. These indicate that the increase in the number of total electron acceptors, Sm^{3+} ions, does not lead to a higher conversion, i.e. response. This result is somewhat non-intuitive, but is apparent when comparing the response values of 0.2% and 5% Sm doped FA glasses in Figure 5.10 and Figure 5.14, which have a marked difference in response values to the same irradiation conditions. While lower concentrations lead to larger a conversion from Sm^{3+} to Sm^{2+}, there is a trade off in the stability of the sample. Figure 5.14 indicates that 1% Sm-doped FA is a stable sample that does not change after irradiation while still showing strong conversion, and is an ideal candidate for MRT dosimetry purposes.

The dose rate and energy dependence of dosimeters is an important consideration. MRT relies on adjacent healthy tissue aiding in the repair of tissue damaged from radiation. The success of MRT requires minimal movement of the patient in order to prevent "smearing" of the microbeams which would cause a decrease in the PVDR. MRT uses dose rates up to thousands of Gy/s, so the response of the detector should not change as the incident dose rate is altered. Figure 5.10 indicates that there is no evidence of a dose rate dependence resulting from the irradiation of the samples, which is an important discovery in this work. It appears that the conversion from Sm^{3+} to Sm^{2+} and the hole trapping process is not influenced by the flux of incident x-rays.

The dependence of the response on the incident dose is shown in Figure 5.12 at different photon energies. It is important to emphasize that each point represents a different sample so that the dose is not accumulated dose. Using a single sample and then carrying out measurements from one dose to the next would not necessarily represent the true response vs. dose characteristics because in the latter case the dose would be a "cumulative dose". The dependence of the response on the x-ray energy can be understood from the dependence of the actual energy deposited as the photon energy increases. Although the incident dose in air is the same for all the exposures (1 kGy in air) in Figure 5.11, the deposited energy in the FA glass decreases with photon energy because the photoelectric effect's cross section falls more rapidly with energy than the linear attenuation coefficient; around 40 keV, they are approximately the same. Consider the change in the response in Figure 5.11 from 40 keV to 130 keV. The photon fluence Φ_{ph} in the two cases are different. We can calculate Φ_{ph} from the Boone equation [49],

$$\Phi_{ph} = \frac{1}{a + b\sqrt{E}\ln E + \dfrac{c}{E^2}} \qquad [\text{photons mm}^{-2}\ \text{mR}^{-1}] \tag{5.3}$$

here E is the photon energy in keV, and $a = -5.0233\times10^{-6}$, $b = 1.8106\times10^{-7}$, $c = 0.0088387$. 1 kGy in air is equivalent to 114 kR so that Equation (5.3) at 40 keV gives $\Phi_{ph} = 2.41\times10^{15}$ photons cm^{-2}, and at 120 keV it gives $\Phi_{ph} = 2.24\times10^{15}$ photons cm^{-2}, a small difference of about 7%, The change in the fluence along with the large reduction in the energy absorption coefficient μ_{en} can provide a qualitative explanation of the energy dependence in Figure 5.11 and Figure 5.12. The attenuated photon fluence within Δz is $\mu\Phi_{ph}\Delta z$ where μ is the linear attenuation coefficient. The total energy deposited, $\Delta E_{deposited}$, into a volume within Δz from the surface per unit area (cm^{-2}) would be,

$$\Delta E_{deposited} = (\mu_{en}/\mu)(E\times10^{3}\times1.602\times10^{-19})(\Phi_{ph}\mu\Delta z) \qquad [\text{J cm}^{-2}] \tag{5.4}$$

in which the photon energy E is kept in keV. Using the photon fluence from Equation (5.3) and the appropriate values for μ_{en} for the FA glass, within 20 μm, the deposited energy at 1 kGy is 183 J cm^{-2} at 40 keV. It is smaller at 130 keV with values of 18 J cm^{-2} for the photoelectron effect and 41.3 J cm^{-2} for incoherent scattering, a total energy deposition of 59 J cm^{-2}, a decrease by a factor of 3 from 40 to 130 keV at the same dose level. One can immediately see that the difference can

qualitatively explain the reduction in the response with increasing photon energy. The deposited energy would change the concentration of structural defects created and hence the concentration of hole traps needed for the Sm^{3+} to Sm^{2+} conversion as previously discussed [27 - 34]. While the experimental results can be explained qualitatively from fundamental physical arguments, a detailed kinetic model would be needed that has multiple rate equations to predict the exact dependence, which is beyond the scope of this paper.

Ideally, the detector medium should be tissue equivalent so that the measured deposited dose is similar to dose in tissues. Tissue equivalent detectors, such as diamond detectors [18,50] are obviously very attractive in dosimetry. Unfortunately, Sm-valance conversion in glasses has only been seen in a few selected systems such as fluoroaluminate and fluotophosphate glasses, which are not tissue equivalent. Nonetheless, there is still much research interest in finding host material which are closer to being tissue equivalent.

The response of a dosimeter is generally a function of the radiation beam quality and the beam energy. For MRT purposes there is currently not a mutually agreed ideal energy for treatment purposes. Ideally, a dosimeter should not have a strong energy dependence. In practice however, when measuring an incident x-ray energy range that varies over hundreds of kiloelectronvolts, the response of a dosimeter will require calibration. The energy range can differ widely depending on the application and the target, from small animal experiments, to the eventual treatment of human patients. What is of primary importance is the incident x-ray energy range is sufficient to penetrate deep into the desired region of the tissue, the maximization of dose rate, the PVDR, and increasing the energy in order to reduce the overall dose that is deposited near the exterior of the subject, thus minimizing surface dose. Figure 5.12 indicates that a wide range of doses can be detected by 1% Sm-doped FA glass at multiple energies and is a suitable candidate for MRT purposes. Figure 5.13 indicates that at high doses (1 kGy) and lower energies such as 40 keV, the response *R* is shown to be constant within the first 20 μm of the Sm-doped FA glass samples, whereas for higher energies this does not play a significant role. The overall findings of this research illustrate that Sm-doped FA glasses, in comparison with Sm-doped FP glasses, are excellent candidates for high-dose and high-resolution applications for MRT dosimetry purposes and the optimum doping level points to 1% Sm.

5.9 Conclusions

Sm-doped Fluoroaluminate and fluorophosphates glasses have been examined for the purposes of high-dose measurements in microbeam radiation therapy (MRT) dosimetry. These samples utilize the valence conversion of Sm^{3+} ions to Sm^{2+} after irradiation as a measurement of the dose delivered. These two ions yield distinct and separable PL signals that can be detected using a fluorescence (PL) confocal microscopy system designed to separate and detect the emission wavelengths of these two ions. These Sm-doped glass detector plates were then characterized for high-dose dosimetry by investigating the detector response (defined in terms of the relative intensities of the Sm^{2+} and Sm^{3+} PL signals) as a function of the incident x-ray energy (using monochromatic x-rays at the Canadian synchrotron) as well as the dose rate and the total dose incident on the detector (up to 2000 Gy in air). Each irradiation and subsequent measurements used a new but identical sample to avoid effects arising from accumulated dose.

Energy (keV)	R_o	D_o (Gy)	R^2 Exponential fit
120	1.94 ± 0.22	1014 ± 156	0.9902
100	2.19 ± 0.27	789 ± 142	0.9723
80	2.62 ± 0.32	773 ± 128	0.9752
60	2.33 ± 0.18	359 ± 41.3	0.9840
40	3.20 ± 0.25	423 ± 43.8	0.9860

Table 5.1 The best fits of $R = R_o[1 - \exp(-D/D_o)]$ to the experimental data in Figure 5.12. R^2 is the so-called R-squared goodness of fit or the coefficient of determination.

It was found that the response of the irradiated glass plates did not show any dependence on the dose rate from 7×10^{-3} Gy_{air}/s to 5 Gy_{air}/s at 50 keV (monoenergetic x-rays). Numerous samples were irradiated with doses up to 2×10^{3} Gy_{air} and it was shown that the detector glass plates can be suitably calibrated over the large dose range accessed in this work, following an exponential behavior of the form $R = R_o[1-\exp(-D/D_o)]$ from 40 – 120 keV. The constants R_o and D_o depend on the x-ray energy and are listed in Table 5.1. They are independent of the dose rate. Under low doses, the response vs. dose behavior was linear but falls below linearity at high doses.

The dependence of the response on the focal depth *d* of the objective lens from the surface of the sample was also investigated. The optimum depth *d* was determined to be 15–20 μm. This choice of *d* was in good agreement with the vertical range determined by using a surface Sm^{2+}-ion implanted FA glass plate. The choice of *d* also minimized the photodarkening effect, which had to be included in analysis in works [32] that did not use an optical microscope and the signals had to cross the whole sample thickness of several millimeters. The lateral resolution of the optical readout technique for measuring the response of Sm-doped FA glass plates was determined to be under 1 μm. The readout technique was demonstrated to be capable of determining the microbeam profile at 50 keV at the CLS.

Various glass sample compositions were irradiated in order to select the most suitable candidate for Sm-valence dosimetry. It was demonstrated that increasing the total number of Sm-dopants leads to a smaller Sm^{3+} to Sm^{2+} conversion, while lower concentrations lead to a spontaneous reconversion of Sm^{2+} to Sm^{3+} within hours after irradiation, which is not desirable. Further, photodarkening, which has a stronger presence in FP glasses, leads to complications in the readout method as a result of the change of absorbance in the same region as the emitted Sm^{3+} signals. The consideration of these factors lead to the choice of 1% Sm-doped FA as probably the most suitable Sm-doped glass. Overall, 1% Sm-doped FA glass has shown excellent conversion of Sm^{3+} to Sm^{2+} over a wide range of doses and energies and has shown no evidence of any dose rate dependence.

5.10 Acknowledgements

We thank both the Natural Sciences and Engineering Research Council of Canada (NSERC) Discovery Grants Program and the New Zealand Ministry of Business, Innovation, and Employment. This work was also supported by The Royal Society (London) through an International Exchange Award (IE160035) and by the UK Engineering and Physical Sciences Research Council (EPSRC) Grant No. EP/N020057/2. We would like to thank Albert Hanson and Fred Geisler for their work involving the simulations of microbeams in FA glass with the MCNP radiation transport computer code. We would also like to thank Chris Varoy for his previous work on FA and FP glass samples that lead to the refinement of the glass making process. Research described in this paper was performed at the Canadian Light Source, which is supported by the

Canada Foundation for Innovation, Natural Sciences and Engineering Research Council of Canada, the University of Saskatchewan, the Government of Saskatchewan, Western Economic Diversification Canada, the National Research Council Canada, and the Canadian Institutes of Health Research.

5.11 References

[1] G. Blasse and B.C. Grabmaier, Luminescent Materials, Springer-Verlag, Heidelberg, 1997

[2] L. Boetter-Jensen, S.W.S. McKeever, A.G. Wintle, Optically Stimulated Luminescence Dosimetry, Elsevier Science B.V. Amsterdam, 2003

[3] E G Yukihara and S W S McKeever, Optically stimulated luminescence (OSL) dosimetry in medicine, Phys. Med. Biol. **53** R351 – R379 (2008)

[4] E.G. Yukihara and S.W.S. McKeever, Optically Stimulated Luminscence: Fundamentals and Applications , John Wiley and Sons Ltd, Chichester, UK, 2011 (ISBN: 978-0-470-69725-2)

[5] E. G.Yukihara, S. W.S.McKeever, M. S.Akselrod, State of art: Optically stimulated luminescence dosimetry – Frontiers of future research, Radiation Measurements, **71**, 15-24 (2014)

[6] A. Edgar, Ch: 38, Luminescent Materials in S.Kasap and P. Capper (eds), Springer Handbook of Electronic and Photonics Materials, Second Edition, Springer International Publishing AG, Cham (Switzerland), 2017

[7] R. Chen and V. Pagonis, Advances In Physics And Applications of Optically And Thermally Stimulated Luminescence, World Scientific, Singapore, 2019

[8] D. N. Slatkin, F. A. Dilmanian, P. Spanne, M. Sandborg, Microbeam radiation therapy. Med. Phys. **19**, 1395-400 (1992)

[9] R. Lewis, Medical applications of synchrotron radiation x-rays (topical review), Phys. Med. Biol. **42** 1213 – 1243 (1997), and references therein

[10] H. Blattmann, J. Gebbers, E. Bräuer-Krisch, A. Bravin, G. Le Duc, W. Burkard, M. Di Michiel, V. Djonov, D. N. Slatkin, J. Stepanek, J. A. Laissure, Applications of synchrotron x-rays to radiotherapy. Nucl. Instrum. Methods Phys. Res., Sect. A. **548**, 17–22 (2005)

[11] A. Dilmanian, Z. Zhong, T. Bacarian, H. Benveniste, P. Romanelli, R. Wang, J. Welwart, T. Yuasa, E. M. Rosen, D. J. Anschel, Interlaced xray microplanar beams: A radiosurgery approach with clinical potential. Proc. Natl. Acad. Sci. U.S.A. **103** 9709–14 (2006)

[12] C. Crosbie, R. L. Anderson, K. Rothkamm, C. M. Restall, L. Cann, S. Ruwanpura, S. Meachem, N. Yagi, I. Svalbe, R. A. Lewis, B. R. G. Williams, P. A. W. Rogers, Tumor cell response to synchrotron microbeam radiation therapy differs markedly from cells in normal tissues. Int. J. Radiat. Oncol. Biol. Phys. **77**, 886–94 (2010)

[13] E. Bräuer-Krisch, R. Serduc, E. A. Siegbahn, G. Le Duc, Y. Prezado, A. Bravin, H. Blattmann, J. A. Laissue, Effects of pulsed, spatially fractionated, microscopic synchrotron x-ray beams on normal and tumoral brain tissue. Mutat. Res. Mutat. Res. **704**, 160–6 (2010)

[14] M.A. Grotzera, E. Schültke, E. Bräuer-Krisch, J.A. Laissue, Microbeam radiation therapy: Clinical perspectives, Physica Merdica, **31**, 564 – 567 (2015)

[15] J C Crosbie, I Svalbe, S M Midgle, N Yagi, P A W Rogers and R A Lewis, A method of dosimetry for synchrotron microbeam radiation therapy using radiochromic films of different sensitivity, Phys. Med. Biol. **53**, 6861 (2008)

[16] E. Bräuer-Krisch, A. Rosenfeld, M. Lerch, M. Petasecca, M. Akselrod, J. Sykora, J. Bartz, M. Ptaszkiewicz, P. Olko, A. Berg, M. Wieland, S. Doran, T. Brochard, A. Kamlowski, G. Cellere, A. Paccagnella, E. A. Siegbahn, Y. Prezado, I. Martinez-Rovira, A. Bravin, L. Dusseau, P. Berkvens, Potential high resolution dosimeters for MRT. AIP Conf. Proc. **1266**, 89-97 (2010)

[17] M Petasecca, A Cullen, I Fudulia A Espinoza, C Porumb, C Stantona, A H Aldosari, E Bräuer-Krisch, H Requardt, A Bravin, X-Tream: a novel dosimetry system for Synchrotron Microbeam Radiation Therapy, J. Instrum. (IOP) **7,** P07022 (2012) (doi:10.1088/1748-0221/7/07/P07022)

[18] Jayde Livingstone , Andrew W. Stevenson , Duncan J. Butler, Daniel Häusermann, Jean-François Adam, Characterization of a synthetic single crystal diamond detector for dosimetry in spatially fractionated synchrotron x-ray fields, Med. Phys., **43**, 4283-4293 (2016)

[19] J. A Davis, J. R Paino, A. Dipuglia, M. Cameron, R. Siegele , Z. Pastuovic, M. Petasecca, V. L Perevertaylo, A. B Rosenfeld, and M. L F Lerch, Biomed. Phys. Eng. Express **4** 044002 (2018)

[20] J. Archer, E. Li, J. Davis, M. Cameron, A. Rosenfeld, M. Lerch, High spatial resolution scintillator dosimetry of synchrotron microbeams. Scientific Reports. **9**, 6873 (2019)

[21] E.G.Yukihara, V.H.Whitley, S.W.S.McKeever, A.E.Akselrod, M.S.Akselrod, Effect of high-dose irradiation on the optically stimulated luminescence of Al_2O_3:C, Radiation Measurements **38,** 317 – 330 (2004)

[22] D. L. Griscom, E. J. Friebele, K. J. Long, J. W. Fleming, Fundamental defect centers in glass: Electron spin resonance and optical absorption studies of irradiated phosphorus-doped silica glass and optical fibers. J. Appl. Phys. **54**, 3743-62 (1983)

[23] K. Miura, J. Qiu, S. Fujiwara, S. Sakaguchi, K. Hirao, Three-dimensional optical memory with rewriteable and ultrahigh density using the valence-state change of samarium ions. Appl. Phys.Lett. **80**, 2263-5 (2002)

[24] E. Malchukova, B. Boizot, G. Petite, D. Ghaleb, Optical properties and valence state of Sm ions in aluminoborosilicate glass under β-irradiation. J. Non-Cryst. Solids. **353**, 2397-402 (2007)

[25] A. Nag, T. Kutty, The light induced valence change of europium in Sr_2SiO_4 : Eu involving transient crystal structure. J. Mater. Chem. **14**, 1598-1604 (2004)

[26] H. Luo, A. Bos, P. Dorenbos, Controlled electron-hole trapping and detrapping process in $GdAlO_3$ by valence band engineering. J. Phys. Chem. **120**, 5916-25 (2016)

[27] S. Vahedi, G. Okada, C. Koughia, R. Sammynaiken, A. Edgar, S. Kasap, ESR study of samarium doped fluorophosphate glasses for high-dose, high-resolution dosimetry. Optical Materials Express. **4**, 1244-56 (2014)

[28] G. Okada, J. Ueda, S. Tanabe, G. Belev, T. Wysokinski, D. Chapman, D. Tonchev, S. Kasap, Samarium-doped oxyfluoride glass-ceramic as a new fast erasable dosimetric detector material for microbeam radiation cancer therapy applications at the Canadian synchrotron. J. American Ceramic Society. **97**, 1976-80 (2014)

[29] B. Morrell, G. Okada, S. Vahedi, C. Koughia, A. Edgar, C. Varoy, G. Belev, T. Wysokinski, D. Chapman, R. Sammynaiken, S. Kasap, Optically erasable samarium-doped fluorophosphate glasses for high-dose measurement in microbeam radiation therapy. J. Appl. Phys. **115**, 063107 (2014)

[30] G. Belev, G. Okada, D. Tonchev, C. Koughia, C. Varoy, A. Egar, T. Wysokinski, D. Chapman, S. Kasap, Valency conversion of samarium ions under high dose synchrotron generated x-ray radiation. Phys. Status Solidi C. **8**, 2822-25 (2011)

[31] A. Edgar, C. Varoy, C. Koughia, G. Okada, G. Belev, S. Kasap, High-resolution x-ray imaging with samarium-doped fluoroaluminate and fluorophosphate glass. Journal of Non-Crystalline Solids. **377**, 124-128 (2013)

[32] S. Vahedi, G. Okada, B. Morrell, E. Muzar, C. Koughia, A. Edgar, C. Varoy, G. Belev, T. Wysokinski, D. Chapman, S. Kasap, X-ray induced Sm^{3+} to Sm^{2+} conversion in fluorophosphate and fluoroaluminate glasses for the monitoring of high-doses in microbeam radiation therapy. Journal of Applied Physics. **112**, 073108 (2012)

[33] G. Okada, B. Morrell, C. Koughia, A. Edgar, C. Varoy, G. Belev, T. Wysokinski, D. Chapman, S. Kasap, Spatially resolved measurement of high doses in microbeam radiation therapy using samarium doped fluorophosphate glasses. Applied Physics Letters. **99**, 121105 (2011)

[34] G. Okada, S. Vahedi, B. Morrell, C. Koughia, G. Belev, T. Wysokinski, D. Chapman, C. Varoy, A. Edgar, S. Kasap, Examination of the dynamic range of Sm-doped glasses for high-dose and high-resolution dosimetric applications in microbeam radiation therapy at the Canadian synchrotron. Optical Materials. **35**, 1976-80 (2013)

[35] F. Chicilo, C. Koughia, R. Curry, R. Gwilliam, R. Ahumada-Lazo, A. Edgar, D. Binks, D. Chapman, S. Kasap, X-ray induced Sm-ion valence conversion in Sm-ion implanted

fluoroaluminate glasses towards high-dose radiation measurement. J Mater Sci: Mater Electron. 1-7 (2019)

[36] J. Izewska, G. Rajan, Chapter 3: Radiation dosimeters. Podgorsak EB, editor. Radiation oncology physics: a handbook for teachers and students. (2015)

[37] N. Kitamura, J. Hayakawa and H. Yamashita, Optical properties of fluoroaluminate glasses in the UV region J. Non-Crst. Solids, **126**, 155-160 (1990)

[38] D. Ehrt, T.Kittel, M. Will, S. Nolte, A. Tünnermann, Femtosecond-laser-writing in various glasses. J. Non-cryst. Solids. **345-346**, 332-7 (2004)

[39] J. Livingstone, A. W. Stevenson, D. Häusermann, J.-F. Adam, Experimental optimisation of the X-ray energy in microbeam radiation therapy, Physica Medica, **45**, 156 – 161 (2018)

[40] J. Punnoose, J. Xu, A. Sisniega, W. Zbijewski and J. H. Siewerdsen Technical Note: spektr 3.0—A computational tool for x-ray spectrum modeling and analysis Med. Phys. **31** 3057–67 (2016)

[41] A. Lipson, S. G. Lipson, H. Lipson, Chapter 12: Image formation. Cambridge University Press. Optical Physics. (2018)

[42] F. Salvat, M. Fernández-Varea, and J. Sempau, PENELOPE, a code system for Monte Carlo simulation of electron and photon transport. NEA Data Bank, Workshop Proceeding. 4-7 (2003)

[43] A.L. Hanson, F.H. Geisler, Microbeam Advancement, Inc. and Copernicus Dynamics, Inc., To be published

[44] T. Goorley, M. James, T. Booth, F. Brown, J. Bull, L. Cox, Initial MCNP6 Release Overview - MCNP6 version 1.0. Nuclear Technology. **180**, 298-315 (2012) DOI: 10.13182/NT11-135

[45] J. Qiu, K. Miura, T. Suzuki, T. Mitsuyu, Permanent photoreduction of Sm^{3+} to Sm^{2+} inside a sodium aluminoborate glass by an infrared femtosecond pulsed laser. Appl. Phys. Lett. **74**, 10-12 (1999)

[46] Bocharova T V, Karapetyan G O, Mironov A M, Mishchenkov N M and Tagil'steva N O 2006 Irradiation induced and postirradiation processes in fluoroaluminate glasses Inorg. Mater. **42** 671–80

[47] Griscom D Defect centers in heavy-metal fluoride glasses: a review J. Non-Cryst. Solids, **161,** 45–51 (1993)

[48] L. Ruihua, W.Haobing, G. Fuxi, ESR study of temperature dependence of colour centers in γ-ray irradiated fluoride glasses J. Non-Cryst. Solids. **140**, 194-8 (1992)

[49] J.M. Boone, X-ray production, interaction, and detection in diagnostic imaging Handbook of Medical Imaging vol 1 ed J Beutel, H L Kundel and R L Van Metter (Bellingham: SPIE Press, 2000) Chapter 1, pp 1–78, Equation 1.22b.

[50] B. Górka, B. Nilssona, R. Svensson, A. Brahme, P. Ascarelli, D.M. Trucchi, G. Conte, R. Kalish, Design and characterization of a tissue-equivalent CVD-diamond detector for clinical dosimetry in high-energy photon beams2000 X-ray production, interaction, and detection in diagnostic imaging Handbook of Medical Imaging, Physica Medica, **24 (**2008), 159-168

Chapter 6

Dose Profiles and X-ray Energy Optimization for Microbeam Radiation Therapy by High-dose, High-resolution Dosimetry Using Sm-doped Fluoroaluminate Glass Plates and Monte Carlo Transport Simulation

Submitted as:

Farley Chicilo, Al Hanson, Fred Geisler, George Belev, Andy Edgar, Kieran Ramaswami, Dean Chapman, and Safa Kasap. "Dose profiles and x-ray energy optimization for microbeam radiation therapy by high-dose, high resolution dosimetry using Sm-doped fluoroaluminate glass plates and Monte Carlo transport simulation" *Phys. Med. Biol.* **65**, 075010 (Accepted February 6th , 2020) https://doi.org/ 10.1088/1361-6560/ab7361

Author contributions:

The main experimental work, data analysis, and manuscript preparation in this work was performed by Farley Chicilo. Al Hanson performed MCNP6 simulations of radiation interactions within this work for verification purposes. George Belev, Fred Geisler, and Al Hanson were present during irradiations performed at the CLS and assisted with experiments. Andy Edgar synthesized samples used in this work. Kieran Ramaswami assisted in this work by providing a MATLAB code that performed rotational calculations before averaging two dimensional images into one dimensional profiles. Andy Edgar, Dean Chapman, Safa Kasap, Fred Geisler, and Al Hanson offered comments and suggestions for improving the manuscript.

6.1 Abstract

Microbeam radiation therapy (MRT) utilizes highly collimated synchrotron generated x-rays to create narrow planes of high dose radiation for the treatment of solid tumors. Individual microbeams have a typical width of 30 to 50 μm and are separated by a distance of 200 to 500 μm.

The dose delivered at the center of the beam is lethal to cells in the microbeam path, on the order of hundreds of Grays (Gy). The tissue between each microbeam is spared and helps aid in the repair of adjacent damaged tissue. Radiation interactions within the peak of the microbeam, such as the photoelectric effect and incoherent (atomic Compton) scattering, cause some dose to be delivered to the valley areas adjacent to the microbeams. As the incident x-ray energy is modified, radiation interactions within a material change and affect the probability of interactions, as well as the directionality and energy of ionizing particles (electrons) that deposit energy in the valley regions surrounding the microbeam peaks. It is crucial that the valley dose between microbeams be minimal to maintain the effectiveness of MRT. Using a monochromatic x-ray source with x-ray energies ranging from 30 to 150 keV, a detailed investigation into the effect of incident x-ray energy on the dose profiles of microbeams was performed using samarium doped fluoroaluminate (FA) glass as the medium. All dosimetric measurements were carried out using a purpose-built fluorescence confocal microscope dosimetric technique that used Sm-doped FA glass plates as the irradiated medium. Dose profiles are measured over a very a wide range of x-ray energies at micrometer resolution and dose distribution in the microbeam are mapped. The measured microbeam profiles at different energies are compared with the MCNP6 radiation transport code, a general transport code which can calculate the energy deposition of electrons as they pass through a given material. The experimentally measured distributions can be used to validate the results for electron energy deposition in fluoroaluminate glass. Code validation is necessary for using transport codes in future treatment planning for MRT and other radiation therapies. It is shown that simulated and measured micro beam-profiles are in very good agreement, and micrometer level changes can be observed using this high-resolution dosimetry technique. Full width at 10% of the maximum peak (FW@10%) was used to quantify the microbeam width. Experimental measurements on FA glasses and simulations on the dependence of the FW@10% at various energies are on good agreement. Simulations on energy deposited in water indicate that FW@10% reaches a local minimum around energies 140 keV. In addition, variable slit width experiments were carried out at an incident x-ray energy of 100 keV in order to determine the effect of the narrowing slit width on the delivered peak dose. The microbeam width affects the peak dose, which decreases with the width of the microbeam. Experiments suggest that a typical microbeam width for MRT is likely to be between 20 – 50 μm based on in this work.

6.2 Introduction

Microbeam radiation therapy (MRT) is a cancer treatment technique that utilizes synchrotron radiation to deliver large doses in narrow, parallel, and segmented planar microbeams to solid tumors. Irradiated healthy tissue has shown the ability to quickly repair adjacent damaged tissue, whereas tumors have not shown this ability and take much longer to recover [1 - 11]. In MRT low divergent, highly collimated x-rays pass through a multi-slit collimator (MSC) which segments the x-rays before it is delivered to the patient. The planar beams involved in MRT can have a width that is typically of the same scale as a human cell, ranging from 20 to 50 μm, and are separated by a distance of several healthy cells, approximately 100 to 400 μm, center-to-center distance. This results in regions of high dose, commonly referred to as "peaks", interspaced with regions of low dose, commonly referred to as "valleys". The dose delivered in the valleys is due to x-rays scattering, along with ejected electrons from the atoms, which diffuse away from the area of incident irradiation, depositing energy as they slow down in the tissue.

The peak-to-valley dose ratio (PVDR) is of major importance to the success of MRT. The dose delivered must be maximized within the center region of the planar beams, while the sections between these beams requires minimal energy deposition in order to exploit the therapeutic effect of MRT. The difference between the "peak" dose and the "valley" dose can vary by thousands of Grays (Gy) over a distance of micrometers, and the dose distribution can be affected by the incident x-ray energy. Currently there is not a consensus regarding the ideal energy for clinical MRT, though, depending on the application and irradiation geometry, predicted energy ranges are between 90 – 300 keV [12 - 14]. Radiation interactions within the regions of the microbeam lead to dose being deposited outside this area, into the surrounding valley region, referred to as "tails". The probability of radiation interactions within a material are energy dependent; within the energy range of interest for MRT, these interactions consist of the photoelectric effect, which dominates at lower energies, and atomic Compton scattering, which dominates at higher energies. Not only can the x-ray interactions within a given material change as a function of energy, but also the direction and distance travelled by the ionizing particles, which deposit dose and change the beam characteristics. These interactions are not simple to predict and can lead to the undesirable extending of the width of the microbeam into the valley region. The extended portion of the

microbeam beyond its original shape defines the so-called "tail" of the microbeam. The experimental measurement of the effect of incident monochromatic x-ray energies and the resulting radiation interactions on the dose distributions is examined within this paper. These interactions lead to the prediction of ideal energies that would minimize the extending tails, which are characterized by measuring the full width at various values of the maximum peak dose value. The quality of the beam is related to these measured width values and should be considered along with the PVDR. The exact width value to utilize in human clinical medicine would need to be determined by the biological response of both the specific tumor and the adjacent normal tissue to the microbeam radiation treatment. The potential biologic variability resulting from radiation dose delivered to the regions adjacent to the microbeam serves as motivation for investigating the shape of the "tails" in detail.

The accurate measurement and characterization of the dose distribution delivered by a microbeam is critical to the success of MRT. A detector must be able to simultaneously measure a dose range that includes low (valley) and high (peak) doses over a distance of micrometers with sufficient resolution. Ultimately, a two-dimensional cross-sectional image of the microbeam should be obtained in order to accurately measure the characteristics of the beams. Multiple techniques have been discussed for the purposes of MRT dosimetry including Gafchromic films, MOSFET detectors, and silicon strip detectors amongst others [15 - 19]. Extensive research has shown that valence conversion of rare earth ions, if embedded in a suitable host, can be used to measure various forms of excitation, such as x-rays, β and γ-irradiation, and photoexcitation [20 - 24]. Samarium is a rare-earth that has two common valences, Sm^{3+} and Sm^{2+}. Samarium has a particular advantage inasmuch as the distinct photoluminescence (PL) signatures of Sm^{3+} and Sm^{2+} ions can be easily distinguished, and emit in the orange and red visible spectral regions, which are well suited for detection by sensitive photomultiplier tubes. The dose delivered to the sample can be readily measured by detecting the amount of conversion of ions from the trivalent state (Sm^{3+}) to the divalent state (Sm^{2+}). The conversion process strongly depends on the host material. Previous research has demonstrated that fluoroaluminate (FA) glasses have shown excellent conversion of these ions over a large dose range, and can be used to measure microbeam profiles with a resolution on the order of micrometers [25 - 34]. Additionally, it has been shown that if the concentration of Sm^{3+} within the glass composition is too high, valence conversion is minimal.

Conversely, if the Sm concentration is too low, it can cause the spontaneous reconversion of Sm^{2+} back to Sm^{3+}. Overall, it was found that Sm 1% FA glass shows strong conversion with excellent stability and is an ideal candidate for MRT dosimetry; therefore this concentration is used throughout the paper to maintain good sensitivity and stability [34]. Measurement of the PL from Sm^{3+} and Sm^{2+} ions in irradiated FA glass samples are done using a custom fluorescence confocal microscopy detection system that is tuned to the emission wavelengths of these ions. The confocal microscopy system collects a high-resolution, two-dimensional image, which can be transformed into a one-dimensional profile by averaging along the axis of the microbeam. These resulting beam profiles allow for the measurement of small changes in the overall shape of the beam that result from the modification of the incident x-ray energy.

The change in the beam profile due to the photoelectric effect and Compton scattering can be modeled using a Monte Carlo transport code, such as GEANT, EGS, PENELOPE or MCNP. These codes have been used to simulate the photon and electron transport and deposited dose distributions within a selected material. Indeed, MC simulations have been used as a way of optimizing MRT conditions [35 - 45]. Use of a code determines how contributions from the photoelectric effect and scattering affect the beam profile at multiple energies by assuming a monochromatic, collimated x-ray energy source. Simulations using MCNP6 have been performed in both Sm-doped FA glass and in water, the latter of which can be used as an approximation for human tissue. Small changes resulting from the dose deposited by ejected and scattered electrons and photons cannot be accurately measured in tissue; however, the beam profiles in Sm-doped FA glass can be measured with a resolution at the micrometer level, which can be used to verify the MCNP6 code calculations for dose distributions. In this paper we show that the predicted and measured changes in the beam-shape are in very good agreement and that the MCNP6 code can be used to predict optimization conditions for therapeutic purposes.

The aim of this work is to demonstrate that the spatial resolution and dynamic range of Sm doped FA glasses allows for the verification of MCNP6 simulations of absorbed dose, including the effects of photoelectrons and Compton scattered electrons, in materials. This will aid in the optimization of treatment planning for MRT. The results show that the experimental measurements performed over the available energy range (30 keV to 150 keV) at the Biomedical Imaging and

Therapy (BMIT) beamline at the Canadian Light Source (CLS) are in good agreement with simulated results. In addition to the incident energy playing an important factor for treatment purposes, the selection of the microbeam width is critical in order to utilize the desirable tissue sparing effect associated with MRT. Increasing the microbeam width can lead to the decrease of the tissue sparing effect [40,45 - 49]. However, if the slit width is decreased significantly, MCNP6 transport codes show that the maxima of the peak is decreased. Put differently, as the slit is narrowed, the fraction of electrons ejected from within the beam interacting with the target material results in dose distributions with significant top rounding and decreasing maxima of the central peak. This decrease in peak dose intensity is related to the dose deposited into the tails, because the peak radiation becomes "spread"; the ratio of dose in the tails compared to the dose in the peak region increases greatly with small slit widths (<20μm). The variable slit width simulations are verified by experimental results. The findings in this paper compare the experimental and measured values of slits with variable width at 100 keV. It should be mentioned in passing that while the beam width is a critical issue towards the success of MRT, microbeam separation is also an important factor as highlighted in [6,9,50].

Currently MRT is not available for human clinical trial stages; the optimization of treatment conditions is of critical importance before trials can be attempted. It is known that the dose deposited between microbeams reduces the overall desirable effects of MRT and it has been shown that dose in the valley regions has a greater influence on tissue response when compared to the peak regions [51 - 53]. By using Sm-doped FA glass plates we can measure changes on the order of micrometers that show the energy deposited by the ionization of ejected electrons and scattering from photons cause dose to be deposited away from the region of initial irradiation. Importantly, these regions show significant change as a function of the monochromatic incident x-ray energy. The findings of this paper show that the experimentally measured microbeam dose distributions in FA glass closely match simulations performed by MCNP6 code. In practice, most MRT treatment involves polychromatic energy sources in order to maximize the dose rate delivered to a patient, however, the understanding of interactions at single energies is important in the guiding of treatment planning as well as understanding the basic processes. Polychromatic energy sources can be easily modeled as a linear combination of spectrum of individual energies.

The experimental verification of this code demonstrates the high level of confidence that can be placed in the predictions of these simulations in biomaterials, such as human tissue.

6.3 Experimental Procedure

The synthesis of fluoroaluminate glasses was carried out by using a melt quenching technique which has been described previously [25-34]. Starting materials were mixed in a dry nitrogen atmosphere and loaded in a carbon crucible which was then loaded into a RF furnace at 1000 °C and held at that temperature for 120 minutes. The glass was then quenched on a temperature controlled plate at 380 °C and annealed for 8 hours in an argon atmosphere to prevent cracking. The composition for the glass in molar percentage is 10.0 MgF_2 – 35.0AlF_2 – 20.0CaF_2 – 10.0SrF_2 – 14.0YF_3 – 10.0BaF_2 – 1.0SmF_3. After samples were synthesized, they were cut into approximately 2 mm by 3 mm pieces and polished to optical quality prior to irradiation.

Samples were irradiated at the Biomedical Imaging and Therapy (BMIT) 05ID-2 beamline at the Canadian Light Source (CLS, the Canadian synchrotron). The facilities at the BMIT beamline allows for the selection of monochromatic x-rays using a double crystal bent Laue monochromator that can be tuned from 30 to 150 keV with a resolution ($\Delta E/E$) of 10^{-3}. Previous work with 1% Sm-doped FA glass has shown that there is no dose rate dependence to the response of the material, so the maximum available incident dose rate was selected in order to perform experiments in a timely manner [34]. The total dose delivered to the sample was measured by a high dose rate ionization chamber (model 31022 PTW-Freiburg). The response of the FA glass to radiation has been shown to be energy dependent [34] so samples irradiated with 30-90 keV x-rays received a total of 200 Gy_{air}, and those irradiated with 100-150 keV x rays received doses of 1000 $Gy_{air.}$ The doses delivered with the 100-150 keV x-rays were chosen so as to maintain appropriate signal-to-noise ratios at the higher energies. All beam profiles are normalized to their measured maximum response value. Samples were irradiated in the dark and wrapped in aluminum foil until readout experiments were complete.

Two sets of investigations are described here. The first investigation of the change of beam-shape as a function of incident x-ray energy was performed at the CLS using a MSC. X-ray exposures were done using a spatially broad beam irradiation, which passes through an MSC with

75 total slits with a width of 50 μm and a center-to-center spatial periodicity of 400 μm. The tungsten collimator was manufactured by Usinage et Nouvelles Technologies and the length of each tungsten slit is 8 ± 0.05 mm. Samples were placed a distance of 25 cm behind the MSC in the center of the beam for uniform irradiation conditions at individual microbeams.

The second investigation examined distributions created by a single slit of varying width. For these measurements, tungsten alloy blocks with a thickness of 4 cm were polished to a mirror finish. After the tungsten blocks were polished, spacers were used to adjust the slit width ranging from 7.8 μm to 110 μm. The samples were irradiated at an energy of 100 keV with a total dose of 400 Gy_{air} as measured by an ionization chamber. The MSC and tungsten blocks were aligned using a rotational and translational stage and were rotated until a maximum fluence was measured using a (Hamamatsu) AA60+CCD detector.

After irradiation, samples were mounted on a microscope slide and read out using a custom confocal fluorescence microscopy readout system, which has been described in detail elsewhere [34]. A modified confocal microscope (MultiProbe 2001 TM CLSM, Molecular Dynamics) serves as a measurement apparatus, and uses a 473 nm diode-pumped solid-state laser as an excitation source. Upon excitation, Sm^{3+} and Sm^{2+} ions emit distinct and separable PL signals, which are guided from an objective lens and then collected by a pair of photomultiplier tubes (PMTs) tuned to each ion's emission signal. The Sm^{3+} and Sm^{2+} emissions are separated using a 650 nm dichroic mirror that splits the signals into two beams that are steered towards two PMTs fronted with a 600 nm filter (595 - 615 nm FWHM), and a 660 nm filter (660 – 720 nm FWHM), respectively. The PL spectra of Sm^{3+} and Sm^{2+} ions are shown in Figure 6.1. A two-dimensional image of the Sm-doped glass plates is recorded using a galvo mirror which raster-scans the surface of the glass within the field of view of the objective lens. To achieve the high-resolution scans used in this paper, single microbeams had to be measured. Focal depth of the incident laser is set to be 20 μm from the surface of the glass which allows for a larger PL signal collection without attenuation from the glass itself.

Once the samples have been measured and digitized from the fluorescent confocal microscope system, a background subtraction is performed using an unirradiated sample with the

same dimensions in the x and y directions. The intensity for an individual point within a two dimensional image is then calculated as,

$$\text{Response}\ (x_i, y_i) \equiv \left.\frac{I_{PMT(2+)}}{I_{PMT(3+)}}\right|_{\text{Irradiated}\ (x_i,y_i)} - \left.\frac{I_{PMT(2+)}}{I_{PMT(3+)}}\right|_{\text{Non-irradiated}\ (x_i,y_i)} \quad (6.1)$$

where $I_{PMT(2+)}$ and $I_{PMT(3+)}$ are the measured signals at coordinates x_i, y_i from the PMTs which are tuned to the emission wavelengths of Sm^{2+} and Sm^{3+} ions respectively. After the background subtraction has been performed, the section around an individual microbeam is cropped and rotated. In order to average the two-dimensional image into a one-dimension profile, the image is rotated using a custom MATLAB program. This program fits a first order Gaussian across the cropped section of the measured image and measures the full width at half maximum (FWHM) as a function of rotational angle in steps of 0.01° until a minimum value is found. After the image has been rotated, the profile is averaged along the microbeam that is parallel to the y-axis. An example of a microbeam after cropping and rotation is applied is shown in Figure 6.2.

Uncertainty in the measured values were determined using a uniformly irradiated Sm-doped glass plates. Multiple samples were irradiated with a total dose of 240 Gy_{air} at an energy of 50 keV, and each sample was vertically scanned through the beam ten times at a speed of 1 mm/s to ensure the total dose delivered was constant across the sample. After irradiation, samples were readout using the confocal microscopy system, a background subtraction was performed, and all uniformly irradiated Sm –doped glass plates were averaged in order to remove errors related to glass defects that may be present. Overall, nine uniformly irradiated Sm-doped glass plates were averaged. The resulting response value across the field of view should be constant. However, when evaluating the response across the field of view, there was an observed standard deviation of 4.57% across 120,531 data points. The error bars of measured values used throughout this paper are taken from this deviation in the measurement procedure.

The measured dose distributions have been compared to dose distributions calculated using the MCNP6 computer code [54]. MCNP6 is a generalized radiation transport computer code developed at Los Alamos National Laboratory for the nuclear weapons program. The software

development was initiated in 1957and continuously updated and improved through the decades and years with the latest updated version of 6.2 in January 2018. Because it is a general radiation transport code that can model complicated geometries and can follow multiple radiation particles, it has become widely used for modeling nuclear reactors, particle accelerator interactions and for medical physics applications [35,36,41]. The original MCNP only followed neutrons and photons, but the present 6.2 version supports the transport of various particles, including electrons and photons. Electron transport is important, since photon interactions within matter results in the ejection of energetic electrons from the atoms. Those electrons passing through matter deposit energy as radiation dose away from the point of the initiating interaction between the irradiating beam photon and target electron interaction.

For these calculations, the default cutoff minimum energy of 1 keV was used for both photons and electrons. This cutoff means that when a particle's energy is reduced to 1 keV or below, the particle is eliminated from the calculation and the remaining energy is deposited at that point. A computational cutoff energy of 1 keV has been shown to be appropriate for calculations such as this [55,56].

Two sets of calculations were performed, one with a multi-slit collimator (MSC) having 75, 50 μm wide slits spaced every 400 μm and the other set being a single slit of a variable width: 7.6, 15.2, 22.8, 50.8, and 110 μm. For the simulations with the MSC, the source was modeled as being 0.4 cm wide and 2 cm high and for the single slit calculations the source width was set at 100 μm wide and 2 cm high for the 7.6, 15.2, 22.8, and 50.8 μm slit widths and 520 μm wide by 2 cm high for the 110 μm slit width. All simulation models used tungsten collimators downstream of the source, duplicating the experiments. The divergence of the CLS beam in this experimental setup is 0.2 milliradians in the vertical direction and 4 milliradians in the horizontal direction and because of this small divergence compared to the length of the collimators, it was set to zero for these calculations. However, this simulation allows for scattering of x rays by the tungsten collimators. The calculations with the MSC used 2×10^{10} source photons; the single slit calculations with the 100 μm wide source used 5×10^{9} source photons and the single slit calculation with the 520 μm wide source used either 1×10^{10} or 2×10^{10} source photons depending

on the statistics. The uncertainty in the calculated peak dose as provided by MCNP was maintained in the 0.1-0.3% range.

The composition of the glass, as provided in the beginning of Section 2, was assumed to be uniform with a density of 3.74 g/cm^3. The dose distributions within the glass were calculated within the first 20 μm from the surface, the focal depth of the conformal microscope. Dose distributions were calculated along the horizontal plane ("*x*" direction) with data tallied every 1 μm. This was accomplished with the MESH tally feature of MCNP6 which allows a computational grid to be laid over the volume of interest without specifically dividing the sample into discrete cells.

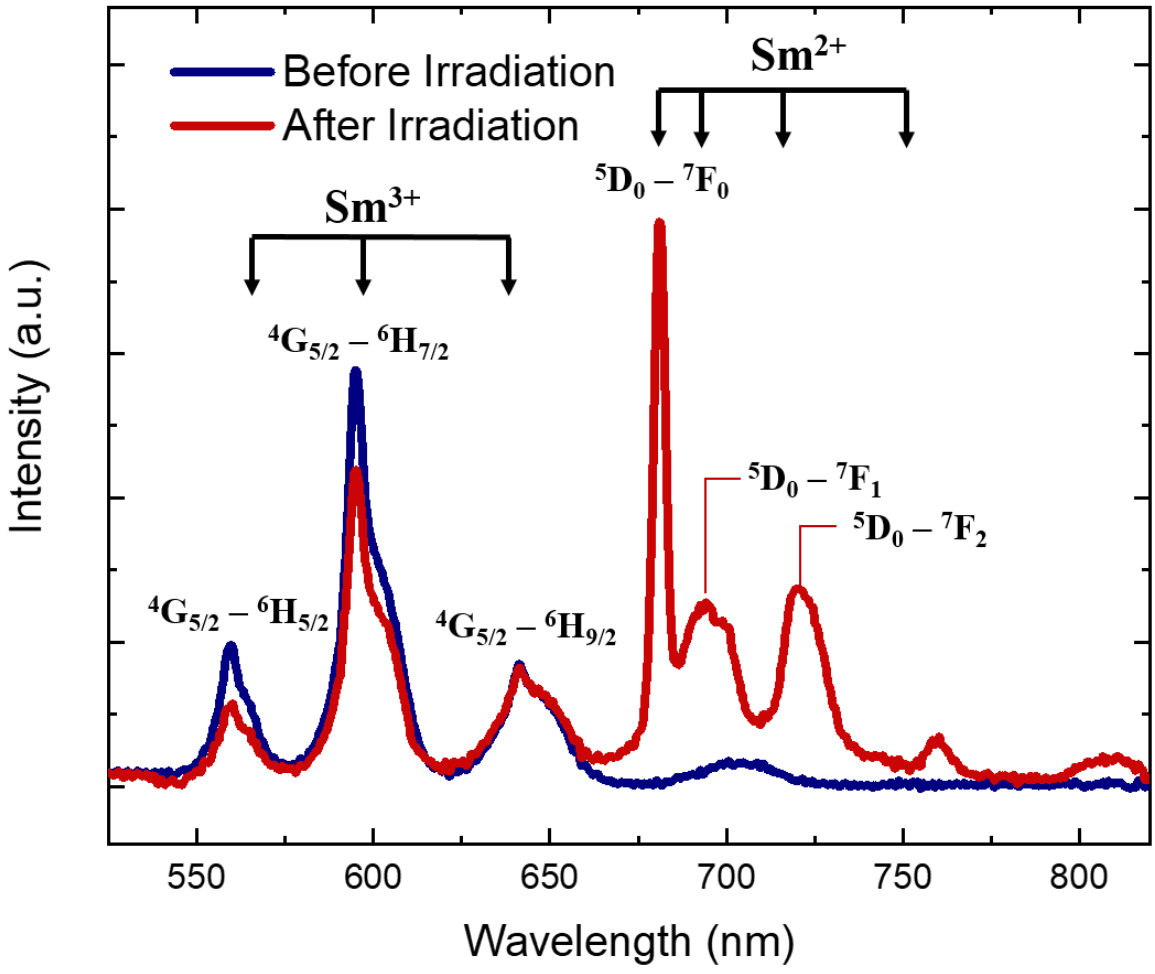

Figure 6.1 PL spectra of irradiated (red) and non-irradiated (blue) 1% Sm FA glass which shows the presence of Sm^{2+} ions after x-ray exposure (data taken from [34]).

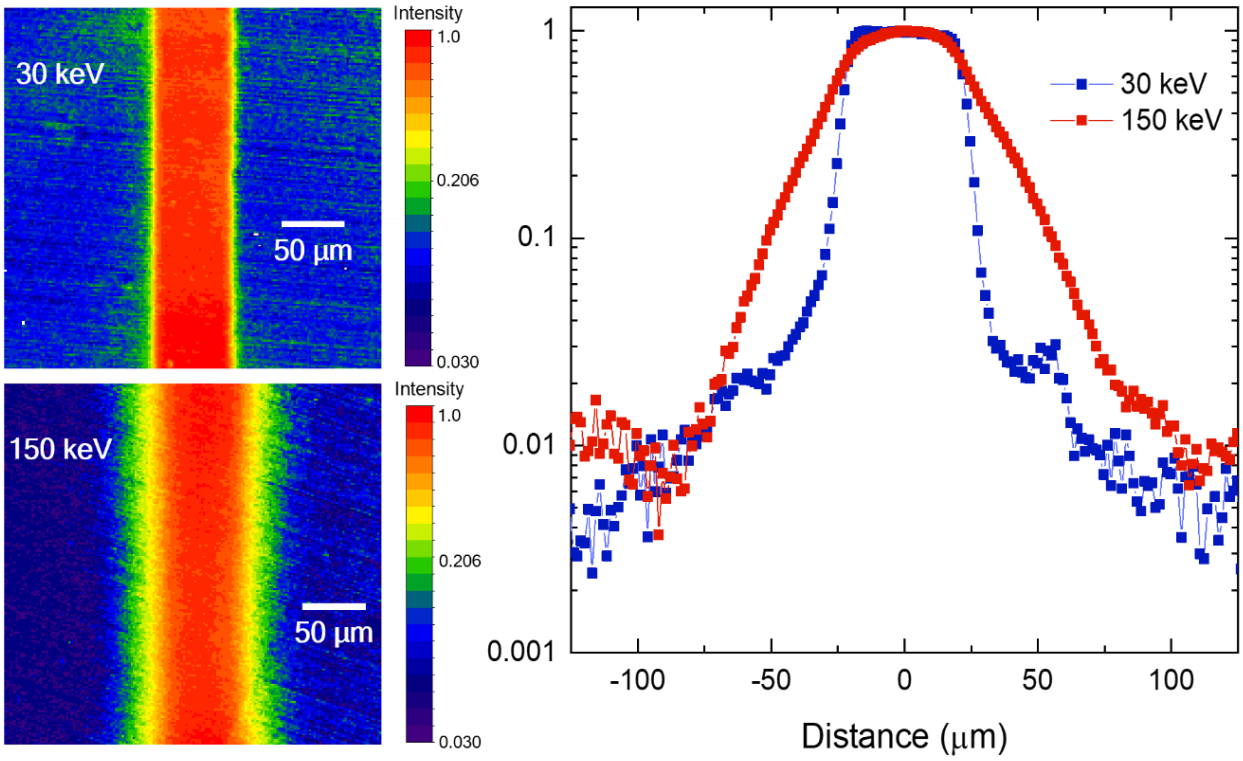

Figure 6.2 (left) Two dimensional normalized graphs of microbeams with incident energies of 30 keV and 150 keV after processing. Images of 30 keV microbeams show sharp edges, whereas at 150 keV energies there is noticeable blurring. (right) Normalized one-dimensional profiles of the images after averaging along the microbeam, parallel to the y-axis. Changes in the "tails" around the beam peaks are clearly visible. All of the above graphs are shown on a log scale for intensity.

6.4 Results

Samarium doped fluoroaluminate glasses are of particular interest and usefulness for the study of electron transport in a material. As high energy x-rays pass through the Sm-doped glass, electrons are ejected through the photoelectric effect or atomic Compton scattering. When these ejected electrons pass through the glass matrix, outside the central x-ray beam, the samarium ions, which usually reside as Sm^{3+}, gain an electron and convert to Sm^{2+}. The dose delivered can be measured by the change in the well-defined and separable PL signatures shown in Figure 6.1. Using this valence conversion allows for the measurement of microbeam profiles, and by increasing the incident x-ray energy from 30 to 150 keV it is clearly evident that the interactions that occur within the region of the microbeam, in fact, cause some of the dose to be deposited outside the region of the slits. Figure 6.2 compares the two-dimensional images and one-dimensional normalized

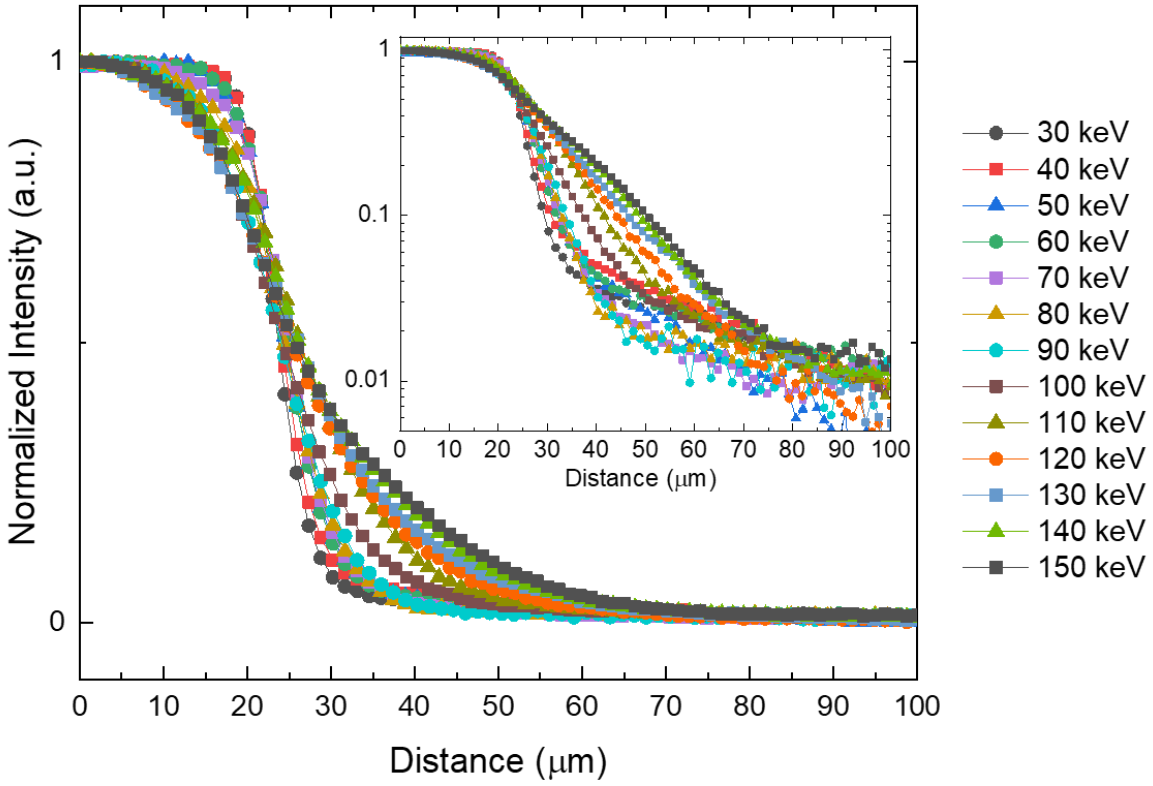

Figure 6.3 Measured profiles of 50 μm width microbeams in 1% Sm FA glass from 30 to 150 keV taken from the center of the width of the beam. Insert shows log-scale of data to better demonstrate the change of the surrounding "tails" which widen as a function of energy. Left and right sides of the beam are averaged for each profile. As the energy is increased there is a decrease in the PVDR within the bulk Sm-doped glass sample.

profiles of microbeams in a 1% Sm doped FA glass plate with identical irradiation geometry at monochromatic x-ray energies of 30 keV and 150 keV, which shows the remarkable and distinct changes in the dose delivered. In order to achieve high resolution, single 50 μm wide microbeams are measured within a 0.75 × 0.75 mm field of view. The change can be further observed as the incident energy is modified in 10 keV steps from 30 keV to 150 keV. If the normalized and stacked beam profiles are compared from the center of each microbeam over the available energy range, the results indicate that the "tails" surrounding the area adjacent to the 50 μm wide microbeams extend within the Sm-doped glass, as shown in Figure 6.3. As a way of quantifying the measurement of the change in beam profile, the full width at percentages of the maximum normalized heights were measured. These widths aid in the understanding of the beam quality and should be considered alongside the PVDR. While the FWHM of the one dimensional beam profiles

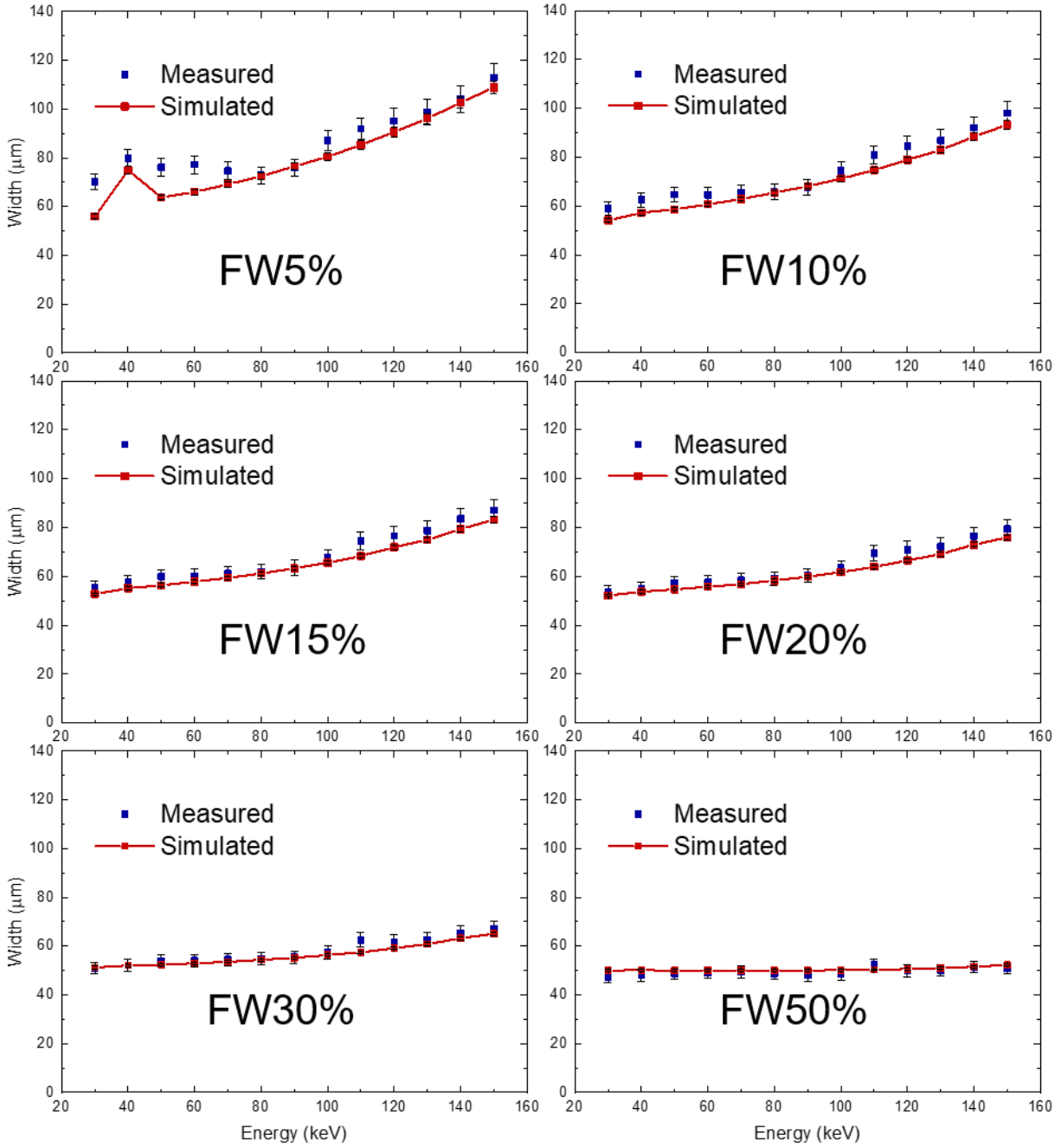

Figure 6.4 Changes in the full width (FW) at various percentages of the maximum vs the incident x-ray energy. These values are compared to the calculated MCNP values which show that the two are in excellent agreement and that the 1% Sm-doped FA glasses can be used as a verification of the calculated transportation of ejected and scattered photons and electrons within various materials.

shows minimal change as the incident x-ray energy is increased, the full width at values of 5% or 10% demonstrate obvious widening, as is shown in Figure 6.4.

A key requirement in the success of MRT is the collimation of the beam source of the incident x-rays prior to passing through the MSC. While synchrotron generated x-rays exhibit minimal divergence, it is not entirely absent from the wiggler source. The beam divergence in the horizontal and vertical direction, while quite small, are not identical. The divergence at the BMIT beamline is 0.2 mrad in the vertical direction and 4 mrad in the horizontal direction. Simulations performed using MCNP6 assume x-rays of normal incidence with no divergence. To investigate how a small change in divergence may affect the overall beam-shape, the orientation of the MSC was changed from the vertical to horizontal direction at energies ranging from 30 – 120 keV. Figure 6.5 compares the horizontal and vertical orientations at multiple energies and indicates that

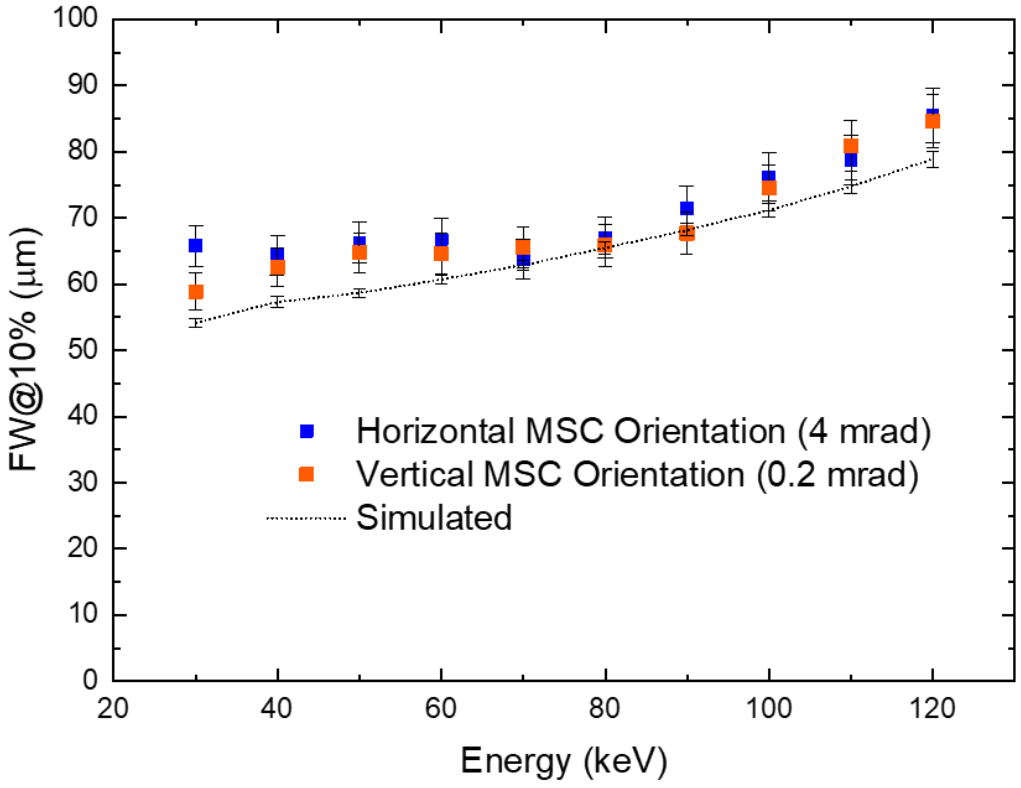

Figure 6.5 Comparison of measured widths at 10% of the maximum for the MSC that align with vertical MSC orientation, with a divergence of 0.2 mrad, and that of horizontal MSC orientation, which has a beam divergence of 4 mrad. These results for the horizontal and vertical beam divergence are in close agreement with each other, as well as the simulated values over the x-ray energy range investigated (30 – 120 keV).

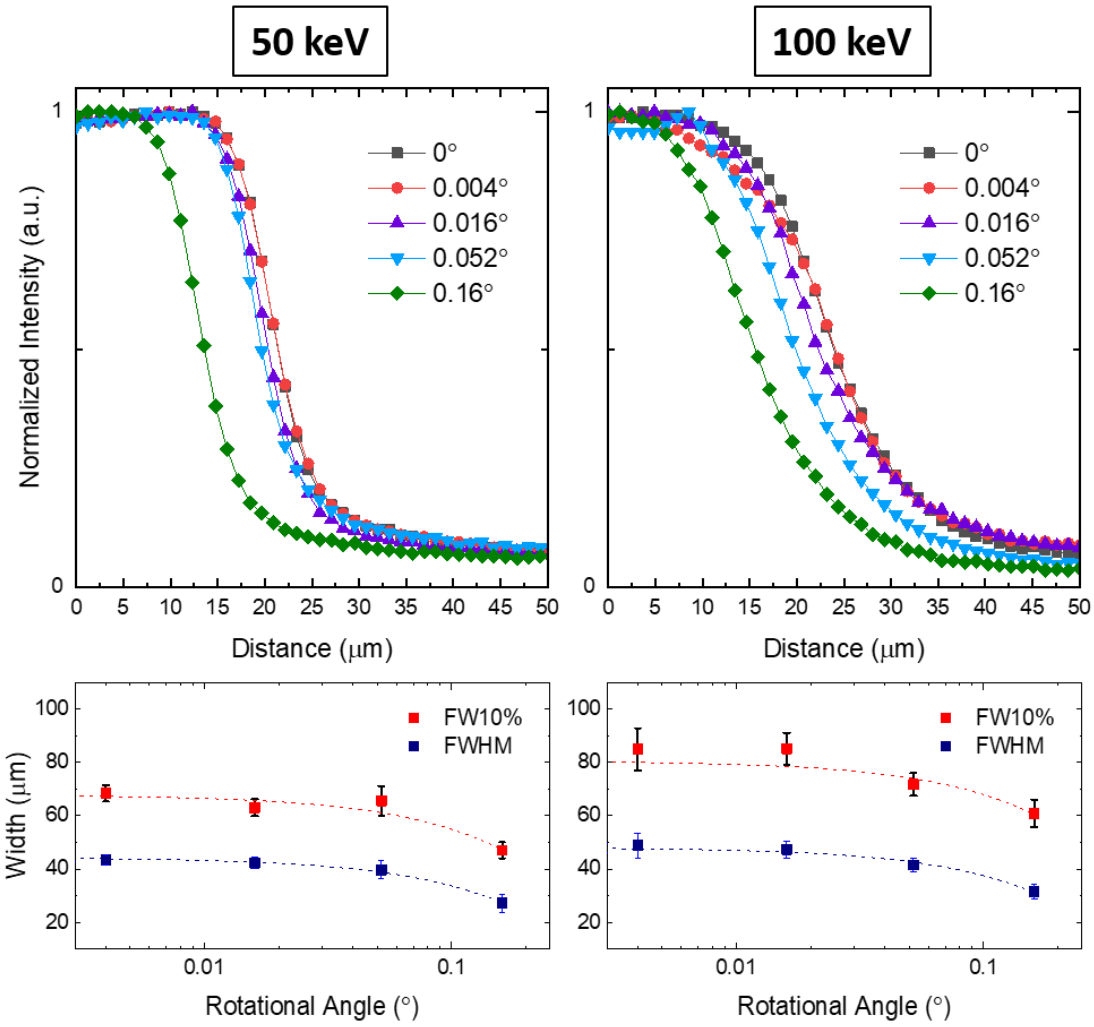

Figure 6.6 As the MSC is rotated out of alignment, the beam width will narrow. The measured narrowing was not observed to be significant until the collimator is misaligned by 0.052°, which is unlikely to occur experimentally. This figure shows the change in normalized beam profile (top) and width changes (bottom) for incident x-ray energies of 50 and 100 keV. These x-ray energies were chosen to determine if the change in scattering within the collimator and improper misalignment would significantly affect the beam shape.

there is not a significant change in the full width at 10% of the maximum intensity over the energy range investigated. Since the MCNP6 model does not include divergence of the beam, these findings indicate that the comparisons between simulated and measured values are not substantially changed by scattering within the collimator, so long as the divergence is minimal.

MSC alignment was also examined to determine if a slight misalignment can significantly modify the microbeam profile through internal scattering and geometry changes of the experimental set up. If the MSC is misaligned it could hypothetically produce a change in beam profile that could be misattributed to effects brought on by a change in the incident x-ray energy. By measuring a maximum x-ray fluence as a function of rotational angle using a CCD detector, a center alignment point was determined. The MSC was then purposely misaligned from the smallest step size of 0.004° to 0.160° at energies of 50 and 100 keV. Figure 6.6 shows no significant change in the overall beam-shape until the MSC is misaligned to 0.052°, which is unlikely to occur during experimental set up. Overall, these results indicate that experimental and simulated values are in very good agreement.

Simulated beam profiles for monochromatic x-ray energies in 1% Sm-doped FA glass using MCNP6 simulations are shown in Figure 6.7 shows over an energy range of 30 - 150 keV which demonstrating the widening of the tails of the microbeams and the rounding of the peak values. If the contributions to the x-ray attenuation coefficients of two materials of interest are compared, as in 1% Sm-doped FA glass and water shown in Figure 6.8, we can see that the transition from the photoelectric effect to atomic Compton scattering occurs at energies of 28 keV and 160 keV for water and 1% Sm-doped FA glass, respectively. Using MCNP6 simulations, monochromatic microbeams were calculated in the center of an 8-cm sphere of water and at a 20 μm depth of 2 mm thick Sm-doped FA glass. Figure 6.8 (b) shows that the FW@10% gradually increases for FA glass over the energy range from 50 – 300 keV. However, we see that over the same energy range in water, there is an observed increase in FW@10% up to 100 keV, after which these features begin narrowing until a minimum is reached at approximately 150 keV. This energy range (120-200 keV), leads to energy being deposited within the microbeam region and leads to the minimization of the surrounding "tails". If the dose deposited in the surrounding area is reduced, the tissue adjacent to the tissue has less dose deposited, which is ideal for therapeutic applications.

In addition to incident x-ray energy having a significant effect on the PVDR, the size of the slit width can cause a change in the intensity of the beam center, or peak dose, which has been previously reported [40,46 - 49]. This effect is due to electron trajectories leaving and photons

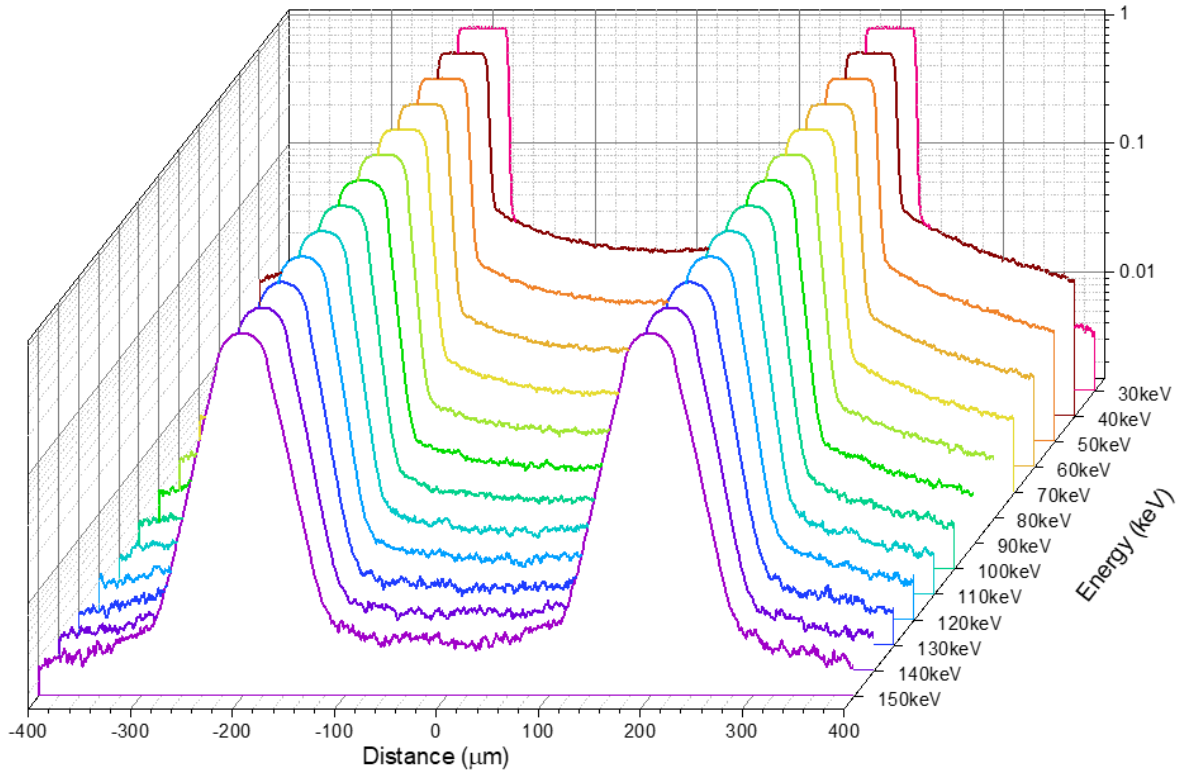

Figure 6.7 Simulated monochromatic microbeams from 30 – 150 keV in 1% Sm-doped FA glass. The beam profile widens over this energy range. Note that there is barium present in the FA glass material, and a barium K-edge at 37.4 keV, which causes the pronounced beam-shape change between 30 and 40 keV.

scattering out of the sections of irradiation, and is not due to attenuation. The incident x-ray dose was measured to be the same prior to passing through the collimator at variable slit widths. The resulting peak intensity decreases with slit width, as is shown in Figure 10. These variable slit widths were examined at an incident x-ray energy of 100 keV, which show that the enhanced intensity in the "tails" adjacent to the beam is correlated with the decrease in peak intensity. Figure 10 compares measured and simulated peak intensities as normalized to the maximum intensity of the 110 μm slit width. Figure 11 compares the peak intensity decrease in 1% Sm-doped FA glass against the slit width, where widening of the beam is pronounced through scattering and the photoelectric effect.

6.5 Discussion

Samarium doped fluoroaluminate glass has been used to measure the dose distribution of microbeams using monochromatic incident x-ray energies. The dose delivered to the sample can be measured by detecting the resulting distinguishable photoluminescent spectra from the conversion of Sm^{3+} to Sm^{2+} as shown in Figure 6.1. Since the sample is uniformly doped with Sm-ions within the glass matrix, the maximum resolution is limited by the optical readout and can reach sub-micrometer level [26-32,34]. In order to achieve this high resolution, single microbeams are measured to experimentally determine the changes to the beam quality using monochromatic x-rays, such as changes to the peak dose and extending "tails" surrounding the microbeams.

One of the commonly used methods to describe the beam quality used in MRT is the PVDR. While selecting the peak dose is a trivial task, the determination of the valley dose is more difficult. The valley dose is of significant clinical importance, as the healthy tissue in the valleys

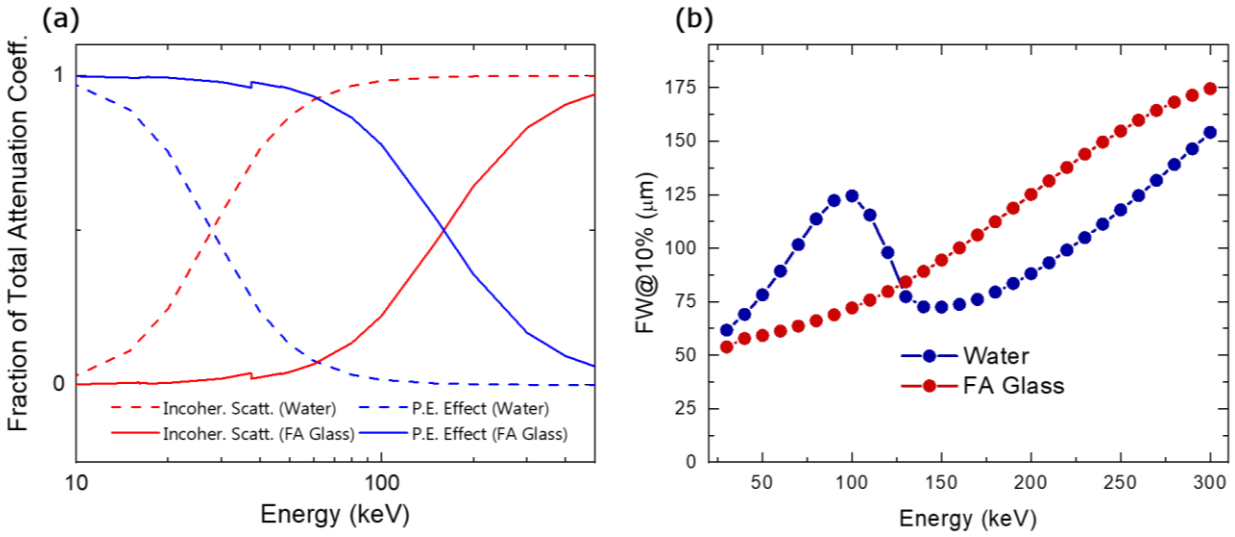

Figure 6.8 (a) Contributions of the photoelectric effect (blue) and incoherent scattering (red) attenuation coefficients for water (dotted line) and 1% Sm-doped FA glass (solid line). The crossover from the photoelectric effect to scattering occurs at approximately 28 keV for water and 160 keV for 1% Sm-doped FA glass. (b) Simulated values for the FW@10% maximum of 50 μm microbeams in water and 1% Sm-doped FA glass from 30 keV to 300 keV. In the glass material the beams widen over the energy range from 50 – 150 keV whereas in water the beams widen from 50 – 90 keV and then begins narrowing from 100 – 140 keV. The regions where the microbeam widths narrow are ideal energies for clinical MRT in human patients.

is responsible for the recovery of adjacent irradiated tissue. If the peak dose delivered to a patient is on the order of hundreds of Gys, then the extending of the "tails" can deliver a dose that is harmful to adjacent tissues and diminishes the beneficial bystander effect. The measured and simulated values of the widths are compared and are seen to be in good agreement; indicating that the MCNP6 code used to calculate the transportation of electrons and photons are experimentally validated. As mentioned above, single microbeams are experimentally measured using this high-resolution measurement technique. As a result, effects such as the field size or center to center spacings are not necessary to be considered, which with multi-slit collimators have an important effect on the PVDR, as demonstrated by [7,9,13,38,39,42,46,47,56]. The aim of this work is to examine the influence of monochromatic x-rays on the dose distribution and so effects that account for multiple microbeams are not investigated, although they remain important factors for MRT treatment planning.

The dose distribution in the "tails" surrounding the center of each microbeam show clear signs of broadening within Sm-doped FA glass as the x-ray energy is increased (Figure 6.2 and Figure 6.3). This broadening is attributed to contributions from radiation processes occurring over an energy range within the given material. Over the energy range investigated in this paper, the interactions are limited to the photoelectric effect, and coherent (Rayleigh) and incoherent (atomic Compton) scattering [57]. Incident x-rays interact with atoms and causes energy to be deposited via the ejection of charged particles, i.e. electrons, and their transport through the medium. In the case of the range of energies used in MRT, energy is deposited either through the photoelectric effect or atomic Compton scattering; as Rayleigh scattering is a coherent interaction, this process does not result in any energy deposition, although scattered photons can still deposit dose elsewhere. In the interaction, the photons can be scattered or absorbed and the electrons are ejected. After ejection, the electrons slow down, depositing energy through scattering and ionization of the medium.

The photoelectric effect and Compton scattering are processes that cause electrons to be ejected from atoms and deposit dose. The photoelectric effect is the dominant process for lower energy x-rays. Photoelectrons can be ejected into any direction, although there is a higher probability of ejection in the same direction as incident x-rays [57,58]. As the incident x-ray energy

is increased, the photoelectron is more likely to be ejected in the forward direction [57,59]. In addition to the ejection angle range narrowing at higher energies, the energy and range of the photoelectron will increase within a given material, which will affect the regions in which energy is deposited.

Additionally, the dose profile will be influenced by scattering interactions, which can be divided into either coherent (Rayleigh) or incoherent (Compton) scattering. In Rayleigh scattering, the energy of the incident photon is unchanged, only the direction of the x-ray. However, this photon can deposit energy elsewhere in a material after changing its path. Conversely, in Compton scattering, a portion of the energy is transferred to the electron. The amount of energy transferred in the collision depends on the angle of the scattered photon. The photon energy is maximum when scattered in the forward direction, however, the energy of the ejected electron is maximum when the photon is backscattered at a 180° angle. Only a portion of the energy of the photon is transferred to the ejected electron in Compton scattering. The maximum energy of the ejected electron is much less than that of the incident x-ray energy, for example, a 100 keV incident x-ray can depart a maximum energy of approximately 28 keV to the ejected electron if the photon is backscattered. As the incident x-ray energy is increased, the photon is more likely to be scattered in the forward direction and thus the electron is ejected at a wider angle.

At higher energies a photoelectron is more likely to be ejected in the same direction as the incident microbeam, whereas an ejected electron from atomic Compton scattering will be more likely to ejected away from the direction of the incident microbeam. Additionally, the energy of a photoelectron will be larger than that of an ejected electron from atomic Compton scattering within the energy range of interest in MRT, and will travel a greater distance within a material, causing ionization along the path. The probability of these two interactions occurring change as a function of energy, and is dependent on the material in which the interactions are taking place. Accounting for all directional radiation contributions, the incident x-ray energy causes changes in the beam profile are that complicated to predict. Works by [12-14,36,38,39,56] have shown noticeable changes to the beam shape by modifying the incident x-ray energy, and verification of the predicted changes to the properties of microbeams is crucial. Livingstone et. al. [12] have demonstrated the capability of comparing experimental results to Monte Carlo simulations using a microDiamond

detector. However, the high-resolution measurement of subtle changes to the beam quality, and the comparison of the results with MCNP6 transport codes over a large energy range presented in this work have not been examined systematically before.

The probability, directionality, and energy of these ionizing particles show an overall widening of the microbeams within 1% Sm-doped FA glass, which is verified by MCNP6 simulations, as shown in Figure 6.4. Further, Figure 6.7 illustrates the widening of microbeams within the Sm-doped glass dosimeter as calculated by the MCNP6 code. If we then extend the energy region of interest up to 300 keV through simulations, which is beyond the energy range of the 05ID beamline at BMIT facilities at the CLS, we see that predicted microbeams show widening in 1% Sm-doped glass, shown in Figure 6.8 (b). However, if we consider these same conditions in a material such as water, which can be used as an approximation for human tissue, then we observe that the crossover of radiation interactions from the photoelectric effect to scattering occurs at a much lower energy, as is shown in Figure 6.8 (a). This change in interaction probabilities and energies results in the observed features in water in Figure 6.8 (b). We see that the contributions from the photoelectric effect and incoherent scattering cause an increase in the width (FW@10%) of the beam from 50 to 90 keV, followed by a narrowing from 100 to 140 keV, and widening from 140 keV onward. It is this local minimum in water (in Figure 6.8 (b)) from 120 to 200 keV that results from radiation interactions depositing dose in the same direction as the incident x-rays and should be considered as an ideal energy range for therapeutic applications, whether the incident energy is monochromatic or not.

Ideally, a dosimeter should be tissue equivalent so that dose distributions within the dosimetric material resemble dose deposited in human patients. In the case of Sm-doped glasses, the material cannot be considered to be tissue equivalent. This is a result of the relative difficulty of synthesizing glass materials that are transparent and are capable of Sm^{3+} to Sm^{2+} conversion upon exposure to ionizing radiation. Indeed, samarium valence conversion has only been observed in a few select materials, such as fluoroaluminate and fluorophosphate glasses. There remains much interest in finding host materials that are transparent, exhibit conversion, and are closer to being tissue equivalent.

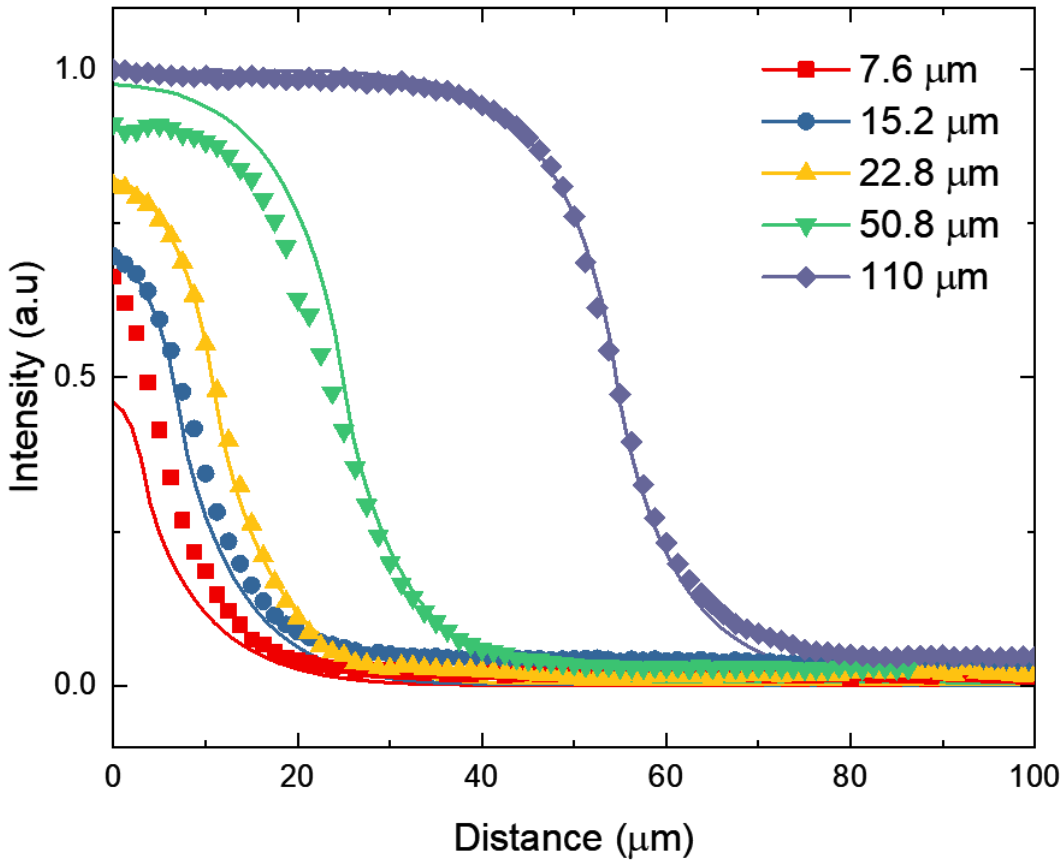

Figure 6.9 Variable slit widths with incident energy of 100 keV with the identical doses delivered before passing through a collimator of variable width. Solid lines represent simulated profiles and dots represent measured values. As the slits narrow, the dose delivered at the peak of the microbeam decreases.

After samples have been irradiated, they are readout at a focal depth of 20 μm to maximize the recorded response signals. At present, readout of the beams in three dimensions are not possible using the current confocal microscopy system. However, it would be of great interest to measure the dose deposited as a function of depth at various energies in order to determine how this might change the beam quality. Future work is planned to investigate the distribution of dose within various materials through simulations, but experimental verification of electron transport in the MCNP6 code is a much more immediate and challenging task.

In order to maintain the desirable tissue sparing effect resulting from repair of adjacent healthy tissues from MRT, slit widths must be kept smaller than some threshold value, typically

on the order of single cell dimensions. However, if the slit width is exceedingly small, it can lead to a significant decrease of the overall energy deposited within the microbeam region, which is shown in Table 6.1, the calculated reduction of the center intensity as a function of slit width, compared to a beam > 500 μm wide. As the "tails" surrounding the areas adjacent to the area of irradiation in a given material increase, the peak intensity as a function of the variable slit width is also affected, as shown in Figure 6.9. Within Sm-doped FA glass, there is a significant decrease in the energy deposited at the peak of the beam between 50.8 and 22.8 μm at 100 keV. It is likely that if these same irradiation conditions were repeated in a material such as tissue at this energy, the contributions from surrounding tails would cause a more significant decrease in peak intensity, due to more energy being deposited outside the irradiation volume. The optimal microbeam width is known to be within the range predicted in Figure 6.10, and is not a new result. However, the examination of the effect of radiation interactions on the peak intensity is meant to serve as an explanation, as well as demonstrating that too narrow a beam would be detrimental towards the peak dose output.

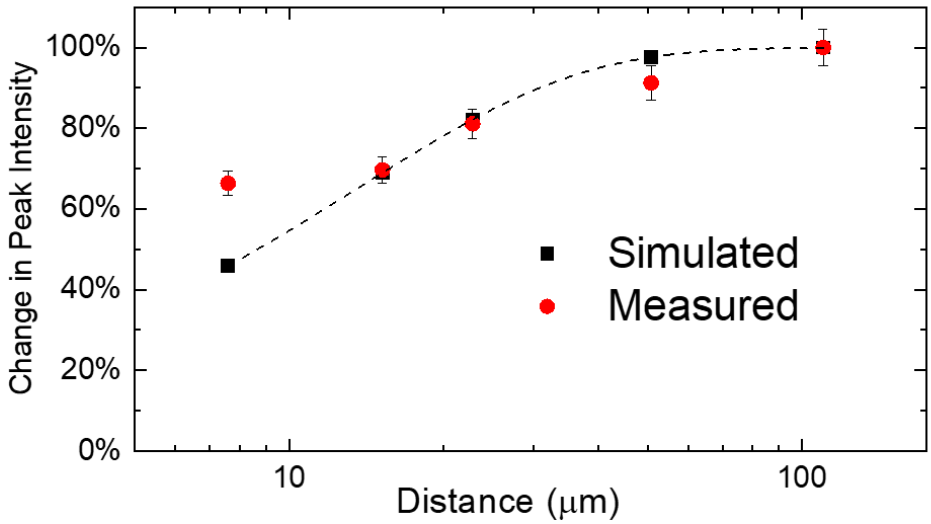

Figure 6.10 Change in peak intensity for 100 keV incident x-rays in 1% Sm-doped FA glass when normalized to the 110 μm slit width intensity. The change in peak intensity becomes more significant at width less than 20 μm. This is due to a large amount of electrons depositing dose outside of the area of irradiation in 1% Sm-doped FA glass. The curve is fitted using an exponential decay of the form $P = A(1 - e^{-w/B})$ where A and B are constants, P, is peak intensity and w is the slit width.

The output factor, sometimes referred to as the total scatter factor or relative dose factor, for the individual slit widths have not been considered in this work; they are instead compared to the normalized intensity of the 110 μm wide slit, shown in Figure 6.9. The determination of output factors for small fields is not a trivial task, as has been demonstrated by [60,61,62,63]. Effects such as internal scattering within the collimator affects the measured peak intensity. However, MCNP6 simulations performed in this work are normalized per source photon with no divergence prior to entering the collimator incident on the 1% Sm-doped FA glass, which predicts a decrease in peak intensity due to radiation interactions within the material. The change in peak intensity is therefore more likely to be attributed to dose being deposited away from the peak in sufficiently narrow collimator widths. These peak intensities are then compared with experimentally measured values in Figure 6.10, which show that the assumptions made in the code can be assumed to be correct.

It is worth noting that the measured and simulated profile dimensions for variable slit widths are not in perfect agreement, which is likely due to the fact that the laboratory-constructed variable slit width collimator in this work was not perfect, whereas the energy dependence comparisons were from a commercially manufactured MSC. Since the collimator used in the variable slit widths experiments consisted of two, approximately 4 cm thick, polished blocks of tungsten with various spacers, it is likely that the tungsten blocks may not have been perfectly parallel, nor have had the exact widths as the simulated values. Nonetheless, this experiment is a proof-of-concept to show that as the slit width is narrowed, the peak dose will decrease, and that this decrease is likely due to radiation interactions in the material and not attenuation or scattering in the collimator. For the purposes of therapeutic treatments, the ideal slit width should be between

Width (μm)	% Reduction
7.6	55%
15.2	33%
22.8	20%
50.8	5%
110	3%

Table 6.1 Reduction in the simulated peak intensity for 100 keV x-rays in 1% Sm-doped FA glass as compared to a 500 μm wide beam at various slit widths.

20 – 50 μm, in order to avoid significantly decreasing the peak dose intensity while still taking advantage of the desirable tissue sparing effect that takes place at these narrow volumes of irradiation.

6.6 Summary and Conclusions

Sm-doped fluoroaluminate glasses were used to examine the effect of the incident x-ray energy on the overall shape of monochromatic microbeams generated at the Canadian Light Source. The Sm-doped samples display the conversion of Sm^{3+} to Sm^{2+} after x-ray exposure to serve as a measure of the delivered dose. The two different valence states produce distinct and separable PL signals that, upon photoexcitation, can be distinguished using a custom confocal fluorescence microscopy system with micrometer resolution [34]. Sm-doped FA glass detector plates were irradiated at the CLS and then readout and digitized using this custom experimental confocal set-up. The results show that the nominally 50 μm width microbeam exhibits significant widening at the base of the beam profile, i.e. "tails", as the incident x-ray energy was increased. The widening arises because of the ejected and scattered electrons resulting from the photoelectric effect and Compton scattering, which contribute to dose being deposited in the region surrounding the volume of irradiation.

The PVDR is an important consideration in clinical applications for MRT, but the definition of the valley dose can be subjective. In order to quantify the observed changes in the beam shape, the beam-profiles were normalized to the maximum measured intensity and the widths at various percentages of the maximum intensity were measured. These results were then compared with simulated beam profiles that were calculated using the MCNP6 radiation transport program that is capable of simulating energy deposition including electron transport within various materials. It was found that the simulated and measured widths and profiles showed very good agreement, which demonstrates that Sm-bulk doped FA glass samples can be used to experimentally verify electron transport in media. Further, tests were performed to show that small changes in the beam divergence and alignment of the collimator do not significantly affect the observed results and therefore the agreement between the experimental and calculated values is valid. This finding is significant, as these radiation interactions are subtle and deposit dose on a very small spatial scale. Ultimately, this confirmation of simulated contributions from the

photoelectric effect and Compton scattering requires a dosimeter with a large dynamic range, detection over a wide range of x-ray energies, and micrometer level resolution.

The above findings indicate that incident x-ray energy can have an important effect on the dose deposited outside the area of the microbeams. If the experimental results verify the simulated values in 1% Sm-doped FA glass, then the MCNP6 code can also be used in various materials, which will aid in MRT treatment planning and the designing of synchrotron facilities. The selection of an appropriate incident x-ray energy range in order to maximize the dose delivered within the narrow microbeam sections is vital. Using water as an approximation for human tissue, calculations performed using MCNP6 indicate that the energy region from 120 – 200 keV has a minimum width at 10% of the maximum value. This range is ideal for human MRT treatment, since the various interactions through the photoelectric effect and Compton scattering deposit dose in the same direction as the incident x-rays and lead to the maximization of the PVDR.

In this work the comparisons between simulated and measured dose distributions have been done using monochromatic x-rays. In clinical applications, the incident x-ray energy would likely be polychromatic in order to reach a maximum dose rate to minimize blurring from patient movement. However, the understanding of radiation interactions as a function of energy is critical in order to choose the most appropriate polychromatic energy range. The maximization of the PVDR and minimization of beam widths at energies that can penetrate sufficiently into tissue is important for therapeutic applications. Additionally, variable slit width experiments demonstrate that there is a range of collimator widths that allows for lethal doses to be delivered to single cells, while not significantly decreasing the peak dose delivered at the center of the beam. This ideal width changes as a function of the selected x-ray energy, but this range would likely be between 20 – 50 μm, as others have reported. Overall, Sm-doped FA glasses have been used for high resolution, large dynamic range MRT dosimetry to verify MCNP6 code that is capable of simulating electron and photon transport in a variety of materials.

6.7 Acknowledgements

We thank both the Natural Sciences and Engineering Research Council of Canada (NSERC) Discovery Grants Program and the New Zealand Ministry of Business, Innovation, and

Employment for financial support. We thank the Canadian Light Source and staff for their assistance with this project. We would also like to thank Chris Varoy for his previous work on FA and FP glass samples that lead to the refinement of the glass making process. Research described in this paper was performed at the Canadian Light Source, which is supported by the Canada Foundation for Innovation, Natural Sciences and Engineering Research Council of Canada, the University of Saskatchewan, the Government of Saskatchewan, Western Economic Diversification Canada, the National Research Council Canada, and the Canadian Institutes of Health Research.

6.8 References

[1] D. N. Slatkin, F. A. Dilmanian, P. Spanne, M. Sandborg, Microbeam radiation therapy. Med. Phys. **19**, 1395-400 (1992)

[2] R. Lewis, Medical applications of synchrotron radiation x-rays (topical review), Phys. Med. Biol. **42** 1213 – 1243 (1997)

[3] Avraham Dilmanian, Gerard M. Morris, Nan Zhong, Tigran Bacarian, James F. Hainfeld, et. al., Murine EMT-6 Carcinoma: High Therapeutic Efficacy of Microbeam Radiation Therapy, *Radiation Research*, **159** (5) 632-641 (2003)

[4] H. Blattmann, J. Gebbers, E. Bräuer-Krisch, A. Bravin, G. Le Duc, W. Burkard, M. Di Michiel, V. Djonov, D. N. Slatkin, J. Stepanek, J. A. Laissure, Applications of synchrotron x-rays to radiotherapy. Nucl. Instrum. Methods Phys. Res., Sect. A. **548**, 17–22 (2005)

[5] A. Dilmanian, Z. Zhong, T. Bacarian, H. Benveniste, P. Romanelli, R. Wang, J. Welwart, T. Yuasa, E. M. Rosen, D. J. Anschel, Interlaced xray microplanar beams: A radiosurgery approach with clinical potential. Proc. Natl. Acad. Sci. U.S.A. **103** 9709–14 (2006)

[6] F. Avraham Dilmanian, Terry M. Button, Géraldine Le Duc, Nan Zhong, Louis A. Pena, Jennifer A.L. Smith, Steve R. Martinez, Tigran Bacarian, Jennifer Tammam, Baorui Ren, Peter M. Farmer, John Kalef-Ezra, Peggy L. Micca, Marta M. Nawrocky, James A. Niederer, F. Peter Recksiek, Alexander Fuchs, Eliot M. Rosen, Response of rat intracranial 9L gliosarcoma to microbeam radiation therapy, Neuro-Oncology, **4**, Issue 1: 26–38, (2002)

[7] C. Crosbie, R. L. Anderson, K. Rothkamm, C. M. Restall, L. Cann, S. Ruwanpura, S. Meachem, N. Yagi, I. Svalbe, R. A. Lewis, B. R. G. Williams, P. A. W. Rogers, Tumor cell response to synchrotron microbeam radiation therapy differs markedly from cells in normal tissues. Int. J. Radiat. Oncol. Biol. Phys. **77**, 886–94 (2010)

[8] E. Bräuer-Krisch, R. Serduc, E. A. Siegbahn, G. Le Duc, Y. Prezado, A. Bravin, H. Blattmann, J. A. Laissue, Effects of pulsed, spatially fractionated, microscopic synchrotron x-ray beams on normal and tumoral brain tissue. Mutat. Res. Mutat. Res. **704**, 160–6 (2010)

[9] E. Bräuer-Krisch, Jean-Francois Adam, E. Alagoz, S. Bartzsch, J. Crosbie, C. DeWagter, A. Dipuglia, M. Donzelli, S. Doran, P. Fournier, J. Kalef-Ezra, A. Kock, M. Lerch, C. McErlean, U. Oelfke, P. Olko, M. Petasecca, M. Povoli, A. Rosenfeld, E. A. Siegbahn, D. Sporea, B. Stugu, Medical physics aspects of the synchrotron radiation therapies: Microbeam radiation therapy (MRT) and synchrotron stereotactic radiotherapy (SSRT), Physica Medica, **31**, Issue 6, : 568-583 (2015)

[10] M.A. Grotzera, E. Schültke, E. Bräuer-Krisch, J.A. Laissue, Microbeam radiation therapy: Clinical perspectives, Physica Merdica, **31**, 564 – 567 (2015)

[11] R. W. Smith, J. Wang, E. Schultke, C. B. Seymour, E. Bräuer-Krisch, J. A. Laissue, H. Blattmann, C. E. Mothersill, Proteomic changes in the rat brain induced by homogenous irradiation and by the bystander effect resulting from high energy synchrotron X-ray microbeams, Int. J. Rad. Bio. **89:2**, 118-27 (2013)

[12] J. Livingstone, A. W. Stevenson, D. Häusermann, J. F. Adam, Experimental optimisation of the X-ray energy in microbeam radiation therapy, Physica Medica, **45**, 156-61 (2019)

[13] L. M. L. Smyth, L. R. Day, K. Woodford, P. A. W. Rogers, J. C. Crosbie, S. Senthi, Identifying optimal clinical scenarios for synchrotron microbeam radiation therapy: A treatment planning study, Physica Medica, **60**, 111-9 (2019)

[14] K. Shinohara, T. Kondoh, N. Nariyama, H. Fujita, M. Washio, Y. Aoki, Optimization of X-ray microplanar beam radiation therapy for deep-seated tumors by a simulation study, J. X-ray Sci. and Tech. **22**, 395-406, (2014)

[15] J C Crosbie, I Svalbe, S M Midgle, N Yagi, P A W Rogers and R A Lewis, A method of dosimetry for synchrotron microbeam radiation therapy using radiochromic films of different sensitivity, Phys. Med. Biol. **53**, 6861 (2008)

[16] E. Bräuer-Krisch, A. Rosenfeld, M. Lerch, M. Petasecca, M. Akselrod, J. Sykora, J. Bartz, M. Ptaszkiewicz, P. Olko, A. Berg, M. Wieland, S. Doran, T. Brochard, A. Kamlowski, G. Cellere, A. Paccagnella, E. A. Siegbahn, Y. Prezado, I. Martinez-Rovira, A. Bravin, L. Dusseau, P. Berkvens, Potential high resolution dosimeters for MRT. AIP Conf. Proc. **1266**, 89-97 (2010)

[17] M Petasecca, A Cullen, I Fudulia A Espinoza, C Porumb, C Stantona, A H Aldosari, E Bräuer-Krisch, H Requardt, A Bravin, X-Tream: a novel dosimetry system for Synchrotron Microbeam Radiation Therapy, J. Instrum. (IOP) **7,** P07022 (2012)

[18] J. A Davis, J. R Paino, A. Dipuglia, M. Cameron, R. Siegele , Z. Pastuovic, M. Petasecca, V. L Perevertaylo, A. B Rosenfeld, and M. L F Lerch, Characterisation and evaluation of a PNP strip detector for synchrotron microbeam radiation therapy, Biomed. Phys. Eng. Express **4** 044002 (2018)

[19] J. Archer, E. Li, J. Davis, M. Cameron, A. Rosenfeld, M. Lerch, High spatial resolution scintillator dosimetry of synchrotron microbeams, Scientific Reports. **9**, 6873 (2019)

[20] D. L. Griscom, E. J. Friebele, K. J. Long, J. W. Fleming, Fundamental defect centers in glass: Electron spin resonance and optical absorption studies of irradiated phosphorus-doped silica glass and optical fibers. J. Appl. Phys. **54**, 3743-62 (1983)

[21] K. Miura, J. Qiu, S. Fujiwara, S. Sakaguchi, K. Hirao, Three-dimensional optical memory with rewriteable and ultrahigh density using the valence-state change of samarium ions. Appl. Phys.Lett. **80**, 2263-5 (2002) h

[22] E. Malchukova, B. Boizot, G. Petite, D. Ghaleb, Optical properties and valence state of Sm ions in aluminoborosilicate glass under β-irradiation. J. Non-Cryst. Solids. **353**, 2397-402 (2007)

[23] A. Nag, T. Kutty, The light induced valence change of europium in Sr_2SiO_4 : Eu involving transient crystal structure. J. Mater. Chem. **14**, 1598-1604 (2004)

[24] H. Luo, A. Bos, P. Dorenbos, Controlled electron-hole trapping and detrapping process in $GdAlO_3$ by valence band engineering. J. Phys. Chem. **120**, 5916-25 (2016)

[25] S. Vahedi, G. Okada, C. Koughia, R. Sammynaiken, A. Edgar, S. Kasap, ESR study of samarium doped fluorophosphate glasses for high-dose, high-resolution dosimetry. Optical Materials Express. **4**, 1244-56 (2014)

[26] G. Okada, J. Ueda, S. Tanabe, G. Belev, T. Wysokinski, D. Chapman, D. Tonchev, S. Kasap, Samarium-doped oxyfluoride glass-ceramic as a new fast erasable dosimetric detector material for microbeam radiation cancer therapy applications at the Canadian synchrotron. J. American Ceramic Society. **97**, 1976-80 (2014)

[27] B. Morrell, G. Okada, S. Vahedi, C. Koughia, A. Edgar, C. Varoy, G. Belev, T. Wysokinski, D. Chapman, R. Sammynaiken, S. Kasap, Optically erasable samarium-doped fluorophosphate glasses for high-dose measurement in microbeam radiation therapy. J. Appl. Phys. **115**, 063107 (2014)

[28] G. Belev, G. Okada, D. Tonchev, C. Koughia, C. Varoy, A. Egar, T. Wysokinski, D. Chapman, S. Kasap, Valency conversion of samarium ions under high dose synchrotron generated x-ray radiation. Phys. Status Solidi C. **8**, 2822-25 (2011)

[29] A. Edgar, C. Varoy, C. Koughia, G. Okada, G. Belev, S. Kasap, High-resolution x-ray imaging with samarium-doped fluoroaluminate and fluorophosphate glass. Journal of Non-Crystalline Solids. **377**, 124-128 (2013)

[30] S. Vahedi, G. Okada, B. Morrell, E. Muzar, C. Koughia, A. Edgar, C. Varoy, G. Belev, T. Wysokinski, D. Chapman, S. Kasap, X-ray induced Sm^{3+} to Sm^{2+} conversion in fluorophosphate and fluoroaluminate glasses for the monitoring of high-doses in microbeam radiation therapy. Journal of Applied Physics. **112**, 073108 (2012)

[31] G. Okada, B. Morrell, C. Koughia, A. Edgar, C. Varoy, G. Belev, T. Wysokinski, D. Chapman, S. Kasap, Spatially resolved measurement of high doses in microbeam radiation therapy using samarium doped fluorophosphate glasses. Applied Physics Letters. **99**, 121105 (2011)

[32] G. Okada, S. Vahedi, B. Morrell, C. Koughia, G. Belev, T. Wysokinski, D. Chapman, C. Varoy, A. Edgar, S. Kasap, Examination of the dynamic range of Sm-doped glasses for high-dose and high-resolution dosimetric applications in microbeam radiation therapy at the Canadian synchrotron. Optical Materials. **35**, 1976-80 (2013)

[33] F. Chicilo, C. Koughia, R. Curry, R. Gwilliam, R. Ahumada-Lazo, A. Edgar, D. Binks, D. Chapman, S. Kasap, X-ray induced Sm-ion valence conversion in Sm-ion implanted fluoroaluminate glasses towards high-dose radiation measurement. J Mater Sci: Mater Electron. 1-7 (2019)

[34] F. Chicilo, G. Okada, G. Belev, D. Chapman, A. Edgar, R. J. Curry, S. Kasap, Instrumentation for high-dose, high-resolution dosimetry for microbeam radiation therapy using samarium-doped fluoroaluminate and fluorophosphate glass plates. Meas. Sci. Technol. **00** (2019)

[35] Goorley, John T., James, Michael R., Booth, Thomas E., Brown, Forrest B., Bull, Jeffrey S., Cox, Lawrence J., Durkee, Joe W. Jr., Elson, Jay S., Fensin, Michael Lorne, Forster, Robert A. III, Hendricks, John S., Hughes, H. Grady III, Johns, Russell C., Kiedrowski, Brian C., Martz, Roger L., Mashnik, Stepan G., McKinney, Gregg W., Pelowitz, Denise B., Prael, Richard E., Sweezy, Jeremy Ed, Waters, Laurie S., Wilcox, Trevor, and Zukaitis, Anthony J. Initial MCNP6 Release Overview - MCNP6 version 1.0. United States: N. p., (2013)

[36] E.A. Siegbahn, E. Bräuer-Krisch, J. Stepanek, H. Blattmann, J.A. Laissue, A. Bravin, Dosimetric studies of microbeam radiation therapy (MRT) with Monte Carlo simulations, Nuclear Instruments and Methods in Physics Research Section A: Accelerators, Spectrometers, Detectors and Associated Equipment, **548**, Issues 1–2, 54-8 (2005)

[37] H. Nettelbeck G. J. Takacs M. L. F. Lerch A. B. Rosenfeld, Microbeam radiation therapy: A Monte Carlo study of the influence of the source, multislit collimator, and beam divergence on microbeams, Med. Phys., **36**: 447-456 (2009)

[38] I. Martínez-Rovira, J. Sempau, Y. Prezado, Monte Carlo-based treatment planning system calculation engine for microbeam radiation therapy, Med. Phys., **39**: 2829-38 (2012)

[39] I. Martínez-Rovira J. Sempau Y. Prezado, Development and commissioning of a Monte Carlo photon beam model for the forthcoming clinical trials in microbeam radiation therapy, Med. Phys., **39**: 119-131 (2012)

[40] [Paper awaiting publication] A. L. Hanson, F. H. Geisler, Establishing Design Criteria for a Synchrotron Radiation Based MBRS/MRT Clinical Facility

[41] M. De Felici, E. A. Siegbahn, J. Spiga, A. L. Hanson, R. Felici, C. Ferrero, A. Tartari, M. Gambaccini, J. Keyrilainen, and E. Brauer-Krisch. Monte Carlo code comparison of dose

delivery prediction for microbeam radiation therapy. In Journal of Physics: Conference Series, **102**, 012005, (2008)

[42] I. Orion, A. B. Rosenfeld, F. A. Dilmanian, F. Telang, B. Ren, Y. Namito, Monte Carlo simulation of dose distributions from a synchrotron-produced microplanar beam array using the EGS4 code system, Phys. Med. Biol. **45**, 2497-508 (2000)

[43] D. Anderson, E. Albert Siegbahn, B. Gino Fallone, R. Serduc, B. Warkentin, Evaluation of dose-volume metrics for microbeam radiation therapy dose distributions in head phantoms of various sizes using Monte Carlo simulations, Phys. Med. Biol. **57**, 3223-48 (2012)

[44] N. M. Esplen, L. Chergui, C. D. Johnstone, M. Bazalova-Carter, Monte Carlo optimization of a microbeam collimator design for use on the small animal radiation research platform (SARRP), Phys. Med. Biol. **63**, 175004 (2018)

[45] Hui Lin, Jia Jing, Liangfeng Xu, Xiaoli Mao, Monte Carlo study of the influence of energy spectra, mesh size, high Z element on dose and PVDR based on 1-D and 3-D heterogeneous mouse head phantom for Microbeam Radiation Therapy, Physica Medica, **44**, 96-107 (2017)

[46] N. Mukumoto, M. Nakayama, H. Akasaka, Y. Shimizu, S. Osuga, D. Miyawaki, K. Yoshida, Y. Ejima, Y. Miura, K. Umetani, T. Kondoh, R. Sasaki, Sparing of tissue by using micro-slit-beam radiation therapy reduces neurotoxicity compared with broad-beam radiation therapy, J. Radiat. Res. **58**, 17-23 (2017)

[47] R. J. Griffin, N. A. Koonce, R. P. M Dings, E. Siegel, E. G Moros, E. Bräuer-Krisch, P. M Corry, Microbeam Radiation Therapy Alters Vascular Architecture and Tumor Oxygenation and is Enhanced by a Galectin-1 Targeted Anti-Angiogenic Peptide, Radiation Research, **177**(6), 804-812, (2012) \

[48] A. Uyama, T. Kondoh, N. Nariyama, K. Umetani, M. Fukumoto, K. Shinohara, E. Kohmura, A narrow beam microbeam is more effective for tumor growth suppression than a wide microbeam: An in vivo study using implanted human glioma cells, J. Synchrotron Rad. **18**, 671-8 (2011)

[49] R. Serduc, A. Bouchet3, E. Bräuer-Krisch, J. A. Laissue, J. Spiga, S. Sarun, A. Bravin, C. Fonta, L. Renaud, J. Boutonnat, E. A. Siegbahn, F. Estève, G. Le Duc, Synchrotron microbeam radiation therapy for rat brain tumor palliation—influence of the microbeam width at constant valley dose, Phys. Med. Biol. **54,** 6711

[50] P. Regnard, G. Le Duc, E Bräuer-Krisch, I Troprès, E Albert Siegbahn, A. Kusak, C. Clair, H. Bernard, D. Dallery, J. A. Laissue, A. Bravin, Irradiation of intracerebral 9L gliosarcoma by a single array of microplanar x-ray beams from a synchrotron: balance between curing and sparing, Phys. Med. Biol, **63**, 175004 (2018)

[51] L. M. L. Smyth, S. Senthi, J. C. Crosbie, P. A. W. Rogers, The normal tissue effects of microbeam radiotherapy: What do we know, and what do we need to know to plan a human clinical trial? International Journal of Radiation Biology, **92**, 1-10 (2016)

[52] M. J. Ibahim, J. C. Crosbie, Y. Yang, M. Zaitseva, A. W. Stevenson, P. A. W. Rogers, P. Paiva, An evaluation of dose equivalence between synchrotron microbeam radiation therapy and conventional broadbeam radiation using clonogenic and cell impedence assays, PLoS ONE e100547, **9**, 1-10 (2014)

[53] L. M. L. Smyth, J. F. Donoghue, J. A. Ventura, J. Livingstone, T. Bailey, L. R. J. Day, J. C. Crosbie, P. A. W. Rogers, Comparative toxicity of synchrotron and conventional radiation therapy based on total and partial body irradiation in a murine model, Sci. Rep., **8**, 1-11 (2018)

[54] D. B. Pelowitz, et al., MCNP6 user's manual, version 1.0, LA-CP-13-00634 (2013)

[55] Joneja O P, Negreanu C, Stepanek J and Chawla R, Comparison of Monte Carlo simulations of photon/electron dosimetry in microscale applications, Australasian Phys. & Eng. Sci. in Med. **26**, 62-68 (2003)

[56] M. DeFelici, R. Felici, M. Sanchez del Rio, C. Ferrero, T. Bacarian, F. Dilmanian, Dose distribution from x-ray microbeam arrays applied to radiation therapy: an EGS4 Monte Carlo study, Med. Phys. **32**, 2455-63 (2005)

[57] C. M. Davisson, R. D. Evans, Gamma-ray absorption coefficients, Rev. Modern Phys, **24**, 79-107 (1952)

[58] J. A. R. Samson, Angular distributions of photoelectrons and partial photoionization cross-sections, Phil. Trans. Roy. Soc. Lond. A. **268**, 141-6 (1970)

[59] F. Sauter, Ann. Physik **9**, (1931)

[60] O. A. Sauer, J. Wilbert, Measurement of output factors for small photon beams, Med. Phys., **34**, no. 3, 1983–8, (2007)

[61] W. U. Laub, T. Wong, The volume effect of detectors in the dosimetry of small fields used in IMRT, Med. Phys., **30**, no. 3, 341-7, (2003)

[62] R. Azimi, P. Alaei, P. Higgins, The effect of small field output factor measurements on IMRT dosimetry, Med. Phys., **39**, no. 8, 4691- 4, (2012)

[63] K. Krongkietlearts, P. Tangboonduangjit, N. Paisangittisakul, Determination of output factor for 6 MV small photon beam: comparison between Monte Carlo simulation technique and microDiamond detector, J. Phys.: Conf. Ser. **694** (2016)

Chapter 7

Conclusions and Suggested Future Works

The objective this Ph.D. work involves the characterization of the properties of Sm-doped fluoroaluminate (FA) and fluorophosphate (FP) glasses, and their use in Microbeam Radiation Therapy (MRT) for high-resolution, high-dose dosimetry. These Sm-doped glass plates have been shown to be excellent candidates for detecting x-ray radiation, particularly in the application of MRT dosimetry. The detection method is based on conversion of trivalent Sm^{3+} ions to divalent Sm^{2+} ions upon exposure to x-ray radiation, which can then be readout with high resolution by using a purpose built confocal microscopy system. These Sm-doped samples are capable of measuring doses in the range from 5 Gy to over 2000 Gy, with achievable spatial resolution on the order of single micrometers or better.

The work in the following section briefly summarizes the dosimetry technique used for the measurement of microbeams in this thesis. Section 7.2 summarizes the published works done to characterize Sm-doped FA and FP glasses, including ion implantation, energy and dose rate response of the materials, characterization of the readout technique, and high resolution measurements of microbeam profiles at multiple monochromatic energies. Section 7.3 recommends several potential future experiments in order to improve the dosimetric materials for clinical or commercial use.

7.1 Summary of Dosimetry Technique for Large Dynamic Range, High-Resolution Measurements

A more detailed description of the measurement technique used in this research is given in Chapter 3, however, this section briefly summarizes the concept behind the dosimetric material. The technique utilizes the photoluminescent (PL) properties of Sm^{3+} and Sm^{2+} ions in a particular host medium, which emit in the orange and red region of the visible spectrum and can be easy distinguished. Upon exposure to x-rays Sm^{3+} gains an electron and becomes Sm^{2+}, therefore the

change of the ratio of Sm^{3+} ions to Sm^{2+} ions is related to the dose delivered, as is shown in Figure 7.1. Put differently, the dose delivered is proportional to the detected PL signals emitted from the Sm-doped glass samples,

$$\text{Dose} \propto \frac{\text{PL}(Sm^{2+})}{\text{PL}(Sm^{3+})} \tag{7.1}$$

The response of the sample is read out and digitized by a purpose built custom confocal fluorescence microscope technique, which allows for irradiated samples to be readout with high resolution in two dimensions. Fluoroaluminate and fluorophosphate glasses have been found to be excellent detector materials for Sm valence conversion based dosimetry. Further, these samples have been shown to be reusable through the process of UV exposure or annealing. Overall, Sm-doped FA and FP glasses are promising tools for MRT dosimetry applications.

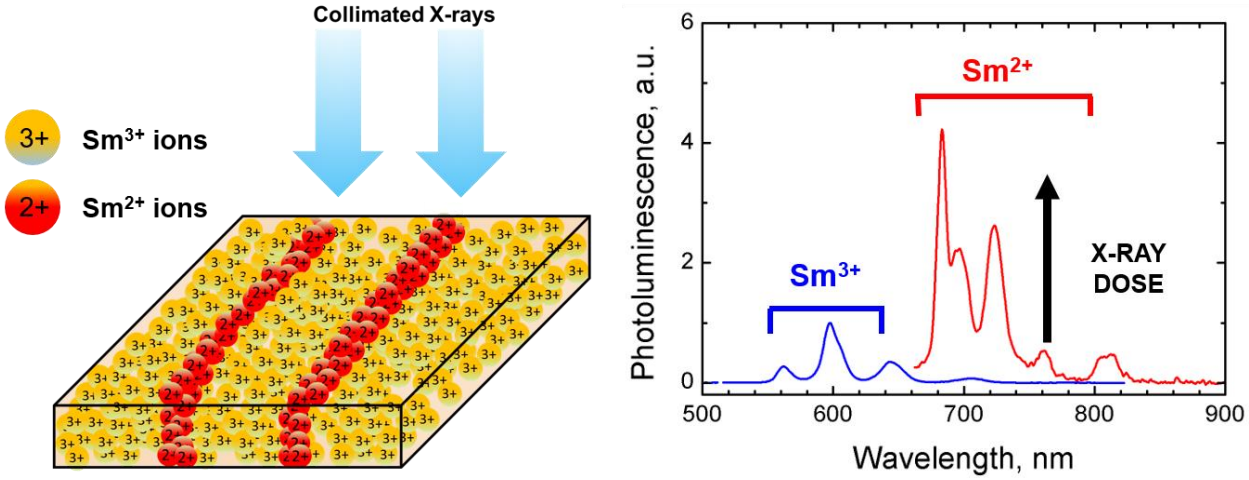

Figure 7.1 Illustration of dosimetric technique using samarium valence dosimetry. (Left) As the Sm doped glass plate is exposed to ionizing radiation, there is conversion from $Sm^{3+} \rightarrow Sm^{2+}$. Using collimated x-ray microbeams causes only the exposed portion of Sm-doped glass plate to undergo conversion. (Right) Photoluminescent spectra of Sm^{3+} and Sm^{2+} are easily separable, and total dose delivered is proportional to the increase of detected Sm^{2+} ions.

7.2 Summary of Manuscripts

7.2.1 Sm-ion Valence Conversion in Ion Implanted Fluoroaluminate Glasses

The fabrication of Sm-ion implanted FA glass has been tested for the purposes of MRT dosimetry. Ion implantation utilizes the result that Sm-ions reside within a thin plane very near the surface of the glass. Ion implantation has an advantage in that the resulting PL from Sm ions is from a well defined thin layer, which allows for calculation of the surface dose, and reduces the amount of light attenuation from Sm^{3+} and Sm^{2+} ions throughout the sample. In this work, Sm-ions were successfully implanted with a fluence of 5×10^{15} ions/cm^2 at an energy of 2 MeV. After implantation, Sm ions exist in both the divalent and trivalent forms, and by annealing above the glass transition temperature, Sm^{2+} ions are reconverted to Sm^{3+}. After annealing the Sm-ion implanted samples, subsequent irradiation showed evidence of conversion from Sm^{3+} to Sm^{2+} ions, as well as a broad overlapping emission spectra which is likely associated with x-ray induced structural defects within the host glass matrix. These defect related signals are "allowed" transitions and have fast emission lifetimes when compared with the "forbidden" f-f transitions associated with Sm^{2+} and Sm^{3+} ions. The PL signals from Sm ions and defect related signals are quite weak when compared to signals collected from bulk Sm-doped glass samples. However, by using a phase sensitive (quadrature frequency resolved spectroscopy) photodetection technique, it is possible to isolate the Sm ion emissions, which have emission lifetimes in the millisecond range, from the broad overlapping signals, which have radiative emission times on the nanosecond scale. This technique uses a modulated laser source and a lock in amplifier to separate the signals. Using this measurement technique, Sm-ion implanted samples can be used to measure a dynamic range up to 800 Gy.

Overall, Sm-ion implanted FA glass samples have been shown to be capable of Sm valence conversion for the purposes of dosimetry. Further, the resulting PL signals from Sm^{3+} and Sm^{2+} ions emit from the surface of the material, simplifying dose calculations resulting from the extent of Sm-valence conversion in the bulk. A limitation to the ion-implanted FA plate, however, is the spatial resolution of the resulting photoluminescence upon excitation. Because of the overlapping defect signals, the fluorescent confocal microscope system built for measuring bulk doped samples cannot separate the signals associated with the slow and fast emissions. Additionally, the resulting

PL from Sm-ion implanted samples are much less intense than those from bulk Sm-doped glass samples and would require a more sensitive readout technique. Despite these limitations, Sm-ion implanted samples are unique, and demonstrate that Sm-valence conversion is possible in Sm-ion implanted samples, which was previously unknown. Sm-ion implanted materials serve as a proof of concept for Sm-ion implanted glass plate dosimetry. It was also demonstrated that using a lifetime sensitive phase separation technique allows for the separation of overlapping PL signals, provided the emission lifetimes are sufficiently different.

7.2.2 Energy and Dose Rate Dependence of the Response of Sm-doped FA and FP Glasses

The response values of Sm-doped FA and FP glasses with varying Sm-dopant concentrations was examined over a large dynamic range up to 2000 Gy. The amount of $Sm^{3+} \rightarrow Sm^{2+}$ conversion was measured as a function of x-ray dose, dose rate, incident photon energy, focal depth, Sm-dopant concentration, and stability for Sm-doped FA and FP glasses in order to determine the optimum conditions for x-ray dosimetry.

The conversion of Sm^{3+} to Sm^{2+} is controlled by a hole trapping process, as previously discussed. This hole trapping process leads to a larger response value at lower concentrations of Sm-dopants $\left(\text{Response} = [I_{PMT(2+)}/I_{PMT(3+)}]_{\text{Irradiated}} - [I_{PMT(2+)}/I_{PMT(3+)}]_{\text{Non-irradiated}}\right)$. Additionally, while FA and FP glasses have been shown to be excellent host materials, the extent of photodarkening resulting from x-ray induced defects between the two host glass matrices is not equal, and photodarkening is more pronounced in FP glasses than in FA glasses. Thus, the energy and dose rate responses of various Sm-dopant concentrations and host materials have been examined to determine the change in response values in order to determine the most suitable composition.

The dose rate and energy dependence of dosimetric materials is a crucial consideration and the amount of conversion from divalent to trivalent Sm should not change significantly as these parameters are modified. In this work, the response of 1% Sm-doped FA and FP glasses was measured over a dose rate extending over four orders of magnitude, from 0.7 mGy/s to 5 Gy/s. Over this dose rate range, the response of 1% Sm doped FA and FP glasses was found to be constant, which is an important result. The incident x-ray energy dependence was also investigated

over the range of 30 – 130 keV and was found to decrease as a function of energy. Ideally, a dosimeter should have no significant energy dependence, but over such a large energy range, it is likely that some extent of calibration would be required. Multiple Sm-dopant concentrations were measured over this range and all exhibited a similar decrease in Sm-valence conversion as a function of energy.

As a result of the dose rate and energy responses having little variation over multiple Sm-dopant concentrations and host materials, the maximization of the response signal should be of primary importance. The overall response value has an inverse relationship with Sm-dopant concentration, that is, increasing the total number of Sm^{3+} ions does not increase the response value. However, when considering dopant percentages lower than 1% Sm, there is evidence of spontaneous recombination from Sm^{2+} back to Sm^{3+}, meaning that the response value immediately after irradiation will change over an approximate 24 hour period, which is undesirable. As a result, it was found that a 1% Sm dopant concentration is ideal for Sm-valence dosimetry purposes. Additionally, FP glasses exhibit a greater extent of photodarkening as a function of radiation dose, and so 1% Sm-doped FA glass is likely to be the most suitable candidate, overall, for high resolution, large dynamic range dosimetry.

1% Sm-doped FA glass materials were examined over a dose range of 5 to 2000 Gy at incident photon energies of 40, 60, 80, 100, and 120 keV, which shows that doses can be measured over a wide range of energies up to 2 kGy. Additionally, it was shown that the response values can vary not only as a function of energy, but also as a function of laser focal depth within the sample. Within the focal depth range of 5 – 20 μm, the response of 1% Sm-doped FA glass is constant, regardless of the energy, but the signal to noise increases at larger depths. If the focal depth is increased beyond this point, then the response values can decrease depending on the energy. This change in response as a function of depth is likely to be due to photodarkening at higher response values. Consequently, using the current fluorescent confocal microscopy system, the focal depth should be around 20 μm. This value is further confirmed by measuring the response of Sm-ion implanted FA glasses as a function of depth, which shows that a Gaussian curve can be used to measure the signal decay as the focal depth is increased. Since the detected Sm signal is only present at the surface of the glass, the resulting PL is due to photons outside the focal spot being

collected as the focal depth of the laser increases. The measured FWHM of the fitted Gaussian is approximately 21 μm, meaning that this represents the optimum focal length for collecting the PL signal.

For 1% Sm-doped FA glass samples, the achievable lateral resolution is conceivably less that one micron, and ultimately limited through the optical resolution of the instrument. Using the custom confocal fluorescence microscopy system, the dwell time at each point in a two dimensional image is dictated by the radiative emission lifetimes of Sm^{3+} and Sm^{2+} ions in order to prevent PL from neighboring pixels to affect the intended collection data point. Since Sm ions have emission-lifetimes in the millisecond range, the higher the desired spatial resolution, the larger the overall collection time. The measurement technique, including the lateral resolution, focal depth, and collection time were examined in this work, and it was determined that 1% Sm FA glass is an ideal candidate for the purposes of MRT dosimetry.

7.2.3 Microbeam Profiles as a Function of Incident X-ray Energy and Slit Width

The effectiveness of MRT relies on maximizing the peak while minimizing the dose delivered between each microbeam, in the "valleys" or "tails" adjacent to the intended region of irradiation. The dose delivered within this narrow region, must be lethal to the cells, while still allowing for adjacent healthy tissue to aid in the repair of damaged tissue, an ability that tumours do not exhibit. The widths of the microbeams must be sufficiently narrow in order to achieve the desirable tissue sparing effect, typically on the order of single cells, from 30 – 50 μm.

What has not been systematically studied in the past, is how the incident x-ray energy can have an effect on the microbeam profile properties, which would ultimately affect treatment conditions. As the incident x-ray energy is changed, so too is the probability of radiation interaction processes and the directionality of ejected electrons and scattered photons. At low energies considered in MRT, the photoelectric effect is the primary process, whereas scattering interactions dominate at higher energies. It is thought that the ideal energy for human therapy treatment conditions would likely be between 90 – 300 keV, which would allow for x-rays to sufficiently penetrate into human tissue and deposit dose at the intended target. Using a monochromatic and collimated x-ray source at the CLS, experiments were performed using 1% Sm-doped FA glasses

to determine how the characteristics of a microbeam profile might change over a wide energy range, from 30-150 keV. Ideally, a microbeam should deposit the entirety of the dose delivered within the material directly nadir from the collimator, resulting in a profile that resembles a step like function. As the incident x-ray energy is changed, however, the directionality, probability, and particle range change as well. This energy increase results in the deposition of radiation dose into the surrounding "tails" and a rounding of the radiation "peak" of microbeams detected with Sm-doped glass plates. These same irradiation conditions are repeated using MCNP6 code used to simulate photon and electron transport within 1% Sm doped FA glass using the same dimensions as the multi-slit collimator used during experiments at the CLS.

Both experimental and simulated values found that, as the incident energy of the x-rays increased, the overall beamshape exhibited widening of the beam width within 1% Sm-doped FA glass. The widening of the beamshape is characterized by measuring the normalized full width at 10% of the maximum value (FW@10%), and individual beams were measured with micrometer level resolution. The verification of the MCNP6 code is important, as it demonstrates the confidence that can be placed in the technique when designing treatment planning for MRT and other radiation therapies. Indeed, using the MCNP6 code, it was calculated that the microbeam widths at FW@10% will continue widening up to energies of 300 keV in FA glass. However, by simulating the same conditions in a material such as water, which can be used as an approximation for human tissue, it was found that there exists an ideal energy range from 120 – 200 keV, where interactions resulting from scattering and the photoelectric effect cause the microbeams to narrow, increasing the effectiveness of MRT.

In addition to the x-ray energy playing an important role in the success of MRT treatment planning, the size of the individual microbeams is also an important consideration. It is known that too large of a beam width reduces the effectiveness of the technique by eliminating the "bystander effect". Likewise, if the beam width is too narrow, this causes complications in the fabrication of multi-slit collimators, and the "peak" intensity is likely to decrease overall. In this work, a constructed single slit collimator devised from placing spacers between two pieces of polished tungsten was used to examine the overall change in intensity using a monochromatic energy source. The dose delivered prior to passing through the collimator was kept constant and the

resulting intensity was compared to MCNP6 simulations. The size of the slit widths had a range between 7.6 μm and 110 μm and each slit width intensity was compared to the normalized value of the largest slit, 110 μm. As the slit width narrowed, the measured and simulated intensities both decreased appreciably. Since the MCNP6 code does not include beam divergence, it is unlikely that this effect is due to scattering within the collimator alone. Instead, it is hypothesized that the change in intensity is related to the dose deposited outside the region of irradiation in the "tails". At sufficiently narrow widths, the change in intensity is significant, and so widths less approximately 20 μm would require a greater dose prior to entering the collimator.

The exact slit width and incident energy in human treatment planning would ultimately need to be verified by a biological response in tissue and irradiated tumour. Nevertheless, the radiation interactions resulting from changes in energy and irradiation volume greatly aid in the understanding of the processes involved and it is unlikely that other dosimetric materials can provide the necessary resolution afforded by Sm-doped glass samples.

7.3 Suggested Future Works

Sm-doped glass samples have been shown to be excellent candidates for high resolution, large dynamic range MRT dosimetry. Further, it has been demonstrated that 1% Sm-doped FA glass is transparent, reusable, stable, and is capable of strong $Sm^{3+} \rightarrow Sm^{2+}$ conversion. A custom built confocal fluorescent microscopy system has been characterized and is capable of measuring samples with micrometer or better resolution. However, there are improvements on both material synthesis and sample measurement that could be further developed upon in future works. The proposed future works are listed as follows,

1. While it has been demonstrated that materials capable of $Sm^{3+} \rightarrow Sm^{2+}$ conversion are difficult to successfully synthesize, much interest remains in tissue equivalent dosimetric materials. Tissue equivalent materials would allow for simplified calculations of dose delivered to a patient, and could be used during patient irradiations without significantly changing the measured beam quality.

2. Once samples have been synthesized by collaborators at the University of Wellington, they are sent to our lab and are cut and polished for experimental purposes. However, when examining samples at high resolutions, such as is the case in measuring subtle changes in the beamshape as a function of energy, the surface quality of the glass becomes more important. In order to increase the resolution of the Sm-doped glass materials, improvements to the processing of materials could be enhanced in order to reach higher optical quality.

3. The readout method using the current confocal microscopy system can be improved upon in order to more efficiently characterize and measure irradiated samples. The required improvements are related to total measured area, which could be expanded to measure multiple microbeams. This could be accomplished by implementing a motorized stage that is capable of scanning the sample over the entire area of the detector at high resolution.

4. The total collection time for irradiated samples should be reduced, particularly in samples which require high resolution across a large field of view. Currently, the dwell time at each pixel is limited by the forbidden emission transition lifetimes that are characteristic of Sm ions, and the speed of the scanning instrument. As an example, measurements collected in the investigation into the change of beamshape as a function of energy required approximately 6 hours to collect for each sample. If one wanted to measure the entire field of view at the highest possible resolution, the collection time would be in excess of 30+ hours. Previous works have shown that glass ceramic materials exhibit $Sm^{3+} \rightarrow Sm^{2+}$ conversion with much faster decay times, but was not capable of high resolution. Alternatively, other fluorescent confocal microscopy systems are capable of measuring the entire FOV using selectable excitation sources with selected emission wavelengths. This technique would likely not allow for simultaneous measurement of PL resulting from Sm^{3+} and Sm^{2+} ions, but if properly calibrated, the increase in Sm^{2+} ions could be used as a measurement of the total dose delivered.

5. Dose deposited as a function of depth would be of great interest to investigate. Unfortunately, the current confocal fluorescence microscopy system is not capable of measuring samples in three dimensions without signal bleaching Sm-ions in the z-axis from

the excitation source. Using a two-photon confocal microscopy system, it may be possible to measure the resulting Sm^{3+} and Sm^{2+} within a selected depth without bleaching the surrounding volume. Such measurements would be of great interest for experimentally validating simulations over multiple energies and volume depths within dosimetric samples.

6. Sm ion implanted samples showed successful conversion of $Sm^{3+} \rightarrow Sm^{2+}$, demonstrating the possibility of this technique within a thin volume near the surface of the sample. However, this technique was ultimately limited by overlapping defects related to either x-ray or implantation defects. It is possible that thin film deposition of Sm-doped FA glass samples may result in valence conversion without resulting overlapping PL signals and can be used for measurement of surface dose.